A coherent microwave interface for manipulation of single optical photons

BALL, SIMON,WILLIAM

A coherent microwave interface for manipulation of single optical photons

Simon William Ball

A thesis submitted in partial fulfilment

of the requirements for the degree of

Doctor of Philosophy

Department of Physics
University of Durham

November 2017

Abstract

This thesis proposes a means of implementing quantum information processing using photonic qubits as information carriers. Electromagnetically-induced transparency (EIT) is used to store information encoded in photons into Rydberg excitations in a cloud of cold atoms, where strong dipole-dipole interactions induce interactions between qubits. After a storage time, information is mapped back into photons collectively emitted from the cloud again via EIT.

A new experimental apparatus is built to implement non-linear Rydberg quantum optics. A high repetition rate is achieved owing to a 2D-MOT atom source, and high optical resolution for trapping and probing microscopic atomic ensembles is achieved by the use of aspheric lenses inside the vacuum chamber. A new, high resolution computer control scheme is implemented.

This thesis demonstrates that, during the holding time, multiple collective Rydberg excitations at a controlled separation interact with each other to imprint a non-uniform phase gradient resulting in anti-correlation of photon emission. Interactions are observed at up to 15 times the wavelength of the photonic qubits. These long range interactions offer a promising approach to scaling all-optical quantum computing.

Applying resonant microwave fields during the storage time is demonstrated to offer a competitive method of performing sensitive microwave electrometry. A sensitivity of $12 \pm 7\,\mu\mathrm{V\,cm^{-1}}\,\sqrt{\mathrm{Hz}}^{-1}$ is found at a frequency of 7.7 GHz. The high sensitivity is shown to arise from remnant, Rydberg excitations providing an additional source of atom loss from the atomic ensemble, leading to a suppression of photon storage and retrieval efficiency. An additional stage of microwave driving to sanitise the atomic ensemble for recycling is shown to successfully suppress the atom-loss mechanism.

Abstract

The use of successive microwave pulses is shown to provide a feasible approach to interfacing microwave and optical quantum information processing systems. Information encoded as the presence or absence of a microwave field is translated into information encoded as early or late retrieval of single photons, demonstrating proof of principle for an approach to implementing a proposal for an all-optical controlled-z gate.

Externally driven microwave fields are used to provide rapid, low-loss modulation of the signal retrieved from an atomic ensemble, demonstrating the proof of principle of implementing a probabilistic single photon source that can intensity modulate with low-loss at frequencies of at least 27 MHz, with evidence that modulation may be achievable at rates in excess of 500 MHz.

Declaration

The work in this thesis is based on research carried out at the Department of Physics, Durham University. No part of this thesis has been submitted elsewhere for any other degree or qualification. Where presented material originates in joint work, the work of others has been indicated in the text.

Simon William Ball
Odense, 2017/11/20

Acknowledgements

Firstly, I must express my thanks to Charles Adams for his support and most especially for his tireless and infectious enthusiasm and creativity throughout my PhD. My thanks must also go to Matt Jones, as co-supervisor, for guidance, patience, and a certain relentless encouragement to work through the (many!) obstructions along the path. It has been a privilege to work with them both.

Likewise, I must extend my gratitude to the students and post-doctoral researchers of the Rydberg Quantum Optics team, without whose contributions this experiment would most likely still be in pieces. Hannes Busche's wealth of laboratory experience, driving perfectionism, and forceful opinions about the correct way to do things have been invaluable in building a functional, and mostly reliable, experiment. David Szwer's extensive knowledge and work with LabView and DExTer have made lasting impressions that now (if, perhaps, not then!) I greatly appreciate. Paul Huillery must receive my particular gratitude for the talent, motivation, and inspiring competence he made available in so many aspects: from nursing ailing laser systems back to health to crystal clear explanations of physical phenomena. Teodora Ilieva has my thanks for the many long hours spent together in the lab, helping to repair the apparatus following the Incident, and reminders to take regular coffee breaks to avoid going crazy. I wish her and Nicholas Spong the best of luck in operating the experiment after me.

I must also thank members of the AtMol research group, past and present, for the excellent working environment. Thanks must especially go to Ifan Hughes, whose superb lecture course 'Atoms, Photons, Qubits' inspired me to pursue research in this area to begin with. Kevin Weatherill, Simon Cornish, James Keaveney, Steve Hopkins, Danielle Boddy, Elizabeth Bridge, Robert Bettles, Ana Rakonjac, Nikola Šibalić, Dan Whiting,

Alistair Bounds and Pete Moloney have all helped in one way or another, through discussions of physics over tea, to providing excellent cake. My thanks go to past members - Tim Wiles for writing DExTer, for I doubt I could have produced such a useful and general purpose piece of kit; Dan Maxwell and Jon Pritchard for building a fine experiment on whose evolution and replacement I have worked.

I cannot fail to mention my gratitude to the technicians in the mechanical workshop, and especially Stephen Lishman and Malcolm Robertshaw for always being available to discuss my designs, and their explanations of how it should actually be done. Without Malcolm's machining skills, the apparatus would be very much the poorer.

Finally, my thanks to those outside academia for their continuing support and occasional showers of baked goods. To my parents, brother and sister: your advice about coffee was finally heeded, and eventually appreciated. To Kristine, for support through the years of laboratory work and months of writing: my unequivocal gratitude.

Contents

List of Figures

1. Introduction

This thesis describes work to realise a system that exhibits controllable non-linearity at the level of single optical photons. The motivation for producing such a system is outlined in the following section.

1.1. Aims and motivation

The invention of the laser in 1958 [1] provided a new tool well suited to the preparation, manipulation, and study, of the quantum state of particles. One area of particular interest is that of QIP[1]. Classically, information is stored as *bits* which have a well defined state: in the context of digital computing, this state may take *either* the value 0 *or* 1. Information stored in a quantum system is encoded in a *qubit*, or quantum bit, which exists in a superposition of 0 *and* 1. For certain classes of problems, information stored in a quantum system may be processed more efficiently than for information stored classically [2, 3].

A variety of quantum systems have been proposed as physical systems to implement quantum storage of information, such as ions [4], Rydberg atoms [5, 6], superconducting Josephson junctions [7, 8], electrons [9] and photons [10].

The work described in this thesis focuses on the latter: *optical* QIP using photons as information carriers. The ease of transmission and robustness against interaction with the environment make photons particularly attractive as information carriers, and they are already widely used as a communications medium between classical computers [11].

[1] Quantum information processing

To process information physically stored in the state of multiple qubits requires an interaction between those physical systems. The absence of strong interactions which renders photons such excellent information carriers substantially hinders their suitability as a medium for information processors. The experiments discussed in this thesis take two approaches to the problem of inducing interactions between optical qubits to achieve information processing:

- Constructing a system in which strong effective interactions between photons can be induced to permit processing in an all-optical scheme [12],
- Bypassing the problem by demonstrating a means by which information can be coherently transferred between different quantum systems with complementary strengths and weaknesses in a hybrid QIP scheme.

1.1.1. Effective photon-photon interactions

An interaction between photons is logically equivalent to a system which exhibits one form of behaviour in the presence of one photon, and a different behaviour in the presence of two. Such non-linearity is rare at low optical powers, and early evidence for non-linear behaviour was only found after the development of lasers provided high intensity fields [13]. Classical non-linear optics focuses on the study of these high intensity systems. Extensive work has been dedicated to the search for systems that exhibit non-linearity at progressively lower optical intensities, leading to the logical conclusion of non-linearity arising at the level of single photons [14, 15].

Non-linearity at the level of single photons principally requires a high probability of interaction between the single photon and some medium, commonly atoms or ions. A common method of achieving this strong coupling has been to place the atom and photon within a high quality cavity; an area of research that has been dubbed CQED[2]. In the microwave domain, these schemes have demonstrated non-linear behaviour at the level of single quanta [16, 17]. Optical cavities have also been used to demonstrate non-linearity

[2]Cavity quantum electrodynamics

at the single photon level [18, 19]. CQED has been used to demonstrate a number of all-optical device-like behaviours, such as switches [20, 21] and a deterministic quantum gate [22].

Rydberg non-linear optics

CQED offers an effective toolset to achieve the high coupling necessary between the single-photon light field and atom,[3] but requires that photons exist in the same cavity mode in order to interact with the *same* quantum emitter. An alternative scheme to mediate effective photon-photon interactions is to use a system that exhibits its own strong, long-ranged interactions, and that may also reversibly interact with the single photon field. In this way, the effect of one single photon may be transferred to a second photon that propagates nearby, but not in an identical mode. In this thesis, collective Rydberg excitations in an atomic ensemble are used as the underlying physical system. Highly excited Rydberg atoms exhibit strong dipolar interactions [5, 25] that may be observed at distances of many microns [26].

In Rydberg non-linear optics [27–29], EIT[4] [30–32] is used as a coherent method to reversibly map Rydberg interactions to a photonic field [33]. A second optical field is introduced that couples the medium to a third level: for Rydberg non-linear optics, this third level is a highly excited Rydberg state. In the simplest case of EIT, where both fields are resonant with atomic transitions, the coupling field renders the medium transparent to the first optical field (the 'probe' field). The creation of a single Rydberg excitation causes strong dipolar interactions which shift nearby atoms out of resonance, destroying the transparency and creating a blockaded volume in which exactly one excitation may exist [34–39].

By exerting dynamic control over the intensity of the control field, the propagation of the probe field may be controlled, and in the extreme case of switching off the control

[3] Or other media: non-linearity in a high-Q resonator has also been shown with other quantum systems, such as semiconductor quantum dots [23, 24].

[4] Electromagnetically-induced transparency

field, the probe field group velocity may be reduced to zero to reversibly store the field quanta as atomic spin-waves [40, 41]. Due to the dipole blockade effect arising from the use of Rydberg states, the system has been shown to act as an effective filter to emit non-classical states of light even when the input pulse is a classical, coherent state [42, 43]. Variations on the approach have been used to implement a deterministic single photon source [44], all-optical transistors [45–47], atom-photon entanglement [48], single photon subtraction [49, 50], optical phase shifters [51, 52] and microwave-switched light [53, 54].

Contactless effective photon-photon interactions

All-optical QIP has been attempted with strictly local non-linearities, such as the giant Kerr effect in EIT [55], but it has been shown that these cannot offer sufficiently strong interactions [56, 57]. The use of Rydberg states offers a potential route to overcome this limitation to allow for deterministic all-optical quantum gates [58, 59]. The long range nature of interactions between Rydberg excitations allows in principal for non-linearity to occur non-locally - that is, between photons propagating in separate, non-overlapping modes. A wide variety of techniques have been proposed to implement such gates [58–62].

This thesis expands on the work of H. Busche *et al* in demonstrating effective interactions between photons propagating in separate, non-overlapping, spatial modes [63]. In analogy to experiments that observe interaction behaviour as a function of separation between individual Rydberg excitations within a single mode by means of temporal resolution [37, 38, 64], we implement spatial resolution by the creation of two separate, side-by-side, channels in which photons may be stored as collective Rydberg excitations. Interactions are observed by anticorrelation in photon emission from light storage in the two channels, separated by a distance $\mathcal{O}(10\lambda)$, arising from disturbance of the spin-wave phase due to a nearby excitation [44, 53, 65, 66]. Similar work has demonstrated the ability to reliably generate a $\pi/2$ phase shift in independent modes [67].

1.1.2. Information transfer in a hybrid QIP scheme

QIP schemes have typically relied on minimising transfer between disparate physical systems as far as possible, due to the potential for decoherence, which is one of the motivations for achieving all-optical processing [10]. However, as noted no individual system presents as a perfect candidate. Hybrid QIP offers the potential to harness multiple schemes with complementary strengths [68–70]. One of the most basic tasks presented in QIP is the ability to coherent transfer quantum states between nodes of a processor [19, 71, 72].

In particular, while superconducting qubits have been demonstrated to exhibit remarkably high fidelity [73–78], efficient quantum state transport remains a hard problem due to extremely short coherence times [79, 80]. In order to minimise decoherence due to blackbody radiation, such qubits are typically confined to extremely bulky helium dilution refrigerators in order to achieve mK temperature environments. Recent work has begun to improve on this limitation, allowing multiple qubits (still in mK environments) to reliably communicate via a noisy channel only cooled to 4 K, which can be achieved more easily [81, 82]. However, such a communication scheme falls far short of the convenience of optical photons in fibres, if translation between the quantum systems can be reliably achieved.

Atomic [83, 84] and ionic [85, 86] qubit systems have also demonstrated considerable success as systems suitable to QIP, but likewise suffer from the ability to transfer information of the quantum state between physically discrete systems [87]. Optical photons offer ideal characteristics for translating this information, given a means of transferring information to the optical system.

Due to the long lifetime of Rydberg states [25], collective Rydberg excitations can be considered similarly to individual atom systems. Microwave fields are used to couple between nearby energy levels of these 'superatoms' [53]. Shifting population between states induces additional dipolar interactions that act as a stronger filter for retrieved Fock states [54].

Microwave driven single photon shaping

This thesis uses the extreme sensitivity of Rydberg excitations to microwave fields [25, 88–90] to demonstrate the ability to transfer information encoded as microwave photons to single optical photons. Microwave to optical interface techniques are an expanding area of study to take advantage of the strengths of optical photons as a communications medium [91–96].

Earlier work by D. Maxwell [53, 54] studying the behaviour of collective Rydberg excitations exposed to microwave fields resonant with Rydberg-Rydberg transitions is revisited. This previous work found behaviour that was not consistent with contemporary theory [97]. The collective excitations underwent coherent Rabi oscillations in retrieval probability, as expected, but demonstrated an unexpected suppression in retrieval probability at certain rotation angles, with the degree of suppression shown to be dependent on the number of collective Rydberg excitations simultaneously present.

This work is reproduced as a potential means of performing sensitive microwave electrometry, and yields sensitivity competitive with published results [89]. It is then extended by considering previously neglected atomic population, and the suppression is shown to be a function of accelerated atom loss from the atomic ensemble rather than directly as a result of interactions between collective excitations. By applying multiple microwave pulses to more fully sanitise the experimental medium, the expected Rabi oscillation profile emerges. The use of multiple microwave pulses are then used to produce delayed photon retrieval. This serves as proof-of-principle for converting information encoded in microwave photons into early or late emission of single optical photons.

By extending the methods used to reproduce and study D. Maxwell's work, rapid amplitude modulation of single photons is demonstrated. Applying a microwave field during the retrieval window, simultaneously with the coupling laser beam, results in Rabi oscillations to a dark Rydberg state from which no retrieval occurs. By temporarily shelving excitations in this dark state, the resulting retrieved photons can have their temporal mode shaped. In comparison to electro-optical techniques which require a herald photon [98], the time dependence of photon retrieval presents a reliable trigger. Modulation

techniques exhibit low loss in comparison to conventional EOM[5] based techniques, while offering theoretically comparable bandwidth. Future upgrades to improve the control bandwidth in principle permit the creation of arbitrary photon profiles, such as those demonstrated in CQED systems [99, 100].

1.2. Thesis structure

This thesis contains the following chapters:

- Chapter 2 reviews the important properties of dipole interactions between atoms, and the important phenomenon of dipole blockade.
- Chapter 3 discusses the interactions between atoms and multiple electromagnetic field. The concept of EIT and photon storage are introduced and summarised.
- Chapter 4 introduces the new experimental apparatus, and presents some some characterising data to demonstrate its performance.
- Chapter 5 introduces and demonstrates effective contactless interactions between non-overlapping single photons in spatially distinct channels.
- Chapter 6 discusses the use of collective Rydberg excitations as a tool for performing sensitive microwave electrometry. It demonstrates that the high sensitivity arises from Rydberg-mediated atom loss, and re-interprets previous work in that light.
- Chapter 7 demonstrates the use of a second Rydberg state, as an interface to control the optical output of the system via an applied microwave field. Two approaches are pursued: converting information encoded by the presence or absence of a microwave photon into early or late emission of an optical photon; and high speed, low-loss intensity modulation of an optical photon.

[5] Electro-optical modulator

1.3. Rydberg quantum optics in Durham

Scientific experiments of this level of complexity do not take place in a vacuum.[6] The work presented here has benefited from the contributions of the present and past members of the Rydberg Quantum Optics team at Durham University over the past decade.

The experimental apparatus discussed in this thesis is the third generation built to study quantum optics in a cold atomic medium with Rydberg character. The first generation was built by K. Weatherill and J. Pritchard, and used to demonstrate the potential of Rydberg physics for generating strong optical non-linearities at the level of few photons [27, 101, 102].

The second generation was built by J. Pritchard, D. Maxwell and D. Paredes-Barato to study the storage of photons as collective Rydberg excitations. This generation represented a step change by confining the atomic ensemble to a microscopic volume with dimensions of the same order as the dipole blockade radius. A key result of the second generation was to demonstrate the potential to apply a microwave field to the collective excitation to drive a transition to a nearby Rydberg state. The application of the microwave field resulted in a precisely controlled adjustment of the interaction potential between nearby collective excitations which could be detected by the statistics of the subsequently emitted photons [53, 54, 103]. The approach was subsequently proposed as a method by which to implement an all-optical quantum controlled-phase logic gate [61, 104].

The third generation experimental apparatus, discussed in chapter 4, was proposed in order to overcome certain limitations of the second generation apparatus while maintaining its strengths. It was designed by K. Weatherill and H. Busche, and subsequently built jointly by H. Busche and the author. The third generation remains in operation, as of the date of publishing, operated by T. Ilieva and N. Spong. The work of H. Busche gives an overview of the early results produced by this latest generation [105], resulting in papers published jointly with the author [63, 106]. The most notable result is the

[6] Metaphorically speaking

demonstration of optical non-linearity for a photon within an atomic ensemble arising from the presence in a nearby, but separate and non-contiguous atomic ensemble, of a second photon [63]. This work was carried out by H. Busche, and subsequently extended by the author (discussed in chapter 5).

In addition to the extension of H. Busche's work, the author's work in this thesis focuses on reproducing a set of results observed by D. Maxwell that were not well explained at the time. It is intended to combine the non-contact interactions demonstrated with H. Busche with the microwave-controlled variable interactions to implement the all-optical logic gate proposed by D. Paredes-Barato.

1.4. Publications arising from this work

- H. Busche, S. W. Ball and P. Huillery, *A high repetition rate experimental setup for quantum non-linear optics with cold Rydberg atoms*, Eur. Phys. J. Special Topics **225**, 2839-2861 (2016). [106]
- H. Busche, P. Huillery, S. W. Ball, T. Ilieva, M. P. A. Jones and C. S. Adams, *Contactless non-linear optics mediated by long-range Rydberg interactions*, Nat. Phys. **13** 655-658 (2017). [63]

2. Rydberg atoms

In order to realise the goal of inducing effective photon-photon interactions, this project performs a coherent, reversible, mapping of quantum information encoded by the presence or absence of photons into atomic excitations (covered in chapter 3) in order to take advantage of strong and controllable atom-atom interactions.

This chapter will cover the pertinent physics of Rydberg atoms, and the various effects arising from that physics that will offer these strong, controlled, interactions.

2.1. Rydberg states

A Rydberg state is a state of a atom with a high principal quantum number, n. These states can exist in a wide variety of physical systems; but in the work presented in this thesis, all experiments are performed using cold rubidium (^{87}Rb) atoms.

Many Rydberg properties may be well understood by the use of the simple, classical, Bohr model of the hydrogen atom, in which a point-like electron orbits a point-like proton. The electron experiences a simple, Coulombic potential, dependent on the radius of its orbit, which depends on the principal quantum number, n. The binding energy is given by

$$W = -\frac{\mathrm{Ry_H}}{n^2}, \tag{2.1}$$

where Ry is the element-specific Rydberg constant. As n increases, the electron orbits at a greater distance, and experiences a weaker potential. Consequently, the required ionisation energy becomes very low, and the electron is extremely susceptible to the effects of external electric fields [25]. For atoms other than hydrogen, where the proton number $Z > 1$ and the nucleus is shielded by closed electron shells, this model breaks

Property	Scaling
Orbital radius	n^2
Binding energy	n^{-2}
Dipole moment	n^2
Radiative lifetime	n^3
Energy separation	n^{-3}
Polarisability	n^7

Table 2.1.: Scaling laws for properties of Rydberg states.

down at low n values, due to screening of the nuclear charge. For atoms with a similar electronic structure to hydrogen (alkali metals such as rubidium), the difference from hydrogen is given by the quantum defect, δ_{nlj}, such that

$$W = -\frac{\mathrm{Ry}_{\mathrm{Rb}}}{(n-\delta_{nlj})^2}. \tag{2.2}$$

The quantum defect is greatest for the states with the lowest orbital angular momentum l. These states have highly elliptical electron orbits, resulting in a greater deviation from a purely Colombic potential due to penetrating the screening electron shell [25]. For rubidium, these quantum defects have been measured and are available in the literature [107–109].

This very simple model with its n^2 radius scaling allows the scaling of several other key properties to be derived [25]. These are shown in table 2.1.

The n^2 scaling of the dipole moment allows the interaction strength between Rydberg atoms to be tuned over a large dynamic range through careful choice of the atomic state used [5]. The narrow energy spacing of adjacent states n^{-3} makes this tuning highly experimentally convenient, where the gain bandwidth of a diode laser may allow a single instrument to select from a large choice of states, without requiring many different excitation sources.

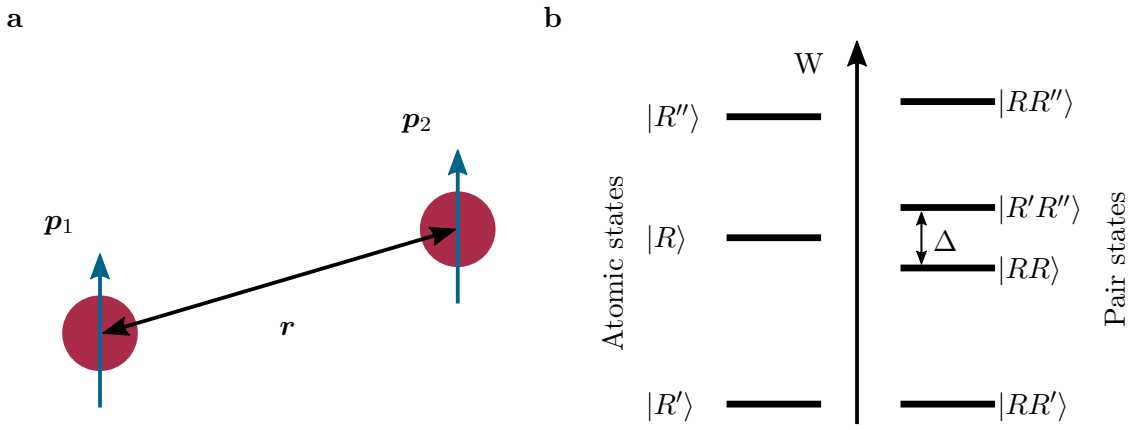

Figure 2.1.: Dipole-dipole interactions between a pair of atoms. *a*: induced dipole moments $\boldsymbol{p}_{1,2}$ separated by distance $\boldsymbol{r}$. *b*: Energetically local states in atomic and pair state bases. The latter show near-resonant states coupled by the dipole-dipole interactions, with an energy separation Δ.

2.2. Dipole-dipole interactions

Consider a pair of atoms, 1 and 2, separated by distance $\boldsymbol{r}$, each initially in the same state $|R\rangle = |n, l, j\rangle$, as shown in figure 2.1 (a). The presence of the second atom results in a polarisation of the charge distribution of the first atom and vice versa. The electric dipole-dipole interaction energy between the two atoms can be written as [110]

$$V(\boldsymbol{r}) = \frac{1}{4\pi\epsilon_0}\left(\frac{\boldsymbol{p}_1 \cdot \boldsymbol{p}_2}{r^3} - 3\frac{(\boldsymbol{p}_1 \cdot \boldsymbol{r})(\boldsymbol{p}_2 \cdot \boldsymbol{r})}{r^5}\right), \tag{2.3}$$

where $\boldsymbol{p}_{1,2}$ are the induced dipole moments of these atoms. The energy shift due to the dipole dipole interaction can be illustrated by considering the pair state basis (see figure 2.1b). At infinite distance $r = \infty$, such that the interaction energy is zero, the pair state is given by $|RR\rangle$. At finite distance, this initial state is coupled to the state $|R'R''\rangle$ by the interaction $V(r)$ with an energy separation given by

$$\Delta = W_{|R'\rangle} + W_{|R''\rangle} - 2W_{|R\rangle}, \tag{2.4}$$

which is equal to the difference in energies of the pair states at infinite distance.

The eigenvalues of the Hamiltonian describing this interaction are

$$\lambda_{\pm} = \frac{\Delta \pm \sqrt{\Delta^2 + 4V(r)^2}}{2}. \tag{2.5}$$

From this, it can be seen that the spatial dependence of the dipole-dipole interaction will behave differently depending on whether the Δ or $V(r)$ terms dominate.

The short range limit such that $\Delta \ll V(r)$ is called the resonant dipole-dipole regime, as the magnitude of the interaction is of the same order as the energy defect Δ [111]. The shift in energy is given by

$$\Delta W = \pm V(r) = \pm \frac{C_3(n)}{r^3} \propto \frac{n^4}{r^3}. \tag{2.6}$$

The n scaling is given by $V(r) \propto p^2 \propto (n^2)^2$ [5]

The long range limit where $\Delta \gg V(r)$ is called the vdW[1] regime. The shift in energy is given by

$$\Delta W = -\frac{V(r)^2}{\Delta} = \frac{C_6(n)}{r^6} \propto \frac{n^{11}}{r^6}. \tag{2.7}$$

In addition to the n scaling of $V(r)$, an additional term is contributed by $\Delta \propto n^{-3}$ [5].

The two regimes cross over at the vdW radius $V(r_{\text{vdW}}) = \Delta$, such that $r_{\text{vdW}} = \sqrt[6]{|C_6/\Delta|} \propto n^{7/3}$.

External field control

Thus far, this treatment has considered only the interaction between two atoms in identical states $|R\rangle$, in which case the interaction behaviour may only be tuned by adjusting the inter-atomic spacing. An experimentally easier alternative is to apply an external field to induce additional energy shifts in order to bring the experimental system into one regime or the other.

DC electric fields have been used to Stark shift pair states into resonance [112–114], as have off-resonant microwave frequency AC fields [115]. In these methods, the states $|R\rangle$, $|R'\rangle$ and $|R''\rangle$ experience differential DC- or AC- Stark shifts such that Δ is minimised and the initial state $|RR\rangle$ is degenerate with $|R'R''\rangle$, leading to resonant dipole-dipole

[1] van-der-Waals

interactions. These $\Delta = 0$ resonances are called Förster resonances [114, 116]. Microwave dressing of Rydberg states allows arbitrary states to be tuned into resonance [117, 118].

An alternative technique is to couple resonantly to a nearby opposite parity Rydberg state $|R'\rangle$ via microwave field, to produce the initial atom pair $|R'R\rangle$, which is exactly resonant with the state $|RR'\rangle$. In this case, resonant dipole-dipole interactions dominate [53, 118, 119]. This technique will be used extensively for the work presented in this thesis.

2.3. Dipole blockade

Dipole-dipole interactions play a significant role in the process of creating multiple Rydberg excitations in the atomic ensembles considered in this thesis. In the work presented in this thesis, Rydberg excitations are created by illuminating an atomic ensemble with laser light resonant with the transition from ground state $|g\rangle$ to Rydberg state $|R\rangle$. The lasers provide frequency-stabilised, narrow linewidth light (described in detail in sections 4.1.2 and 4.4.1).

Consider a pair of atoms in the ground state separated by distance $\boldsymbol{r}$. The pair state is given by $|gg\rangle$. It is assumed that the inter-atomic separation $\boldsymbol{r}$ is never small enough such that interactions between ground state atoms contribute a meaningful correction, such that the energy of the state $|gg\rangle$ is not distance dependent. Likewise, it is assumed that the interaction strength between a Rydberg excitation and a ground state atom is negligible at all achievable separations. The atom pair is illuminated by a laser source with a linewidth γ that is resonant with the transition from $|g\rangle$ to $|R\rangle$. This is shown in figure 2.2.

In the presence of this laser, only a single Rydberg excitation can be created, $1/\sqrt{2}(|gR\rangle \pm |Rg\rangle)$, regardless of inter-atomic separation. For large separations, the double Rydberg state $|RR\rangle$ can also be excited. At smaller separations, the interactions between Rydberg excitations shift the energy of $|RR\rangle$, such that the laser is no longer resonant. At some critical distance r_{B}, the shift in energy of the $|RR\rangle$ state exceeds the linewidth of the laser, $\hbar\gamma$.[2] This effective detuning strongly suppresses the probability of excitation

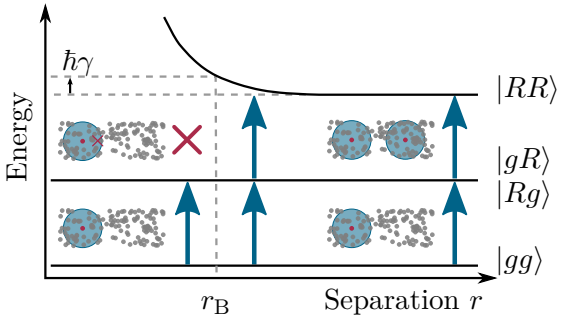

Figure 2.2.: Dipole blockade. A pair of atoms in the ground state, $|gg\rangle$, have no interactions at any achievable inter-atomic separation. Exciting one atom to $1/\sqrt{2}(|gR\rangle \pm |Rg\rangle)$ is always possible. For inter-atomic separations less than r_B, the energy shift of $|RR\rangle$ is greater than the excitation linewidth. Within this radius, the interaction-induced detuning prevents further Rydberg excitations.

to the $|RR\rangle$ state. This effect is commonly referred to as *dipole blockade* [34, 39, 120].

The blockade radius, r_B can be found by equating the form of the interaction with the linewidth of the excitation source. Assuming that the interaction is of the vdW form, as is typical during Rydberg excitation in the work presented in this thesis, this gives [121]

$$r_B = \left(\frac{C_6}{\hbar\Gamma}\right)^{\frac{1}{6}}. \tag{2.8}$$

Consequently, in the vdW regime, the blockade radius scales $\propto n^{11/6}$, which has been observed experimentally [26]. For a given ensemble of atoms, for sufficiently large n such that r_B is much greater than the average inter-atomic separation, then each Rydberg excitation will blockade many atoms. Within this group, the excitation is shared by all atoms [34], which produces several collective effects. Principally, the blockaded atom ensemble can produce directional emission of a single photon [122, 123], an effect which will be exploited to perform the photon storage protocol described in detail in section 3.2.3. Blockade behaviour has been observed to act as a filter that can produce sub-

[2]The effective linewidth is set by one of three scales. In the simplest case, the effective linewidth is the excitation source linewidth, γ. If the transition is power broadened, the effective linewidth will be dominated by the Rabi frequency Ω. If the source is rapidly pulsed, the linewidth will be Fourier broadened to $1/t_{\text{pulse}}$.

Poissonian counting statistics [124–126].

Within a blockade radius of an excitation, the energy shift prevents further excitation. This behaviour was first observed as a saturation of the number of excitations that could be simultaneously created in a cold atomic gas, due to each excitation blockading many additional atoms [35, 36]. Close to saturation, this behaviour can lead to emergent ordering [97] and the development of crystalline behaviour [127, 128].

3. Atom-light interactions

This chapter will discuss the interaction between a light field and an ensemble of atoms. In section 3.1, a simple two-level system will be introduced, and studied using a semi-classical treatment, in which a quantised atom interacts with a classical EM[1] field. Section 3.2 introduces a third level and a second field, using the same approach as the two-level system. Electromagnetically induced transparency, coherent population trapping, and photon storage, phenomena arising from the presence of a third level are discussed. Section 3.3 briefly discusses the addition of a fourth level and a third field.

A monochromatic light field $\boldsymbol{\mathcal{E}}$ applied to a dielectric medium produces a polarisation

$$\boldsymbol{P} = \epsilon_0 \chi \boldsymbol{\mathcal{E}}, \tag{3.1}$$

where ϵ_0 is the vacuum permittivity and χ is the susceptibility of the medium. The polarisation of the medium, $\boldsymbol{P}$, is the average dipole moment $\langle \boldsymbol{d} \rangle$ per unit volume of the dielectric medium

$$\boldsymbol{P} = \langle \boldsymbol{d} \rangle / V. \tag{3.2}$$

Passing through the medium leads to some change in the transmitted intensity and phase of the electric field. Provided that χ is small and the electric field intensity obeys the requirement $I_0 \ll I_{\text{sat}}$, these can be characterised by the Beer-Lambert law

$$T = \frac{I}{I_0} = e^{-k \operatorname{Im}(\chi) l}, \tag{3.3}$$

where I is the intensity after transmission through a length l of the medium, k is the wave-vector of the field, and $\operatorname{Im}(\chi)$ is the imaginary component of the susceptibility χ.

[1] Electromagnetic

Transmission is often described by the logarithmic quantity OD[2]: $\mathrm{OD} = -k\,\mathrm{Im}(\chi)l$.

Here we see that absorption in the medium is linked to the imaginary part of the susceptibility. The real component is responsible for a phase shift of the form $\Delta\phi = k\,\mathrm{Re}(\chi)l/2$. This is related to the refractive index of the medium, n_{ri}, by $n_{\mathrm{ri}} = \sqrt{1 + \mathrm{Re}(\chi)}$.

3.1. The two-level atom

We consider an atom with two states, $|1\rangle$ and $|2\rangle$, separated by a resonant frequency ω_{21} and in the presence of a classical probing laser field with a frequency of ω_p. The probe field is detuned by $\Delta_p = \omega_p - \omega_{21}$. It has a Rabi frequency Ω_p. Spontaneous emission gives a decay rate from $|2\rangle$ of Γ_2. The linewidth of the probe field, γ_p, contributes additional decoherence: $\gamma_2 = \Gamma_2/2 + \gamma_p$ [129]. This atom is shown in figure 3.1.

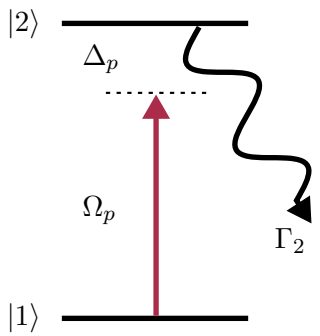

Figure 3.1.: The two level atom. A probing laser field is used to excite from $|1\rangle$ to $|2\rangle$. It is detuned from resonance by Δ_p and has a Rabi frequency of Ω_p. Population in state $|2\rangle$ decays at a rate Γ_2.

3.1.1. Time evolution of the atomic state

The evolution of the atom in the presence of the probing light field can be obtained by using the time dependent Schrödinger equation

$$i\hbar\frac{\partial}{\partial t}|\psi\rangle = \mathcal{H}_{\mathrm{tot}}|\psi\rangle\,, \tag{3.4}$$

[2]Optical depth

where $\mathcal{H}_{\text{tot}}$ is the Hamiltonian for the combined atom-light system. This is given by

$$\mathcal{H}_{\text{tot}} = \mathcal{H}_{\text{atom}} + \mathcal{H}_{\text{int}}, \tag{3.5}$$

where $\mathcal{H}_{\text{atom}}$ is the Hamiltonian for the atom in the absence of any light field and $\mathcal{H}_{\text{int}}$ is the Hamiltonian describing the interaction between the atom and the probing laser field.

We make the assumption that only the interaction between the light field and the electric dipole moment of the atom is considered, neglecting higher order terms as minor contributions [130]. Additionally, we make the approximation that the electric field has no spatial variation as the wavelength of the light field is much greater than the extent of the atom (electric dipole assumption) [131].

Consequently, the interaction Hamiltonian is given by

$$\mathcal{H}_{\text{int}} = -\boldsymbol{d} \cdot \boldsymbol{\mathcal{E}}, \tag{3.6}$$

where $\boldsymbol{d}$ is the electric dipole moment and $\boldsymbol{\mathcal{E}} = \mathcal{E}_0 \cos(\omega_p t)$ is the classical probing laser field. The electric dipole moment describes the splitting between positive and negative electric charges within the atomic system, and characterises the coupling between atomic levels. In the considered two-level atomic system, it can be found by

$$\boldsymbol{d} = d_{21} \left(|2\rangle\langle 1| + |1\rangle\langle 2| \right). \tag{3.7}$$

Recasting the electric field in terms of exponentials, the interaction Hamiltonian is therefore

$$\mathcal{H}_{\text{int}} = \frac{d_{21}\mathcal{E}_0}{2} \left(|2\rangle\langle 1| + |1\rangle\langle 2| \right) \left(e^{i\omega_p t} + e^{-i\omega_p t} \right). \tag{3.8}$$

By introducing the angular Rabi frequency $\Omega_p = d_{12}\mathcal{E}_0/\hbar$ and making the rotating wave approximation [132], we can rewrite this as

$$\mathcal{H}_{\text{int}} = \frac{\hbar}{2} \begin{pmatrix} 0 & \Omega_p e^{i\omega_p t} \\ \Omega_p e^{-i\omega_p t} & 0 \end{pmatrix}. \tag{3.9}$$

3.1.2. The density matrix formalism

The wavefunction of the atom can be expressed as

$$|\psi\rangle = \sum_a c_a |a\rangle \tag{3.10}$$

where the coefficient c_a is the complex probability amplitude of the atom being in state $|a\rangle$. We can represent the density operator for the state of the atom as $\hat{\rho} = |\psi\rangle\langle\psi|$. For a two-level atom, this can be expressed as a density matrix

$$\rho = \begin{pmatrix} c_1 c_1^* & c_1 c_2^* \\ c_2 c_1^* & c_2 c_2^* \end{pmatrix} = \begin{pmatrix} \rho_{11} & \rho_{12} \\ \rho_{21} & \rho_{22} \end{pmatrix}, \tag{3.11}$$

where the diagonal terms ρ_{aa} give the probability of finding the atom in state $|a\rangle$ and the off-diagonal terms ρ_{ab} give the coherences between states $|a\rangle$ and $|b\rangle$ [130]. In this formalism, we can express the atomic Hamiltonian by

$$\mathcal{H}_{\text{atom}} = \begin{pmatrix} \hbar\omega_1 & 0 \\ 0 & \hbar\omega_2 \end{pmatrix} = \begin{pmatrix} 0 & 0 \\ 0 & \hbar\omega_{12} \end{pmatrix}. \tag{3.12}$$

Substituting equations 3.9 and 3.12 into equation 3.5, the total Hamiltonian can be written in matrix form as

$$\mathcal{H}_{\text{tot}} = \frac{\hbar}{2} \begin{pmatrix} 0 & \Omega_p e^{i\omega_p t} \\ \Omega_p e^{-i\omega_p t} & 2\omega_{12} \end{pmatrix}. \tag{3.13}$$

Where the time evolution is described by a Hamiltonian, the time evolution of the density matrix can be determined from Liouville's Equation [130].

$$\frac{\mathrm{d}\rho}{\mathrm{d}t} = \frac{i}{\hbar}[\rho, \mathcal{H}_{\text{tot}}]. \tag{3.14}$$

Using the density matrix formalism permits the inclusion of decoherent processes that cannot be described by a Hamiltonian, such as spontaneous emission. This is accounted for by the inclusion of a phenomenological decay term $\hat{\mathcal{L}}$. The resulting equation is called the Lindblad, or master, equation [133].

$$\frac{\mathrm{d}\rho}{\mathrm{d}t} = \frac{i}{\hbar}[\rho, \mathcal{H}_{\text{tot}}] + \hat{\mathcal{L}}. \tag{3.15}$$

For a two-level system, this decay term is

$$\hat{\mathcal{L}} = \frac{1}{2}\begin{pmatrix} 2\Gamma_2\rho_{22} & -\Gamma_2\tilde{\rho}_{12} \\ -\Gamma_2\tilde{\rho}_{21} & -2\Gamma_2\rho_{22} \end{pmatrix}, \tag{3.16}$$

where $\tilde{\rho}_{12} = \rho_{12}e^{-i\omega_p t}$, $\tilde{\rho}_{21} = \rho_{21}e^{i\omega_p t}$ and $\tilde{\rho}_{ab} = \tilde{\rho}^*_{ba}$.

3.1.3. Optical Bloch equations

By substituting equations 3.14 and 3.16 into the master equation (3.15), the time evolution of the density matrix can be obtained as a series of coupled, first order differential equations, known as the optical Bloch equations [134]:

$$\dot{\rho}_{11} = \frac{i\Omega_p}{2}(\tilde{\rho}_{12} - \tilde{\rho}_{21}) + \Gamma_2\rho_{22}, \tag{3.17a}$$

$$\dot{\tilde{\rho}}_{12} = \frac{i\Omega_p}{2}(\rho_{11} - \rho_{22}) + \tilde{\rho}_{12}\left(-i\Delta_p - \frac{\Gamma_2}{2}\right), \tag{3.17b}$$

$$\dot{\rho}_{22} = \frac{i\Omega_p}{2}(\tilde{\rho}_{21} - \tilde{\rho}_{12}) - \Gamma_2\rho_{22}, \tag{3.17c}$$

$$\dot{\tilde{\rho}}_{21} = \frac{i\Omega_p}{2}(\rho_{22} - \rho_{11}) + \tilde{\rho}_{21}\left(i\Delta_p - \frac{\Gamma_2}{2}\right). \tag{3.17d}$$

In the steady state where $\frac{\mathrm{d}\rho}{\mathrm{d}t} = 0$, and assuming conservation of population where $\rho_{11} + \rho_{22} = 1$, these four equations can be further reduced:

$$\tilde{\rho}_{21} = \frac{i\Omega_p/2}{\gamma_2 - i\Delta_p}(\rho_{22} - \rho_{11}). \tag{3.18}$$

3.1.4. Macroscopic optical response

For an atomic ensemble with a constant number density $\mathcal{N}$, the susceptibility of the medium can be calculated from the off-diagonal coherences of the density matrix [102, 129]:

$$\chi = -\frac{2\mathcal{N}d_{21}^2}{\epsilon_0\hbar\Omega_p}\tilde{\rho_{21}} \tag{3.19}$$

In the limit that the Rabi frequency is low ($\Omega_p \ll \Gamma_2$), the population exists almost entirely in the lower state, $|1\rangle$ ($\rho_{11} \approx 1$). Using this approximation, equations 3.18 and 3.19 yield

$$\chi = \frac{i\mathcal{N}d_{21}^2}{\epsilon_0\hbar}\frac{1}{\gamma_2 - i\Delta_p} = \mathrm{Re}(\chi) + i\,\mathrm{Im}(\chi). \tag{3.20}$$

The component $\mathrm{Re}(\chi)$ has a dispersive lineshape, while $\mathrm{Im}(\chi)$ has a Lorentzian lineshape. These components are shown in figure 3.2. The optical properties of the system are characterised by a refractive index, $n_{\mathrm{ri}} = \sqrt{1+\chi}$. Where $|\chi| << 1$, this is well described by the approximation $n_{\mathrm{ri}} \approx 1 + \chi/2$.

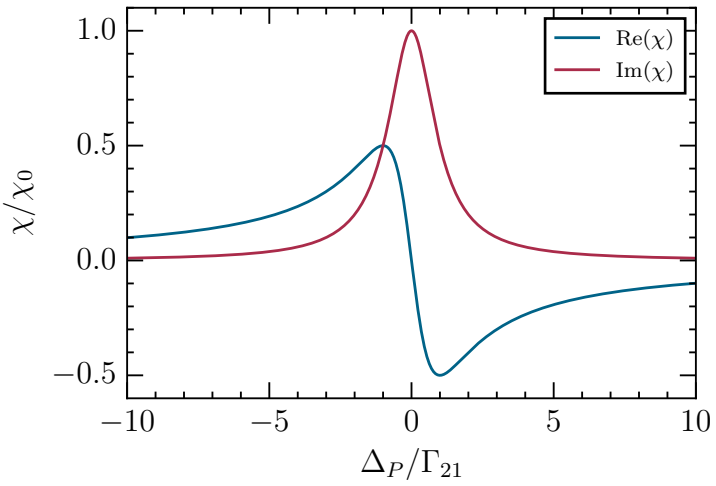

Figure 3.2.: Susceptibility of a two-level atom. Real (blue) and imaginary (red) components of the steady state susceptibility of the two level system as a function of detuning of the probing field for $\Omega_p = 0.1\gamma_{21}$. The susceptibility is normalised to the susceptibility on resonance, $\chi_0 = 2\mathcal{N}d_{21}^2/\epsilon_0\hbar\gamma_{21}$.

3.1.5. Rabi oscillations

Abandoning the approximation that $\rho_{11} = 1$, the evolution of the state populations in the presence of a strong driving field can be considered. In the special case of negligible spontaneous emission from the excited state, the probability that the atom is in the ground state is

$$P(|1\rangle) = \cos^2\left(\frac{\Theta}{2}\right), \tag{3.21}$$

where the rotation angle $\Theta = \Omega_p t$. By setting $\Theta = \pi$, population can be transferred from $|1\rangle$ to $|2\rangle$. This is commonly referred to as a π-*pulse*. Similarly, a 2π-pulse will bring the population from $|1\rangle$ back to $|1\rangle$, via $|2\rangle$, with an additional π phase shift.

In the more general case where spontaneous emission occurs from the excited state, the Lindblad equation (3.15) can be solved numerically to evaluate the probability of the atom being in a given state. Figure 3.3 plots the excited state population fraction over time in the case of an on-resonant probe ($\Delta_p = 0$) for a range of decay rates. Where the decay rate is small, there are high-contrast oscillations between the ground and excited state. As the ratio between the driving and decay frequency decreases, these oscillations become damped and reach a steady state more rapidly.

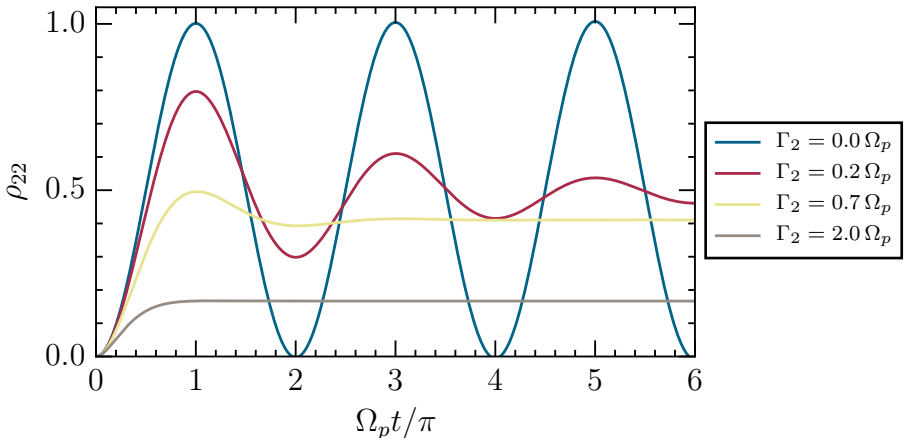

Figure 3.3.: Rabi oscillations in a two level atom. The excited state population fraction is plotted as a function of time for different decay rates.

3.2. The three-level atom

A third level, $|3\rangle$ is added, separated from $|2\rangle$ by resonant frequency ω_{32}. A coupling laser field is added, ω_c, detuned by $\Delta_c = \omega_c - \omega_{32}$ and with a linewidth of γ_c. It has a Rabi frequency Ω_c. Spontaneous emission from $|3\rangle$ is given by Γ_3. Of the three possible configurations of a three level system, a ladder scheme is used in this work [129], which is illustrated in figure 3.4. Throughout this work, we distinguish between the *probe* laser

ω_p coupling the ground and intermediate states ($|1\rangle$ to $|2\rangle$), which is used for detection; and the *coupling* laser ω_c coupling the intermediate and most excited states ($|2\rangle$ to $|3\rangle$), which is not detected directly.

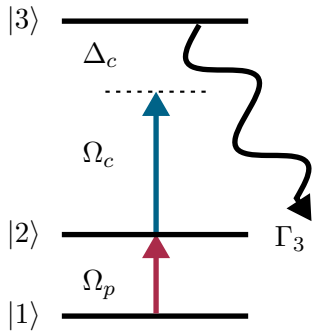

Figure 3.4.: The three level atom. A second laser field with Rabi frequency Ω_c and detuning Δ_c is added to couple $|2\rangle$ to $|3\rangle$ in a ladder scheme.

3.2.1. Electromagnetically induced transparency

The three level system can be understood using the same process as that followed for the two level system in section 3.1.1. Using the dipole and rotating wave approximations, the Hamiltonian of the system is given by

$$\mathcal{H}_{\text{tot}} = \mathcal{H}_{\text{atom}} + \mathcal{H}_{\text{int}} = \frac{\hbar}{2}\begin{pmatrix} 0 & \Omega_p & 0 \\ \Omega_p & -2\Delta_p & \Omega_c \\ 0 & \Omega_c & -2(\Delta_p + \Delta_c) \end{pmatrix}. \tag{3.22}$$

The off-diagonal coupling provided by Ω_p and Ω_c means that the states $|1\rangle$, $|2\rangle$, $|3\rangle$ are no longer eigenstates of the atomic system. In the two-photon resonance condition $\Delta_p + \Delta_c = 0$, diagonalising the matrix to find the new eigenstates yields

$$\left|a^+\right\rangle = \sin(\theta)\sin(\phi)\,|1\rangle + \cos(\theta)\,|2\rangle + \cos(\theta)\sin(\phi)\,|3\rangle\,, \tag{3.23a}$$

$$\left|a^0\right\rangle = \cos(\theta)\,|1\rangle - \sin(\theta)\,|3\rangle\,, \tag{3.23b}$$

$$|a^-\rangle = \sin(\theta)\cos(\phi)\,|1\rangle - \sin(\theta)\,|2\rangle + \cos(\theta)\cos(\phi)\,|3\rangle\,, \tag{3.23c}$$

with the mixing angles given by

$$\tan(\theta) = \frac{\Omega_p}{\Omega_c}, \tag{3.24a}$$

$$\tan(2\phi) = \frac{\sqrt{\Omega_p^2 + \Omega_c^2}}{\Delta_p}. \tag{3.24b}$$

The energies of the $|a^{\pm}\rangle$ states are shifted relative to $|a^0\rangle$ by [32, 117]:

$$\hbar\omega_{\pm} = \frac{\hbar}{2}\left(\Delta_p \pm \sqrt{\Delta_p^2 + \Omega_p^2\Omega_c^2}\right). \tag{3.25}$$

States $|a^{\pm}\rangle$ radiate to populate $|a^0\rangle$ on a timescale of $1/\Gamma_2$. Because $|a^0\rangle$ has no contribution from $|2\rangle$, it does not interact with the probe laser Ω_p. In the context of a lambda EIT scheme, where $|3\rangle$ is a ground state, $|a^0\rangle$ is non-radiative and is therefore called a *dark state*. A ladder scheme is used in the work presented here, where $|3\rangle$ has a long, but finite, lifetime, and so $|a^0\rangle$ is nearly dark, but not perfectly so . This results in the atomic population becoming progressively trapped in the non radiative state $|a^0\rangle$. This phenomenon is called *coherent population trapping* [134, 135].

The effect of decoherence can be understood once again by the use of the Lindblad equation (3.15). For a three-level system, the phenomenological decay matrix is given by

$$\hat{\mathcal{L}} = \frac{1}{2}\begin{pmatrix} 2\Gamma_2\rho_{22} & -\Gamma_2\tilde{\rho}_{12} & -\Gamma_3\tilde{\rho}_{13} \\ -\Gamma_2\tilde{\rho}_{21} & 2(\Gamma_3\rho_{33} - \Gamma_2\rho_{22} & -(\Gamma_2+\Gamma_3)\tilde{\rho}_{23} \\ -\Gamma_3\tilde{\rho}_{31} & -(\Gamma_2+\Gamma_3)\tilde{\rho}_{32} & -2\Gamma_3\rho_{33} \end{pmatrix}. \tag{3.26}$$

By substituting the three-level total Hamiltonian $\mathcal{H}_{\text{tot}}$ from equation 3.22 and the decay term from equation 3.26 into the Lindblad equation (3.15), the three-level optical Bloch equations can be derived. For brevity, only the coherence terms are included here [32]

$$\dot{\tilde{\rho}}_{21} = \frac{i\Omega_p}{2}(\rho_{22} - \rho_{11}) - \frac{i\Omega_c}{2}\tilde{\rho}_{31} + (i\Delta_p - \frac{\Gamma_2}{2})\tilde{\rho}_{21}, \tag{3.27a}$$

$$\dot{\tilde{\rho}}_{31} = \frac{i\Omega_p}{2}\tilde{\rho}_{32} - \frac{i\Omega_c}{2}\tilde{\rho}_{21} + (i(\Delta_p + \Delta_c) - \frac{\Gamma_3}{2})\tilde{\rho}_{31}, \tag{3.27b}$$

$$\dot{\tilde{\rho}}_{32} = \frac{i\Omega_c}{2}(\rho_{33} - \rho_{22}) - \frac{i\Omega_p}{2}\tilde{\rho}_{31} + (i\Delta_c - \frac{\Gamma_2 + \Gamma_3}{2})\tilde{\rho}_{32}. \tag{3.27c}$$

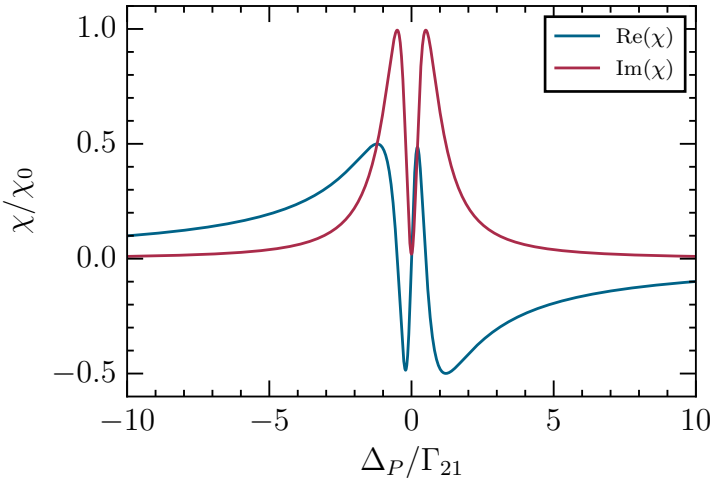

Figure 3.5.: Susceptibility of a three-level atom. The real (blue) and imaginary (red) components of the steady state susceptibility of the system as a function of detuning of the probing field for $\Omega_c = \Gamma_2$ and $\Gamma_3 = \Gamma_2/100$. Δ_c is set to 0, such that the two photon resonance occurs at $\Delta_p = 0$.

In the weak probe limit, where $\Omega_p \approx 0$ and $\rho_{22} = \rho_{33} \approx 0$, the coherence $\tilde{\rho}_{21}$ in the steady state is given by [129]

$$\tilde{\rho}_{21} = -\left(\frac{i\Omega_p/2}{\gamma_2 - i\Delta_p + \frac{\Omega_c^2/4}{\gamma_3 - i(\Delta_p + \Delta_c)}} \right), \tag{3.28}$$

where $\gamma_3 = \Gamma_3/2 + \gamma_p + \gamma_c$.

The susceptibility can be calculated by substituting equation 3.28 into equation 3.19, giving

$$\chi = \frac{i\mathcal{N}d_{21}^2}{\epsilon_0\hbar} \left(\frac{1}{\gamma_2 - i\Delta_p + \frac{\Omega_c^2/4}{\gamma_3 - i(\Delta_p + \Delta_c)}} \right). \tag{3.29}$$

The real and imaginary components of which are plotted in figure 3.5. In the limiting case $\Omega_c = 0$, equation 3.29 is equivalent to the two-level case, equation 3.20, shown in figure 3.2.

The presence of the coupling field acts to create a narrow window at the two-photon resonance in which the probe field experiences dramatically lower absorption, hence

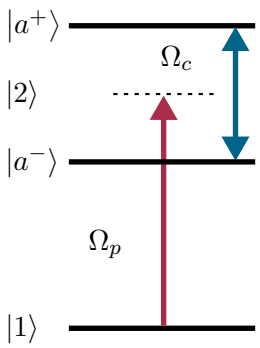

Figure 3.6.: The dressed states of a three-level atom under EIT conditions. The states $|a^{\pm}\rangle$ are split by the Rabi frequency of the coupling laser Ω_c. At the two-photon resonance, the probability of the population being transferred to $|a^+\rangle$ destructively interferes that of being transferred to $|a^-\rangle$, leading to transparency. At greater detuning of the probe from the two-photon resonance, the probabilities do not maximally overlap and the degree of interference is reduced, leading to absorption. At $\Omega_c = 0$, $|a^{\pm}\rangle$ are degenerate, and consequently, the transition probabilities do not interfere, equivalent to the two-level system in figure 3.1.

EIT[3] [31]. This windows appears due to Fano interference between excitation pathways [32]: the probability of the transition to $|a^+\rangle$ destructively interferes with that of the transition to $|a^-\rangle$. The depth of the transmission window is set by the quality of the interference, and is reduced under conditions of greater decoherence.

The dressed state picture can be a more intuitive method of interpreting this interference, shown in figure 3.6.

The width of the transparency window, in the limit in which $\gamma_3 = 0$, is given by [32]

$$\Delta_{\mathrm{EIT}} = \frac{|\Omega_c|^2}{\gamma_2}. \tag{3.30}$$

To a first approximation, the transparency window can be described by a Gaussian with a width given by [135]

$$\Delta_{\mathrm{trans}} = \Delta_{\mathrm{EIT}} \frac{1}{\sqrt{\mathrm{OD}}}, \tag{3.31}$$

[3] Electromagnetically-induced transparency

where the optical depth is that of the medium in the absence of the coupling field ($\Omega_c = 0$).

From equation 3.3, the optical depth is a function of the density-length product. In a medium in which this product $k\mathcal{N}l \gg 1$, the transparency window is narrowed such that only probe frequencies very close to the two-photon resonance are transmitted [136].

3.2.2. Slow light

Figure 3.5 shows that in close proximity to the two-photon resonance, the real part of the susceptibility has a large positive gradient, approximately linear with respect to the detuning of the probe field. This is associated with the reduction in the group velocity of a pulse of probe light travelling through the medium [32, 137]

$$v_{\mathrm{gr}} = \left.\frac{\mathrm{d}\omega_p}{\mathrm{d}k_p}\right|_{\Delta_c=\Delta_p=0} = \frac{c}{n_{\mathrm{ri}} + \omega_p \frac{\mathrm{d}n_{\mathrm{ri}}}{\mathrm{d}\omega_p}} = \frac{c}{1 + \mathrm{Re}(\chi)/2 + \frac{\omega_p}{2}\frac{\mathrm{d}\,\mathrm{Re}(\chi)}{\mathrm{d}\omega_p}}. \tag{3.32}$$

On the two-photon resonance, this is equivalent to $v_{\mathrm{gr}} = c/n_{\mathrm{gr}}$, where n_{gr} is the group index of the medium, given by [32]

$$n_{\mathrm{gr}} = \frac{6\pi}{k^2}\frac{\mathcal{N}c\Gamma_2}{\Omega_c^2 + \gamma_3\gamma_2}. \tag{3.33}$$

As with the width of the transparency window of the EIT, both group index and group velocity are a function of Ω_c. The decoherence terms set an upper limit on the value of the group index. This places a lower limit on achievable group velocities, although in optimised systems this limit can be as low as $\mathcal{O}(10\,\mathrm{m\,s^{-1}})$ [55, 138, 139].

Within the medium, a photon pulse is spatially compressed by the ratio v_{gr}/c, while the electric field strength remains the same [140]. In the absence of loss, the photon flux through the medium is constant, the total number of probe photons inside the medium is reduced by the same fraction, due to the spatial compression. The remaining photons are temporarily stored in the combined system of atoms and coupling field [32].

A useful way to visualise the motion of a pulse of light within a medium is to consider the motion of a quasi-particle (called a *polariton* [40]). These quasi-particles are superpositions of both atomic and EM excitations. Under EIT conditions, where popu-

lation becomes coherently trapped in the $|a^0\rangle$ state, these polaritons do not include any component of the $|2\rangle$ state, and are thus referred to as *dark-state polaritons*.

From [40], the dark state polariton field is given by

$$\Psi(z,t) = \cos(\theta)\mathcal{E}_p(z,t) - \sin(\theta)\sqrt{N}\hat{\rho}_{31}(z,t)e^{iz\Delta k}, \tag{3.34}$$

where $\mathcal{E}_p(z,t)$ is the electric field propagating through the medium in the z direction, $\hat{\rho}_{31}$ is the coherence operator between $|3\rangle$ and $|1\rangle$, N is the number of atoms within the volume of the EM field and the effective wave vector $\Delta k = k_c - k_p$. The atomic component of the polariton, $\hat{\rho}_{31}$, is referred to as a spin wave. The mixing angle θ is given by

$$\cos(\theta) = \frac{\Omega_c}{\sqrt{\Omega_c^2 + g^2 N}}, \tag{3.35a}$$

$$\sin(\theta) = \frac{g\sqrt{N}}{\Omega_c^2 + g^2 N} \tag{3.35b}$$

where g is the field coupling constant [40, 141]. This gives a polariton group velocity of

$$v_{\mathrm{gr}} = c \times \cos^2(\theta). \tag{3.36}$$

3.2.3. Photon storage

The treatment thus far has assumed that all fields are unchanging. Now we consider the dynamic case in which the Rabi frequency of the coupling laser varies with time: $\Omega_c = \Omega_c(t)$. Consider the case in which Ω_c is adiabatically switched from a high value to zero at time t_0, and switched back to a high value at time t_1, where $t_1 - t_0 \ll \Gamma_3^{-1}$, shown in figure 3.7.

$$\begin{aligned} &\Omega_c(t) \gg g^2 N \qquad && t \ll t_0, \\ &\Omega_c(t) = 0 && t_0 \ll t \ll t_1, \\ &\Omega_c(t) \gg g^2 N && t \gg t_1. \end{aligned}$$

From equation 3.35, the mixing angle between the atomic and photonic components of the polariton is dependent on Ω_c. When $\Omega_c \gg g^2 N$, $\cos(\theta) \approx 1$ and $\sin(\theta) \approx 0$, such that the polariton has an entirely photonic character (equation 3.34). When $\Omega_c = 0$, the situation is reversed and the polariton has an entirely atomic character. In addition:

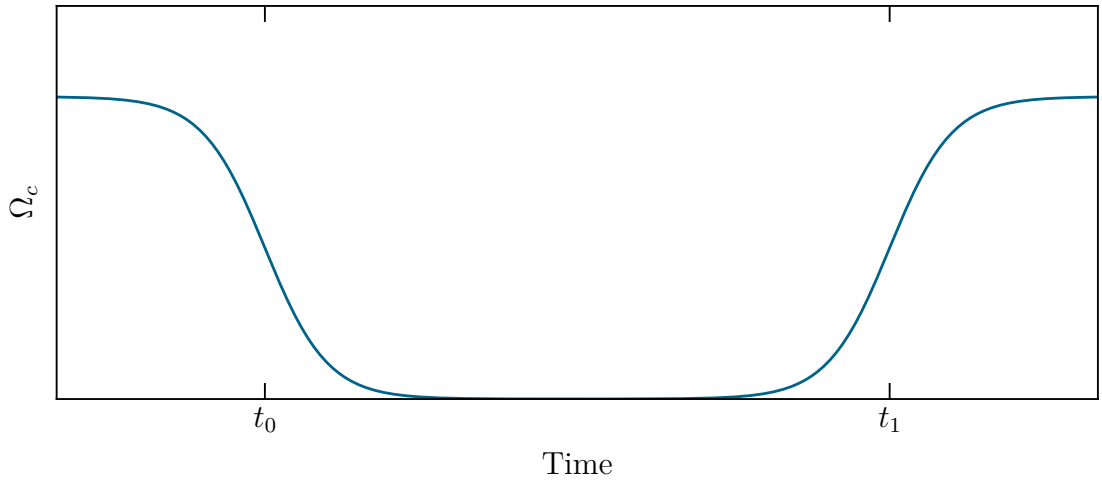

Figure 3.7.: Dynamic behaviour of Ω_c for photon storage.

- From equation 3.36, the group velocity within the medium will reduce towards zero.
- From section 3.2.1, the dark state $|a^0\rangle$ will shift from being dominated by an atomic population in $|1\rangle$ to $|3\rangle$.

When $\Omega_c, (t)$ is switched back to a high value, provided that $|3\rangle$ has not spontaneously decayed, the polariton is restored to a photonic nature, and will be emitted from the medium. This phenomenon is referred to as *photon storage* (and retrieval) [41, 142].

The state of the spin wave in which a single photon has been stored can be written as [122]

$$|\mathcal{W}\rangle = \frac{1}{\sqrt{N}} \sum_{j=1}^{N} e^{i\phi_j} |3_j\rangle \,, \tag{3.37}$$

where $|3_j\rangle$ is the state $|1_1, 1_2, 1_3 \ldots 3_j \ldots 1_N\rangle$, in which atom j is in state $|3\rangle$ while all others are in $|1\rangle$, and the phase factors $\phi_j = \boldsymbol{\Delta_k} \cdot \boldsymbol{r_j}$. Arising from this definition, the term 'collective excitations' will be used interchangably with 'polaritons' in the remainder of this thesis.

The phase factors in equation 3.37 preserve the coherence of the stored photon: as long as they remain in relative phase, the photon will be collectively emitted back into

the same mode from whence it originated [41, 143]. Emission into any other mode does not occur due to destructive interference between the emission of each atom. If the phase shifts evolve non-uniformly, the destructive interference is reduced, decreasing the directionality of emission. In the limit in which the relative phases decay entirely, the photon will be emitted in a completely random direction, equivalent to spontaneous decay of a single atom.

The phase factors must not only remain relatively consistent, but also consistent in relation to the atom's position: emitting with the correct phase but from the wrong position will similarly reduce the degree of destructive interference into all other modes. Consequently, motion of the atoms arising from a finite temperature ('motional dephasing') is a limiting factor in photon retrieval.

Motional dephasing arises from movement of the atoms in the time between storing and retrieving the photon. From [141], it is shown that the retrieval efficiency decays exponentially in the time domain in which motion is the dominant source of dephasing:

$$\eta_{\text{ret}} = \exp\left(-\frac{t^2}{\tau^2}\right), \tag{3.38}$$

where η_{ret} is the efficiency of retrieval and τ is the $1/e$ lifetime of the spin wave,

$$\tau = \frac{1}{(k_c - k_p)v}. \tag{3.39}$$

Here v is the atomic velocity - as expected, the greater the movement of the atoms in the medium, the more rapidly the spin wave decays due to motion. In addition, there is a contribution from the difference in wave vector between the probe and coupling beams.

Consequently, long storage lifetimes necessitate the use of ultra-cold atoms, and are assisted by the use of extremely similar probe and excitation wavelengths. Lambda EIT schemes between the two ground hyperfine states of rubidium has demonstrated combined storage and retrieval efficiencies in excess of 95% [144], and long storage times ($\mathcal{O}(10\,\text{s})$) [145]. Storage has also been achieved, for substantially shorter periods (1 ns), in thermal vapours [146].

Due to the use of a ladder-type EIT scheme coupling to a highly energetic Rydberg state (with consequent mismatch between the probe and coupling wave-vectors), the

motional dephasing lifetime in this experiment is $\mathcal{O}(1\,\mu\text{s})$ [44, 53].

The efficiency with which a pulse of light can be stored relies on simultaneously satisfying competing criteria. The finite width of the EIT window Δ_{EIT} limits the bandwidth of the light pulse that is transmitted. Frequency components outside this window are absorbed (scattered) by the medium. The window can be widened by increasing the initial value of Ω_c in order to avoid limiting the bandwidth of the probe pulse. However, in order to store the entire probe pulse, it must be spatially compressed into the extent of the medium. This either requires a very short pulse time - which increases the Fourier bandwidth of the pulse - or requires a high compression ratio, and thus a low group velocity (associated with a low value of Ω_c).

In order to satisfy both of these requirements simultaneously, the optical depth of the medium (specifically, the medium contained within the dipolar blockade radius r_{B}) must satisfy $\text{OD} \gg 1$ [147, 148], with higher optical depths contributing both to a greater storage efficiency, and a greater probability of collectively emitting a successfully stored photon back into its original mode.

Note that here we distinguish between the efficiency with which a single photon can be stored and, separately, the probability with which it is retrieved. In the remainder of this thesis, these two values are conflated into a single storage/retrieval efficiency (or probability).

3.2.4. Interaction-induced dephasing of Rydberg polaritons

In the work presented here, $|3\rangle$ is typically chosen to be a Rydberg state. As discussed in chapter 2, Rydberg atoms exhibit strong and long-ranged dipole-dipole interactions. If two (or more) Rydberg excitations are present, dipolar interactions can contribute additional phase shifts and consequently additional dephasing, reducing the probability of successfully retrieving a stored photon [44, 53, 63].

Considering the case of two collective excitations spatially separated from one another such that no individual atom simultaneously contributes to both spin waves, the two-polariton state can initially be written as the product of their individual states $|\mathcal{W}\rangle =$

$|\mathcal{W}\mu\rangle \otimes |\mathcal{W}\nu\rangle$. The time evolution of the combined state can be written as [149]

$$|\mathcal{W}(t)\rangle = \frac{1}{\sqrt{N_\mu}} \frac{1}{\sqrt{N_\nu}} \sum_{j=1}^{N_\mu} \sum_{k=1}^{N_\nu} \left[e^{i\phi_{\mu,j}} e^{i\phi_{\nu,k}} \left(|s_{\mu,j}\rangle \otimes |s_{\nu,k}\rangle \right) e^{V_{jk}t} \right], \tag{3.40}$$

where $V_{j,k}$ is the form of the interaction between each possible Rydberg excitation pair j, k. While this is discussed in depth in chapter 2, V_{jk} is a function of the distance between the two excitations, r_{jk}. If the extent of each polariton is small compared to the separation between the two, the phase factors will evolve close to uniformly, leading to minimal disruption of the overall phase pattern of each polariton. If the extent of each polariton is similar to the separation, then the phase factors will evolve non-uniformly, leading to a reduced probability of the stored photon being successfully emitted back into the original mode.

3.3. The four-level atom

A fourth level, $|4\rangle$, can be added to the model, separated by frequency ω_{43} and with spontaneous decay rate Γ_4. A third EM field couples these states with frequency ω_μ, detuning $\Delta_\mu = \omega_\mu - \omega_{43}$ and linewidth γ_μ. This is shown in figure 3.8 (a).

Once again using the rotating wave and dipole approximations, solving the optical Bloch equations for $\tilde{\rho}_{21}$ and substituting into equation 3.19, the steady state susceptibility may be found

$$\chi = \frac{iNd_{21}^2}{\epsilon_0 \hbar} \left(i\Delta_p - \gamma_2 + \frac{\Omega_c^2/4}{i(\Delta_p + \Delta_c) - \gamma_3 + \frac{\Omega_\mu^2/4}{i(\Delta_p + \Delta_c + \Delta_\mu) - \gamma_4}} \right)^{-1}. \tag{3.41}$$

The real and imaginary components are plotted in figure 3.8 (b). As with the addition of the second laser field, adding a third laser field splits the energy levels again. An absorption peak appears on resonance, with two transparency windows.

Collective Rydberg excitation dynamics

In the static case, applying the third field Ω_μ simultaneously with the probe and coupling fields, the effect is to further dress the eigenstates as shown in figure 3.8 (b). Here we

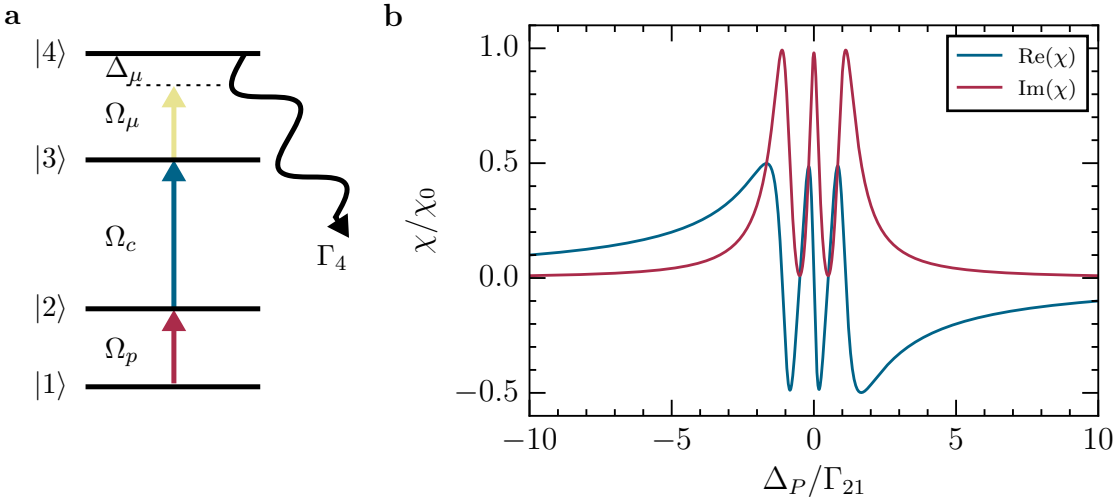

Figure 3.8.: The four level atom. *a*: One possible configuration of a four-level scheme. $|4\rangle$ is typically energetically very close above or below $|3\rangle$, coupled by an EM field with frequency ω_μ, detuning Δ_μ and Rabi frequency Ω_μ. In this thesis, this is always a microwave, rather than optical, transition. *b*: Real (blue) and imaginary (red) components of the steady state susceptibility of the four level atom as a function of detuning of the probing field for $\Omega_c = 2\Gamma_2$, $\Omega_\mu = \Gamma_2$ and $\Gamma_4 = \Gamma_2/100$. $\Delta_c = \Delta_\mu = 0$, such that the three photon resonance occurs at $\Delta_p = 0$.

consider the consequences of a time dependent field $\Omega_\mu(t)$, switched high during the window in which a photon has been stored as a collective (Rydberg) excitation, and resonant with the transition ω_{34}.

$$\begin{aligned} \Omega_c(t) &\gg g^2 N \qquad \Omega_\mu(t) = 0 \qquad t \ll t_0, \\ \Omega_c(t) &= 0 \qquad\quad \Omega_\mu(t) = p \qquad t_0 < t < t_1, \\ \Omega_c(t) &\gg g^2 N \qquad \Omega_\mu(t) = 0 \qquad t \gg t_1. \end{aligned}$$

A collective Rydberg excitation, given in equation 3.37, exists as a single excitation in $|3\rangle$, shared among all N atoms within the volume defined by the dipole blockade radius r_B (see section 2.3) [34]. Applying field resonant with ω_{34} drives Rabi oscillations in that single, shared, excitation between $|3\rangle$ and $|4\rangle$. The choice of state $|4\rangle$ is extremely flexible due to the density of states in the Rydberg manifold. In the work presented in this thesis,

nearby states are used, such that the energy spacing scales as $\Delta \propto n^{-3}$ [25], and the transition ω_{34} is always in the microwave region of the spectrum (300 MHz − 300 GHz [150]).

Due to selection rules, states $|3\rangle$ and $|4\rangle$ must be of opposite parity. For convenience, the collective states will be labelled according to the quantum numbers they typically take in the experiments presented in this thesis. The collective states may then be stated as

$$|S\rangle = \frac{1}{\sqrt{N}} \sum_{k=1}^{N} e^{i\phi_k} |s_k\rangle \,, \tag{3.42a}$$

$$|P\rangle = \frac{1}{\sqrt{N}} \sum_{k=1}^{N} e^{i\phi_k} |p_k\rangle \,, \tag{3.42b}$$

where N is the number of atoms within the dipole blockade radius and $|s_k\rangle$, $|p_k\rangle$ are the states $|1_1, 1_2, 1_3 \ldots s_k \ldots 1_N\rangle$, $|1_1, 1_2, 1_3 \ldots p_k \ldots 1_N\rangle$ respectively. 1 indicates an atom in the ground state, s_k and p_k indicate atom k excited to the Rydberg state $nS_{1/2}$ and $n'P_j$ respectively. ϕ_k is the phase factor.

This scenario is often characterised as the *super-atom* picture, in which the collective excitation behaves similarly to a single atom [151], such as the two-level system described in section 3.1. This is complemented by the long lifetime of highly excited Rydberg states in comparison to the time scale over which the collective excitation remains in phase ($\mathcal{O}(1\,\mu\text{s})$, see section 3.2.3). Therefore, we may consider both $|S\rangle$ and $|P\rangle$ to be effectively as stable as the true ground state.

Provided that the microwave field driving Rydberg-Rydberg transitions has a long wavelength relative to the extent of the collective excitation, all collective excitations stored in the atomic medium experience the same phase of the microwave field. This acts to preserve the phase structure of the collective excitations.

While a resonant microwave field is applied, the collective excitation will evolve according to equation 3.21. For $\Theta = \Omega_\mu t$ not a multiple of 2π, at the end of the microwave driving, the collective excitation has a non-zero probability of being in $|P\rangle$. As $|P\rangle$ is of opposite parity to $|S\rangle$, it is forbidden by selection rules from the photon retrieval process discussed in section 3.2.3. Consequently, any population present in $|P\rangle$ will remain there

until the excitation decays.

4. Experimental apparatus

The hardware requirements for the work presented here are shaped by the nature of the physical phenomena under study: quantum non-linear optics. Quantum optics implies the use, and study, of light fields at or close to the level of single photons; while non-linearity implies interactions between these fields. The system of choice in this work is ultra-cold atoms. From these three statements, the conceptual requirements may be established:

- An environment in which to cool atoms to extremely low temperatures - a UHV[1] chamber;
- A laser system to cool, trap, and excite atoms;
- A detection system of sufficiently high sensitivity and SNR[2] to detect single photons;
- A control system to automate experiments;
- The capability to perform and repeat individual experimental shots sufficiently rapidly in order to build up statistically meaningful data sets, where each shot will only yield $\mathcal{O}(1)$ photon, in a reasonable period of time.

All five of these requirements were met in the previous generation apparatus, described in the work of D. Maxwell [103] and D. Paredes-Barato [104]. However, the fifth point proved to be a limiting bottleneck. Consequently, a new generation apparatus was

[1] Ultra-high vacuum
[2] Signal-to-noise ratio

designed by, and jointly built with, H. Busche [105, 106] to improve on the repetition rate. The opportunity was taken to integrate a number of other improvements to the experiment: both to allow additional physics to be studied; and to improve the efficiency of the human-experiment interface that would make the experiment easier to operate, maintain, and further develop.

This chapter is in part based on the following publication:

- H. Busche, S. W. Ball and P. Huillery, *A high repetition rate experimental setup for quantum non-linear optics with cold Rydberg atoms*, Eur. Phys. J. Special Topics **225**, 2839-2861 (2016). [106]

4.1. Cooling and trapping atoms

A primary motivation for building a new experimental apparatus to replace the previous generation was to improve the rate at which data could be collected. In the previous generation, the principal bottleneck was the time required to load a MOT[3] [103]. Consequently, the new generation implements a high density, switchable atomic beam source to permit faster MOT loading, offering an order-of-magnitude improvement in repetition rate. This section discusses the new vacuum chamber, including the 2D-MOT[4] atom beam source, and comments on the resulting improvement in laser cooling rate.

4.1.1. The new UHV system

The UHV system contains a pair of vacuum chambers, shown in figure 4.1. Atoms are pre-cooled into a high density, switchable, atomic beam in a 2D-MOT [152] inside a glass cell ('2D-MOT chamber'). In the science chamber, a MOT is rapidly loaded from the atomic beam in preparation for experiments. The two regions are separated by a differential pumping tube. The science chamber operates at a background pressure of

[3] Magneto-optical trap
[4] Two-dimensional magneto-optical trap

below 10^{-10} mbar,[5] while the 2D-MOT chamber is assumed to have a higher background pressure to produce the atomic beam.

2D-MOT chamber

The upper half of the new apparatus is a 2D-MOT based on the designs of [153, 154]. The chamber is a UHV rectangular class cell with internal dimensions 25 mm × 25 mm × 150 mm. Two 250 mg natural abundance Rubidium dispensers[6] are located below the glass cell, to emit hot atoms upwards. These dispensers are wired independently through electrical feed-throughs, with one kept in reserve to limit (or preferably eliminate) the necessity to refuel the 2D-MOT during the lifetime of the experiment.

The glass cell, differential pumping tube, electrical feedthroughs and an all-metal valve are mounted on a stainless steel cube. A small ion pump is also mounted, but is not in operation, due to suspected contamination during assembly. The 2D-MOT chamber can be isolated from the science chamber via a gate valve, permitting independent vacuum breaks if necessary, such as for refueling.

Optics for the cooling light are mounted on an aluminium cage around the glass cell. 2D-MOTs conventionally use highly elliptical beams to produce an elongated cooling region; but in order to produce a more compact optical setup, a different geometry is used here, based on [153]. Light is delivered via two PM[7] optical fibres (one for each axis) to produce a circular beam with a $1/e^2$ beam diameter of 18 mm. The beam is split with PBSes[8] and HWPs[9] to produce four individual cooling regions within the glass cell. Light is retro-reflected with rectangular prisms, saving the cost and complexity of additional QWPs[10] to set the reflected helicity [155].

Additional light is directed vertically along the axis of the atomic beam. This 'pushing' beam is tuned to retard atoms travelling the wrong way along the atomic beam, in order

[5] The pressure is measured by the ion pump, which has a response floor of 10^{-10} mbar.
[6] Alvatec Alvasource type F×6 mm
[7] Single-mode, polarisation-maintaining
[8] Polarising beam splitters
[9] Half-wave plates
[10] Quarter-wave plates

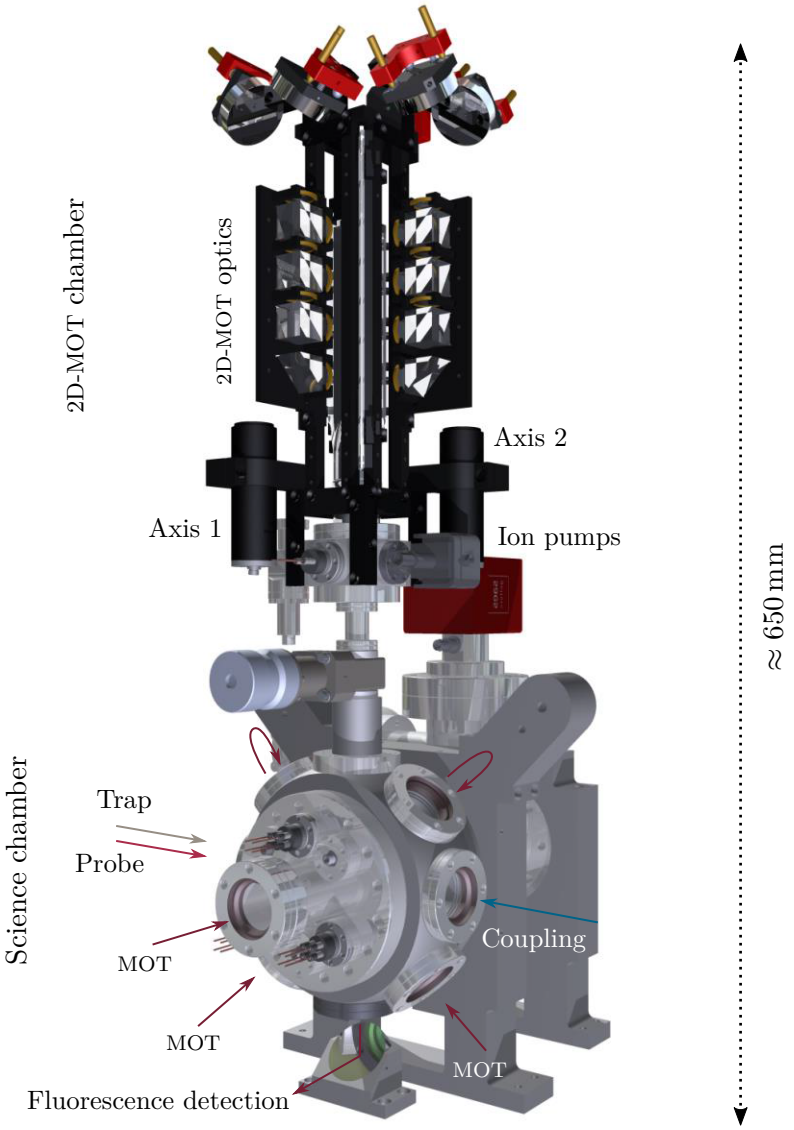

Figure 4.1.: New experimental apparatus. Experiments take place in the lower (science) chamber. A fast experimental repetition rate is facilitated by a 2D-MOT atom source mounted above. MOT coils are mounted internally, as are near-diffraction-limited aspheric lenses, electrodes for field control, and three microwave antennae for driving Rydberg-Rydberg transitions. All data read-out is conducted optically, so no ion detection is implemented. Courtesy of H. Busche.

to increase the total atomic flux from which the primary MOT can be loaded.

For compactness and simplicity, an elongated quadrupole magnetic field is produced using permanent rare-earth magnets [156] with a radial field gradient of $\approx 16\,\mathrm{G\,cm^{-1}}$. Rectangular Helmholtz coils are mounted outside the optics to shift the field zero to best alignment with the differential pumping tube aperture and to compensate for stray magnetic fields.

Science chamber

The science chamber is a non-magnetic stainless steel spherical octagon,[11] mounted with the major axis in the horizontal plane. Its two CF100 ports are used to provide electrical connections, access to an ion pump for vacuum maintenance, and the single horizontal MOT beam path. Seven of the eight CF40 ports are used for optical access, with a seventh mounting the 2D-MOT chamber vertically above.

The central feature of the science chamber is a pair of high NA[12] aspheric lenses,[13] permitting near-diffraction-limited optical resolution of the cold atomic ensembles produced. The lenses have an effective focal length $f_{\mathrm{eff}} = 10\,\mathrm{mm}$, a working distance of $f_{\mathrm{wd}} = 7.0\,\mathrm{mm}$ and a NA of 0.5. The lenses are aligned to focus and re-collimate an incident beam of light at a wavelength of 780 nm. Due to the short working distance, the lenses are cut to an angular profile, providing greater optical access for MOT beams, shown in figure 4.2 (a). The aspheric surfaces of the lenses are AR[14] coated for the wavelength range $450 - 1070\,\mathrm{nm}$. The planar surfaces are coated in a layer of ITO[15] for electric field control. The ITO coating is not index matched, resulting in a loss of $\approx 20\%$ light per surface at 780 nm. The lenses are mounted in a titanium cradle pictured in figure 4.2 (b). Titanium was chosen for its superior thermal expansion and magnetic properties over non-magnetic stainless steel, as well as reduced out-gassing [157].

[11] Kimball Physics MCF600-SphOct-F2C8
[12] Numeric aperture
[13] LightPath Technologies 355561
[14] Anti-reflection
[15] Indium-tin-oxide

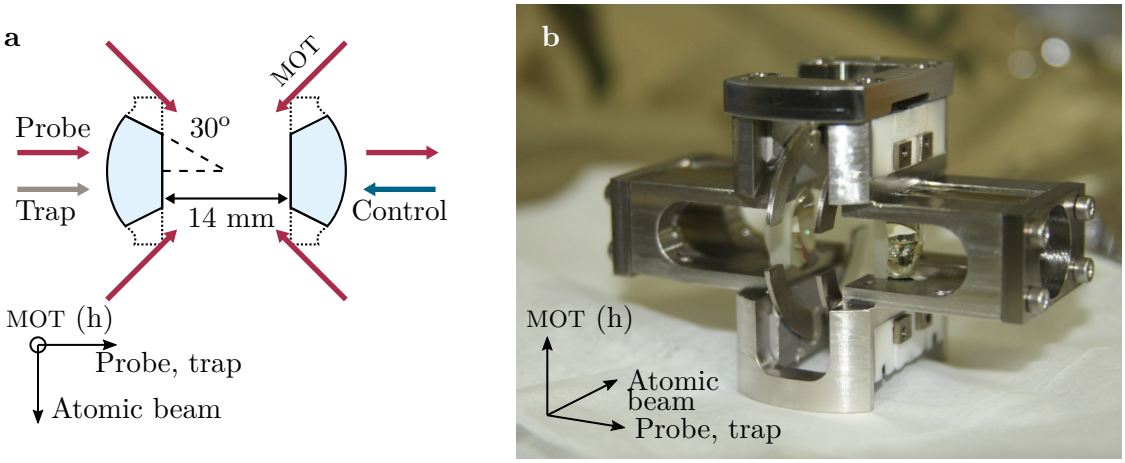

Figure 4.2.: In-vacuum aspheric lenses. *a*: Cut profile of aspheric lenses. Courtesy of H. Busche [106]. *b*: Lenses and field compensation electrodes mounted in titanium lens cradle.

All probing of atomic ensembles occurs via the axis defined by the internal lens pair. A pair of magnetic coils are mounted outside the science chamber to provide a quantisation magnetic field along this axis. In the remainder of the thesis, it will be referred to as the probe, or quantisation, axis.

Due to the high sensitivity of Rydberg states to electric fields [5, 25, 102], eight electrodes are included, in two split rings around the lenses, for electric field control. Each electrode can be independently addressed via external electrical connections. Electric field control is complicated due to the choice of titanium as a construction material, which was discovered after initial machining work was completed, but before assembly [158, 159]. Like aluminium, the surface of titanium rapidly oxidises to form a protective dielectric layer (TiO_2). This layer leads to reduced out-gassing rates, but is also non-conductive. Due to the presence of titanium surfaces in close proximity to the atomic beam pathway, MOT location, and location of Rydberg excitation, there exists the possibility for small spots of adsorbed ^{87}Rb metal to form and develop patch charges. To avoid this issue, all titanium surfaces are coated with a conductive 50 nm layer of platinum.[16] For the same reason, the inner (planar) surfaces of the aspheric lenses are coated

in conductive, transparent, ITO, which is electrically contacted to the platinum layer.

Three microwave antennae are positioned inside the chamber, close to the lenses. Each has an independent SMK[17] feedthrough rated for DC – 40 GHz. The antennae are discussed further in section 4.5.

To conserve bench space, a pair of 55-turn magnetic coils are mounted internally to provide an anti-Helmholtz field for the MOT. The coils are individually addressed by four external electrical connections, to permit reconfiguring the magnetic field to Helmholtz if desired. The coils are passively cooled via conduction to the flange on which all internals are mounted. This cooling channel offers minimal thermal conductance and so coil current must be limited to prevent excessive heating (and corresponding out-gassing from the Kapton wire coating). The coils generate an axial gradient of $5.297 \pm 0.009\,\mathrm{G\,cm^{-1}\,A^{-1}}$. Due to thermal limits, the MOT is formed at a gradient of $35.5\,\mathrm{G\,cm^{-1}}$, and briefly raised to $48\,\mathrm{G\,cm^{-1}}$ during a compressed MOT phase [160]. Due to the low currents involved, the MOT coil gradient is controlled directly via the analogue current control input of a DC power supply.[18] The power supply slew rate sets the rate at which coils can switch to 2 ms 10-90 rise time. Current safety limits are approximated by setting the power supply's over-voltage protection to 10% higher than the steady state voltage at 9.0 A.

At the rear of the science chamber is a $100\,\mathrm{L\,s^{-1}}$ combined ion-getter pump.[19] The ion pump current is used as a measurement of vacuum quality, and remains below the minimum sensitivity at $< 10^{-10}$ mbar. A backup atomic dispenser is also located to the rear of the main chamber, to permit emergency MOT diagnostics in the event that the 2D-MOT atom source becomes non-operational.

[16] Pt coatings applied by A. Hindmarch from the Centre for Materials Physics in Durham
[17] SubMiniture version K
[18] Electro-Automatick EA-PS 3016-20-B
[19] Saes-Getter NexTORR D100-5

4.1.2. Laser cooling

Diode lasers are used to provide stable, narrow linewidth light to the experiment for cooling, trapping, imaging, and excitation of atoms. ^{87}Rb is the species used in this experiment, as in many others, due to its simple atomic structure, and the availability of reliable, high power diode lasers. The level structure of ^{87}Rb is given in figure 4.3.

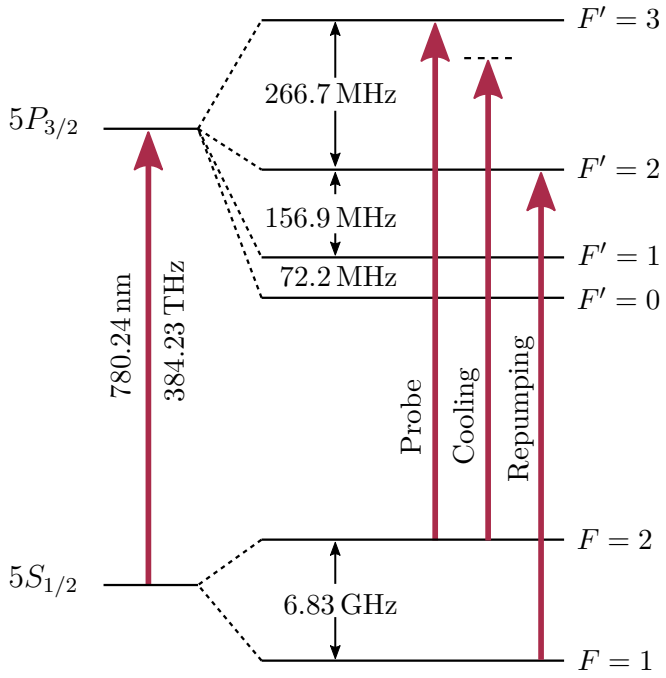

Figure 4.3.: Level scheme of ^{87}Rb D^2 line. Laser cooling in both the primary MOT and 2D-MOT takes place on the $F = 2 \rightarrow F' = 3$ transition. Due to detuning, this transition is weakly open, requiring repumping on the $F = 1 \rightarrow F' = 2$ transition. Probe light for Rydberg excitation uses the $F = 2$, $m_F = 2 \rightarrow F' = 3$, $m_{F'} = 3$ transition. Data from [161].

780 nm: the red laser system

The laser system provides coherent, narrow-linewidth light for cooling, trapping, and excitation of Rubidium atoms. A schematic of the excitation and cooling lasers is shown in figure 4.4.

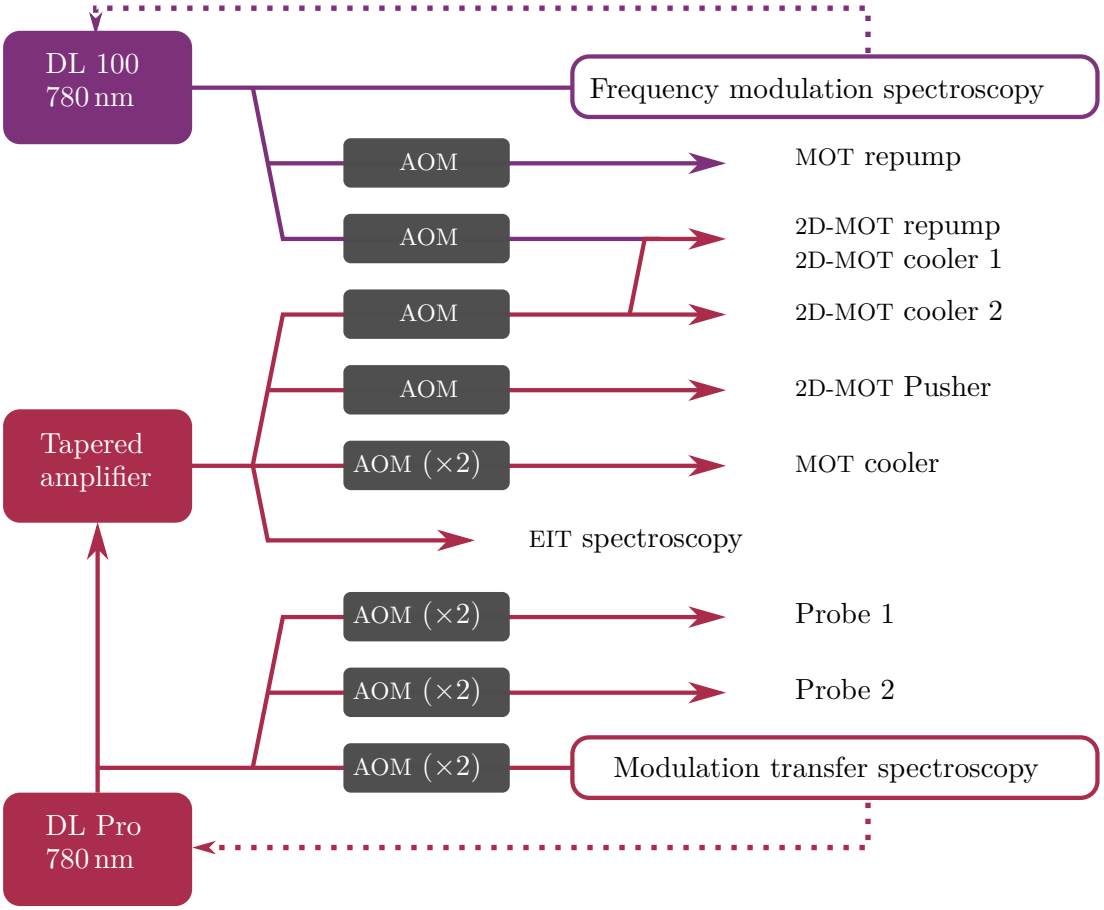

Figure 4.4.: Overview of the 780 nm laser system. Diode lasers and a TA provide cooling and repump light. AOMs provide frequency and intensity control. Light is delivered via PM fibre.

Excitation light is provided by a diode laser.[20] Cooling light is also derived from this laser. Due to the large interaction volume of the 2D-MOT, a TA[21][22] seeded by the excitation laser is used to provide approximately 1300 mW of light at 780 nm for laser cooling. The excitation and cooling master laser is frequency stabilised 140 MHz red detuned from the $5S_{1/2}\,F = 2 \rightarrow 5P_{3/2}\,F' = 3$ transition of ^{87}Rb by modulation transfer

[20] Toptica DL Pro
[21] Tapered amplifier
[22] Toptica BoosTA

spectroscopy [162]. AOMs[23][24] are used to provide frequency and intensity control. For the MOT cooler and the two probe beams, the laser is tightly focused and retro reflected through the AOM in a double pass configuration. This provides both fast switching ($t_{10:90} \approx 20\,\text{ns}$) for the probe beams, and the ability to change the frequency without (substantially) changing the beam pointing and coupling into the PM fibres. The cooling and pushing beams for the 2D-MOT go through their respective AOMs once, without focusing, to maximise diffraction efficiency and where fast switching is not required.

Repumping light is provided by a diode laser,[25] which produces more than 80 mW of light. This laser is frequency stabilised to the $\mathrm{F} = 1 \rightarrow \mathrm{F}' = 1 \times 2$ crossover resonance by frequency modulation spectroscopy [163]. AOMs are used to provide intensity control.

All laser light is delivered to the experiment via PM fibres. Cooling and repumping light for the MOT are delivered by two separate fibres, and then combined into a single $1 \rightarrow 3$ single mode, non-polarisation-maintaining beamsplitter to form a conventional 3-beam MOT.

Total power at 780 nm delivered to the experiment amounts to

- 75 mW × 2 cooling light and 12 mW repumping light for the 2D-MOT,
- 8 mW × 3 and 0.5 mW repumping light for the MOT,
- Up to 500 μW × 2 excitation light for probing the atomic ensembles.[26]

MOT performance

Figure 4.5 shows the sequence used to prepare the atomic ensemble. The 2D-MOT and MOT are switched on for up to 200 ms (with 100 ms being the typical time). At the end of the loading, the 2D-MOT light is switched off, which reduces the atomic beam flux to

[23] Acousto-optical modulators
[24] Gooch and Housego 1080-122
[25] Toptica DL100
[26] The power budget is designed to provide sufficient probing light for manual alignment work, for example using a power meter or regular photodiode. Experimental probing at the single photon level makes use of neutral density filters to reduce the probing power by as much as −120 dB.

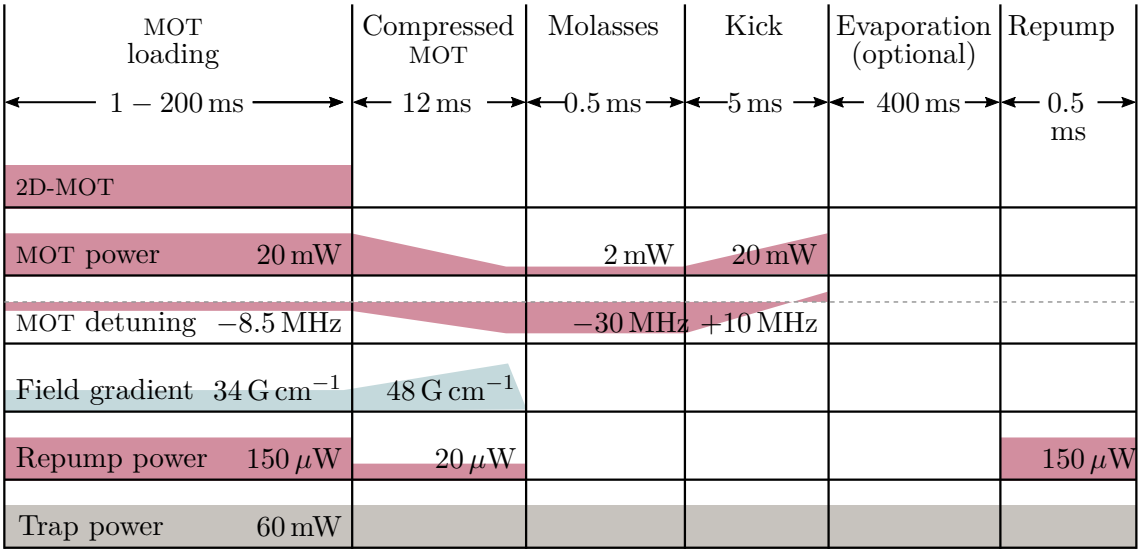

Figure 4.5.: Preparation of the atomic ensemble. The MOT is loaded for $1 - 200\,\text{ms}$. A compression stage increases atomic density, followed by a molasses stage to lower temperature. Atoms not trapped in the optical trap are expelled by a kick stage. Optionally, an evaporation stage is included to reduce the dimensions of the atomic ensemble. After evaporation, if any, the repump laser is briefly restored to pump the atomic population into the upper ground state in preparation for probing.

a negligible level. The optical trap is switched on throughout the atomic preparation, creating an effective dark spot at the centre of the MOT due to AC Stark shifts, where atoms are no longer subject to light-indued collisions [164]. Atomic density is increased by compressing the MOT [160], by ramping up the field gradient and ramping down the repumping power, and cooling power and detuning. The magnetic field gradient is then ramped to zero. A dark optical molasses stage is used to further cool the atomic cloud [165, 166].

After the molasses stage, any atoms not loaded into the optical trap are of no further interest, and serve only to decrease the certainty of the dimensions of the atomic ensemble in which experiments take place. Due to the high repetition rate desired, gravity and ballistic expansion do not remove the atoms fast enough. Therefore, to speed their removal from the region of interest, a 'kick' stage is included, in which cooler power is ramped up and cooler detuning is ramped from red to blue. Atoms in the optical

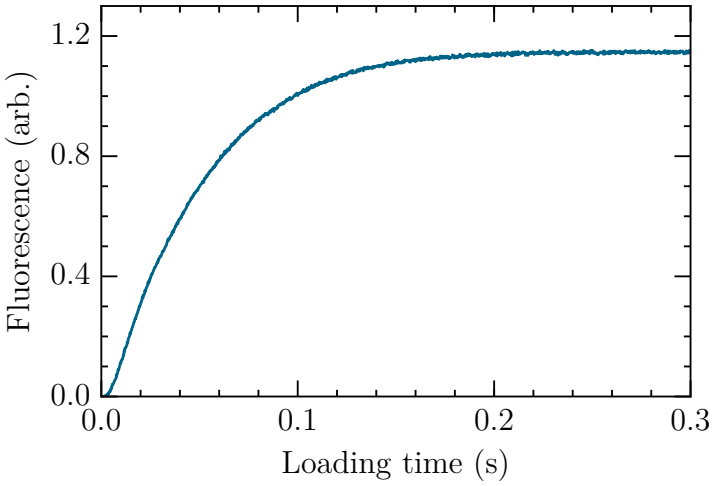

Figure 4.6.: MOT fluorescence as a function of loading time. The MOT saturates after $\approx 200\,\mathrm{ms}$.

trap are not affected due to the AC Stark shift induced by the high trapping intensity. Finally, an evaporation stage is included, for some experiments,[27] to further cool and reduce the dimensions of the trapped atomic ensemble [167].

Figure 4.6 shows a loading curve for the MOT, observed via fluorescence. The MOT saturates after $\approx 200\,\mathrm{ms}$, with an atom number of $\approx 10^8$. Due to the large number of reflective surfaces inside the chamber, it is probable that fluorescence-based measurements over-estimate atom number slightly. Absorption imaging suggests a saturated atom number of $(2.5 \pm 0.2) \times 10^7$ [105]. The loading rate is of greater relevance to the overall performance of the new experimental apparatus, as only a tiny fraction of the MOT can be loaded into the microscopic optical trap. MOT saturation in 200 ms already provides an order of magnitude improvement in repetition rate in comparison to the previous generation.

[27] Experiments presented in chapter 5 use the evaporation stage, and it is further discussed in section 5.2.1. All other experiments omit the evaporation stage in the interests of a higher repetition rate.

4.1.3. Atomic state preparation

Optical cooling exploits the closed atomic transition from $5S_{1/2}\,F = 2 \leftrightarrow 5P_{3/2}\,F' = 3$. Due to the detuning of of the cooling laser, there is a small probability of an atom being excited into the $5P_{3/2}\,F' = 2$ state and thence decaying to the $5S_{1/2}\,F = 1$ ground state. To fully close the cycle, the repumping laser recirculates atoms in this lower ground state. During the molasses stage, the repumping laser is switched off, resulting in the atomic cloud being optically pumped into the lower ground state $5S_{1/2}\,F = 1$.

After the kick stage and optional evaporation stage, the repumping laser is briefly switched on to pump atoms back into the upper ground state $5S_{1/2}\,F = 2$. The magnetic sub-levels, $m_F \in (-2, 2)$ are equally populated as no quantisation field is applied.

Conventionally, an optical pumping stage would subsequently take place to preferentially transfer atomic population into the stretched state $5S_{1/2}\,F = 2, m_F = 2$ [165]. Optical pumping applies circularly polarised light along the axis of a homogenous magnetic field. However, no optical axis is suitable for this stage in the experimental apparatus presented here. Along the horizontal MOT beam axis, the dimensions of the vacuum chamber render the creation of a homogenous magnetic field difficult; while along the lens axis, the extremely tight focusing of the in-vacuum aspheric lenses prevent the application of an optical pumping beam to the entire ensemble.

4.1.4. Optically trapping an atomic ensemble

After cooling in the MOT, atoms are loaded into a pair of tightly focused optical traps [168]. Each trap is formed by focusing a red-detuned, far off-resonant laser beam ($\lambda_{\text{trap}} = 910\,\text{nm}$) through the high NA aspheric lenses inside the vacuum chamber to a waist of $4.5 \pm 0.3\,\mu\text{m}$. As the aspheric lens pair is aligned to re-collimate a 780 nm beam, the trapping beam must be slightly convergent to overlap its focal spot with that of a collimated 780 nm beam at the centre of the lenses. The optical trapping beams are delivered by a single PM optical fibre to provide a high purity TEM_{00} mode, and the convergence is set by adjusting the position of the collimating lens on a micrometer translation stage. This is shown in figure 4.7. Before replacement of the optical trapping

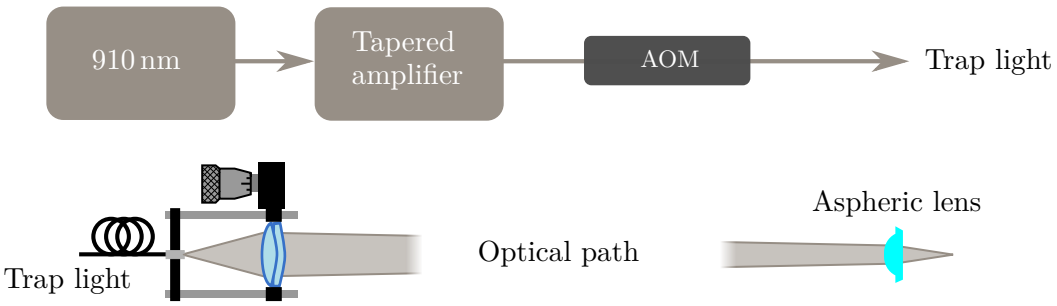

Figure 4.7.: Overview of optical trapping system. Light is provided by a laser diode and TA and switched by a single pass AOM. A Gaussian mode is provided through the use of a PM fibre, and the z-position of the focal waist is controlled by translating the lens that collimates light from the fibre to weakly converge.

laser source (see appendix A), all available power was used to produce the trap[28] with approximately $63 \pm 2\,\mathrm{mW}$ before the chamber. Accounting for the ITO coating on the in-chamber lens surface, the estimated trap depth is $400\,\mu\mathrm{K}$ [105].

Optical trap optics

Due to the use of tightly focused beams to produce and probe microscopic atomic ensembles, alignment of the trapping and probing beams is a critical and delicate operation.

In order to simplify the alignment of multiple separate trap and probe pairs, an optical configuration was chosen that would, in principle, allow this alignment to be performed once for all pairs simultaneously. This is shown in figure 4.8.

The optical trapping beam emerges from a single fibre, and is later split between two regions. Before this splitting, it is overlapped in free space with both probe beams (which are resolved via polarisation), in order to closely co-locate the trap and probe focal spots in the xy plane at the centre of the lenses.

The trap and probes are then split on a PBS, spatially resolving the two probes and dividing trap power as desired (typically equally). The two beam paths form arms of

[28] At maximum, approximately 280 mW was available from the fibre tip. A large fraction of this power is lost, due to the optical configuration used to produce multiple optical traps.

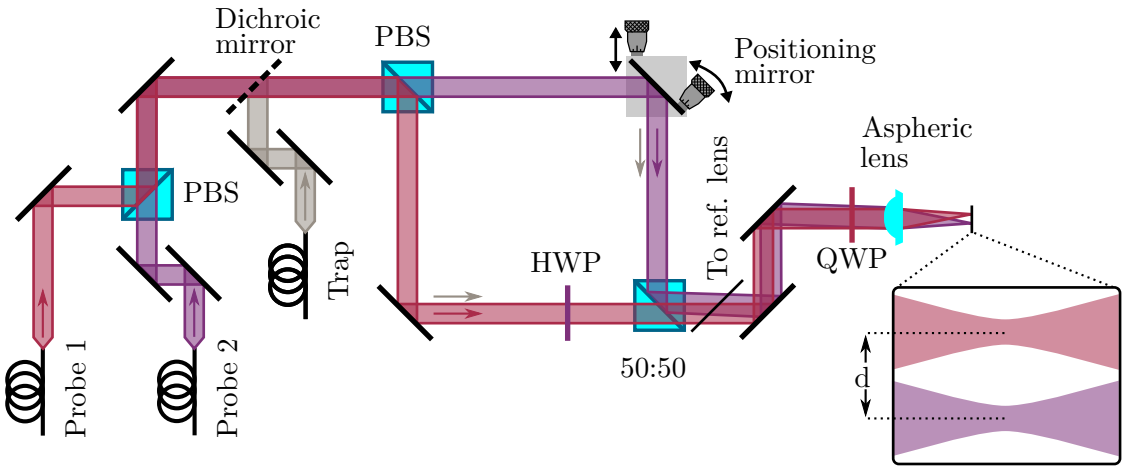

Figure 4.8.: Optical layout to generate two ensembles. Independent probe beams are initially distinguishable by polarisation and overlapped with each other and optical trapping light for ease of alignment. Spatial separation is achieved by inducing an angle between the beams on the surface of the aspheric lens. The separation can be controlled by adjustment of the angle and position of the mirror labelled 'positioning mirror'. After separating the two probe beams on the second PBS, their polarisation is set independently to allow probing of the same transition, and recombined on a 50:50 nPBS. A flipper mirror allows the probes to be redirected to an external reference aspheric lens and camera for diagnostics.

a configuration similar to a Mach-Zehnder interferometer, and it will be referred to as such, although it should be emphasised that interference is explicitly *not* the goal. The two beam paths are reflected and re-combined on a nPBS[29]. This choice discards 50% of trap power, but allows both probe beams to be adjusted to be equivalently polarised, in order to drive identical atomic transitions.

During re-combination, the two beam-pairs are deliberately not perfectly overlapped. A small angle between the two pairs is created.

The two pairs of beams are then directed onto the first aspheric lens inside the vacuum chamber. The angle between the two pairs results in a spatial separation between the focal spots. The extent of the separation may be varied in a controlled fashion by

[29]Non-polarising beam splitter

adjusting the angle of the reflecting mirror in one arm of the 'interferometer' to modify the angle between the beam pairs. Aberrations are minimised by maximising the overlap of the beam pairs on the surface of the aspheric lens. The adjustable reflecting mirror is mounted on a linear micrometer stage to facilitate this step.

Optical trap performance

As each shot will typically only result in $\mathcal{O}(1)$ photon, it is clearly necessary to perform many shots per MOT load, in order to achieve a meaningful repetition rate, with the previous generation typically using 3000 shots per MOT load [103]. The atomic ensemble is held in an optical trap to maintain it long enough for multiple shots. Due to the high intensities required to produce an optical trap, the atoms in the trap experience a strong, position dependent, AC Stark shift in their energy levels. In order to minimise problems arising from these shifts, the optical trap is rapidly modulated, switching off for a short period to perform individual experimental shots, and then back on to re-confine the atomic ensemble. With each shot and modulation, the atomic ensemble experiences a degree of heating and atom loss, placing an upper limit on the number of modulations.

This performance is characterised by evaluating the OD of the atomic ensemble as a function of shot number, averaged over many MOT loads. Typically, shots are considered in 'slices' of 2500, up to the upper limit of shots used on any given day. An example is shown in figure 4.9.

Optical trap geometry

The dipole potential of a EM field is given by [168]

$$U = -\frac{1}{2}\left\langle \mathrm{Re}(\boldsymbol{d}) \cdot \boldsymbol{\mathcal{E}} \right\rangle , \tag{4.1}$$

where the angled brackets represent the time average of the rapidly oscillating electric field and dipole moment.

Each optical trap is formed from a single, red-detuned, focused Gaussian laser beam.

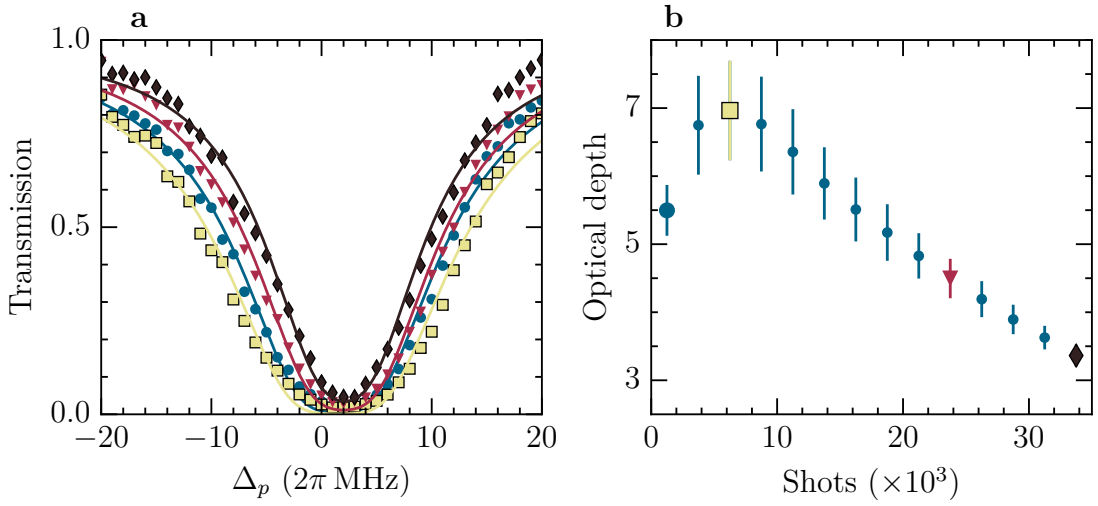

Figure 4.9.: Evolution of atomic ensemble during recycling. After forming a MOT and loading the optical trap, the atomic ensemble is probed 3.5×10^4 times. Probe transmission is observed as a function of probe detuning to derive a value for OD. Slices of 2500 shots are evaluated together. *a*: frequency scans for slices identified in (b). *b*: Optical depth evolution.

Consequently, the potential is of the form [169]

$$U(r,z) = U_o \frac{w_0^2}{w^2(z)} e^{-\frac{2r^2}{w^2(z)}}, \tag{4.2}$$

where $w(z)$ is the $1/e^2$ radius of the beam

$$w(z) = w_0 \sqrt{1 + \left(\frac{z}{z_R}\right)^2}, \tag{4.3}$$

w_0 is the minimum (i.e., focal) waist radius and z_R is the Rayleigh range

$$z_R = \frac{\pi w_0^2}{\lambda_{\text{trap}}}. \tag{4.4}$$

Provided that the energy of the ensemble is substantially less than the potential depth, it may be modelled as a harmonic potential [168]. The size of a thermal cloud at temperature T in a harmonic potential is given by

$$\sigma_{\text{rad}} = \sqrt{\frac{k_B T w_0^2}{4U_0}}, \tag{4.5a}$$

$$\sigma_{\mathrm{ax}} = \sqrt{\frac{k_B T z_R^2}{2U_0}}, \tag{4.5b}$$

where σ_x is the standard deviation of a Gaussian density distribution along the axis x.

Using a single beam per optical trap results in a simple trapping scheme, but results in a lengthened, cigar or oblate ellipsoid shaped cloud with weak axial confinement, and a length several blockade radii long. The length can be compressed by narrowing the waist, but too extreme a reduction results in too small an atomic ensemble since both are dependent on w_0.

As stated above, the waist is chosen to be $w_0 = (4.5 \pm 0.3)\,\mu\mathrm{m}$. The resulting atomic ensemble has a waist of $\sigma_{\mathrm{rad}} \approx 2\,\mu\mathrm{m}$. Due to the optical access within the chamber, σ_{ax} cannot be directly measured, as sufficient magnification cannot be achieved perpendicular to its axis. The traps can fluorescence imaged along their axis through a $\times 39$ magnification telescope onto an EMCCD[30] camera,[31] as shown in figure 4.10.

The small depth of field resulting from high magnification limits the ability to accurately image the cloud, as a substantial fraction of the photons that reach the camera are emitted from atoms well outside the focal plane. Consequently, the fluorescence images are unfocused and of limited use in measuring the size of the atomic ensembles or their temperature.

4.2. Detection system

Unlike conventional Rydberg experiments [153, 170] which typically detect the presence of Rydberg excitations via ions on a microchannel plate or channeltron, this experiment is inherently optical. As an experiment investigating quantum optics [28, 29], both inputs to, and outputs from, the experiment are photons, and all signal detection is performed optically [27, 171, 172], which is a coherent process [33]

To detect extremely weak light fields, photodetectors with extremely high sensitiv-

[30] Electron-multiplied charge-coupled device
[31] Andor Ixon

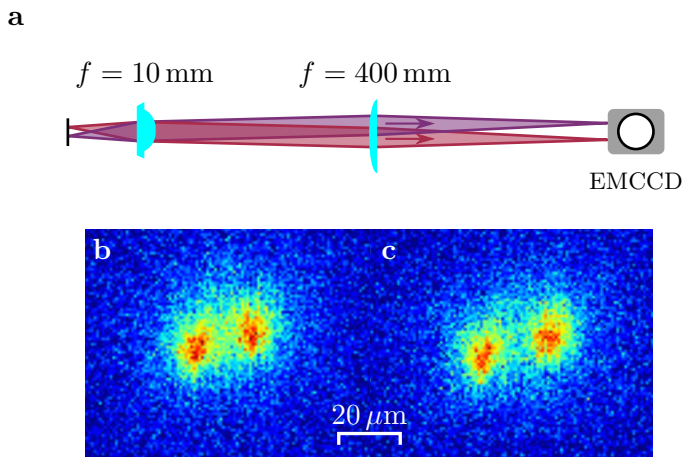

Figure 4.10.: Fluorescence imaging multiple optical traps. *a*: ensemble fluoresence is imaged via a ×39 magnification telescope onto an EMCCD. *b, c*: Due to imaging along the trap axis and after a sufficient integration time, the images are dominated by photons emitted well away from the telescope focus.

ity and low noise are required. This experiment makes use of SPADs[32], in commercial SPCMs[33].[34,35]

The SPCM signals the detection of a photon by sending a nominally TTL[36] compatible voltage pulse to the data acquisition system (see section 4.3.4). Each SPCM has a nominal time resolution of 28 ps; although in practice this is limited by the edge-detection scheme implemented in data acquisition. After detecting a photon, the SPCM becomes unresponsive for approximately 25 ns. This *dead time* results in a non-linear response that under-counts strong input signals, and saturates completely at count rates above $1/t_{\mathrm{dead}} \approx 40 \times 10^6\,\mathrm{cps}$. A correction factor can be applied to estimate the true count rate. The photon count rate during the probing window is usually sufficient that the linearity factor must be considered (a count rate of 4×10^6 cps results in linearity factors

[32] Single photon sensitive avalanche photo diodes
[33] Single photon counting modules
[34] Two separate models are used (Perkin-Elmer SPCM-AQRH-14-FC and Excelitas SPCM-780-14-FC)
[35] While these two terms are often used interchangably, the former, SPAD, strictly only refers to the diode, while the latter, SPCM, covers the entire module, electronics included.
[36] Transistor-transistor logic

between $1.08 - 1.13$ for the four SPCMs); while during the detection window, the count rate is at least two orders of magnitude lower and the linearity factor is essentially unity.

The choice of optical detection via SPCMs has the advantage that the data acquisition system does not merely record intensity as a function of time, but can record the arrival time of each individual photon. This wealth of data is crucial to the investigation of the *statistics* of the photons emitted by the quantum phenomena under investigation. The data acquisition system is integrated into the experimental control system discussed in section 4.3

4.2.1. Detector configuration

The dead time prevents a single SPCM from being able to count accurately photons that are closely bunched in time. In order to partially overcome this limitation, SPCMs are used in pairs in a HBT[37] configuration [173].

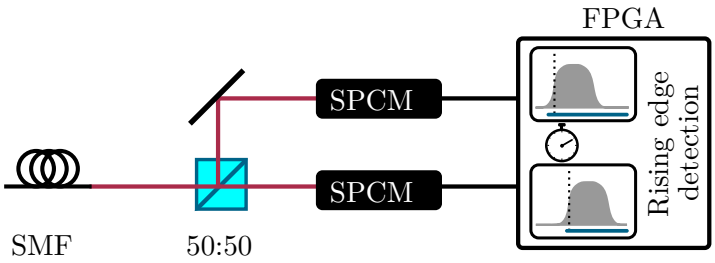

Figure 4.11.: HBT detector configuration. The incident signal is split on a 50:50 nPBS and observed by two SPCMs. SPCMs convert the photonic signal to an electronic signal that can then be processed by the data acquisition system.

The use of multiple detectors allows the observation of multiple photons arriving within time windows shorter than the detector dead time. The number of detectors sets an upper limit on the largest photon number event that may be accurately detected. As the beamsplitter is probabilistic, only a fraction of multi-photon events will be accurately observed as such; but the true rate of such events can be reconstructed provided the behaviour of the beamsplitter is known and consistent.

[37] Hanbury-Brown Twiss

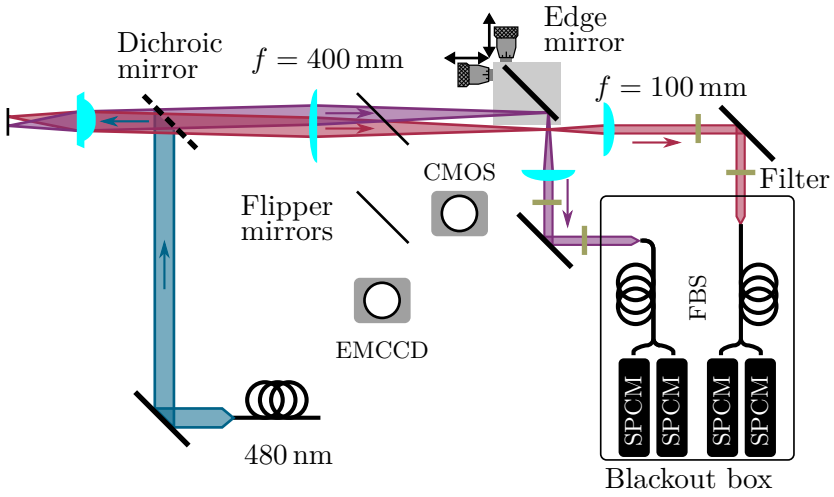

Figure 4.12.: Optical layout to resolve and detect two signals. The probe beams are spatially resolved by imaging the sites with ×39 magnification. A translatable edge mirror at the focus of the imaging system separates the two probes. Bandpass filters extinguish trapping and coupling light. Each probe is detected by a pair of fibre-coupled SPCMs. Flipper mirrors allow the probe light to be redirected to a CMOS camera for measuring the spatial separation or to an EMCCD for fluorescence imaging of the optical traps.

Due to the use of two optical channels in this experiment, a total of four SPCMs are used, configured as two HBT observer pairs. The optical configuration to achieve this is shown below.

Spatially resolving multiple optical channels

Due to the angle induced between the two pairs of beams (figure 4.8), the two probe beams may be spatially resolved after the chamber by imaging the focal plane of the in-chamber aspheric lenses. A ×39 magnification telescope is used to separate the focal points further, with an edge mirror located at the focus, to separate the probe beams into completely separate optical paths. The two probes are then independently coupled into

SM[38] FBSes[39] and delivered to the HBT detector pairs. The fibres delivering signal light to the detectors are aligned to maximise detection of the probe beam transmitted through the chamber. This choice will later serve as a discriminant for retrieval of photons that maintained the original stored phase pattern.

Flipper mirrors are used to redirect probe light to a pair of cameras for diagnostic purposes: a CMOS[40] camera[41] for imaging the distance between the two optical traps, and a previously mentioned EMCCD camera for fluorescence imaging of the optically trapped atomic ensembles (section 4.1.4).

4.2.2. Detection noise

Detection at the level of single photons requires considerable attention in order to reduce the level of background level sufficiently to achieve a meaningful SNR.

There are two principal sources of noise in measurements presented in this thesis:

- DC[42]: electronic noise arising from imperfections in the SPCM electronics. The electronics produce a certain rate of false photon counts even in the perfect absence of photons to detect.

- Optical noise. Real photons that do not comprise part of the signal that we wish to detect. Sources include laboratory lighting and the various lasers in use for atomic cooling, trapping, and excitation.

The detectors were chosen on the basis of several specifications: low-DC, high detection efficiency, and short dead time. The specified performance data of each of the four SPCMs used are given in table 4.1, including the specified QE[43]. Aside from the choice made at the time of purchase, very little can be done to affect the detector DC in practice.

[38] Single-mode, non-polarisation-maintaining
[39] Fibre beam splitters
[40] Complementary metal-oxide-semiconductor
[41] Thorlabs DCC1545M
[42] Dark count
[43] Quantum efficiency

SPCM	Serial Number	QE (%)	DC (Hz)	Calibrated
1	17553	≈ 58	52	2010-02
2	17653	≈ 52	67	2016-01
3	30400	67	33	2016-05
4	30401	66	37	2016-05

Table 4.1.: SPCM specifications. SPCMs 1 and 2 specify a measured QE at a wavelength of 550 nm, and their QE at 780 nm is inferred from the manufacturer's wavelength-QE graphs. DC is the rate at which events are detected due to electronic noise, rather than optical noise

Multiple steps are taken to minimise optical noise: the four SPCMs and associated HBT optics are located within a light-tight black-out box. The box has only two apertures, from which protrude fibre collimator optics. Electrical cables connect to a pass-through panel, rather than directly through a hole in the box wall, and the walls and lid use tongue-in-groove construction to minimise incoming light paths.

After separation on the edge mirror (figure 4.12), the two probe beams pass through laser line filters[44] to extinguish the co-propagating optical trap light. Each path has a pair of filters to provide approximately 122 dB attenuation at 910 nm and 13 dB at 480 nm. Each probe beam is then coupled into a SM FBS at the blackout box boundary.[45] The fibres are also entirely enclosed within the blackout box, to prevent laboratory lighting weakly coupling into the fibre cladding.

The use of SM fibres helps extinguish optical trapping light. Due to the convergence required to set the focal position of the traps (section 4.1.4), only a tiny fraction of the co-propagating light is within the acceptance mode of the fibre. Early tests with multi-mode fibres resulted in substantially higher noise levels.

In addition to the black-out box built on the optical table; the entire optical table

[44] Semrock MaxLine 780

[45] Early experiments presented in this thesis (chapter 5) used free-space beamsplitter cubes in between separate fibres. These were contained in slightly more primitive blackout boxes.

SPCM	SN	DC	OT (+ Hz)		CL (+ Hz)		Blinds (+ Hz)	
		(Hz)	Low	High	Low	High	Closed	Open
1	17553	53.66	1.34	645.8	0.12	8.80	0.00	114.31
2	17653	129.7	1.67	971.0	0.04	4.51	0.02	42.68
3	30400	34.35	0.75	309.0	0.05	3.84	0.05	132.61
4	30401	39.60	0.76	324.0	0.03	3.54	0.04	39.88

Table 4.2.: Optical noise sources and contributions. OT: Optical trap. CL: Coupling laser. Blinds: with room lighting switched on. Data of interest is (typically) measured with the optical trap and coupling laser low, room lighting on and safety blinds closed. Coupling laser high data taken with $P_{\mathrm{CL}} = 12\,\mathrm{mW}$.

is enclosed within a shuttered canopy. This canopy originates in the necessity for laser safety, but serves nearly as well at preventing laboratory light *entering* the table as it does preventing laser light *exiting* the table. The shuttering is *not* light-tight, but nevertheless provides substantial additional attenuation to optical noise.

Finally, during periods in which no experiments of interest are being recorded, the SPCMs are gated off to prevent recording incident photons. Gating is a minor factor in noise reduction, since photon counts in times of non-interest alternatively may be abandoned in post-processing; but makes a substantial contribution to minimising data storage requirements, and reducing post-processing computing overhead.

The contributions of various noise sources were measured in a series of extended experiments. For these experiments, all laboratory equipment not crucial to that experiment was switched off. The experiments were each conducted for 10 hours overnight, when the greatest fraction of electronic equipment in the building would be switched off to minimise disturbance of the electrical supply. The resulting data are shown in table 4.2.

4.3. Computer control and data acquisition

A control system is the combined software and hardware necessary to translate a description of an experiment into the timings and settings for the various instruments to

implement.

The previous generation of this experiment, and similar past projects, made use of a pair of National Instruments I/O[46] expansion cards controlled by a labyrinthine LabView codebase originally written more than a decade previously and since continually modified [102, 103, 174, 175]. The system offered a nominal fine timing resolution of 10 μs.[47] Where greater resolution is required - such as for the $\approx$ 1 μs excitation pulses, the computer was used to trigger arbitrary waveform generators or pulse generators, which could provide the desired precision. As the software ran on top of a Windows PC without interrupt-based programming, this nominal resolution was rarely achieved, as the other background processes could effectively hijack the central processor for many thousands of clock cycles at a time, causing significant jitter.

Due to the increasing difficulty in maintaining and developing the underlying software to implement requirements vastly exceeding its original parameters, the decision was made to move to a new system.

4.3.1. DExTer

Until recently, every single experimental project at Durham developed and operated their own unique control software (and hardware interface). All implemented a large number of extremely similar functions, in addition to experiment specific additions. Each required unique development, maintenance, and operations knowledge.

In 2011, T. Wiles wrote a modular experimental control system for another project in Durham [176]: DExTer[48]. It was designed with the intention of being a general control system, able to be ported to use with other ongoing experimental projects. It is now currently in use, or in the process of adoption, by every cold atom experiment in Durham [177–180].

[46] Input/output

[47] A PCI-DIO-32HS 32 channel digital I/O card and PCI-6713 8 channel analogue output card, using a synchronised 20 MHz clock frequency. The origins of the system used up until the end of the work of D. Paredes-Barato [104] are discussed by K. Weatherill [175].

[48] *D*urham *Ex*perimental *Ter*minal

DExTer has three primary advantages over the previous control scheme.

- Due to a more effective development process, the software is significantly more extensible and easily adapted to other experiments than it was previous written for.
- Arising from this modularity and flexibility, multiple projects use it, allowing pooled expertise and workload in maintenance and development.
- It uses a more advanced hardware interface, allowing better decoupling from the jitter inherent to the PC on which the software runs. Consequently, it allows for a substantially greater timing resolution.

Additional information for future users and maintainers of DExTer is given in appendix B.

Hardware

DExTer's hardware interface is a National Instruments FPGA[49] expansion card.[50] For I/O, it provides 96 digital multipurpose I/O channels, and eight each of 16-bit analogue input and output channels. It has a base clock speed of 40 MHz, which for certain operations is overclocked to 200 MHz. The FPGA acts as a real-time processor, reducing jitter to a maximum of one clock cycle. The FPGA card has a limited amount of RAM[51] located on the card, and offers DMA[52] via the PCIe interface to the host computer RAM.

Separately, a USB[53]-GPIB[54] adaptor[55] is used to control several instruments via the DExTer interface. Since this control does not reference the FPGA base clock, it is referred

[49] Field programmable gate array
[51] Random-access memory
[52] Direct memory access
[52] The work presented here uses NI PCIe-7842R; although other installations of DExTer use other models. Modification to a non-NI FPGA would involve a considerable amount of work, due to the tight integration between National Instrument's software and hardware.
[53] Universal serial bus
[54] General purpose interface bus
[55] Agilent 82357A

to as 'asynchronous'.

Software

The software side of DExTer has two primary components, and a host of associated tools.

A small software kernel is uploaded to the FPGA as firmware. The FPGA core implements this code in hardware by re-programming the interconnects between gates. The kernel reads each pre-computed time step of the experimental sequence from main computer RAM to local RAM and then executes it in real time. In the fork of DExTer used in the work presented here, a data acquisition system is also implemented into the FPGA kernel, recording the time at which each photon detected by the SPCMs is detected and writing it to main computer RAM.

The main terminal provides a UI[56] for a human user to enter an experimental sequence. The UI is presented as a series of time steps. Each time step sets the experimental state (such as a specific digital channel being on or off) for a set period of time.

Once instructed to execute, the human description is translated into the appropriate instructions for the FPGA kernel to implement. In addition to providing instructions to the FPGA kernel, the main terminal controls asynchronous outputs. These allow arbitrary code to be executed on the host computer, allowing more complicated communication via any relevant protocol with other instruments. The timing of these outputs cannot be guaranteed to better than $\mathcal{O}(100\,\mu\text{s})$ accuracy, however, and therefore are all implemented before the FPGA begins synchronous execution. Finally, the main terminal is responsible for reading output from the data acquisition system from main computer RAM and writing it to disk.

A variety of tools are included to simplify various aspects of implementing and using DExTer. These include

- Delay management: since different instruments may have different response delays to a signal input, the user may configure DExTer to automatically factor them into

[56] User interface

sequence processing. This saves the user from having to individually factor in various response times into every new sequence manually.

- Calibration management: Devices controlled by the analogue output channels may not have a linear response to control voltage, or may need the control voltage to be assigned in a very narrow range. Calibration allows the user to specify the actual desired instrument output (for example, x MHz detuning or y G cm^{-1}), rather than calculating the appropriate analogue voltage.
- Channel inversions: Individual digital channels may have their output inverted.
- Manual control: Rather than writing a complete sequence for testing an individual component, all channels may be set to a specific, non-time-limited state.
- Photon counting: A limited capacity to display in real time the number of photons counted by the four SPCM channels during an experimental sequence.

4.3.2. Sub-microsecond timing

DExTer was originally designed to offer a timing resolution of ≈ 800 ns. This was not a fundamental limitation, but a reflection of the requirements of the experiment for which it was written [176]. The experiments presented in this thesis require a considerably greater timing resolution in order to execute accurately the fast controls needed for photon storage and retrieval without resorting to triggering and synchronising multiple arbitrary function generators [28, 29]. Consequently, the code base was forked and extensively modified to implement a limited capacity for 'fast' digital control with nominal timing resolution and jitter of 5 ns.[57]

To achieve this timing resolution, the FPGA hub operates at a $\times 5$ multiplier of its base 40 MHz clock, giving a clock speed of 200 MHz. An individual time step of the main experimental sequence is flagged as a sub-μs sequence, which is defined separately to the

[57] Much of the original work implementing sub-μs pulsing was carried out by David Szwer. Testing, validation, and extension was carried out by the author.

main sequence, although in a similar style. As with the main experimental sequence, a sub-μs event is a sequence of time steps, each of which has a defined length and experimental output state

In order to achieve the 200 MHz clock rate, the entire sub-μs sequence must be pre-loaded into local FPGA RAM, rather than time-step by time-step as with the main sequence. This imposes several limitations on the sub-μs sequence.

- Only 16 digital (and no analogue) channels can operate at this speed.
- Each step must be a multiple of the 5 ns clock cycle.
- The total sub-μs sequence may not exceed 327 μs in length ($2^{16} \times 5$ ns clock cycles).
- The sub-μs sequence may not contain more than 32 time steps.
- Only one unique sub-μs sequence may occur per experimental run, although it may be repeated multiple times within the run.
- The sub-μs sequence may not be repeated more than 65,535 times (2^{16} shots).
- The FPGA has a digital channel rise time of $t_{10:90} \approx 7$ ns.

4.3.3. Repetitions and parameter variation

DExTer implements automated repetitions and scanning of experimental parameters. Parameters are varied in a one-dimensional scan: if multiple parameters a, b, c are to be scanned, they are all scanned simultaneously so that values a_1, b_1, c_1 are followed by a_2, b_2, c_2. Variable parameters include the lengths of time steps, and the values of analogue and asynchronous channels.

Where parameters are varied over the course of a scan, they take a single value for a single experimental run (a MOT load followed by a set number of shots), and the value then changes for a following run.

Repetitions occur in four varieties.

- Sub-μs repeats. These are covered in section 4.3.2.

- Multirun steps. These allow one or more numeric parameters to be changed in subsequent experimental runs.
- Quick repetitions. These immediately repeat the experimental sequence without changing any parameters, avoiding the need to re-process the entire experimental sequence. Two quick repetitions finish slightly faster than two full scans.
- Full scans. These repeat the entire multirun scan.

The order in which parameters are varied may be changed, including to a random order.

4.3.4. Data acquisition

Four digital channels, connected to the four SPCM outputs are monitored for digital inputs in the same time domain as the sub-μs sequence occurs (200 MHz). Rising edge detection is implemented in the FPGA. A fifth digital channel (one of the sub-μs output channels, DIO 15) is also monitored as a 'reference' input. In addition, the four digital channels used to set the SPCM gates are monitored as inputs.

In each clock cycle in which a data event occurs, the FPGA writes a line of data to the main computer RAM. A data event is defined as one or more of:

- The rising edge of a voltage pulse arriving from an SPCM, signalling the detection of a photon,
- The rising edge of a signal on the 'reference' channel. This could arise either from another instrument sending a voltage pulse, or the FPGA itself setting the channel to high,
- The rising or falling edge of a signal on the gate channels, signifying that one or more SPCMs are being switched on or off.

The line of data written is a 64-bit word. The final 16 bits describe the state of all four SPCMs and the reference channel, while the first 48 bits contain the number of the

clock cycle in which the data event happened. The format is described with examples in appendix B.

The clock counter resets to zero with each new experimental run, typically every time the MOT is reloaded. 48 bits of information for a 5 ns clock cycle permit, in principle, about 16 days of operation before the value overflows, while individual experimental runs typically do not exceed 500 ms. The dark count observation experiments discussed in section 4.2 ran for up to 10 hours.

As soon as an experimental run begins, the main DExTer terminal begins monitoring the computer RAM for data being written by the FPGA data acquisition system. Data is read from main computer RAM and spooled out to a single mechanical hard drive. Since the bit-rate of data events can significantly exceed the write performance of a mechanical disk, main computer RAM serves as a high speed, functionally-infinite capacity data buffer.

4.4. Non-linear Rydberg quantum optics

Atoms are excited to a highly excited Rydberg state by a two-photon EIT process [33]. The first excitation stage uses the same transition as the cooling stage ($5S_{1/2} \rightarrow 5P_{3/2}$. The intermediate excited level is coupled to a Rydberg state $nS_{1/2}$ via a high power blue laser (referred to as the coupling laser), at a wavelength of ≈ 480 nm. Due to the density of states in the Rydberg manifold, a wide range of nS states are accessible. The majority of the work presented in this thesis uses the states $80S_{1/2}$ ($\lambda = 479.5$ nm) and $60S_{1/2}$ ($\lambda = 479.6$ nm). The state $30S_{1/2}$ ($\lambda = 482.6$ nm)is used for calibration work. The energy levels used are shown in figure 4.13, with binding energies to scale.

4.4.1. 480 nm: the blue laser system

Coupling light to excite to Rydberg states is provided by a frequency doubled amplified diode laser,[58] shown in figure 4.14. A master diode provides light at half the desired

[58] Toptica TA-SHG-110 Pro

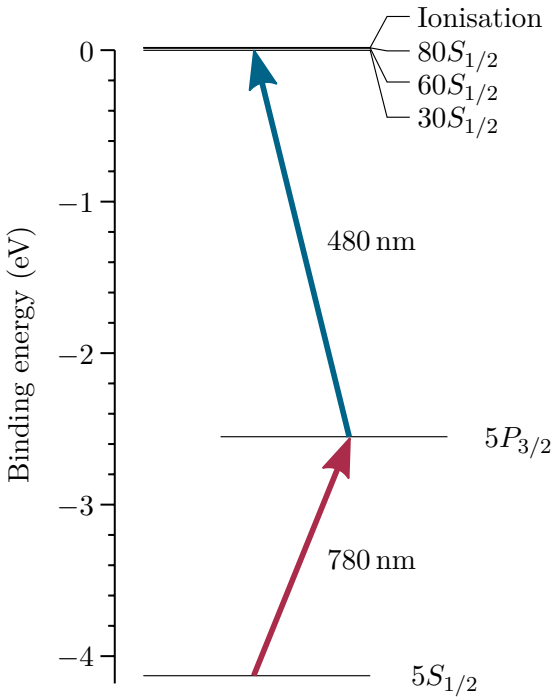

Figure 4.13.: Energy levels of Rubidium. The Rydberg levels used in the experiments presented in this thesis are all extremely close to the ionisation threshold. nD levels are not shown: they are not used due to their anisotropic interactions. Energy levels calculated with Alkali Rydberg calculator [181].

frequency, where semiconductor lasers function very well. The light is amplified by a TA and then frequency doubled by a nonlinear SHG[59] crystal in a bow-tie cavity. The laser can be tuned to resonance with any transition $5\mathrm{P}_{3/2}$, $5\mathrm{P}_{1/2} \rightarrow n\mathrm{S}_{1/2}, n\mathrm{D}_{3/2}$ for states between $n = 27$ and the ionisation threshold ($945\,\mathrm{nm} < \lambda_{\mathrm{master}} < 967\,\mathrm{nm}$). The efficiency of the frequency doubling is strongly wavelength dependent, with up to 350 mW typically available at $\lambda = 483\,\mathrm{nm}$, and 270 mW at $\lambda = 480\,\mathrm{nm}$.

The coupling laser is frequency stabilised by electromagnetically induced transparency spectroscopy [182] to the chosen Rydberg state relative to the excitation laser. This technique provides a degree of common mode noise rejection. The detuning of the probe

[59]Second harmonic generation

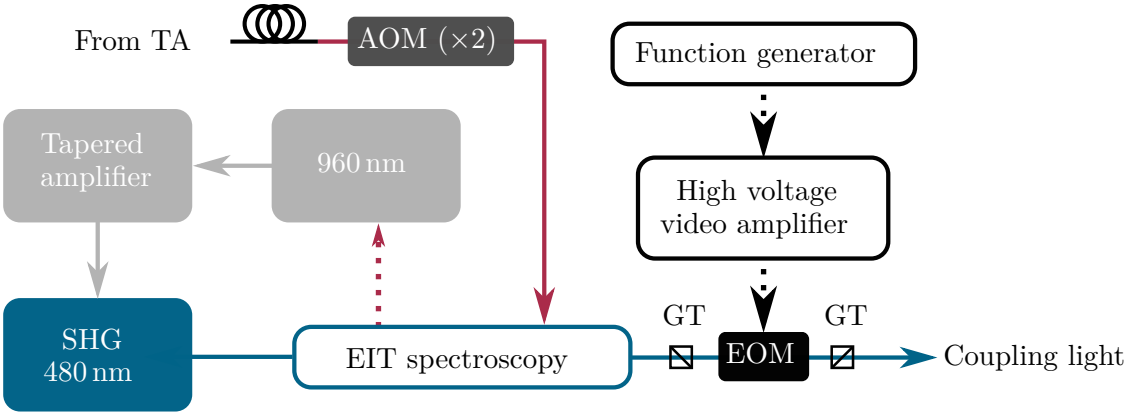

Figure 4.14.: Overview of the 480 nm laser system. Coupling light is derived from an amplified, frequency doubled, diode laser. Light is frequency stabilised on resonance to the desired $5P_{3/2} \rightarrow nS_{1/2}$ state by EIT spectroscopy using stabilised 780 nm light from the cooling laser. A polarisation switching EOM controlled by a arbitrary function generator controls the laser intensity. GT: Glan-Taylor polariser.

light sent to the EIT lock can be set independently to the probe light sent to the chamber, allowing a detuning of up to ±25 MHz relative to $\Delta_p = 0$, which allows compensation for differential electric fields between the vacuum chamber and the ^{87}Rb cell used to generate a frequency stabilisation signal.

As the laser is stabilised on resonance, using an AOM for intensity control would result in off-resonant light. Therefore, intensity modulation is achieved by the use of a polarisation switching EOM[60] between crossed Glan-Taylor polarisers. The polarisation switching achieves only relatively poor intensity extinction (≈ 20 dB), but modifies the transmitted laser mode as well. In combination with the use of a PM fibre, a steady state extinction of > 47 dB can be achieved.

The EOM is controlled via an analogue voltage input to a fast high voltage video amplifier. This control voltage is provided by a 25 MHz arbitrary function generator,[61] triggered by DExTer, as DExTer cannot provide analogue control at the necessary speed

[60] Leysop EM-200K-480
[61] Tektronix AFG3022B

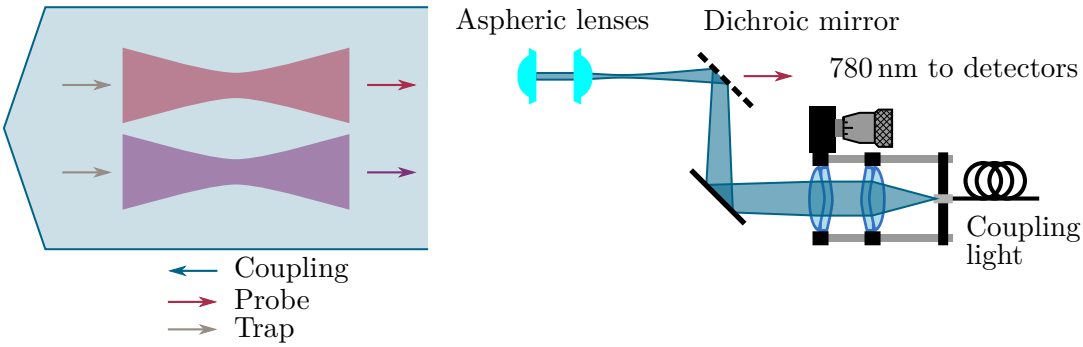

Figure 4.15.: Optical layout to couple to Rydberg levels. The blue light counter-propagates with the probe beam. An $f = +400\,\text{mm}$ achromatic lens focuses the beam in front of the aspheric lens, such that the beam is approximately collimated with a waist $\approx 25\,\mu\text{m}$ over the excitation region. This waist is large compared to both the spacing of the traps, and the extent of the atomic ensembles, such that Ω_c is not spatially dependent.

(section 4.3). The control voltage profile is optimised primarily to maximise transient extinction during the storage time, secondly to optimise steady state extinction during MOT loading, and thirdly to maximise coupling light transmission during EIT and photon retrieval. Typically, when optimal extinction parameters are found, transmission is around 90% of the maximum found if the switch is optimised only for transmission. A fast photodiode monitors the intensity of the coupling laser during the experimental sequence.

The switching speed of the coupling laser is limited by the performance of the video amplifier and the capacitance of the modulator. Typical performance is a fall time $t_{90:10} = 130\,\text{ns}$ and a rise time $t_{10:90} = 185\,\text{ns}$.

4.4.2. Optical alignment of the coupling laser

The coupling laser beam counter propagates through the lens axis of the vacuum chamber with respect to the probe (and trap) beams, as shown in figure 4.12. The coupling beam is not focused onto the atomic ensembles as the probe and trapping beams are. Instead, an external lens is used to focus the coupling light *in front* of the in-vacuum aspheric lens,

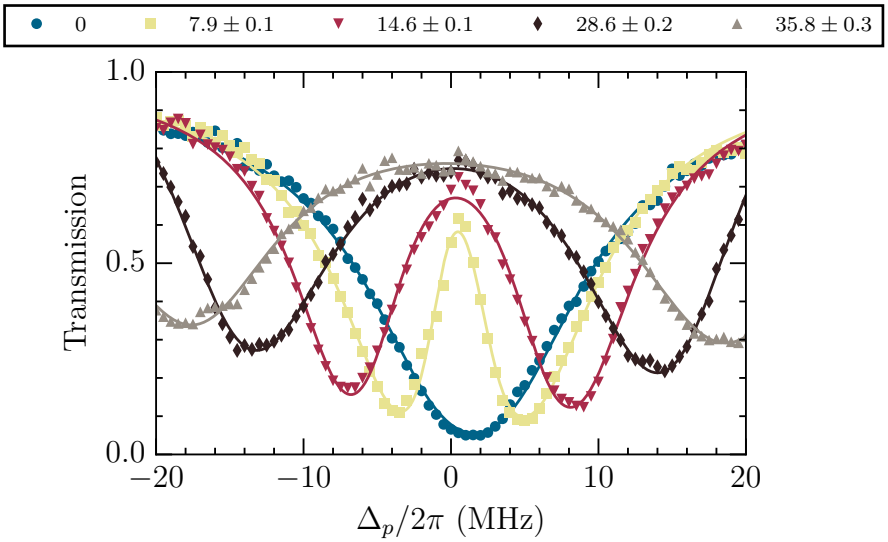

Figure 4.16.: Calibration of Ω_c using $30S_{1/2}$. Autler-Townes splitting of absorption as a function of probe detuning for several coupling beam powers. Solid lines are fits to equation 3.3, using the three-level susceptibility given in equation 3.29, to yield a value of Ω_c. Values stated in the legend are in units of $\times 2\pi$ MHz.

such that over the region of the atomic ensembles the coupling beam is approximately collimated with an estimated beam diameter of 25 μm. A collimated, rather than focused, coupling beam results in a lower coupling Rabi frequency than might be achieved at a focus, but Ω_c is (approximately) constant over the length of the ensemble, and covers both optical traps simultaneously. The layout is shown in figure 4.15

For experiments using both optical traps, the coupling Rabi frequency at each site is observed (and equalised) via AT[62] splitting of the probe laser absorption [117]. Where a large splitting is required, the state $30S_{1/2}$ is used, offering a sufficiently large dipole matrix element in proportion to available laser power. Figure 4.16 shows splitting of the absorption line at a single site for various coupling laser powers. The Rabi frequency is extracted by fitting the absorption profile to equation 3.3, using the three-level susceptibility from equation 3.29.

[62] Autler-Townes

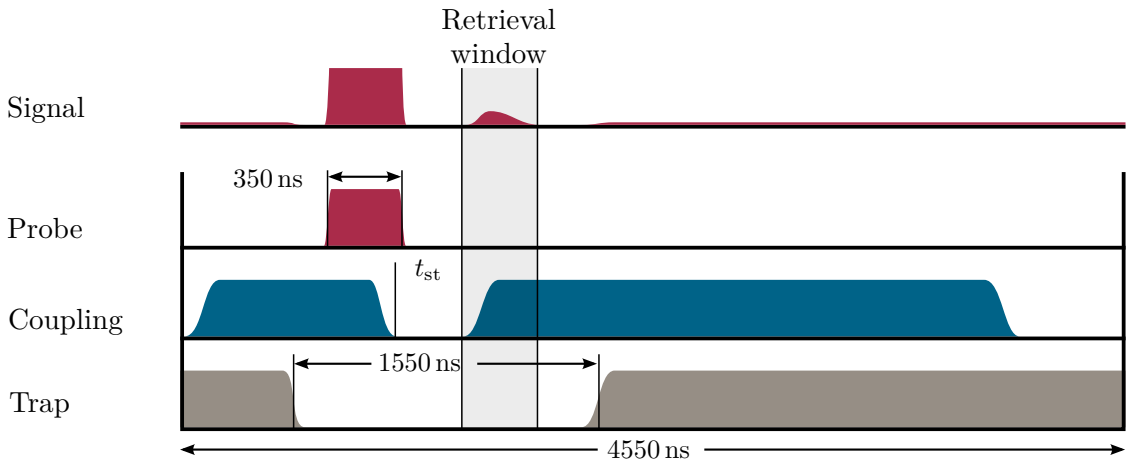

Figure 4.17.: Pulse sequence for photon storage and retrieval. A short probe pulse is transmitted. The coupling laser switches off shortly before the end of the probe pulse, and after a storage time t_{st}, switches back on. The optical trap is modulated off during the storage and retrieval process.

4.4.3. Photon storage

The storage of photons in the atomic medium was discussed in section 3.2.3 [40, 41, 44, 53]. In summary, by applying both probe and coupling laser pulses, and then ramping the coupling Rabi frequency to zero, photons may be stored as collective Rydberg excitations. When the coupling field is restored (or when the Rydberg excitation decays), the photon is released (or 'retrieved', which will be the common notation in this thesis). If the phase pattern originally imprinted on the atoms by the input EM fields is not disturbed, the photons will be retrieved back into the same mode as the laser pulse they originated from. The original mode is coupled to the SPCMs via a single mode fibre. Photons retrieved into the original mode are detected, while emittance into any other mode (as a result of a disturbance in the phase pattern) are not detected, and are regarded as lost.

Figure 4.17 shows the pulse sequence used to achieve a single shot of photon storage and retrieval. A short (typically 350 ns) probe pulse is transmitted. The coupling laser is timed to reach zero intensity approximately 40 ns before the end of the probe pulse. After the desired storage time, the coupling laser intensity is restored. The optical trap modulation is adjusted to bracket the probe, storage, and retrieval window as closely as

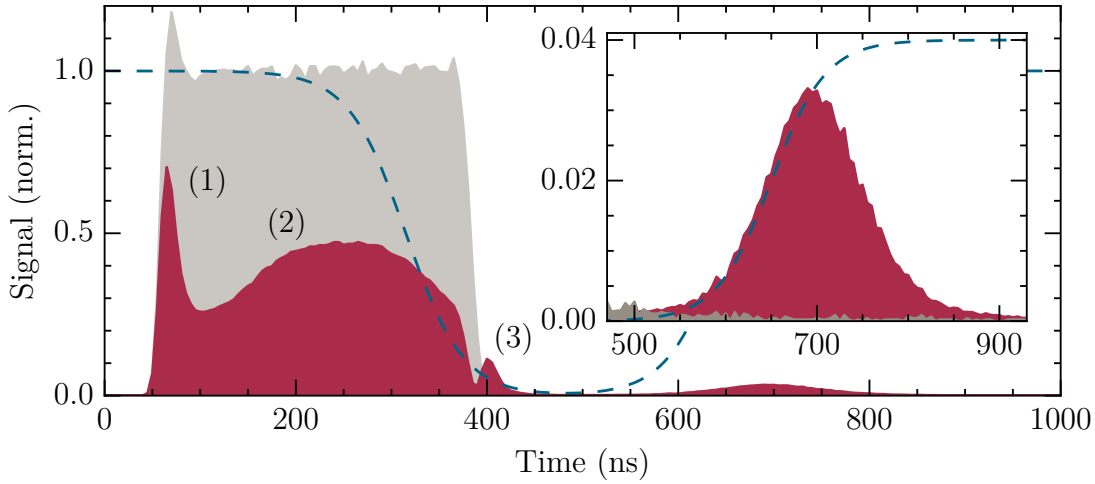

Figure 4.18.: Photon storage and retrieval. Signal intensity for photon storage using the state $80S_{1/2}$. The grey histogram shows the laser pulse in the absence of an atomic medium. The red histogram shows the signal in the presence of an atomic medium. The blue trace shows an approximation of the coupling Rabi frequency profile.

possible.

In this thesis, the storage time is defined as the the time between the digital switch off and switch on command triggers sent to the coupling laser, minus the switch off time of the coupling laser switch $t_{90:10} = 130\,\text{ns}$. For experiments without any microwave driving, typical storage times are 170 ns. Experiments including microwave application during storage typically have $t_{\text{st}} = 500\,\text{ns}$.

Figure 4.18 shows a histogram of photon arrival counts averaged over 2.5×10^7 shots of photon storage and retrieval using the state $|S\rangle = 80S_{1/2}$ and a storage time of $t_{\text{st}} = 170\,\text{ns}$ (red). This is the shortest practical storage time that still allows the retrieval light be be temporally resolved from the tail of the incident probe light. The trace in grey shows the same results of the same experimental sequence if no atomic medium is present.

A pulse of light is sent into the atomic ensemble from the probe laser in the time window $50 - 400\,\text{ns}$, with a mean photon number per pulse of $\overline{n}_{\text{in}} = 2.3 \pm 0.2$. The

trace in red shows the time dependent transmission of the atomic ensemble arising from both the response time of the individual atoms, and the time-dependent coupling Rabi frequency Ω_c. It has three notable transient elements:

1. The intensity spike at 75 ns primarily arises from the non-instantaneous response time of the ^{87}Rb atoms. Transmission is initially nearly full, sharply reducing as the ensemble is polarised by the EM field. There is an additional small contribution from overshoot in the AOM that switches the probe laser.

2. The rise in transmission between $100 - 250$ ns is a similar effect, in which the 3-level transparency develops slowly due to the limited coupling Rabi frequency Ω_c (typically 9 MHz). The transparency subsequently falls between $250 - 370$ ns as the coupling Rabi frequency is reduced.

3. The intensity spike at 410 ns is a sub-radiant flash. The probe laser switches off faster than the lifetime of the atomic fluorescence. Consequently, when the excitation source abruptly terminates, the interference that produces high optical extinction likewise abruptly terminates.

The retrieval histogram shown inset in figure 4.18 is plotted separately in figure 4.19, renormalised to its peak intensity. It exhibits a strong resemblance to a Gaussian distribution, to which it is fit in figure 4.19. The FWHM[63] of the fit, (123 ± 1) ns is similar to the rise-time of the coupling Rabi frequency Ω_c ($t_{10:90} = 185$ ns). A superficial explanation can be given by considering the physical parameters limiting the rising and falling edges of the retrieval window. The rising edge ($500 - 700$ ns) is dominated by the increasing coupling Rabi frequency, which has an approximately sigmoidal distribution, fitting well to the wing of the Gaussian. The falling edge is limited by the maximum number of photons stored in the ensemble: no more photons can be emitted than are stored -and usually fewer, due to decoherence of the collective phase.

The efficiency of the photon retrieval is defined as the ratio between the mean retrieved photon number $\overline{n}_{\text{ret}}$ and the input mean photon number $\overline{n}_{\text{in}}$. Using the state $80S_{1/2}$ and

[63] Full-width at half-maximum

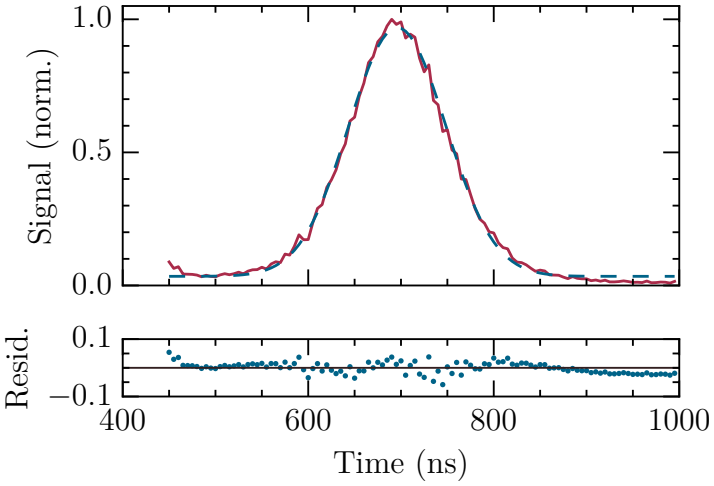

Figure 4.19.: Photon retrieval. The retrieval data shown inset in figure 4.18, renormalised to peak intensity (red), and fit to a Gaussian distribution (broken blue line) with a FWHM of (123 ± 1) ns.

the shortest possible storage time of 170 ns, retrieval efficiency is typically around 2%, averaged across 2.5×10^4 shots per ensemble. The exact efficiency depends upon multiple parameters, principally the ensemble OD and the storage time t_{st}.

The retrieval efficiency of an individual shot varies as a function of shot number, as shown in figure 4.20. The variation in efficiency is similar to that observed in the OD of the optical trap (figure 4.9): retrieval rate initially rises rapidly to a plateau, and then falls off over time. Depending on the performance of the optical trap and the incident photon number $\overline{n}_{\mathrm{in}}$, photon storage remains sufficiently efficient over a greater or smaller number of shots.

4.4.4. Storage blockade

Due to the use of strongly interacting Rydberg states for photon storage, attempting to store a large number of photons as collective excitations can demonstrate the strongly interacting nature of Rydberg excitations.

The effects of dipole blockade can be shown by increasing the number of photons in the probe pulse. Provided that the probe pulse remains in the weak probe regime, the

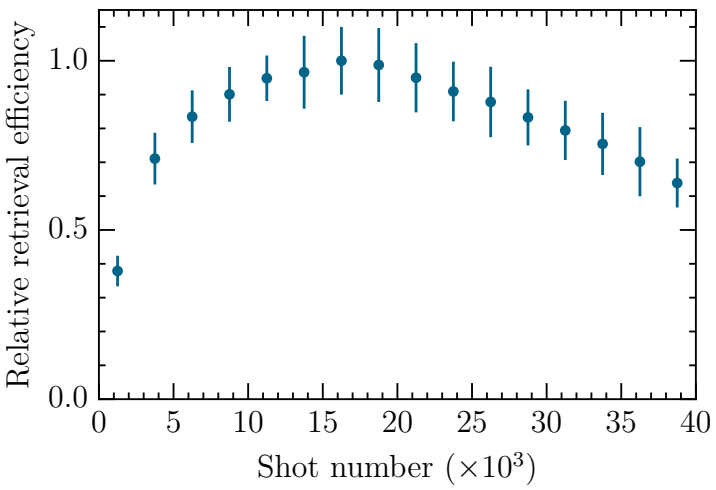

Figure 4.20.: Evolution of photon storage/retrieval efficiency with shot number. As with optical trap performance, performance initially increases sharply, probably due to optical pumping. Efficiency plateaus and falls off gradually as the atomic cloud heats and depletes.

number of collective excitations should be proportional to the incident photon number, and the number of retrieved photons should be proportional to the number stored. Figure 4.21 shows the effect of changing Rydberg state upon this relationship. For the relatively non-interacting state $30S_{1/2}$, the rate of retrieval is proportional across the range tested ($\overline{n}_{\mathrm{ret}} \propto \overline{n}_{\mathrm{in}}$).

More energetic and strongly interacting states demonstrate a saturation effect, where the retrieval rate flattens out to become independent of input photon number at high values. The saturation demonstrates the use of dipole blockade as a means of producing a non-linear optical response.

4.5. Rydberg-Rydberg transitions

The UHV chamber discussed in section 4.1.1 includes three internal antennae (A, B, and C) for applying microwave fields to the atomic ensemble, intended for driving transitions between Rydberg states. The three antennae are orientated in the three cardinal axes,

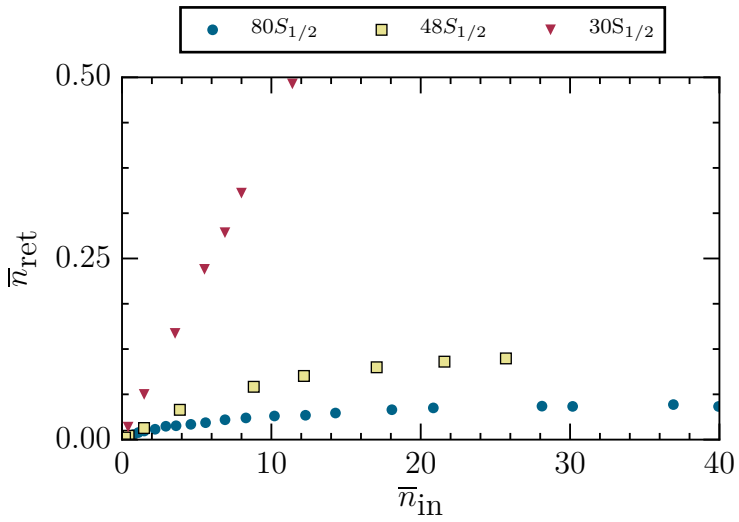

Figure 4.21.: Saturation of photon storage/retrieval due to dipole interactions. Photon retrieval rate $\overline{n}_{\mathrm{ret}}$ as a function of incoming photon number $\overline{n}_{\mathrm{in}}$ for three Rydberg states.

to permit various field vectors to be produced.

Each antennae is a semi-rigid cable with the shielding stripped to expose the solid conductor to a length of 16 mm, intended to produce a quarter-wave stub antennae at a frequency of 18.5 GHz. The shielding is grounded to the metal chamber at the three independent SMK microwave feedthroughs (see appendix D). Each feedthrough is rated for frequencies DC − 40 GHz, although the performance of the antennae away from the design frequency is unknown.

An ideal quarter-wave antennae emits a linearly polarised field in the plane of the emitter [183, 184]. Antennae A and C are orientated such that, if assumed to be ideal, they emit a field linearly polarised perpendicular to the quantisation axis. Under the same assumption, B emits a field linearly polarised parallel to the quantisation axis. Due to the minimal area of the grounded shielding, and the large number of reflective surfaces nearby within the chamber, the ideality of the antennae is unknown.

Due to the extremely large dipole matrix elements of Rydberg-Rydberg transitions, very weak microwave fields are sufficient to achieve acceptable Rabi frequencies. Therefore, simplicity is prioritised. No attempt is made to match impedance between the

antennae and the signal generator. A coaxial isolator is used to minimise harmful signal back-reflections from the presumed impedance mismatch,

4.5.1. Microwave excitation

Microwaves are generated by a commercial analogue signal generator,[64] locally referenced to a temperature stabilised quartz oscillator. The generator is nominally capable of a dynamic range of $-20 - +20\,\mathrm{dBm}$ and a frequency range of $2 - 67\,\mathrm{GHz}$, although the peak output power in practice falls off with frequency. Maximum power in the range $2 - 20\,\mathrm{GHz}$ does not fall below $10\,\mathrm{dBm}$.

The microwave generator is asynchronously controlled via GPIB from DExTer's host computer. Output frequency and power each require up to 30 ms to stabilise, and are therefore configured prior to an experimental run. Due to this slow switching speed, the set frequency and output power set points are only changed in between complete experimental sequences via DExTer's multirun parameter scanning. Rapid microwave switching during the sub-μs sequence is provided by a fast internal pulse modulator installed in the signal generator, controlled by an external signal supplied by DExTer.

The modulator is capable of generating pulses as short as 10 ns (although in certain circumstances, pulses must be a minimum of 50 ns long) with a specified extinction ratio 80 dB and $10 - 90$ rise time of 8 ns. Pulses longer than 100 ns are power-levelled by internal feedback to better than $\pm 0.5\,\mathrm{dB}$. However, the modulator can only switch between zero and maximum power. Consequently, in a 'fast' time domain (see section 4.3.2), the microwave state can *only* switch between high and low. Frequency modulation and partial-depth amplitude modulation cannot be applied on time scales shorter than 1 ms per step, and are therefore not used in any experiments presented in this thesis.

The dynamic range of the generator can be extended with the use of a computer-controlled digital step broadband microwave attenuator[65] offering an additional configurable attenuation of $0 - 60\,\mathrm{dB}$ in 1 dB increments. Fixed broadband 20 dB attenuators

[64] Anritsu MG3696A
[65] AtlantecRF ADA-8000-26000-60/1

are also used in some experiments where additional dynamic range is not required.

Coaxial isolators are used in-line between the signal generator and antenna to minimise reflection of signals from the antenna back into the generator due to the presumed mismatch in impedance arising from the simplistic antennae design.

Due to the delicacy of high frequency coaxial connectors (see appendix D), care must be taken when making and breaking connections between two elements. 50 cm extension cables are attached to each of the three microwave feedthroughs mounted on the vacuum chamber, which permits easier access to select which antenna is used and also serve as sacrificial cables in case of mishap. In the event that damage is caused while making a connection, the extension cable can be more easily replaced than the microwave feedthrough itself, which would require breaking vacuum and dismantling the chamber.

Timing of the microwave pulse is optimised with the use of a microwave sensitive Schottky diode.[66] The diode has a rise time of $t_{10:90} = (260 \pm 20)$ ns, a rise time delay of $t \approx 5$ ns, and a fall time of $t_{90:10} \approx 270\,\mu$s at a frequency of 2.5 GHz. Consequently, the beginning of a microwave pulse can be positioned to an accuracy of $50 - 100$ ns, but the signal generator must be trusted to accurately produce the desired length without verification where short pulses are used.

4.5.2. Microwave antennae performance

The simplest approach to measuring the Rabi frequency of an applied microwave field Ω_μ is to use the same AT splitting technique used in section 4.4.2 to measure the coupling Rabi frequency Ω_c. In this approach, the probe, coupling, and microwave fields are all applied simultaneously to probe the eigenstates of the dressed system. Figure 3.8 (b) plots an example of the susceptibility expected to arise in such a system. The presence of the microwave field acts to split the transparency window into two, such that there are three absorption peaks.

Figure 4.22 (a) shows two EIT traces. Two photon EIT is shown in blue circles, with a fit (solid line) to equation 3.3, using the three-level susceptibility given in equation

[66] AtlantecRF BZD-10018

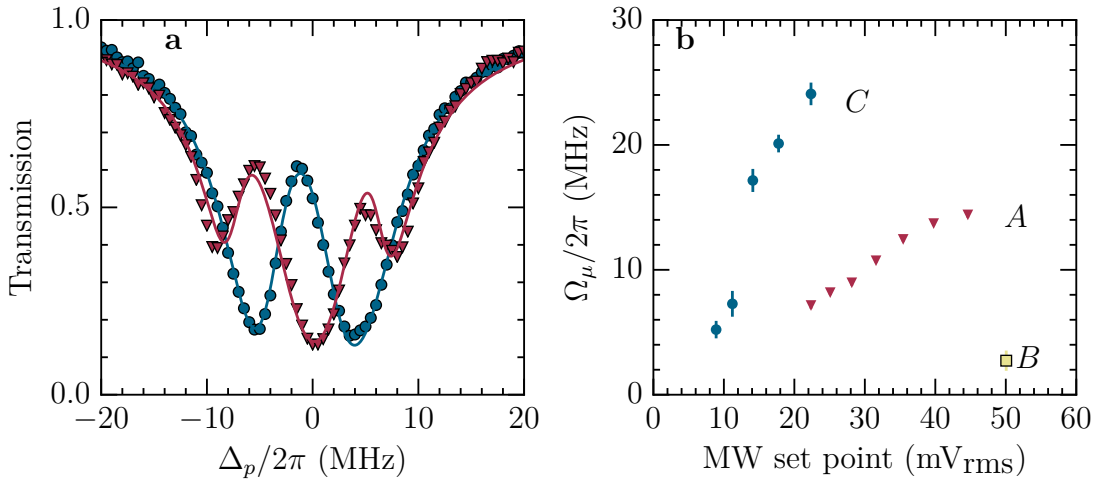

Figure 4.22.: Three-photon AT spectroscopy. *a*: Probe transmission for $\Omega_c = (9 \pm 1) \times 2\pi$ MHz and (blue circles) $\Omega_\mu = 0$ MHz, (red triangles) $\Omega_\mu = (12.4 \pm 0.4) \times 2\pi$ MHz. The slight asymmetry in splitting indicates that Δ_c, $\Delta_\mu \neq 0$. *b*: Comparison of antennae performance.

3.29. Three-photon EIT is shown in red triangles, with a fit to equation 3.3, using the four-level susceptibility given in equation 3.41. The splitting in both traces is slightly asymmetric, indicating that the detunings of both the coupling and microwave fields are not exactly zero. The fit yields a value for Ω_μ, as a function of applied microwave field strength, which is then used in figure 4.22 (b). Due to the large number of parameters in such a fit, it works most accurately at higher Rabi frequencies. This is analogous to the use of a low lying Rydberg state to optimise and align two-photon EIT at a high coupling Rabi frequency (section 4.4.2).

Figure 4.22 (b) shows the results of fitting the three-photon trace for successive applied microwave field strengths for each of the three antennae. *A* and *C* exhibit a far stronger Rabi frequency per driving field strength than *B*. The difference in efficiency between *A* and *C*, with *C* being the most efficient, may arise from many factors - a difference in inductance, a difference in exact antennae dimensions, or position relative to the atoms, or cavity effects arising from reflections inside the chamber.

Except where otherwise stated, all microwave fields used for experiments presented in

this thesis are applied via antenna C.

5. Contactless non-linear quantum optics

Strong dipolar interactions between Rydberg excitations has become well established as a means of creating effective photon-photon interactions by modifying the optical response of an atomic medium [27, 28, 42–46, 48, 53, 54, 66, 67, 185, 186] by coherent mapping between light fields and atomic excitations [143]. All of these experiments rely on the long-range nature of these interactions [5, 25].

To date, virtually all of these experiments have observed non-linearity by the behaviour of photons within a single spatial mode.[1] However, this aspect has been typically been driven by experimental considerations, and is not fundamental. The long range character of dipolar excitations between Rydberg excitations is mediated by virtual microwave photons, and occur with the near field of such photons. As established in chapter 6, microwave coupling between nearby states used in this thesis are of the order of $\mathcal{O}(1\,\mathrm{cm})$. These scales are vastly greater than the scale of the mode used for tight addressing of single (or single digit) dipole blockade radii, ($\mathcal{O}(1\,\mu\mathrm{m})$ in the work presented in this thesis).

In this chapter, effective photon-photon interactions are demonstrated at ranges $d \geq 10\,\mu\mathrm{m}$, between photons propagating in non-overlapping spatial modes. The interaction is mediated through free space between two independent, non-overlapping atomic ensembles.

This chapter is based on the following publications:

- H. Busche, S. W. Ball and P. Huillery, *A high repetition rate experimental setup for quantum non-linear optics with cold Rydberg atoms*, Eur. Phys. J. Special Topics

[1] [67] is a notable exception, published shortly after completion of the work presented in this thesis.

225, 2839-2861 (2016). [106]

- H. Busche, P. Huillery, S. W. Ball, T. Ilieva, M. P. A. Jones and C. S. Adams, *Contactless non-linear optics mediated by long-range Rydberg interactions*, Nat. Phys. **13** 655-658 (2017). [63]

Data presented in this chapter was taken jointly with H. Busche and P. Huillery. The phase shift model introduce in section 5.4 was developed by T. Ilieva and P. Huillery.

5.1. Concept

Past work has relied on tight spatial confinement of atomic ensembles to produce quantum states of light through dipolar blockade [27, 53, 54, 103, 104, 106]. Effective photon-photon interactions were visible through the non-linearity thus produced.

In this work, a new approach is adopted, shown conceptually in figure 5.1. In order to provide additional degrees of freedom, a second, tightly confined atomic ensemble, is created. Collective Rydberg excitations are created simultaneously in both ensembles, allowing interactions to occur over the controlled separation between the two media [5, 25, 28, 53, 54].

In this thesis, the configuration is limited to two separate ensembles and interactions via a single Rydberg state $|S\rangle$. However, the experiment aims to serve as proof of principle for scaling to more complicated systems. In the work presented below, two channels are created by the near-overlap of two pairs of laser beams (one probe beam, and one trap beam, for each channel) on an nPBS. While this technique does not efficiently scale to multiple channels,[2] alternative techniques could, such as using a SLM[3] or DeMA[4] to configure an arbitrary optical trap array [187–190].

[2] Pairs of channels are combined with 50:50 nPBSes, leading to an optical trap power budget scaling with the number of channels κ as $P \propto 2^{\kappa^2}$.
[3] Spatial light modulator
[4] Deformable mirror array

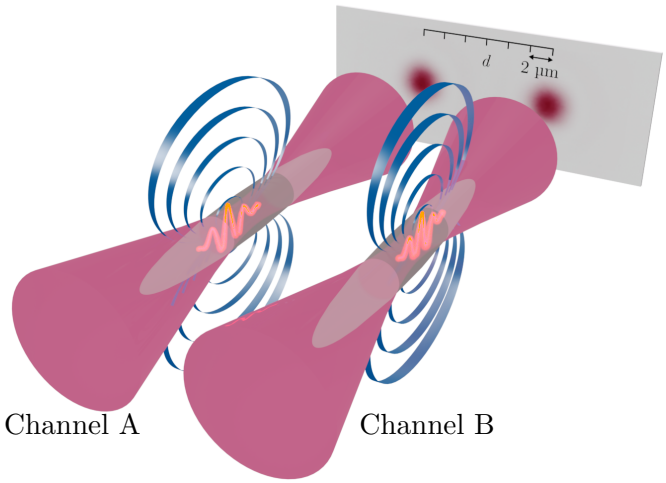

Figure 5.1.: Implementation of spatially separate, strongly interacting channels. Light is focused from two separate modes onto two independent atomic ensembles separated by a distance d. Strong dipolar interactions between Rydberg excitations lead to interactions between the channels, and is detected by analysing the distribution of photons emitted from the two ensembles. Courtesy of H. Busche.

Multiple channel geometry

Introducing a new degree of freedom, d, provides two regimes in which to study interactions between channels, which are presented in figure 5.2. In the case that $d < r_B$, (figure 5.2 (a)), then the second ensemble is largely (or entirely) blockaded by the presence of an excitation in the first ensemble. This is functionally equivalent to storage blockade in a single channel . This regime offers potential for optical gate and transistor experiments, such as [45, 46, 61].

The alternative is illustrated in figure 5.2 (b), with $d > r_B$. This is a fundamentally different scenario, permitting simultaneous creation of - and interactions between - collective excitations in both channels.

Sections 3.2.3 and 3.3 established that the phase factors in the wavefunction of the collective excitation are critical to achieving highly collective emission back into the same spatial mode during photon retrieval. Within a single channel, induced phase shifts result in a suppression of the probability of retrieval [53, 54, 103]. The introduction of

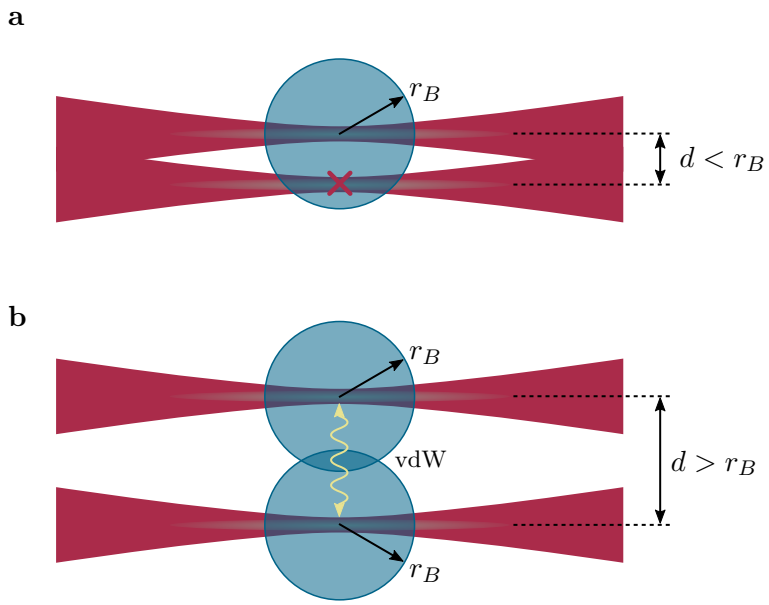

Figure 5.2.: Multiple channel geometry. Dipole blockade effects give rise to a characteristic length scale r_B. The choice of the inter-channel separation d in relation to r_B provides a fundamental change in the nature of expected interactions. *a*: Only one excitation may exist at any given time. *b*: Excitations may simultaneously exist in both channels.

a second collective excitation at a controlled distance d, at which dipole blockade does not prevent excitation but that the interaction strength is non-trivial, acts to induce an additional phase shift, which may likewise be expected to suppress the probability of photon retrieval.

5.2. Experimental implementation

In order to study interactions between photons in spatially separate modes, a second spatial mode (or 'channel') is created by duplicating the first. The optical configuration necessary to achieve this is discussed in section 4.1.4.

A second microscopic ensemble is confined in a second optical trap with a controlled inter-media separation. The second ensemble is illuminated independently (although photons for both channels originate from the same laser, and thus have the same relative

phase). Photons emitted from the second spatial channel are spatially resolved after the vacuum chamber, and detected in a second HBT interferometer, observed by a second pair of SPCMs. This configuration is shown schematically in figures 4.8 and 4.12.

At the smallest separation between the two ensembles, the distance $d \geq 10\,\mu$m is only slightly greater than the radial extent of each atomic cloud $\sigma_{\mathrm{ax}} \approx 2\,\mu$m. It is therefore necessary to ensure that the atomic clouds are prepared in such a way as to minimise the degree of cross-talk.

5.2.1. Cross-talk

Cross-talk is the degree to which elements of each channel that *should not* interact do so. There are two principle elements which may exhibit cross-talk:

- Detection of photons originating from channel x by the SPCMs of channel y (detection cross-talk),
- Absorption of the probe of channel x in the atomic ensemble of channel y (absorption cross-talk).

Detection cross-talk

Detection cross-talk is, in principle, easy to observe. In turn, the fibre which provides each channel's probe beam is blocked, while the other is pulsed, and the number of photons detected on each of the four SPCMs is observed. An extinction ratio is then given in decibels as

$$\mathrm{Extinction}_x = 10 \log_{10} \left(\frac{I_y - I_b}{I_x - I_b} \right), \tag{5.1}$$

where I_x is the rate recorded by the SPCMs of channel x and I_b is the background rate.

In practice, detection cross-talk occurs below a level at which it can be measured. The single-mode fibre coupling to the SPCMs provides sufficient filtering that the extinction ratio achieved between the two channels vastly exceeds other sources of cross-talk. Typical values are $E_{x,y} \gg 70\,\mathrm{dB}$.

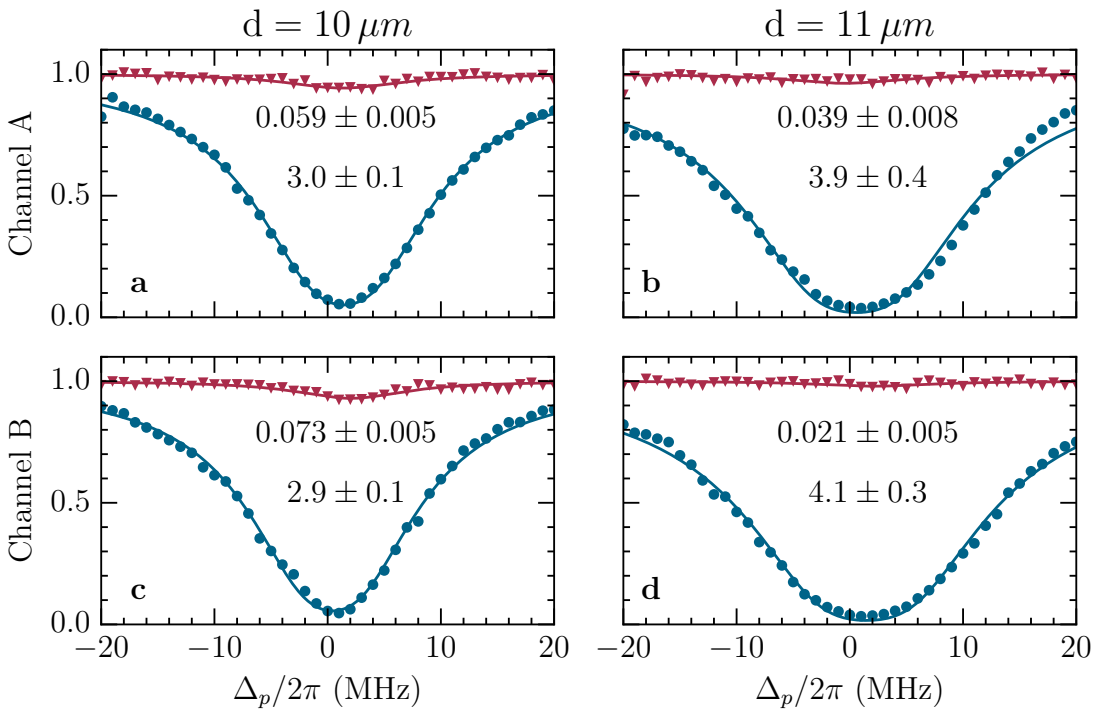

Figure 5.3.: Absorption crosstalk between channels A and B. Blue circles show the absorption of the probe beam for channel x when an atomic cloud is present in both channels x and y. Red triangles show the absorption of the probe beam for channel x when an atomic cloud is only present in channel y (absorption-cross-talk). ODs are printed in the figure from fitting to a $6 \times 2\pi$ MHz wide Lorentzian (solid lines). A small degree of absorption cross-talk is visible at $d = 10\,\mu$m, which is almost entirely suppressed at $d \geq 11\,\mu$m.

Absorption cross-talk

Absorption cross talk is measured per channel by observing the effect on the transmission of the probe beam of one channel by removing the atomic cloud of that channel. This is accomplished by the use of a 780 nm laser line filter[5] to reflect the optical trapping beam for that channel while transmitting the probe beam. The atomic cloud for the other channel remains in place.

[5]Semrock MaxLine 780

Initial measurements exhibited a high degree of absorptive cross talk. To minimise the cross talk, an evaporation stage is added to the experimental sequence. Evaporation is conducted by holding the optical trap at a fixed power level for 400 ms before data is taken during sub-μs shots. The goal of this stage is to reduce the spatial extent of the atomic cloud to minimise absorption cross-talk, with any associated reduction in temperature a strictly secondary benefit. The evaporation stage was added for all data shown in figures 5.3, 5.6, and 5.7.

Figure 5.3 shows measurements of cross-talk for two atomic cloud separations, $d = 10\,\mu$m and $d = 11\,\mu$m, after 400 ms of evaporation. Each plot shows the transmission of the probe beam for that channel where the atomic cloud for that channel is present (blue circles) or absent (red triangles); while the atomic cloud for the *other* channel is present at all times. Each trace is fitted to a Lorentzian distribution with a linewidth of 6 MHz to calculate an associated optical depth, which are printed in the figure.

Both channels exhibit a considerable increase in optical depth at the greater separation, when the atomic cloud is present. This reflects the adoption of the use of an additional degree of freedom to tune the performance of the optical trap after data was taken at a distance of $d = 10\,\mu$m, and is not directly a consequence of the spatial separation.

Both channels exhibit a measurable reduction in cross-talk optical depth by increasing the separation from $d = 10\,\mu$m to $d = 11\,\mu$m, although in all four cases, the cross talk is extremely low at the smallest separation, and diminishes substantially at greater separations. As photon storage/retrieval efficiency is strongly dependent upon the optical depth of the atomic cloud, this provides confirmation that the two channels are satisfactorily spatially independent.

5.2.2. Dual channel photon storage

The protocol for attempting photon storage and retrieval in multiple channels is the same as for a single channel (section 4.4.3). To simplify timing issues, the two channels are illuminated by probe light originating from the same laser, switched by the same

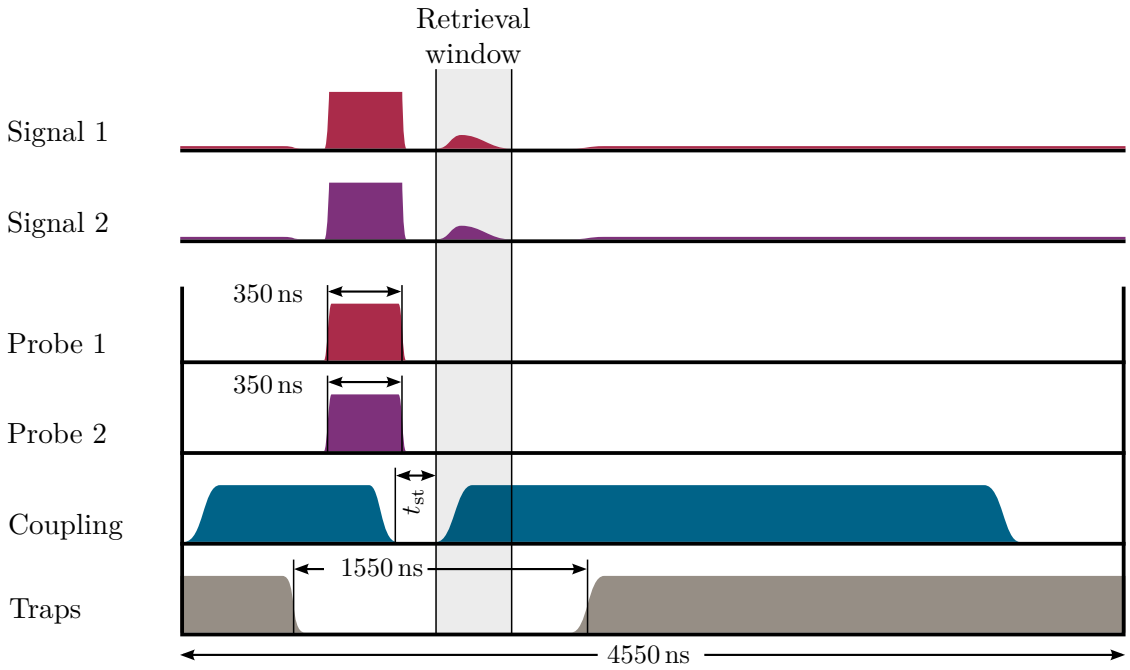

Figure 5.4.: Experimental sequence for observing interactions between spatially separated channels. For the data shown in figures 5.6 and 5.7, $t_{st} = 170\,\text{ns}$. For the data shown in figure 5.8, the storage time (and trap-off time) were extended as necessary.

AOM,[6] split into two modes at the PBS in the 'interferometer' (section 4.1.4). Each cloud is illuminated by a weak coherent pulse of resonant 780 nm light with a mean photon number of $\overline{n}_{in} = 2.2 \pm 0.2$ and a duration of 350 ns.

In order to maintain an equal coupling Rabi frequency across the various n and d values used, Ω_c is measured and adjusted for each shot by Autler Townes splitting. Insufficient power is available to achieve Autler Townes splitting at $n = 80$, and so adjustment is conducted at $n = 30$. The coupling laser beam is aligned before each experimental execution to ensure that Ω_c is equal at both channels. Coupling beam power is adjusted to keep Ω_c consistent across varying n values.

[6]The laser system, shown in section 4.4, can control two probe beams independently, although for the experiment shown in this section, independence is unnecessary and only adds degree of freedom which must be compensated for.

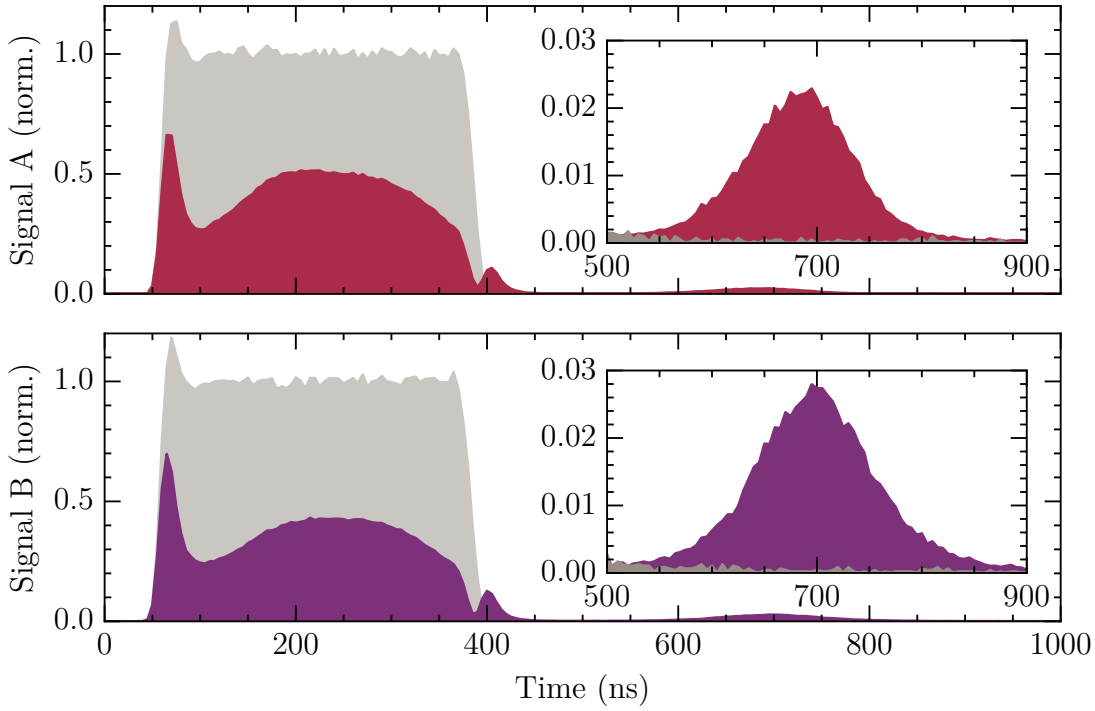

Figure 5.5.: Simultaneous photon storage in two channels at $d = 10\,\mu$m, $n = 80$. No interactions are visible in these intensity plots, as the probability of simultaneous storage is extremely low. Summed photon counts from channels A (red) and B (purple) from simultaneous storage. A reference pulse in which neither channel contained an atomic ensemble is shown in grey. *Inset*: Zoom on retrieval window. The background level in the absence of retrieved photons is visible at levels below 0.002.

As this experiment does not rely on the use of microwave driving, very narrow storage windows can be used to maximise the probability of retrieval. For the data shown in figures 5.6 and 5.7, a storage window of $t_{\mathrm{st}} = 170\,$ns was used, with the duty cycle of the optical trap adjusted to minimise the duration for which the atoms are not trapped. The pulse sequence used is shown in figure 5.4. An example of simultaneous storage is shown in figure 5.5.

5.3. Spatial photon correlations

Due to the low probability of storing and subsequently retrieving a photon in either cloud ($\approx 2\%$), the probability of simultaneous storage and retrieval is negligible in comparison. Consequently, interaction effects cannot be resolved from studying the count rate of each channel, as in figure 5.5. Interaction effects instead require analysis of correlations between photon arrivals at the detectors.

In the absence of interactions between the channels, there should be no correlation in photon arrivals, such that the probability of detecting a photon from both channels simultaneously should be given by the product of the probability of detection for each individual channel:

$$\mathcal{P}_{\mathrm{NI}}(A \cap B) = \mathcal{P}(A) \times \mathcal{P}(B), \tag{5.2}$$

where $\mathcal{P}(x)$ is the probability of detecting a photon in channel x.

In this case, interactions are expected to suppress the probability of retrieving photons simultaneously from both channels as a result of interactional dephasing, such that

$$\mathcal{P}_{\mathrm{I}}(A \cap B) < \mathcal{P}(A) \times \mathcal{P}(B). \tag{5.3}$$

In order to quantify the degree to which spatial correlations are suppressed (if at all), a variant of the second order correlation function $g^{(2)}$ is used. At its most general, this is defined as

$$g^{(2)}_{AB}(\tau) = \frac{\langle N_A(t_A) N_B(t_B) \rangle}{\langle N_A(t_A) \rangle \langle N_B(t_B) \rangle}, \tag{5.4}$$

where $N_A(t_A)$ and $N_B(t_B)$ are the numbers of photons detected at times $t_A\, t_B$ respectively, with $\tau = t_A - t_B$.

In the work presented here, subsequent shots are effectively uncorrelated,[7] and the entire retrieval window (shown in figures 5.4 and 5.5) is treated as a single time bin. Consequently, the time dependence τ can be neglected:

$$g^{(2)}_{AB} = \frac{\langle N_A N_B \rangle}{\langle N_A \rangle \langle N_B \rangle}. \tag{5.5}$$

This yields a metric which has spatial, rather than temporal, dependence, with $N_A\,N_B$ the number of photons detected from channels A and B respectively.

The values of $g^{(2)}_{AB}$ are analogous to te single channel function $g^{(2)}_{A}$ in that a value of 1 indicates no correlations. $g^{(2)}_{AB} < 1$ denotes that photon arrivals are anti-correlated as implied by equation 5.3. Unlike the single channel function $g^{(2)}_{A}$, $g^{(2)}_{AB}$ provides no information about whether or not the light is classical in nature.

5.4. Phase shift model

The phase shift model referred to in this chapter was developed by T. Ilieva and P. Huillery based on [65]. The full model lies outside of the scope of this thesis, and a complete description may be found in [63, 105]. However, a brief summary is included here for reference. This summary is based on the work of H. Busche [105].

The model implements the interaction-induced dephasing discussed in section 3.2.4, taking into account the parameters and geometry of the experiment, as best they are known. This includes the spatial distribution of the atom cloud; and the spatial mode and Poissonian number distribution of the incoming photons. The spatial mode extends the work of [65], which modelled the signal as a plane wave, due to the much larger beam used in those experiments [44].

5.4.1. Modelling a single channel

The model approaches the problem of calculating $g^{(2)}_{A}$ by measuring the overlap of the initial collective ground state of the ensemble $|G\rangle_A$ with the final collective ground state $|G'(t_{\mathrm{st}})\rangle_A$ after a single shot.

[7] Figure 4.20 suggests otherwise, so for the purposes of this analysis, a subsection of shots are selected for analysis such that the photon storage performance is nearly independent of shot number. Additional experimental repetitions were conducted to provide sufficient data within this performance envelope.

Storing and retrieving photons

The collective state of $\mathcal{N}_A$ atoms is given by

$$|G\rangle_A = |g_1\rangle_A \otimes \cdots \otimes |g_{\mathcal{N}}\rangle_A \,. \tag{5.6}$$

Collective excitations are realised with the creation operator

$$S_A^\dagger = \frac{1}{\sqrt{\sum_j \epsilon_A(\boldsymbol{r_j^2}}} \sum_j \epsilon_A(\boldsymbol{r_j}) e^{i\phi_A(\boldsymbol{r_j})} |s_j\rangle_A \langle g_j|_A \,, \tag{5.7}$$

where $|s_j\rangle$ denotes an atom in a Rydberg, $\boldsymbol{r_j}$ denotes the position of atom j, and $\phi_A(\boldsymbol{r_j})$ the combined phase imprinted by probe and control fields. Storage of μ photons produces the multiply excited collective state [122, 123, 191, 192]

$$\left|R_A^{(\mu)}\right\rangle = \frac{1}{\sqrt{\mu!}} \left(S_A^\dagger\right)^\mu |G\rangle_A \,, \tag{5.8}$$

which approximately preserves normalisation of the collective state provided that $\mu \ll \mathcal{N}_A$. Dipole blockade is handled implicitly by choosing a low mean incoming photon number, for simplicity and compatibility with experimental parameters.

Interactions between two atoms j and k that contribute to $\left|R_A^{(\mu)}\right\rangle$, and that are described by $V_{JK}(\boldsymbol{r_j}, \boldsymbol{r_k})$ have a time evolution given by

$$U_A(t_{\mathrm{st}}) = \sum_{j,k>j} e^{-iV_{jk}t_{\mathrm{st}}/\hbar} |s_j\rangle_A \langle s_j|_A \otimes |s_k\rangle_A \langle s_k|_A \,. \tag{5.9}$$

It is assumed that all Rydberg atoms are in the same state nS such that all interactions are of the vdW form

$$V_{jk} = V(\boldsymbol{r_j}, \boldsymbol{r_k}) = \frac{C_6}{|\boldsymbol{r_j} - \boldsymbol{r_k}|^6}. \tag{5.10}$$

The time evolution of the collective state is then given by

$$\left|R_A^{(\mu)}(t_{\mathrm{st}})\right\rangle = U_A(t_{\mathrm{st}}) \left|R_A^{(\mu)}\right\rangle, \tag{5.11}$$

in which each pair of atoms contributing to the collective state have evolved some additional phase, leading to a reduction in the probability of photon retrieval.

Photon retrieval is the reverse of the photon storage process, applying the annihilation operator μ times

$$|G'(t_{\mathrm{st}})\rangle_A = (S_A)^\mu \left|R_A^{(\mu)}(t_{\mathrm{st}})\right\rangle. \tag{5.12}$$

The phase relation between individual atoms in $|G\rangle_A$ has been modified by the interactions between μ collective excitations, such that $|G'(t_{\mathrm{st}})\rangle_A \neq |G\rangle_A$

Calculating photon statistics

Since the input field is a coherent state, and not a Fock state, the probabilistic photon number is handled by a superposition of collective states of various photon numbers [134]. As the experiment is limited to the detection of no more than two photons simultaneously (due to the use of a two-detector HBT configuration), the photon number is truncated at $\mu = 2$:

$$|R\rangle_A = \sum_{\mu \leq 2} c_\mu \left|R^{(\mu)}\right\rangle_A . \tag{5.13}$$

This truncation is justified by the low mean photon number used in the experiment and the low storage/retrieval efficiency: a typical experiment sets $\overline{n}_{\mathrm{in}} \approx 2$ and observes $\overline{n}_{\mathrm{ret}} \approx 0.02$.

The overlap of the initial and time evolved collective state containing exactly μ photons is given by

$$D_A^{(\mu)} = \frac{{}_A\langle G|G'(t_{\mathrm{st}})\rangle_A}{{}_A\langle G|\,(S_A)^\mu (S_A^\dagger)^\mu\,|G\rangle_A}, \tag{5.14}$$

which determines the probability of retrieving μ photons in their original mode. In the case that $V_{jk} = 0$, $D_A^{(\mu)} = 1$. Since events in which only one photon is stored cannot exhibit interaction-induced dephasing, and $\mu > 2$ states are ignored, only the case $D_A^{(2)}$ is of interest, with the probability of retrieving exactly $\mu = 2$ photons given by $\left|D_A^{(2)}\right|^2$. The correlation function can then be calculated as

$$g_A^{(2)} = \frac{2\left|D_A^{(2)}\right|^2 |c_2|^2}{\left(|c_1|^2 + 2\left|D_A^{(2)}\right|^2 |c_2|^2\right)^2} \tag{5.15}$$

5.4.2. Extending the model to two channels

The two-channel case extends the single-channel case by modelling two atomic ensembles illuminated by two similar incoming photon pulses, $\overline{\mu}$ and $\overline{\nu}$, which act upon the collective ground state $|G\rangle_{AB} = |G\rangle_A \otimes |G\rangle_B$ with annihilation operators S_A, S_B, to create the

time evolved state

$$\left|G'(t_{\mathrm{st}})\right\rangle_{AB} = (S_A)^{\mu}(S_B)^{\nu}\left|R^{(\mu,\nu)}(t_{\mathrm{st}})\right\rangle_{AB}. \tag{5.16}$$

The time evolved overlap is similarly calculated for values of μ, ν within the desired photon distribution

$$D_{AB}^{(\mu,\nu)} = \frac{{}_{AB}\left\langle G|G'(t_{\mathrm{st}})\right\rangle_{AB}}{{}_{AB}\left\langle G\right|(S_A)^{\mu}(S_B)^{\nu}(S_A^{\dagger})^{\mu}(S_B^{\dagger})^{\nu}\left|G\right\rangle_{AB}}. \tag{5.17}$$

Again, due to the low incoming mean photon number and storage/retrieval efficiency, the distribution is truncated, to give

$$\left|R\right\rangle_{AB} = \sum_{\mu,\nu\leq 1} c_{\mu,\nu}\left|R^{(\mu,\nu)}\right\rangle_{AB} \tag{5.18}$$

Spatial correlations can then be calculated based on the probability $\left|D_{AB}^{(1,1)}\right|^2$ to simultaneously retrieve exactly one photon from each channel in their original modes, giving

$$g_{AB}^{(2)} = \frac{\left|D_{AB}^{(1,1)}\right|^2\left|c_{1,1}\right|^2}{\left(\left|c_{0,1}\right|^2 + \left|D_{AB}^{(1,1)}\right|^2\left|c_{1,1}\right|^2\right)\left(\left|c_{1,0}\right|^2 + \left|D_{AB}^{(1,1)}\right|^2\left|c_{1,1}\right|^2\right)}. \tag{5.19}$$

5.4.3. Simulation

The model is executed in a Monte-Carlo simulation. Each shot of the simulation performs the following steps:

- Generate two ensembles of $\mathcal{N}_A, \mathcal{N}_B$ atoms, based on a Gaussian density profile from experimentally determined parameters. This gives the set of atoms $[\boldsymbol{r}_{A,1}\cdots\boldsymbol{r}_{\mathcal{N}_A}, \boldsymbol{r}_{B,1}\cdots\boldsymbol{r}_{\mathcal{N}_B}]$.
- Simulate photon storage and retrieval to calculate $D_A^{(2)}, D_B^{(2)}, D_{AB}^{(1,1)}$ given the atom position set, defined interaction potential V_{jk}, specific mean photon numbers $\overline{\mu}$ and $\overline{\nu}$.
- Calculate single- and double-channel correlations $g_A^{(2)}, g_B^{(2)}, g_{AB}^{(2)}$ for the simulation shot.
- Repeat a sufficient number of times to calculate averaged values of $g_A^{(2)}, g_B^{(2)}, g_{AB}^{(2)}$.

5.5. Observation of spatial photon correlations

Collective Rydberg excitations are expected to accumulate phase gradients as a result of interactions with other nearby excitations, leading to a suppression of the rate at which photons can be retrieved where multiple collective excitations have been created.

In the work presented here, collective Rydberg excitations are created in two atomic clouds, with a spacing from centre to centre of between $10 - 16\,\mu$m. As a result of interactions with nearby excitations, each excitation is expected to accumulate a phase gradient scaling as $V_{jk}t_{\mathrm{st}}$. All excitations are in the same state $|S\rangle$, such that dipolar interactions are of the vdW form, such that $V_{jk} = C_6/r_{jk}^6 \propto n^{11}$.

In this section, spatial photon correlations will be demonstrated as a consequence of the three controllable parameters: n, r_{jk}, and t_{st}.

5.5.1. Scaling with principal quantum number

To measure the effect of changing n on spatial photon correlations, the principal quantum number is changed while keeping the distance $d \approx 10\,\mu$m and $t_{\mathrm{st}} \approx 170\,$ns fixed. For each change in n, the power of the coupling laser beam is adjusted to keep $\Omega_c \approx 7 \times 2\pi\,$MHz approximately constant.

The results are shown in figure 5.6. For values of the principal quantum number $n > 65$, spatial correlations are observed with increasing strength, up a final value of $g_{AB}^{(2)} = 0.40 \pm 0.03$ at $n = 80$. The inset figure shows the single channel correlations $g_A^{(2)}$ as a function of n, demonstrating that each channel exhibits quantum behaviour across the entire parameter range shown. Uncertainties are calculated by splitting the data into subsets that are evaluated separately, and then quoting the mean and standard deviation. The figure shows good agreement between the experimental results and the outcome of the phase shift model, which suggests that the observed spatial anti-correlation is a consequence of vdW interactions.

At $n = 50$, both atomic ensembles are displaying clear suppression of multiple photon retrieval ($g_A^{(2)}(n = 50) = 0.6 \pm 0.1$, $g_B^{(2)}(n = 50) = 0.7 \pm 0.1$), while there is no evidence of interaction between the two channels ($g_{AB}^{(2)}(n = 50) = 1.0 \pm 0.1$). The single-channel

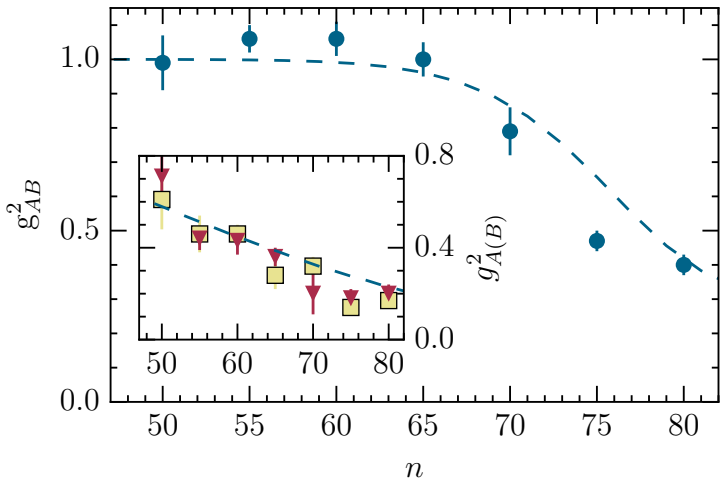

Figure 5.6.: Cross-site correlations as a function of principal quantum number n. Storage time and cloud separation are kept constant. The dashed line gives the expected results based on the phase shift model. Due to the rapid scaling $\hat{U}_{AB} \propto n^{11}$, $g^{(2)}_{AB}, 1$ is only observed for $n > 65$. *Inset*: Single site $g^{(2)}_{A(B)}$ values for each principal quantum number. As expected, these values sharply decline with increasing n, due to larger dipole blockade radii.

suppression is consistently stronger than the two-channel suppression across the range of n tested. This behaviour indicates that two length scales are important to understand the process arising from the geometry of the two ensembles. The single-channel suppression arises from dipole blockade, with r_B setting the minimum distance between collective excitations [34, 39]. The two-channel suppression arises from the channel separation $d = 10\,\mu$m, which represents the minimum possible spacing between collective excitations from which correlations are considered for $g^{(2)}_{AB}$. The shorter spacing permitted by r_B allows stronger interactions, leading to more rapid dephasing and a stronger suppression.

The atomic cloud in each channel has dimensions of approximately $\sigma_{\mathrm{rad}} \approx 1.5\,\mu$m, $\sigma_{\mathrm{ax}} > 40\,\mu$m (section 4.1.4). The dipole blockade radii for the limiting states used here are $r_B\,(50S_{1/2}) \approx 4\,\mu$m and $r_B\,(80S_{1/2}) \approx 9\,\mu$m. As $r_B \gg \sigma_{\mathrm{rad}}$ for all states used here, if multiple excitations are created, they will occur in a linear chain, up to total saturation of the atomic cloud. However, with a mean incident photon number of $\overline{n}_{\mathrm{in}} = 2.2 \pm 0.2$,

total saturation is relatively unlikely even with the highest Rydberg states used ($80S_{1/2}$).

At $n = 80$, the dipole blockade radius $r_B \approx 9\,\mu\text{m} < d$ such that a small fraction of one channel's volume may be blockaded by a collective excitation in the other. However, there is evidence to support that blockade is less important than phase shifts induced by interactions, as suppression of $g^{(2)}_{AB}$ is already evident for $n > 65$ and r_B ($65S_{1/2} \approx 6\,\mu\text{m}$, which is suggestive, but not conclusive. The question of whether interactions or blockade dominate is re-visited where the dependence of $g^{(2)}_{AB}$ on the storage time t_{st} is examined (section 5.5.3) [63].

5.5.2. Scaling with channel spacing

The strength of the interaction V_{jk} is also dependent on the channel spacing, d, with the vdW strength scaling as C_6/r^6_{jk} [5, 25]. This degree of freedom represents a fundamental improvement in the apparatus discussed in this thesis over its previous generation, and other similar projects, as experiments using photons propagating in the same spatial mode cannot vary the spacing in as controlled a manner.

To measure the effect of changing d on spatial photon correlations, storage is conducted at a fixed, high principal quantum number, $n = 80$, to maximise the dynamic range of the spatial correlations. The storage time remains fixed at $t_{\text{st}} = 170\,\text{ns}$ to maximise retrieval probability in the absence of interactions. The inter-channel separation is adjusted over the range $d = 10 - 16\,\mu\text{m}$. At each separation, the coupling laser beam is realigned and power adjusted to equalise $\Omega_c \approx 9 \times 2\pi\,\text{MHz}$ for both channels. The minimum separation was chosen based both on the blockade radius at this value of n ($r_B\,(80S_{1/2}) \approx 9\,\mu\text{m}$), and the absorption cross-talk which increased substantially below $d = 10\,\mu\text{m}$ (section 5.2.1).

The results are shown in figure 5.7. Suppression of spatial correlations are observed for $d < 13\,\mu\text{m}$, with the greatest suppression at the smallest distance as expected due to the $1/r_{jk}$ scaling of the interaction strength. Figure 5.7 also includes the output of the phase shift model (dashed line), showing good agreement with experimental results. The figure inset shows single-channel $g^{(2)}_{A(B)}$, which are approximately constant and independent of

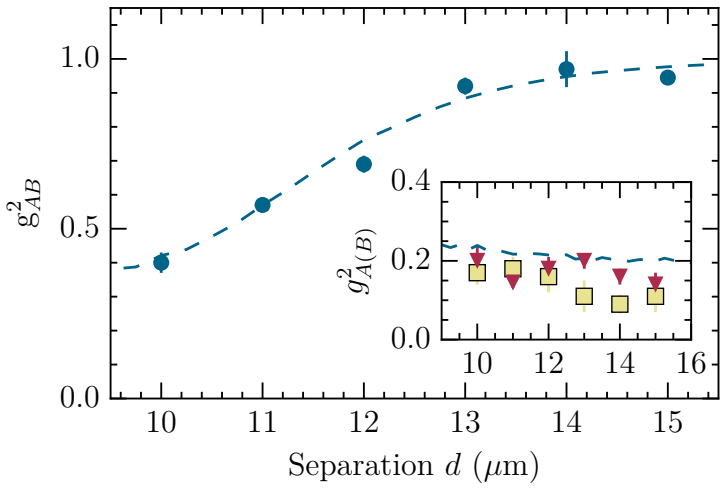

Figure 5.7.: Cross-site correlations as a function of site separation d. Storage time and principal quantum number are kept constant. The dashed line gives the expected results based on the phase shift model. Rapid scaling of $\hat{U}_{AB} \propto 1/r_{jk}^6$ results in interactions only being observed at $d < 13\,\mu$m. *Inset*: Single site $g^{(2)}_{A(B)}$ values for each distance. As expected, these are approximately constant, as they are independent of d.

d, as expected. There is some minor fluctuations, most likely arising from variation in day-to-day performance of the experimental apparatus.

Figure 5.7 clearly shows that the spatial correlations $g^{(2)}_{AB}$ can be adjusted independently of the single-channel correlations $g^{(2)}_{A(B}$. This independence represents a genuinely new degree of freedom to engineer the desired form of effective photon-photon interactions [193].

The degree to which the self- and cross-Kerr non-linearities can be adjusted independently is limited in this implementation by creating both collective Rydberg excitations in the same Rydberg state $|S\rangle = 80S_{1/2}$. Single-channel interactions therefore scale at the same rate as interactions between the two channels. The single- and inter-channel interactions could be further decoupled by performing the initial photon storage in separate, weakly interacting Rydberg states, such that inter-channel interactions are initially negligible, and then switched on by the addition of a new field. Interactions could be

switched either via resonant microwave driving to a state of opposite polarity $|P\rangle$, as in the previous two chapters [53, 54], or via a Stark-tuned Förster resonance [47, 194]. The former technique, resonant microwave driving, is central to an earlier proposal to construct an optical-CZ logic gate [61]. Such techniques are not currently possible on the apparatus discussed here.[8]

The suppression in $g^{(2)}_{AB}$ is visible at a distance substantially greater than either the probe photon wavelength or the diffraction limited spot size that localises the collective excitation. $g^{(2)}_{AB} < 1$ for $d < 13\,\mu\text{m} \approx 17\lambda_p$. These length scales are sufficient to consider a possible interface with other systems, such as fibre based photonic systems [195–197] or multichannel waveguides [198, 199]

5.5.3. Scaling with storage time

As noted in section 5.5.1, the evidence of figures 5.6 and 5.7 agree with the phase shift model and suggests that interactional dephasing is responsible. However, it does not represent conclusive evidence that accumulated phase, rather than dipolar blockade, is responsible. This question can be conclusively answered by observing the effect, if any, of storage time t_{st} upon the spatial correlations between the two channels. If dipole blockade is solely responsible, then no time dependence should be visible: correlations should be evident regardless of storage time. If there is a clear time dependence, then dipole blockade cannot be responsible, and a progressive effect - accumulated phase shift - must be involved.

To measure the effect of changing t_{st} upon spatial correlations, the value of the princi-

[8] The coupling laser (and microwave excitation discussed in section 4.5 and chapters 6 and 7) currently addresses both channels simultaneously. Placing a single channel in a separate Rydberg state requires either simultaneously coupling both channels to separate $nS, n'S$ Rydberg states (using a second and individually addressed coupling laser); or time-division multiplexing, using the individual addressing capability of the probe lasers to selectively excite one channel to $n'P$ or $n'S$[9] via nS, and then the second channel to nS.

[9] Via a two-photon microwave transition. While this is possible with available equipment (see appendix C), it is not a practical approach with a single microwave signal generator.

pal quantum number n and channel separation d were held constant. Two sets of n and d were tested. The storage time was varied by adjusting the delay before the control beam power was restored for photon retrieval. The period for which the optical trap was switched off was lengthened, to a longer duration than that used for the microwave experiments in chapters 6 and 7. Due to the dependence of storage/retrieval efficiency upon storage time (figure 7.4), and the accelerated trap loss arising from longer time-of-flight of the atomic ensemble, these changes required both substantially more shots in total (up to 8× greater), and fewer shots per MOT load (up to 2.5× fewer) to remain within a time-independent performance envelope (section 5.3). In order to generate sufficiently rich data sets within a period of time over which the entire experimental apparatus remains reliably stable, the evaporation stage discussed in section 5.2.1 was omitted. Cross-talk was evaluated in terms of the ratio of storage achieved in channels x and y arising from a probe beam present only in channel x, which in all cases was indistinguishable from background noise.

The results are shown in figure 5.8. The dataset at $n = 70$, $d = 11.5\,\mu$m (blue circles) exhibits a clear change, from $g^{(2)}_{AB}(280\,\text{ns}) = 1.1 \pm 0.2$ to $g^{(2)}_{AB}(790\,\text{ns}) = 0.5 \pm 0.1$. Dashed lines show the results of the phase shift model. The model shows a clear agreement with experimental results and a time-dependent trend is clear, with greater suppression apparent at longer storage time. Uncertainties are greater in the data presented in this figure owing to the strong dependence of photon storage/retrieval efficiency upon storage time and consequently, reduced SNR in the data relative to figures 5.6 and 5.7.

The dataset at $n = 80$, $d = 11\,\mu$m (red triangles) shows a weaker time dependence, as it reaches a shallow floor extremely rapidly, in agreement with the model. A trend is still present: $g^{(2)}_{AB}(170\,\text{ns}) = 0.35 \pm 0.07 > g^{(2)}_{AB}(720\,\text{ns}) = 0.16 \pm 0.07$. Due to limitations on the minimum storage time that can be probed,[10] it is not practical to observe the time dependence of interactions closer to the dipole blockade radius ($r_B\,(80S_{1/2}) \approx 9\,\mu$m).

This represents strong evidence that interaction-induced phase shifts are an important

[10] The switching speed and transient behaviour of the polarisation-switching EOM used to control Ω_c places a practical limitation at $t_{\text{st}} \geq 160\,\text{ns}$, see section 4.4.1.

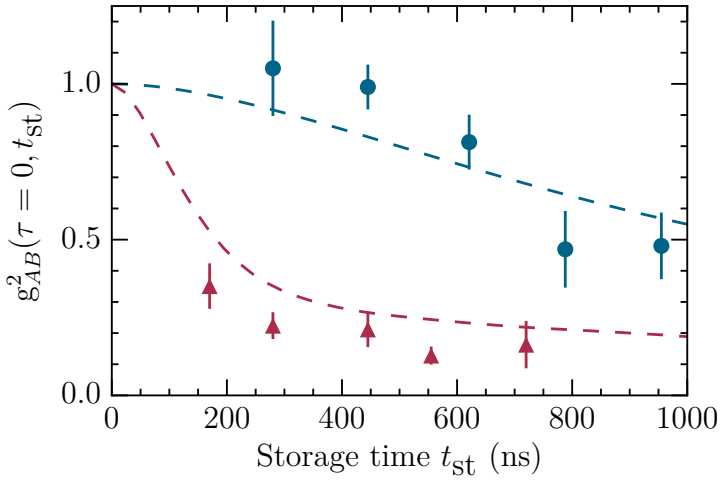

Figure 5.8.: Cross-site correlations as a function of storage time t_{st}. For each data series, principal quantum number and distance are held constant at (blue circles) $n = 70$, $d = 11.5\,\mu$m; (red triangles) $n = 80$, $d = 11.0\,\mu$m. The dashed lines give the results of the phase shift model. The phase shift is expected to scale linearly with storage time, $\hat{U}_{AB} \propto t_{st}$, leading to a fairly low gradient in $g^{(2)}_{AB}$. The evaporative stage discussed in section 5.2.1 was not included for these measurements.

contribution to behaviour beyond the dipole blockade radius, and that the effects shown in this chapter arise from those phase shifts, and not purely from blockade.

6. Microwave electrometry via Rydberg-Rydberg transitions

This chapter will examine the use of photon storage and retrieval techniques in a cold atomic ensemble as a means to perform sensitive measurements of weak microwave fields. The extremely high sensitivity of Rydberg states to microwave fields [25] in combination with the fast repetition rates achieved [105, 106] present an intriguing system for such electrometry.

Axiomatically, the study of physics (or any other quantitative field) necessitates observing a phenomenon and quantifying - measuring - the result. The ability to, and degree to which we may, gain and improve upon our understanding of the world around us relies on making better measurements of phenomena.

The quality of a measurement is typically characterised by its *accuracy* and its *precision*. Accuracy describes the degree of certainty in a measurement relative to an absolute standard, while the precision describes how tightly clustered are a series of measurements [200]. Ideal measurements should have both high accuracy and high precision.

Since complex systems can rarely be perfectly separated out into unique phenomena, a measurement will typically contain both signal - the phenomenon in which we are interested; and noise - other phenomena in which we are not presently interested. This is characterised by the SNR[1]. Noise can contribute to reductions in both the accuracy, and the precision, with which the interesting phenomenon is measured. A key aspect of designing better measurements, and measurement systems, is reducing and filtering out

[1] Signal-to-noise ratio

the noise from a measurement.

The simplest technique to suppress noise in most measurements is to measure over a longer period of time, allowing randomly distributed noise to average away relative to the non-random signal. The rate at which SNR improves as a function of observation time is used to classify different classes of noise [201]. Time is a finite resource, and measurement systems must be designed to achieve the best measurement - the greatest SNR - within the available measurement time.

This is described by the *sensitivity* of a measurement system: the weakest signal level that offers a specific SNR in a specific observation time. The NEP[2] is usually defined as the signal level that results in an Signal-to-noise ratio of 1 in a 1 Hz output bandwidth, equivalent to 0.5 s observation time.

The question of sensitivity was already implicitly addressed in the discussion of the single-photon sensitive optical detection system implemented in this experiment (section 4.2), and a numerical value may be calculated based on the above definition at $25\,\mathrm{aW}\,\sqrt{\mathrm{Hz}}^{-1}$ at a wavelength of 780 nm. Research on the human eye under ideal conditions gives a peak sensitivity at a wavelength of around 510 nm of $1 - 10\,\mathrm{fW}\,\sqrt{\mathrm{Hz}}^{-1}$ [202].

Measurement of weak microwave fields

Measurements of weak microwave fields is attractive for many fields [203], such as radio astronomy [204], advanced communications[3] [81, 82] and both civilian and military radar technology [205–207].

Traceable techniques for measuring and calibrating microwave fields and devices have changed little in over a entury, still being based on the resistively loaded antennae used by Hertz in the 19$^{\mathrm{th}}$ century [208–210]. Measurement techniques for other standards have advanced considerably through the use of quantum objects (such as atoms) which

[2] Noise-equivalent power

[3] The currently evolving '5G' telecommunications standard is expected to rely on frequencies $> 6\,\mathrm{GHz}$ once finalised.

exhibit superb stability and reproducibility [211–214].

There have been multiple demonstrations of exquisitely sensitive microwave measurements based on quantum systems in recent years, using cavity QED[4] [215–217], waveguides [218] and thermal Rydberg atoms [89].

Here, we demonstrate the use of photons stored as collective Rydberg excitations in ultra-cold atoms to translate the presence of a weak microwave field into an optical response, that can be measured with comparable results to published values [89, 90, 219].

Microwave driven photon storage

In previous work, D. Maxwell investigated the effect of driving transitions between Rydberg states of opposite parity in collective Rydberg excitations [103]. Since the second Rydberg state was not resonant with the photon retrieval process, Rabi oscillations were observed in the rate at which photons were retrieved as a function of rotation angle. In comparison to Rabi oscillations between the ground and first excited state of an atom, such as in figure 3.3, the oscillations between two Rydberg states exhibited a strong suppression of storage/retrieval efficiency at non-integer-π rotation angles [53], with a dependence on the mean number of collective excitations simultaneously created. Successive 2π rotations were shown to exhibit a reduction in the second order correlation function $g^{(2)}$ [53, 54].

The suppression of efficiency at non-integer-π rotation angles results in a steep gradient in photon retrieval as a function of applied microwave fields (shown in figure 6.1). The steep gradient indicates an extremely strong sensitivity to weak driving fields that is greater than the typical form of Rabi oscillations. Consequently, photon storage using ultra-cold Rydberg atoms has been proposed and implemented as a technique for microwave electrometry. Provisional results suggest that, even factoring in the time required to prepare and cool atoms for photon storage and absent prolonged optimisation, sensitivities comparable to published results are practical [89].

[4] Quantum electrodynamics

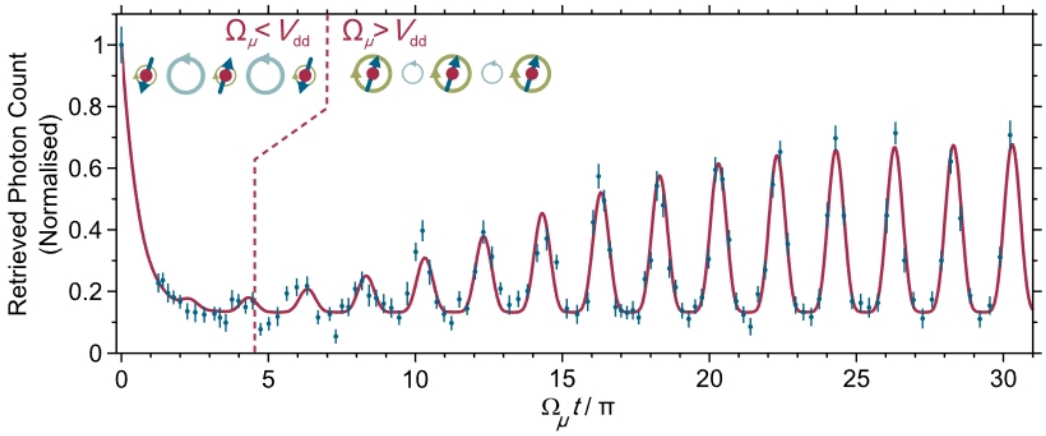

Figure 6.1.: Controlled interactions between Rydberg polaritons. Retrieved signal normalised to the case of zero microwaves plotted as a function of microwave rotation angle. Figure and caption courtesy of D. Maxwell [53].

6.1. Photon storage spectroscopy

In order to probe Rydberg-Rydberg transitions, the resonant frequencies must first be identified. A given transition frequency can be predicted by calculating the difference in energy levels via quantum defects [107–109]. Calculations are simplified by the use of a tool recently written in Durham by N. Šibalić: ARC[5] [181]. Spectroscopic techniques can then be used to perform a local search on the experimental apparatus to find the correct value, accounting for any inaccuracy in published values, instrument calibration, and uncorrected stray fields.

Here, we use photon storage spectroscopy to identify the resonant frequency. In this technique, a short microwave pulse is applied during a longer storage window, $t_{\mathrm{st}} = 550\,\mathrm{ns}$, to drive a fraction of the population from $|S\rangle$ into $|P\rangle$. When the coupling laser is switched back on to retrieve photons from the ensemble, a reduction in the intensity of the retrieval pulse is to be expected. This sequence is shown in figure 6.3. In successive shots, the microwave frequency ω_μ is scanned across a range around the predicted value ω_{pred}.

[5] Alkali Rydberg calculator

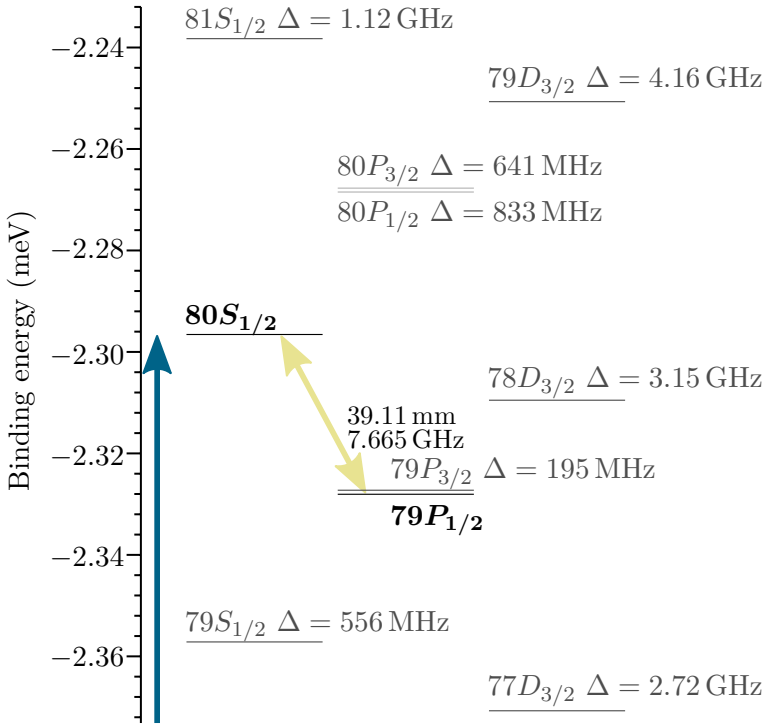

Figure 6.2.: ^{87}Rb Rydberg manifold around $80S_{1/2}$. Microwaves resonant with transition to $79P_{1/2}$ (shown in black). Other nearby states are shown with transition detunings (in grey). S and D states are shown with the two-photon detuning. Levels calculated with ARC [181].

The states $80S_{1/2}$ and $79P_{1/2}$ are chosen for use for $|S\rangle$ and $|P\rangle$ respectively. The transition has a predicted frequency of $\omega_{\mathrm{pred}} = 7.665 \times 2\pi\,\mathrm{GHz}$. The local state manifold is shown in figure 6.2. Due to the density of states, a large number are conceivably accessible via off-resonant one- or two-photon transitions simultaneously with the desired transition. The relevant one- and two-photon detunings are shown in the figure.

This and the following chapter (7) make use of a single optical trap and atomic ensemble, unlike chapter 5. The second channel is physically blocked and the detector pair observing the blocked channel are disabled.

Figure 6.4 shows two photon storage spectroscopy traces taken with different microwave power and pulse widths. The two traces were taken approximately two weeks apart. The difference in centre frequency ($\Delta_{\mathrm{red}} - \Delta_{\mathrm{blue}} = (1.6 \pm 0.1) \times 2\pi\,\mathrm{MHz}$) is

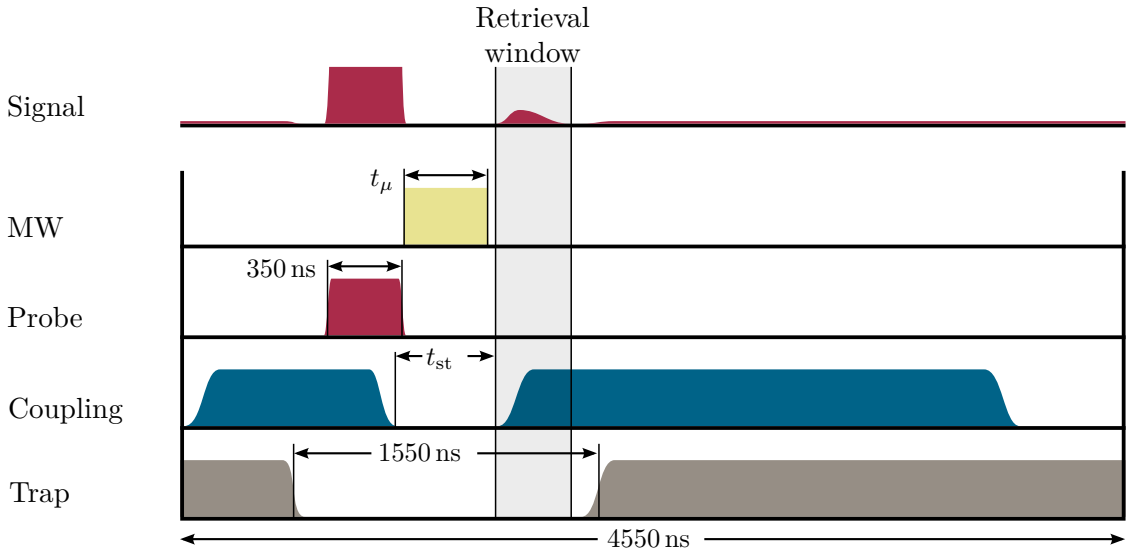

Figure 6.3.: Pulse sequence for photon storage spectroscopy. A similar sequence to figure 4.17. The storage time is extended to $t_{\mathrm{st}} = 550\,\mathrm{ns}$, and a microwave pulse is applied during the storage window.

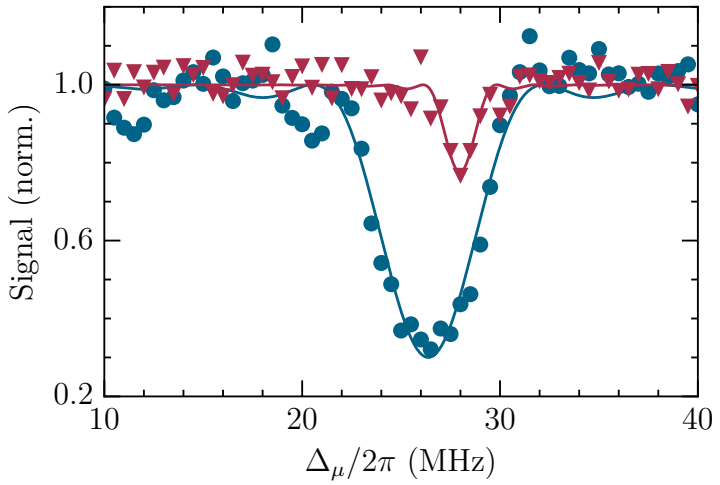

Figure 6.4.: Photon storage spectroscopy of the the $80S_{1/2} \rightarrow 79P_{1/2}$ transition. Microwave detuning given by $\Delta_\mu = \omega_\mu - \omega_{\mathrm{pred}}$. $\omega_{\mathrm{pred}} = 7.665 \times 2\pi\,\mathrm{GHz}$. Solid lines are fits to equation 6.1. Blue circles: $t_\mu = 250\,\mathrm{ns}$. Red triangles: $t_\mu = 450\,\mathrm{ns}$, $\Omega_{\mathrm{red}} = 0.1\,\Omega_{\mathrm{blue}}$.

believed to be due to drift in weak stray electric or magnetic fields.

The carrier wave of the microwave pulse generator is well approximated by a square wave (see section 4.5). Consequently, the line-width of the microwave excitation can be assumed to be a sinc function, as the Fourier broadening far exceeds the specified CW[6] line-width γ_μ of the microwave signal generator. The solid lines in figure 6.4 are fits to the function

$$p(\omega_\mu) = 1 - a_0 \,\mathrm{sinc}^2(a_1 \times (\omega_\mu - \omega_{34})), \tag{6.1}$$

where a_0, a_1, ω_{34} are fitting parameters and $a_1 \leq t_\mu$ gives the effective width of the microwave pulse. This bound on the fitting parameter is motivated by a lack of certainty in how precisely the microwave pulse is sandwiched inside the storage window, rather than overlapping with the storage, or retrieval, pulses. Available hardware tools limit the precision to approximately $\pm 100\,\mathrm{ns}$ (section 4.5).

The data in figure 6.4 shown in red triangles was taken with a weak microwave pulse and a set duration of $t_\mu = 450\,\mathrm{ns}$. The fit gives a effective pulse width of $a_1 = 298 \pm 3\,\mathrm{ns}$. The data shown in blue circles was taken with a greater Rabi frequency (20 dB higher, or 100× increase in power and 10× increase in Rabi frequency) and a shorter set pulse duration of $t_\mu = 250\,\mathrm{ns}$. In combination, the data shown in blue was taken with a rotation angle 5.6× greater than the data shown in red.

Short, high intensity, microwave pulses are well suited to making initial searches for a predicted transition. These produce broad, deep spectroscopic features that retain visibility and contrast in wide, low resolution frequency scans. The central resonant frequency ω_{34} can then be better resolved with a longer pulse and a lower modulation depth to minimise Fourier and power broadening of the transition line.

6.2. Microwave sensitivity

In the work of Sedlacek [89], the Rabi frequency of an applied microwave field was measured by observing the change in transmission of an EIT feature in a thermal cell. Rabi

[6] Continuous-wave

frequency calibration is performed at high microwave power by Autler-Townes splitting of the transmission feature, decreasing on-resonant transmission. Very weak microwave fields were observed by an *increase* in on-resonant transmission due to broadening the resonance to interact with additional velocity classes of atoms.

In a cold atomic system, the Doppler broadening is too small to observe microwave enhanced transmission in the same way, and the Autler-Townes splitting technique used to calibrate both the coupling Rabi frequency Ω_c and the performance of the three antennae (section 4.5.2) is not suited to detecting extremely weak fields.

In order to measure a sensitivity, a technique similar to the spectroscopic approach discussed in 6.1 is used to measure a reduction in photon storage/retrieval efficiency as a function of microwave power where $\Theta \ll \pi$. By comparing this reduction to a prior calibration, a Rabi frequency Ω_μ may be calculated. Using the known dipole matrix element and Clebsch-Gordan coefficient of the transition probed, an electric field strength is calculated, and based on the time taken to conduct the measurement, a sensitivity calculated.

The steep gradient in signal level for $\Theta \ll \pi$ shown in figure 6.1 is promising for this approach, as it suggests that a reduction in retrieved signal may be resolved at a relatively weak microwave field due to the *suppression* of efficiency relative to the $\cos^2(\Theta/2)$ expectation from section 3.1.5.

6.2.1. Rabi oscillations

Rabi oscillations between states $|S\rangle$ and $|P\rangle$ can be observed by using the sequence introduced in section 6.1 (figure 6.3). Photons are first stored in state $|S\rangle$. A microwave pulse is applied within the storage window, and then any photons remaining in state $|S\rangle$ are read out, while excitations in the $|P\rangle$ state do not interact with the retrieval process, resulting in a signal proportional to the population remaining in $|S\rangle$

The mixing angle $\Theta = \Omega_\mu t$ can be modified by varying either the duration of the microwave pulse, or by varying the Rabi frequency (via the intensity). Varying the microwave intensity offers substantially greater resolution, as the microwave generator

offers better than $1\,\mu V_{rms}$ across the range $22.36\,mV_{rms} - 2236\,mV_{rms}$ (approx 2.2 million points). However, for technical reasons, an experiment varying the power cannot include a step in which the power is explicitly set to zero. This requires a zero-Ω_μ data point to be explicitly recorded separately, which may result in subtly different experimental conditions. Varying the excitation time is limited to a resolution of 5 ns by the clock cycle of the control system (see section 4.3), with a practical maximum excitation time of ≈ 500 ns (up to 100 points). Here, the rotation angle is varied by adjusting the Rabi frequency, with a fixed pulse duration.

Figure 6.5 shows Rabi oscillations between the same states used in figure 6.4 ($80S_{1/2}$ and $79P_{1/2}$), figure 6.2 for three different incoming photon numbers $\overline{n}_{in}$ where the rotation is varied by changing the microwave intensity with a fixed pulse duration $t_\mu = 450$ ns. The data are fitted to a function of the form

$$\text{Signal} = a_0 + a_1 e^{-\Theta/a_2} \left|\cos\left(\frac{\Theta}{2} + \phi\right)\right|^{2\mathcal{M}}, \tag{6.2}$$

with five free fitting parameters: a_0 is the minimum retrieval rate or noise floor, a_1 is the amplitude of the oscillations, a_2 is the decay rate of the oscillations, ϕ is the phase shift of the oscillations, and $\mathcal{M}$ is a power law function. In the case of ideal Rabi oscillations, $\mathcal{M} = 1$, while the suppressed efficiency shown in figure 6.1 and [53, 103] results in $\mathcal{M} > 1$. In the work of Maxwell, the parameter $\mathcal{M}$ is interpreted as the mean number of photons stored as collective Rydberg excitations.

Figure 6.5 shows several features consistent between the three traces. All three exhibit a phase shift of $\phi = -0.18\pi$, and the expected first Rabi oscillation at $\Theta \approx \pi$ is strongly suppressed relative to peaks at greater multiples of π. These results are consistent with the previous work by Maxwell [53, 103], which this experiment was intended to reproduce.

The three plots in figure 6.5 are all normalised to the retrieval rate of the highest incoming photon number in the absence of a microwave field. As expected from figure 4.21, in the absence of a microwave field a lower incoming photon number results in a lower retrieved photon number. However, a lower incident photon number also produces greater visibility in the Rabi oscillations. It is probable that this is due to reducing the

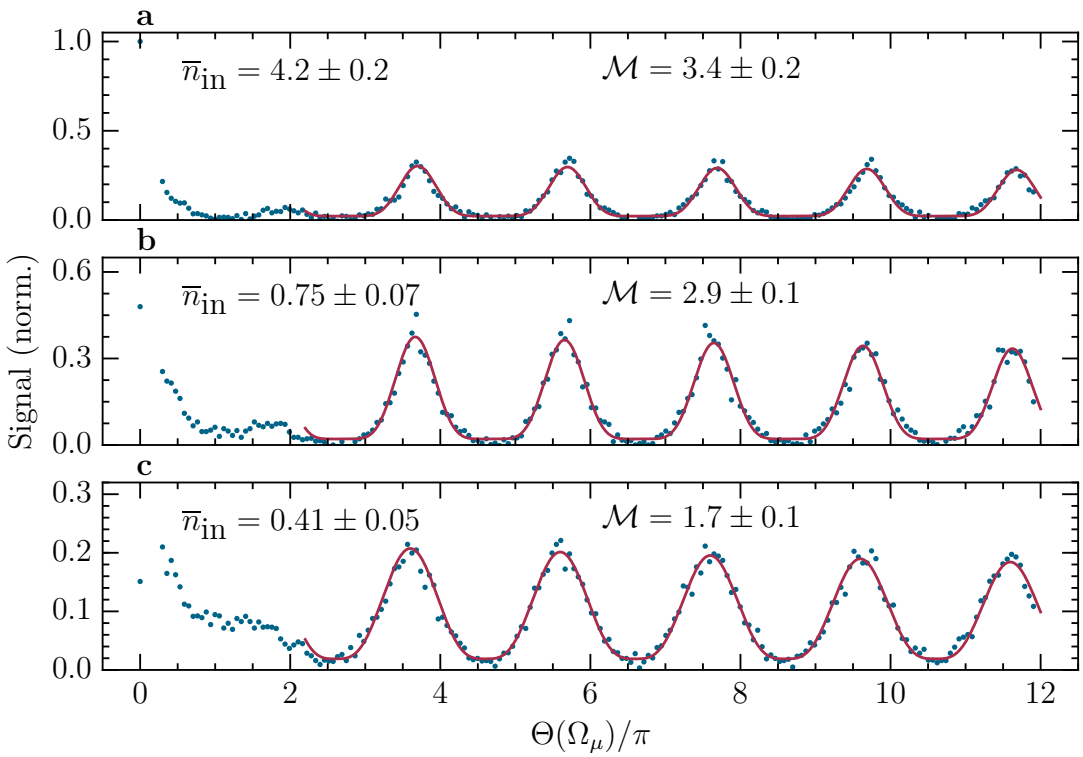

Figure 6.5.: Rabi oscillations in photon retrieval as a function of rotation angle. The rotation angle was changed by varying the intensity of a fixed duration microwave pulse. The three plots are for three different incident mean photon numbers. All three plots are normalised to the zero-microwave retrieval rate of plot (a). The solid lines are fits to equation 6.2. Incident mean photon numbers and fitting parameter $\mathcal{M}$ are given in the plots.

probability of creating multiple collective excitations. As established in section 4.4.4, multiple collective excitations may be stored in the state $|S\rangle$ without blockading or rapidly dephasing each other due to the relatively short range van-der-Waals interactions. Introducing microwave coupling to the $|P\rangle$ state induces much longer ranged resonant dipole interactions causing previously weakly or non-interacting collective excitations to rapidly dephase, and be lost. This is also consistent with the work of Maxwell, which demonstrated that photon correlations were much more strongly suppressed in the 2nd Rabi oscillation peak ($g^2(0) = 0.3$) compared to the case of no storage ($g^2(0) = 0.6$) [103].

The reduction in incoming photon number $\overline{n}_{\text{in}}$ is also visible in the value of the fitting parameter $\mathcal{M}$, which is consistent with the work of Maxwell [53]. For the highest incoming photon number, $\mathcal{M} = 3.4 \pm 0.2$. This shows substantial suppression in storage/retrieval efficiency at microwave fields producing a superposition state, compared to the case of conventional Rabi oscillations ($\mathcal{M} = 1$). For the lowest incoming photon number, $\mathcal{M} = 1.7 \pm 0.1$, corresponding to a relatively minor suppression of efficiency at superposition states.

While this data does not entirely reproduce earlier results (in particular, the $\tanh(\Theta)$ envelope shown in figure 6.1 [53, 97, 103]), it does accurately reproduce the observed efficiency suppression at non-integer-π rotation angles, which is key to the approach of using microwave driven photon storage to perform sensitive microwave electrometry.

6.2.2. Photon storage electrometry

The approach taken here is to measure the strength of an applied microwave field by inferring a rotation angle Θ from an observed reduction in retrieved signal. From figures 6.1 and 6.5, the relationship is more complicated than the simple $\cos^2(\Theta/2)$ function predicted in section 3.1.5. Therefore, the behaviour at small rotation angles must be more carefully studied. Data presented in figure 6.5 provides insufficient resolution at such angles.

The same technique used for the data in figures6.4 and 6.5 is used (shown in figure 6.3). The rotation angle is varied by adjusting the power of a fixed-duration ($t_\mu = 450\,\text{ns}$) microwave pulse. Fixed attenuators are used to position the signal generator's power dynamic range (nominally 40 dB, in practice $\approx 34\,\text{dB}$) such that at maximum power, a rotation angle $\Theta \geq 2\pi$ is achieved. A small, logarithmically distributed step size is used to provide maximum resolution at the smallest rotation angles that the signal generator can probe, given the previous requirement. Separately, a reference value at $\Omega_\mu = 0, \Theta = 0$ is observed.

This calibration data is shown in figure 6.6 for the Rydberg-Rydberg transition $80S_{1/2} \rightarrow 79P_{1/2}$ ($\omega_\mu = 7.691 \times 2\pi\,\text{GHz}$). This is the same transition used in figure 6.5. The range

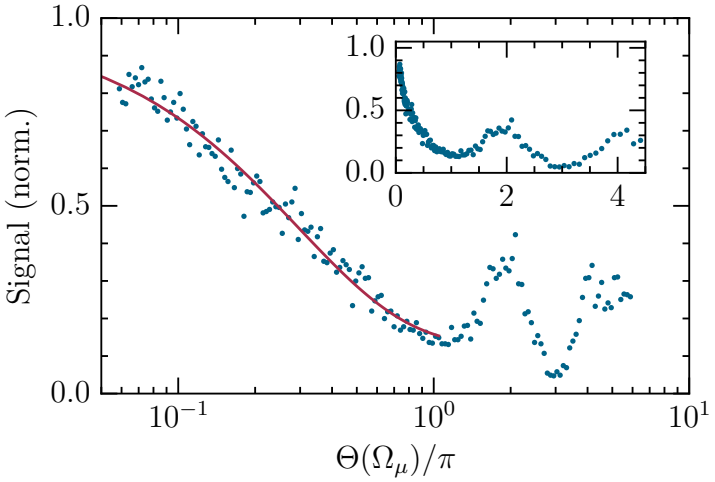

Figure 6.6.: Reduction in photon retrieval under weak microwave conditions. Θ is varied by scanning the microwave power with a step size of 0.25 dB across the signal generator's nominal 40 dB dynamic range. The solid line is a fit to equation 6.3 in the range $0 < \Theta \leq \pi$. The microwave signal generator's maximum output power occurs at $\Theta \approx 4\pi$. *Inset*: Plotted on a linear scale for comparison to figure 6.5.

$0 < \Theta \leq \pi$ is fitted to an exponential of the form

$$\overline{n}_{\mathrm{ret}}(\Theta) \propto \exp(-\Theta/\zeta). \tag{6.3}$$

Data points for $\Theta \geq 4\pi$ break the expected Rabi oscillation pattern, as the microwave generator reached its maximum effective power output at this frequency.

Based on the calibration data presented in figure 6.6, it is possible to calculate the noise-equivalent rotation angle, Θ_{ne}, which may be resolved from a zero rotation angle, $\Theta = 0$. Note that, while the noise equivalent *power* (NEP) was introduced in the introduction, from here we will consider the noise equivalent *voltage*, since the Rabi frequency is proportional to the amplitude, rather than intensity, of the driving EM field.

From the introduction, the noise equivalent signal level is the signal level such that SNR= 1 in a 1 Hz output bandwidth (0.5 s). The noise equivalent rotation angle, therefore, is given by:

$$I(\Theta_{\mathrm{ne}}) = I(\Theta = 0) - \sigma, \tag{6.4}$$

where σ is the deviation of data points around the fit. From figure 6.6, $\Theta_{\mathrm{ne}} = 1.3\times10^{-2}\,\pi$.

The noise equivalent voltage may be calculated by converting the minimum rotation angle into a minimum Rabi frequency via the microwave pulse duration $t_\mu = 300\,\mathrm{ns}$ and factoring in the dipole matrix element of the transition, d:[7,8]

$$E_{\mathrm{ne}} = \frac{\hbar\Theta_{\mathrm{ne}}}{t_\mu d}. \tag{6.5}$$

This gives a value of $E_{\mathrm{ne}} = 6 \pm 3\,\mu\mathrm{V\,cm^{-1}}$, but has not taken account of the observation time required. Each data point in figure 6.6 is the result of 10 independent atomic ensembles, with each ensemble recycled 2×10^4 times, for 2×10^5 shots per point. A single cycle of the experiment requires 128.0 ms to prepare the atomic ensemble, and 91.0 ms to perform 2×10^4 shots; such that each data point is the result of 2.19 s total experimental time.

The following section will examine the characteristics of the noise evident in photon storage retrieval intensity, and how this value can be most appropriately scaled to the requisite 1 Hz bandwidth.

6.2.3. Scaling by observation time

The experimental sequence was tuned to optimise photon retrieval rates in terms of the number of shots per MOT load. Consequently, the total operating time per microwave power step was 2.19 s as previously noted, rather than the ideal 0.5 s. In order to scale the extrapolated field measurements to those expected after the appropriate integration time, the stability of the storage and retrieval cycle must be established. A perfectly stable system with Poissonian noise characteristics will produce a SNR that scales as $1/\sqrt{t}$, and over short time scales, many physical systems reproduce this behaviour extremely well [200]. Typically, over longer time scales, other factors dominate the variance of measurements, such as instrument and temperature drift.

[7] The radial matrix element of the transition $80S_{1/2} \rightarrow 79P_{1/2}$ is $6271\,ea_0$, with a spherical coupling of $\sqrt{2/9}$, calculated with ARC [181].

[8] Assuming that the microwave field is linearly polarised, with no circular polarisations arising from reflections; and that stray electric and magnetic fields do not contribute significant state mixing.

The precise meaning of 'short' or 'long' time scales is unique to each experiment or instrument under consideration. Therefore, the behaviour of photon storage in the apparatus described here must be characterised to establish whether or not the simple scaling law can be applied.

The behaviour of measurement variance over time is typically examined by observing the evolution of the variance of the measure (σ) with the averaging time over which it is calculated (τ). Consequently, this family of measurements are often described as 'sigma-tau' graphs [201]. Most commonly, these techniques are used for observing the frequency and phase stability of frequency standards.

There are numerous methods of calculating the variance of a measurement, in order to identify various forms and sources of noise [201]. The majority of these techniques fall far outside the scope of this thesis. We consider here the overlapping Allan variance [220], which is commonly used as the first step in evaluating noise characteristics.

The Allan variance can best be understood by analogy to the classic variance of N samples:

$$\sigma^2 = \frac{1}{N-1}\sum_{i=1}^{N}(y_i - \overline{y})^2, \tag{6.6}$$

where $\overline{y}$ is the mean over all values $(1/N)\sum y_i$. This variance is typically not used in frequency analysis, as it does not converge for certain common noise types where the mean $\overline{y}$ evolves over time [201] (for example, due to temperature drift of the oscillator).

The family of Allan variances take account of these drifts by comparing individual data points to a local mean calculated over the averaging time τ. The overlapping Allan variance, σ_{oA}^2, calculates the variance over overlapping times τ, such that for N data points and an averaging window over M points, there are $1 + N - M$ means against which to compare. This technique scales poorly to very large datasets, but experimental stability limits ensure that scaling is not an issue for the work concerned here. The overlapping Allan variance is given by:

$$\sigma_{oA}^2(\tau) = \frac{1}{2M^2(N-2M+1)}\sum_{j=1}^{N-2M+1}\left(\sum_{i=j}^{j+M-1}(y_{i+M} - y_i)\right)^2, \tag{6.7}$$

where N measurements taken equally spaced in time by τ_0 are evaluated over averaging

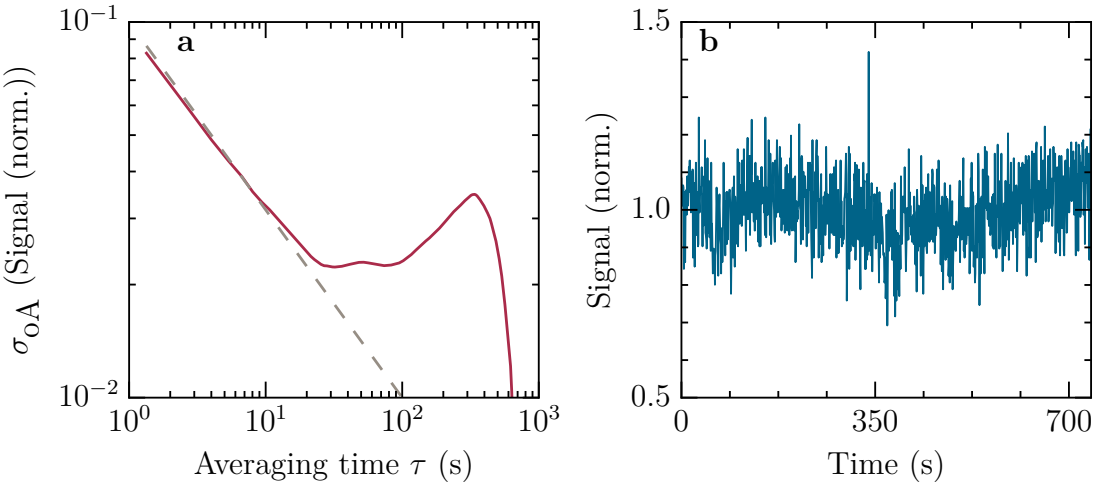

Figure 6.7.: Overlapping Allan deviation of photon retrieval rate over 750 s. No microwaves were applied during this experimental sequence, and so this does not take account of any noise or drift in the microwave signal generator. *a*: Overlapping Allan deviation. For an averaging time of up to $\tau = 25\,\mathrm{s}$, the noise falls as $\sqrt{1/\tau}$ (broken grey line). *b*: Source data. Each data point is the sum of all counts from 2.5×10^4 shots following a single MOT load normalised to the average over the whole data set.

time $\tau = M\tau_0$. The behaviour of the variance with averaging time provides information about what noise sources are dominant over that time scale.

As with the classical variance and deviation, the overlapping Allan deviation is given by $\sigma_{oA} = \sqrt{\sigma_{oA}^2}$.

Figure 6.7 plots the overlapping Allan variance as a function of averaging time for an extended photon storage and retrieval dataset. Here, a single MOT load and subsequent 25,000 shots yields a single measurement of photon retrieval rate. In the range $\tau \leq 25\,\mathrm{s}$, the stability of the retrieval rate scales as $1/\sqrt{t}$, implying that Poissonian noise (analogous to white frequency modulation in frequency measurements) is dominant.

Noise-equivalent voltage

Based on the analysis in figure 6.7, it is reasonable to calculate the noise equivalent voltage level in a 1 Hz bandwidth by scaling the observation with $1/\sqrt{t}$.

As stated at the end of section 6.2.2, the data presented in figure 6.6 required an observation time of 2.19 s per data point, to give a minimum resolvable field amplitude of $E_{\mathrm{ne}} = 6 \pm 3\,\mu\mathrm{V\,cm^{-1}}$.

As a result, we may state a final sensitivity (noise equivalent voltage) of the photon storage system of $12 \pm 7\,\mu\mathrm{V\,cm^{-1}}\,\sqrt{\mathrm{Hz}}^{-1}$. This is comparable to the value published by J. Sedlacek *et al* [89] of $\approx 30\,\mu\mathrm{V\,cm^{-1}}\,\sqrt{\mathrm{Hz}}^{-1}$.

A key factor in consideration of these systems as sensitive microwave detectors is the resonance condition used. Using a resonant atomic transition allows the detection of extremely weak fields, but places an explicit limit on the detection bandwidth, as shown in figure 6.4. The requirement for a short microwave pulse forces a certain level of Fourier broadening, but that is of order $100\,\mathrm{kHz} - 1\,\mathrm{MHz}$, while modern high performance radar may use $\mathcal{O}(\,\mathrm{GHz})$ bandwidths to maximise resolution [221].

A function of the use of resonant atomic transitions is the large dipole matrix elements associated with Rydberg-Rydberg transitions, and their associated frequency dependence. In the work presented here, the transition $80S_{1/2} \rightarrow 79P_{1/2}$ is used, with a wavelength of $\omega_\mu = 7.691 \times 2\pi\,\mathrm{GHz}$ and a radial matrix element of $6271\,ea_0$. The value published by J. Sedlacek *et al* [89] used the $53D_{5/2} \rightarrow 54P_{3/2}$ transition at a frequency of $\omega_\mu = 14.2330 \times 2\pi\,\mathrm{GHz}$ and a radial matrix element of $3611\,ea_0$. Transitions at lower frequencies exhibit stronger matrix elements (as a result of the scaling discussed in chapter 2). Consequently, results based on Rydberg atom systems are not directly comparable if measured on different atomic transitions.

6.2.4. Photon number dependence

The suppression of storage/retrieval efficiency at non-integer-π rotations that renders photon storage suitable for sensitive electrometry is a photon number dependent effect (section 6.2.1 and [103]). This renders the system simultaneously sensitive to an applied

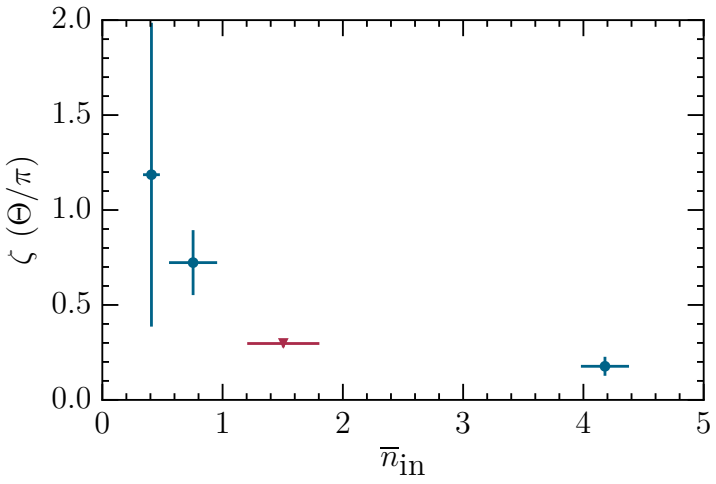

Figure 6.8.: Dependence of microwave sensitivity upon incident photon number $\overline{n}_{\mathrm{in}}$. Exponential decay constant of $\overline{n}_{\mathrm{ret}}$ for $\Theta \leq \pi$ as a function of $\overline{n}_{\mathrm{in}}$, where a cleaning microwave pulse is excluded, from equation 6.3. Blue circles: data from figure 6.5. Red triangle: data from figure 6.6.

microwave field, and to fluctuations in the number of photons in the input pulse which is stored.

Figure 6.8 shows this by plotting the exponential decay time parameter ζ from equation 6.2 as a function of incoming photon number, $\overline{n}_{\mathrm{in}}$, fit to the data already presented in figures 6.5 and 6.6. A small value of ζ corresponds to an extremely rapid exponential fall-off, and a corresponding increase in microwave sensitivity for a given experimental duty cycle.

At low incoming photon numbers, the reduction in retrieved signal intensity ceases to be well described by an exponential, leading to a high uncertainty in fitting the parameter ζ. At high photon numbers, the reduction appears to be moderately insensitive to $\overline{n}_{\mathrm{in}}$. However, attempting photon storage with a high input photon number reduces the number of times that a single atomic cloud can be recycled, reducing the repetition rate and sensitivity of the experiment.

The photon number dependence of the storage efficiency suppression will be examined further in the following section.

6.3. Rydberg pollution of the atomic ensemble

Thus far, in both this work and others [53, 54, 103, 104], only the population fraction remaining in state $|S\rangle$ has been addressed, due to the state selective photon retrieval process. This fraction is observed to vary as a function of rotation angle Θ, as expected. The fraction of the population left in $|P\rangle$ at the end of the microwave driving stage has been implicitly assumed to vanish immediately at the end of each shot, or at least play a negligible role in respect to later shots. The consequences of this assumption will be evaluated in this section.

The phase factors of the collective excitation in $|P\rangle$ will motionally dephase over a period of μs. However, this motional dephasing only affects the mode into which the stored photon will *eventually* be emitted. The Rydberg excitation itself remains present until, by some mechanism, it decays and emits a photon. Possible mechanisms include spontaneous decay to another state; stimulated transition of the dephased collective excitation back to $|S\rangle$ and then photon emission in a subsequent shot; or atomic motion leading to movement of the excitation sufficiently far from the optically trapped region such that interactions play no future role.

In section 2.1, the radiative lifetime of a Rydberg excitation in a low l state was established to scale as n^3. In the absence of black body radiation, the radiative lifetime of the $79P_{1/2}$ state is 1.38 ms.[9] During this time, approximately a further 300 shots will take place. Accelerating only under gravity, an atom will have fallen about 9.4 μm, insufficient distance to have completely escaped either the influence of the coupling laser beam (section 4.4.2), or to have a negligible interaction strength with atoms at the centre of the optical trap (section 5.5.2).

Consequently, there are multiple phenomena by which remnant Rydberg excitations may be influencing subsequent shots. The two most probable pathways by which such influence might act are

- The presence of a nearby Rydberg excitation in $n'P_J$ during the EIT process of

[9] Calculated with ARC [181]

photon storage should lead to resonant dipole-dipole interactions with the state $nS_{1/2}$. As demonstrated in chapter 5, the probability of successful photon storage and retrieval is substantially reduced in the presence of vdW interactions with another $nS_{1/2}$ excitation. The presence of $n'P_J$ excitations would leader to even stronger and longer ranged resonant dipole-dipole interactions.

- The optical trap was not designed to trap Rydberg atoms. Due to the difficulty of trapping Rydberg atoms [222], it is highly likely that neither atoms in nS nor $n'P_J$ are confined by the optical trap. Remnant Rydberg atoms are therefore likely to escape the optical trapping region at a rate substantially greater than ground state atoms, affecting all future shots until a new atomic ensemble is created.

6.3.1. Cleaning the medium

The second possibility - expedited atom loss from the trap - is easier to test experimentally. A new experimental sequence is used (figure 6.9), adding a second microwave driving stage after retrieval of any population remaining in $|S\rangle$. The duration for which the optical trap is switched off is extended. There is therefore a window (after retrieval) during which both the microwave and coupling Rabi frequencies are high. Provided that the window is sufficiently long that both $\Omega_\mu t, \Omega_c t > \pi$, any remnant population left in $|P\rangle$ by the first microwave driving pulse will be rotated back into resonance with the retrieval process. The Rydberg excitation may then be de-excited, and emitted as a photon. This window will be referred to as the 'cleaning' window or pulse. For the purposes of this section, photons are explicitly not counted during or after the cleaning window.

There are two caveats for data presented in the remainder of this chapter:

- The Rydberg states $60S_{1/2}$ and $59P_{1/2}$ are used exclusively, with an transition frequency of $\omega_\mu = 19.005 \times 2\pi\,\text{GHz}$ (shown in figure 6.10).

- Where the microwave rotation angle is changed, it is changed by varying the pulse duration, rather than amplitude. This allows the rotation angle of the cleaning pulse, where used, to retain a fixed and unchanging rotation angle $\Theta_{\text{clean}} = 3.7\pi$.

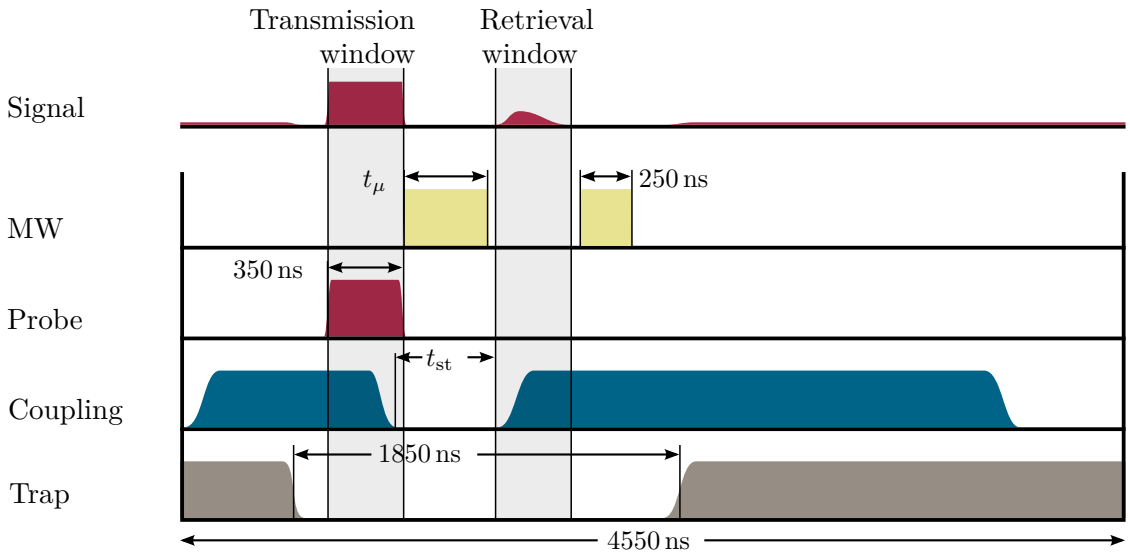

Figure 6.9.: Photon storage spectroscopy with a cleaning microwave pulse. A second microwave pulse is applied, after the retrieval window, and before the optical trap is switched on, to eject any remaining $|P\rangle$. The driving microwave pulse has $t_\mu \leq 450\,\text{ns}$ sandwiched within $t_{st} = 500\,\text{ns}$.

Figure 6.11 compares Rabi oscillations generated *without* a cleaning pulse (a) to data generated *with* the cleaning pulse (b). Both experiments were conducted with the same mean incident photon number, $\overline{n}_{in} = 2.4 \pm 0.2$.

Comparing figures 6.11 (a) and 6.11 (b) shows a similar change in the 'peakiness' of the Rabi oscillations (as denoted by fitting parameter $\mathcal{M}$) to that seen in figure 6.5. However, in figure 6.5, this change is attributed to the incident photon number. Here, the photon number is identical, and the difference in procedure is solely due to the presence or absence of the cleaning pulse.

Figures 6.11 (c) and 6.11 (d) show the transmitted intensity of the probe signal through the cloud (observed during the 'transmission window' shown in figure 6.9). These figures also show a clear change in behaviour. Figure 6.11 (c) shows clear structure in the transmission, with greatly increased transmission at rotation angles associated with a remnant $|P\rangle$ population. The structure is almost entirely absent in figure 6.11 (d), where the $|P\rangle$ population are removed prior to subsequent shots.

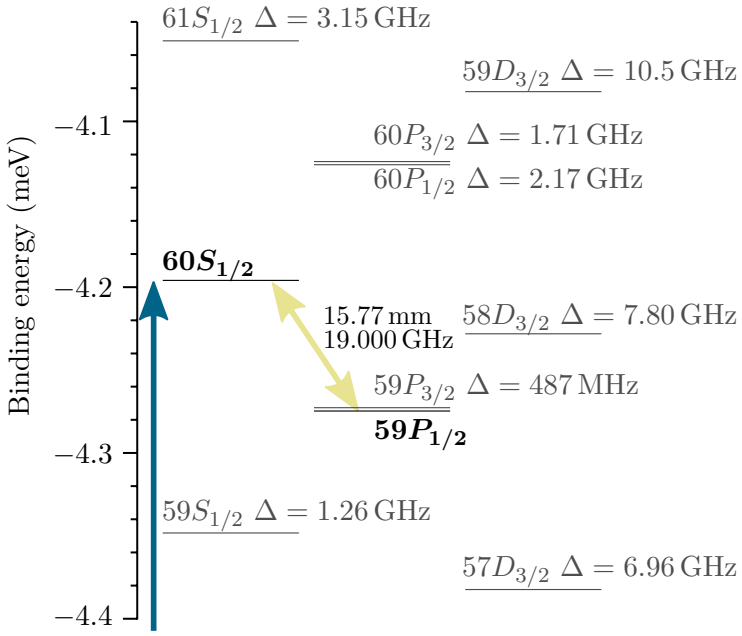

Figure 6.10.: ^{87}Rb Rydberg manifold around $60S_{1/2}$. Applied microwave field is resonant with transition to $59P_{1/2}$ (shown in black). Other nearby states are shown with transition detunings (in grey). S and D states are shown with the two-photon detuning. Levels calculated with ARC [181].

The correlation between increased transmission at rotation angles associated with a remnant $|P\rangle$ population presents a convincing argument against the influence of resonant dipole-dipole interactions. If dipolar interactions were dominating, a reduction in transmission would be expected, such as the reduction in transmission shown in EIT non-linearities [105, 106, 171, 172]

Transmission increasing relative to the case of no microwaves is more suggestive of a mechanism leading to atom loss. A reduction in atom number in the trap will lead both to increased probe transmission, due to a lower optical depth, and a reduction in combined storage/retrieval efficiency (section 3.2.3). Atom loss as an explanation is also consistent with previous observations of a photon number dependence. From figure 4.21, retrieval rate (absent microwave driving) is proportional to photon number, provided that $\overline{n}_{\mathrm{in}}$ is well below the saturation level. All data presented in this chapter, for both $60S_{1/2}$ and $80S_{1/2}$, uses an incoming photon number well below saturation.

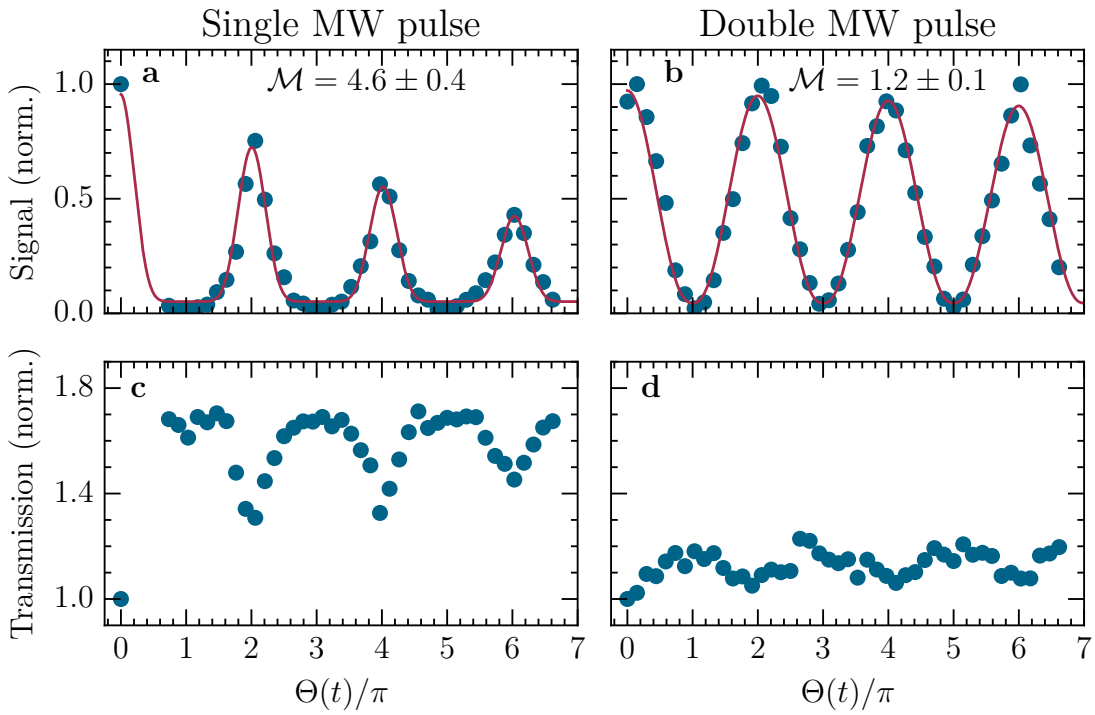

Figure 6.11.: Photon retrieval and ensemble transparency as a function of rotation angle. *Left*: The presence of remnant $|P\rangle$ excitations substantially *increases* the transmission of the atomic ensemble. *Right*: The addition of a second microwave pulse largely removes this effect by cleaning out the fossilised excitations. *Upper (a, b)*: Rabi oscillations in photon retrieval as a function of rotation angle. Solid lines are fits to equation 6.2. *Lower (c, d)*: Averaged transparency of the ensemble normalised (separately by column) to the zero-microwave case.

Therefore, the Rydberg population is also proportional to $\overline{n}_{\text{in}}$, and so any form of atom loss proportional to Rydberg population should likewise be proportional.

6.3.2. Behaviour of Rydberg atoms in optical traps

The optical trap is modulated off to remove Stark shifts for photon storage and retrieval, and back on again to maintain the atomic ensemble for as long as possible to achieve a high repetition rate. The presence of the coupling laser during photon retrieval, and the short lifetime of the first excited state (26.2 ns [223]), ensure that there is a vanishingly

$60S_{1/2} \rightarrow$	λ (nm)
$5P_{3/2}$	480
$5P_{1/2}$	474
$6P_{3/2}$	1012
$6P_{1/2}$	1008
$7P_{3/2}$	1723
$7P_{1/2}$	1713

$59P_{1/2} \rightarrow$	λ (nm)
$5S_{1/2}$	297
$6S_{1/2}$	738
$7S_{1/2}$	1358
$8S_{1/2}$	2160
$5D_{3/2}$	1250
$6D_{3/2}$	2002

Table 6.1.: Optical transitions of $60S_{1/2}$ and $59P_{1/2}$ states of ^{87}Rb. The optical trap used in this work was not designed to trap Rydberg atoms, and due to the near-resonance requirement, no single red-detuned laser offers a method of trapping both $nS_{1/2}$ and nP_J Rydberg atoms.

small probability of any atom in the ensemble not being in the ground state at the time at which the optical trap is switched on.

The optical trap is a focused Gaussian beam at a wavelength of $\lambda \approx 910\,\text{nm}$, far red-detuned from the ^{87}Rb D_2 line. The choice of 910 nm originated in the previous generation of experimental apparatus [103], and was not chosen with the intention of trapping Rydberg atoms. This section will cover some complexities of trapping Rydberg atoms, and evaluate the effect of the optical trap as implemented.

Optical trapping of Rydberg-state atoms is complicated by several factors [224]. Firstly, Rydberg-Rydberg transitions are not optical: optically trapping Rydberg atoms must rely on the extremely weak coupling of highly excited states to weakly excited or ground states. Secondly, the valence electron is extremely weakly bound to the parent nucleus, leading to an additional, repulsive, pondermotive term in the potential experienced by the atoms [225, 226].

This ponderomotive term may be understood by considering the motion of an unbound electron in the presence of a rapidly varying electric field $\boldsymbol{E} = E_0\hat{x}\cos(\omega_l t)$. The electron will vibrate as its charge is driven by the field, raising its energy by the time averaged

kinetic energy [222, 227]

$$\langle \mathrm{KE} \rangle_t = \frac{\omega_l}{2\pi} \frac{e^2 E_0^2}{2 m_e \omega_l^2} \int_0^{2\pi/\omega_l} \sin^2(\omega_l t) \mathrm{d}t, \tag{6.8}$$

resulting in a ponderomotive potential energy of

$$U_p = \frac{e^2 E_0^2}{4 m_e \omega_l^2}, \tag{6.9}$$

where $-e, m_e$ are respectively the charge and mass of the electron and ω_l is the angular frequency of the trapping laser. The force on the electron is given by $\boldsymbol{F}_p = -\Delta U_p$, which acts to repel the electron from regions of high field intensity.

This contribution to the total force experienced by the Rydberg atom results in a generally repulsive effect from regions of high amplitude, except where the trapping laser frequency ω_l is extremely close to resonance [228–230]. Table 6.1 gives the transition wavelengths from the two Rydberg states used in figure 6.11. The optical trapping wavelength used in this experiment, 910 nm, is far detuned from all values in the table, such that the ponderomotive potential dominates over the Lorentz contribution from the induced dipoles. Polarisabilities have only been calculated for $n > 55$, in which range all states $nS_{1/2}$ and nP_J are essentially unaffected by the Lorentz contribution of the optical trap.

The lifetime of Rydberg atoms in the optical trap may be further reduced by photoionisation effects [231, 232]. The valence electron is weakly bound such that scattering a photon from the optical trap laser is sufficient to ionise the Rydberg-state atom.

6.3.3. Rydberg mediated atom loss

In section 4.1.4, the behaviour of the optical trap containing $\mathcal{O}(10^3)$ atoms over $\mathcal{O}(10^4)$ shots was discussed. The rate of atom loss from the trap can therefore be inferred to be a time averaged value of $\ll 0.1$ atoms per modulation in the absence of any coupling light or microwave fields.

Figure 6.12 shows how the transmission of the atomic ensemble evolves with the number of times the cloud is recycled for five different microwave rotation angles (shown in plots 6.12 (a) and (b)), including the case of no microwave rotation to provide a

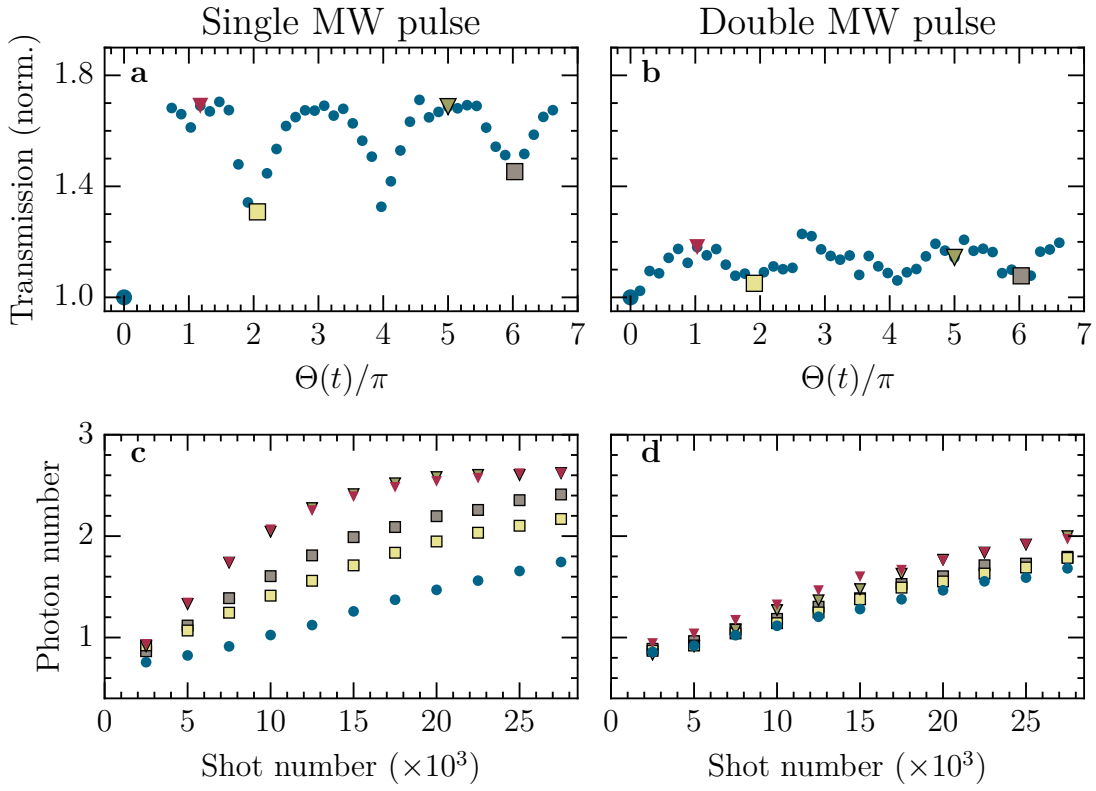

Figure 6.12.: Evolution of the transmission of the atomic ensemble as a function of shot number. The atomic ensemble becomes more transmissive much faster in the case where $\Omega_\mu t$ is not a multiple of 2π. *Upper*: Reproduction of figures 6.11 (c) and (d) for reference. *Lower*: Evolution of transmission of atomic ensemble as a function of shot number for points marker in upper figures. Y-axis is the absolute transmitted photon number. The π and 5π traces (red and grey triangles) saturate to the incoming photon number $\overline{n}_{\text{in}} = 2.6 \pm 0.2$.

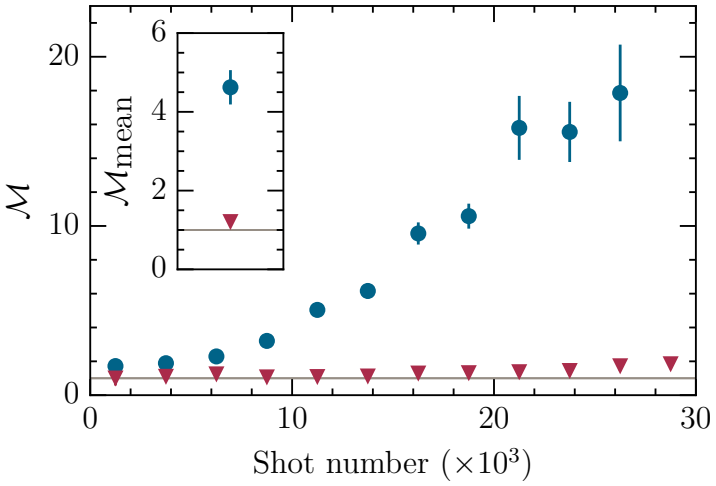

Figure 6.13.: Evolution of the fitting parameter $\mathcal{M}$ as a function of shot number. Blue circles: single microwave pulse. Red triangles: double microwave pulse. Grey line: $\mathcal{M} = 1$. *Inset*: Value of $\mathcal{M}$ averaged across all shots (as shown in figures 6.11a,b). Earlier shots contribute a substantially greater fraction of the total number of detected photons (see figure 4.20).

reference. Figures 6.12 (a) and (b)) are reproduced from figures 6.11 (c) and (d) for reference. Each data point represents the normalised mean of all sub-μs shots at that rotation angle. Figures 6.12 (c) and (d) plot the evolution with shot number of five of those rotation angles. The figures are each normalised such that the mean of the zero-rotation angle data is one.

Considering first the case of no microwave rotation (shown as blue circles in plots 6.12 (c) and (d)), the ensemble becomes progressively more transmissive as a function of shot number. This replicates the behaviour seen in figure 4.9. The evolution is similar regardless of the presence or absence of a microwave cleaning pulse, as is to be expected as there should be no Rydberg population for the cleaning pulse to address.

The effect of any microwave rotation, under any circumstances, is to accelerate the rate at which the ensemble becomes more transmissive. Circumstances which create (and do not remove) a large $|P\rangle$ population - i.e. an odd-integer-π rotation - show a dramatically greater rate of increase. The addition of a cleaning pulse, such that $|P\rangle$

population can return to the ground state before the trapping potential is restored, almost entirely removes the increase in transparency relative to the no-microwave case.

In figure 6.12 (c), the traces for $\Theta = \pi, 5\pi$ (represented by red and grey triangles respectively) saturate to the incoming photon number $\overline{n}_{\text{in}} = 2.6 \pm 0.2$, indicating that after $\approx 2 \times 10^4$ shots, the ensemble has been almost entirely depleted. By comparison, the final shots (3×10^4) show only $\approx 66\%$ transmission. After the addition of the cleaning pulse, the ensemble remains no more than 75% transmissive even after 3×10^4 shots with a rotation angle of $\Theta = 5\pi$.

Figure 6.13 plots how the fitting parameter $\mathcal{M}$ varies as a function of shot number. Inset are the mean values associated with the fits shown in figures 6.11 (a) and (b), which sum across all shots. Uncertainties are calculated from the χ^2 covariance matrix. The plot shows that, in the absence of a microwave cleaning pulse, the parameter increases approximately exponentially with shot number. When the second microwave pulse is present, the parameter remains nearly constant with respect to shot number.

The consistent shot number dependency - and the ability to largely remove it by addressing and ejecting the abandoned $|P\rangle$ population - suggests that the phenomenon being observed is also shot number dependent, and consequently does not arise from inducing resonant dipole-dipole interactions.

Consequently, we reach the conclusion that the suppression of photon storage/retrieval efficiency at non-integer-π rotation angles is a manifestation of Rydberg-enhanced loss from the atomic ensemble, and that while it is correlated with the mean number of collective excitations created, it is not necessarily a direct measure.

6.4. Summary

Photon storage as collective Rydberg excitations in a cold atomic ensemble has proven to be a practical technique for performing sensitive microwave electrometry. Using he photon storage spectroscopy techniques discussed in this chapter, a sensitivity of $(12 \pm 7)\,\mu\text{V}\,\text{cm}^{-1}\,\sqrt{\text{Hz}}^{-1}$ was measured at a frequency of $f = 7.691\,\text{GHz}$, corresponding to a weakest-field observation of $(6 \pm 3)\,\mu\text{V}\,\text{cm}^{-1}$. These values compare favourably to

published sensitivity values using spectroscopy in a thermal cell of $\approx 30\,\mu\mathrm{V\,cm^{-1}}\,\sqrt{\mathrm{Hz}}^{-1}$ at a frequency of 14.2330 GHz and a weakest-field observation of $8 \pm 2\,\mu\mathrm{V\,cm^{-1}}$ [89]. It should be further noted that due to simultaneous on-going experiments (chapter 5, [63, 105]), there was insufficient time to fully optimise the system, and consequently both the value and uncertainty show potential for improvement.

Several further comments must be made regarding the technique used in this chapter, and that used by J. Sedlacek *et al* in the referenced published sensitivities. Since both techniques rely on narrow linewidth, resonant, Rydberg-Rydberg transitions to produce the extreme sensitivities, neither can be directly used as a completely general microwave sensor for measuring an arbitrary field. Producing a broadband detector that would be directly applicable to, for example, deep-space communication networks or low-observability radar applications would require considerable further development. Further, the use of resonant transitions results in a frequency-dependent sensitivity. In the technique presented in this chapter, the effect of a microwave field is observed by the Rabi frequency of the transition it drives, and consequently greater sensitivity may be achieved by studying transitions where an equivalently weak field results in a greater Rabi frequency: as a general rule of thumb, this equates to transitions with a lower transition frequency.

The desired use-case for a microwave electrometer based on atomic techniques will set the characteristics required of such a device. The thermal cell EIT approach of J. Sedlacek *et al* [89] has greater potential to produce a portable device that could be used in mobile applications, as it does not require a large vacuum chamber, or associated pumping equipment. However, in applications where the very highest sensitivities are mandated, it is probable that the superior sensitivity of the system discussed here would justify the larger and more expensive equipment requirements.

The high sensitivity of the system to microwaves arises partly from the use of already highly sensitive Rydberg states, but also from the 'peakiness' of the Rabi oscillations observed by D. Maxwell *et al* [53, 103]. This form was not predicted by contemporary theory [97], and at the time was thought to arise from Rydberg interactions within

the medium. Reproduction and reanalysis of D. Maxwell's work has identified that the effect in fact arose from a tangentially related effect: pollution of the atomic medium by remnant Rydberg atoms, and their subsequent loss from the trap, leading to suppression of storage efficiency. When steps were taken to sanitise these remnants, the expected $\cos^2(\Theta)$ form of Rabi oscillations was observed.

The observation of enhanced atom loss provides a new context in which to understand the electrometry results: the sensitivity observed is in fact a function of three parameters: the applied microwave field; the intensity stability of the probing laser; and the rate at which remnant Rydberg atoms are created, abandoned, and subsequently lost from the ensemble. This does not invalidate the previously stated results, but reinforces the requirement that electrometry rely on robust calibration of the system prior to measurement.

7. A coherent microwave interface for shaping single photons

An effective interface between the optical and microwave region of the EM spectrum have become a topic of considerable interest in recent years [91–96]. A common theme arises in the desire for hybrid systems, which use multiple disparate elements of the spectrum to take advantage of each system's most attractive properties. Optical photons, particularly in the near-infra-red, offer robust communications over long distance [233, 234], while microwave photons are easily manipulated using high performance superconducting circuits [15, 73, 74, 81, 82, 235].

Previous proposals to implement these interfaces have included numerous approaches, including magnetic coupling to ultra-cold atoms [91], or spins [236–240], or optomechanical coupling [241–243]. More recent techniques have included electro-optical techniques [92, 93].

In this chapter, two approaches to controlling the optical output of photon storage/retrieval by an applied microwave field will be discussed. In section 7.1 and 7.2, the techniques demonstrated in chapter 6 will be applied and extended to produce a state-dependent time delay in photon retrieval. Based on the presence (or, in principle, absence) of a microwave pulse, the photon stored as a collective Rydberg excitation is emitted either early or late. This allows a clear pathway to conversion from information encoded in a microwave qubit to information encoded in an optical photon qubit, and provides a step towards the gate proposal outlined in [61].

In section 7.3, a microwave field will be applied during the photon retrieval pulse to simultaneously drive Rabi oscillations to a dark shelving state. Since photons can only

be retrieved from collective Rydberg excitations in the Rydberg state in which they were initially stored, this has the effect of overlaying a sinusoidal intensity modulation on the shape of the retrieved pulse. This modulation technique offers a key benefits over other fast modulators (such as fibre EOMs): low loss. Unwanted emission is delayed by storage in a second Rydberg level, rather than being discarded into a beam dump.

7.1. Concept: delayed photon retrieval

Chapters 3, 4 and 5 all dealt with photon storage in a three level system, in which a photon was stored as a collective Rydberg excitation $|S\rangle$ in the uppermost level $nS_{1/2}$. Chapter 6 followed and extended the work of D. Maxwell [53, 54, 103] by using microwaves to drive population to a second Rydberg state, of opposite parity, $n'P_j$, with the collective state given by $|P\rangle$.

Photon retrieval uses resonant EIT to map the collective Rydberg excitation back to the atomic ground state and collectively emit the stored photon. As expected, and as demonstrated in chapter 6, population in $|P\rangle$ is both non-resonant and dipole-forbidden from the retrieval process. Consequently, there is no, or very weak, retrieval intensity during the retrieval window if the population has been driven to $|P\rangle$ and left there.

Initial work applied a microwave pulse wholly within the storage window (sections 6.1 and 6.2), while in section 6.3 a second microwave pulse was added, simultaneously with high coupling field (figure 6.9). The presence of both EM fields allows remnant $|P\rangle$ excitations to resonantly couple back to a short lived state and be emitted. Data analysis in section 6.3 explicitly excluded any photons emitted from the ensemble after the beginning of this 'cleaning' pulse. Sanitation of the ensemble required only that the collective Rydberg excitations be removed; with no value attached to the emission of the stored photon into the original mode as opposed to any other mode.

However, chapter 6 demonstrated the ability to rotate the ensemble through multiple 2π rotations with minimal loss, demonstrating that, as predicted in section 3.3 and [97], microwave driving should not substantially interfere with the collective phase. Consequently, it is expected that the sanitation pulse should result in collective emission from

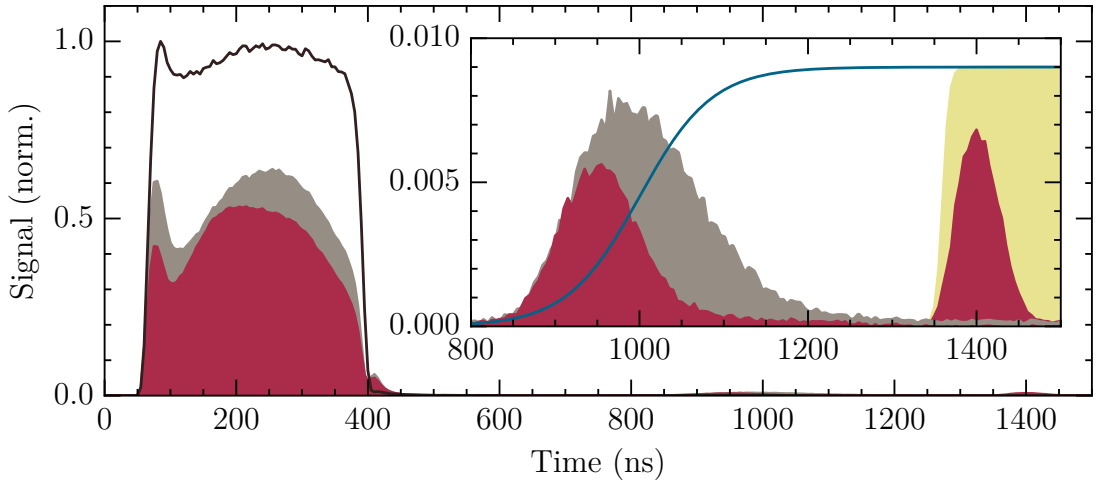

Figure 7.1.: Photon retrieval via the cleaning pulse. Histogram of all photon arrival times arising from a range of microwave rotation angles (red). The window in which photon arrivals are included includes the microwave cleaning pulse discussed in section 6.3. A reference signal retrieved without any microwave driving is shown in grey. *Inset*: Zoom on the retrieval window. The first red peak corresponds to retrieval from $|S\rangle$; the second corresponds to retrieval from $|P\rangle$; while the grey trace remains low during the second red peak. The grey and red traces are shown to the same vertical scale. The blue and yellow traces are guides to the coupling and microwave driving Ω_c, Ω_μ respectively.

$|P\rangle$ when both the microwave and coupling fields are present.

In cases where multiple collective excitations are created, it is to be expected that resonant dipole-dipole interactions will result in strong dephasing at rotation angles resulting in both $|S\rangle$ and $|P\rangle$ presence (at half-integer-π values). However, as noted in section 5.3, such interactions are generally only observed in the statistics of the emitted photons, and make a minimal difference to the total emitted intensity. In previous work, D. Maxwell demonstrated that interactions arising from microwave transitions were visible [54]. Typical experiments use an input pulse with a photon number of up to 5, resulting in a low probability of the simultaneous creation of multiple excitations.

Figure 7.1 presents data from the same experiments as shown in figure 6.11 (b).

Instead of presenting the retrieval intensity as a function of applied microwave rotation angle, it shows a histogram of photon arrival times summed over *all* rotation angles, including the time during which the microwave sanitation pulse is applied (shown in yellow). A reference data trace is shown, normalised to the same scale, where the same mean incoming photon number $\overline{n}_{\text{in}}$ were stored as collective excitations for the same time t_{st}, but no microwave driving was applied (grey).

Figure 7.1 clearly shows that, due to the addition of the cleaning pulse (section 6.3.1), the remnant $|P\rangle$ population is successfully retrieved during the time period in which the cleaning pulse is applied. As the maximum peak intensity of the delayed retrieval pulse is comparable to the initial retrieval pulse, it may be concluded that the collective excitation remains sufficiently in phase to produce a similarly highly directional collective emission.

It is to be emphasised that, whereas the initial pulse is retrieved under conditions of two-photon EIT, by switching the coupling laser Ω_c from low to high; the delayed pulse is retrieved by three-photon EIT, by switching Ω_μ from low to high while Ω_c *remains* high. Colloquially, the first pulse (around $t = 900\,\text{ns}$) may be described as 'retrieval from $|S\rangle$', and the second pulse ($t = 1400\,\text{ns}$) as 'retrieval from $|P\rangle$'. They will also be referred to as 'early' or 'late' respectively.

All three retrieval pulses shown in figure 7.1 exhibit an approximately Gaussian envelope. However, while the early and reference pulses have a near-identical slew rate, the late retrieval pulse has a substantially faster slew rate. These differences can be explained by considering the limiting Rabi frequencies in the retrieval pathways.

In both the reference and early retrieval pulse, retrieval is limited by Ω_c. A sigmoidal curve is plotted in figure 7.1 as a guide to the time evolution of the coupling laser Ω_c, which has a rise time of $t_{10:90} = 185\,\text{ns}$. The reference pulse peak intensity occurs at approximately 50% of peak Ω_c, such that the rising edge of the retrieval pulse can be considered to be limited by the (low) value of Ω_c.

The late retrieval pulse occurs once Ω_c has stabilised at maximum value. The rising edge of the late retrieval may therefore have a faster slew rate, as it is not constrained by a low rate of Ω_c. The rise time of Ω_μ ($t_{10:90} \approx 8\,\text{ns}$), which could pose a constraint, is better

than an order of magnitude faster than Ω_c ($t_{10:90} \approx 185\,\mathrm{ns}$). The peak Rabi frequencies of the coupling laser and microwave source used for this data set are comparable ($\Omega_c = (6 \pm 2) \times 2\pi\,\mathrm{MHz}$, $\Omega_\mu = (8 \pm 1) \times 2\pi\,\mathrm{MHz}$).

The late retrieval pulse has a smaller area, corresponding to a smaller total photon number retrieved. This loss may arise from a large number of possible causes, although the most probable is motional dephasing. Just as a loss of storage/retrieval efficiency was observed going from $t_{\mathrm{st}} = 170\,\mathrm{ns}$ in chapter 5 to $t_{\mathrm{st}} = 500\,\mathrm{ns}$ in chapter 6, a loss is expected due the $t_{\mathrm{st}} = 950\,\mathrm{ns}$ prior to late retrieval.

7.2. Early and late photon retrieval

Figure 7.1 conclusively demonstrates that population may be 'shelved' in $|P\rangle$, and later retrieved, with no more than a modest degree of dephasing. It also demonstrates that retrieval from the population shelved in $|P\rangle$ may be temporally resolved from retrieval from $|S\rangle$ with high precision, through the correct choice of detection windows. This offers a clear path to the implementation of microwave-to-optical interfacing, where the presence or absence of a microwave pulse can be directly converted into an early or late optical photon; or alternatively, the presence or absence of an optical photon in either time window.

Figure 7.2 demonstrates the protocol for implementing time-resolved detection, and the choice of detection windows. With respect to the time axis of figure 7.1, the windows $800 - 1200\,\mathrm{ns}$ and $1300 - 1500\,\mathrm{ns}$ were used for early and late retrieval respectively. The two windows are deliberately of different lengths, due to the difference in slew rate and width of the two retrieval pulses.

Due to the microwave signal generator control scheme (section 4.5), all data making use of a cleaning pulse were taken with microwave intensity fixed, and rotation angle adjusted by changing pulse duration. This choice severely restricts the available resolution of the microwave rotation angle, but ensures that the cleaning pulse is consistent between every shot. Adjusting the intensity instead of the pulse length would either result in an impractically long cleaning pulse; or in shots with weak microwave driving having a

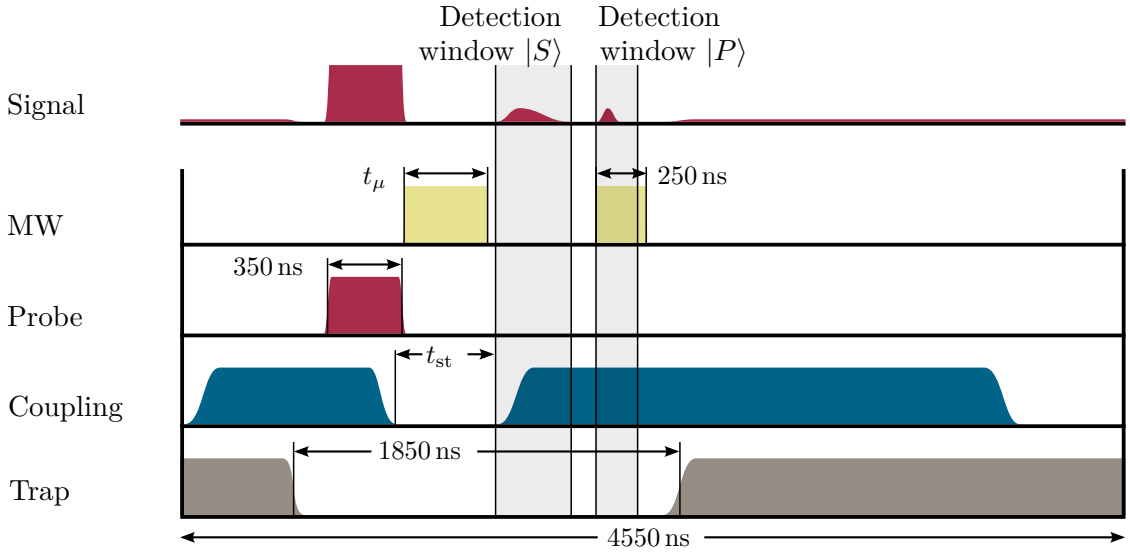

Figure 7.2.: Pulse sequence for state-dependent delayed photon retrieval. A second detection window is added, revealing a second retrieval pulse. This is associated with retrieval from $|P\rangle$ via three-photon EIT.

cleaning pulse with $\Theta_{\text{clean}} \ll \pi$.

All data shown in this section uses the states $60S_{1/2}$ and $59P_{1/2}$, shown in figure 6.10. The microwave transition has a calculated frequency of $\omega_\mu = 19.005 \times 2\pi$ GHz.

7.2.1. Efficiency

Figure 7.3 (a) presents data from the same experimental sequence as figure 6.11 (b), using two separate observation windows to observe Rabi oscillations in the photon retrieval from $|S\rangle$ (blue) and $|P\rangle$ (red) respectively. Figures 7.3 (b), (c), and (d) show photon arrival time histograms for three fixed microwave pulse durations. In these experiments, the probe pulse had a photon number of $\overline{n}_{\text{in}} = 2.6 \pm 0.2$.

Figure 7.3 (a) shows Rabi oscillations in photon retrieval from both the $|S\rangle = 60S_{1/2}$ (blue circles) and $|P\rangle = 59P_{1/2}$ states (red triangles). The data points are generated by counting the number of photon detections in each of the windows shown in figure 7.2. Retrieval from each state is distinguished by a time delay in retrieval of $|P\rangle$ of approximately 450 ns (see figure 7.1). Retrieval from $|P\rangle$ is less efficient, with a peak

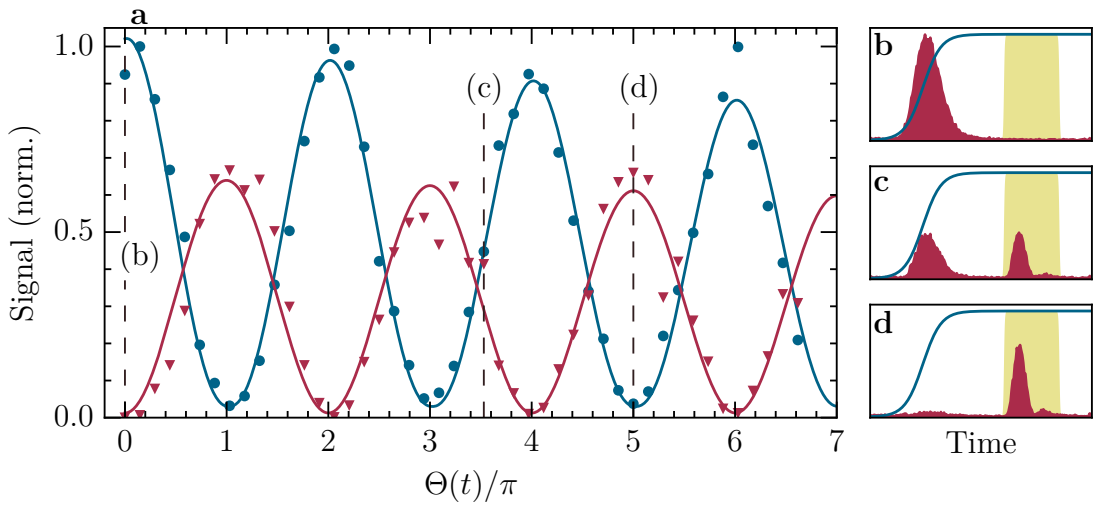

Figure 7.3.: Rabi oscillations in photon retrieval from both $|S\rangle$ and $|P\rangle$. *a*: Early retrieval from $60S_{1/2}$ (blue circles) and time-delayed retrieval from $59P_{1/2}$ (red triangles). *Right*: Photon arrival histograms for three microwave pulse durations. Associated rotation angles are shown in part (a). Red data shows photon arrivals. The blue trace shows Ω_c. The yellow band shows the position of the microwave cleaning pulse. Time and signal scales are shared. *b*: $\Theta = 0$. *c*: $\Theta = 3.5\pi$. *d*: $\Theta = 5\pi$.

retrieval probably approximately 35% lower than the probability of retrieval from $|S\rangle$. Since collective excitations can demonstrably be rotated between $|S\rangle$ and $|P\rangle$ multiple times with minimal loss, this reduction is probably not due directly to the microwave driving, but due to alternative factors.

The most probable source of loss is dephasing of the collective excitation due to the time delay before retrieval. Photons stored as collective excitations in $|S\rangle$ are retrieved after $t_{\mathrm{st}} = 500\,\mathrm{ns}$, while in $|P\rangle$, $t_{\mathrm{st}} = 950\,\mathrm{ns}$. Increasing t_{st} from the $\approx 170\,\mathrm{ns}$ used in chapter 5 to the $t_{\mathrm{st}} = 500\,\mathrm{ns}$ used through chapter 6 resulted in a reduction of storage/retrieval efficiency from $\approx 2\%$ to $\approx 0.5\%$. A further increase in storage time may be expected to have a concomitant loss of efficiency.

Due to circumstances arising (see appendix A), it was not possible to gather data regarding the time-dependent efficiency of retrieval from the $|P\rangle = 59P_{1/2}$ state. However,

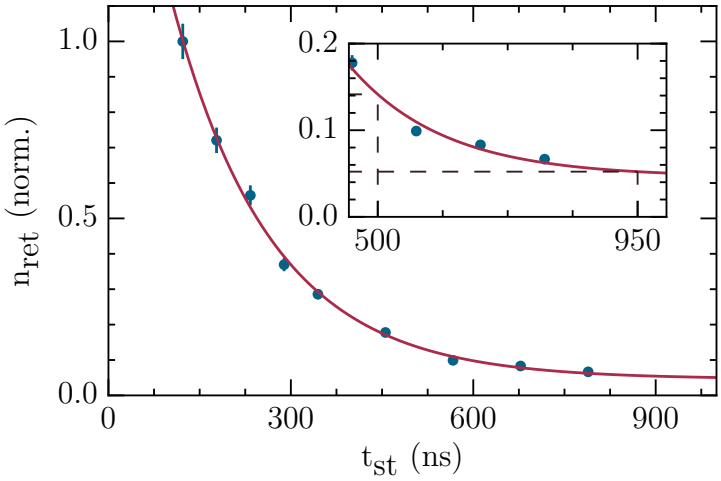

Figure 7.4.: Storage lifetime of photons in $|S\rangle = 80S_{1/2}$. Storage was conducted with $\overline{n}_{in} = 2.5 \pm 0.3$ Solid line is a fit to equation 7.1 with a half life of $\tau = 163 \pm 8\,\text{ns}$. *Inset*: Storage efficiency over the durations of interest for microwaves. $\overline{n}_{ret}(950\,\text{ns}, 80S_{1/2}) = (0.36 \pm 0.05) \times \overline{n}_{ret}(500\,\text{ns}, 80S_{1/2})$.

this data does exist for the state $|S\rangle = 80S_{1/2}$, which can be used as a general guideline, and is shown in figure 7.4 with a fit to the exponential function

$$\overline{n}_{ret}(t_{st}) = a_0 + a_1 \exp(-t_{st}/\tau), \tag{7.1}$$

where a_0 is the noise floor, a_1 is a constant to normalise retrieval to the value at the minimum possible storage time (approximately 125 ns), and τ is the half life of the storage process. A fit to the data in figure 7.4 gives a decay rate of $\tau = 163 \pm 8\,\text{ns}$. From the exponential fit, the retrieval rate from $|S\rangle = 80S_{1/2}$ after $t_{st} = 950\,\text{ns}$ is expected to be 0.36 ± 0.05 of the retrieval rate after $t_{st} = 500\,\text{ns}$.

This is a substantially greater predicted loss of efficiency than is seen in figure 7.3. However, it should be emphasised that the data in figure 7.4 is not directly comparable, as it is the measured lifetime of storage in the state $80S_{1/2}$, while the data presented in figure 7.3 is for photons stored as collective excitations in the states $60S_{1/2}$ and $59P_{1/2}$. Since the demonstrated half-lives of both figures (i.e., all three Rydberg states) are substantially lower than the $\mathcal{O}(1\,\mu\text{s})$ predicted in section 3.2.3, it is probable that in

addition to motional dephasing (which is independent of n), there is a contribution to dephasing of the collective excitation arising from interactions. As predicted in chapter 2 and shown in chapter 5, interactions do exhibit an n dependence. In the event that there is such a contribution, then the lifetime of a collective excitation using the states $60S_{1/2}$ or $59P_{1/2}$ would be different - and most likely longer - than the lifetime of an excitation using the state $80S_{1/2}$, as in figure 7.4.

A second possible source of loss is interaction-induced dephasing between multiple collective Rydberg excitations stored simultaneously. Previous work by D. Maxwell [53, 54] demonstrated that microwave driven Rabi oscillations acted to suppress the value of $g^{(2)}$ observed after multiple rotations, relative to the case of no microwaves. This reduction implies that individual experimental shots in which two or more collective excitations were created were substantially less likely to successfully collectively emit photons that were subsequently detected.

The data sets presented here do not offer sufficient depth to calculate a value of $g^{(2)}$ at specific microwave-driven rotation angles. A value of $g^{(2)}(60S_{1/2}) = 0.43 \pm 0.05$ was measured in a separate experimental run using comparable experimental parameters (notably a similar input photon number, $\overline{n}_{\text{in}} = 2.3 \pm 0.2$), but in the absence of microwave driving. In combination with a typical storage/retrieval efficiency of $\approx 0.5\%$, multi-photon events are an extreme rarity even before any interaction induced suppression. Consequently, interaction-induced loss is considered a negligible contributor to the reduction in signal intensity between the early and late retrieval pulses.

7.2.2. Extinction

The coherent state-dependent behaviour offers clear opportunities for direct control over optical behaviour. Here, the microwave field applied during storage provides a tool for controlling the end-state of the collective excitations, and therefore, the temporal profile of the retrieved photons. With some adjustment, this provides a credible path towards a microwave-controlled optical switch. This provides a first stage towards hybrid quantum computing, allowing high-fidelity semiconductor and superconducting qubits

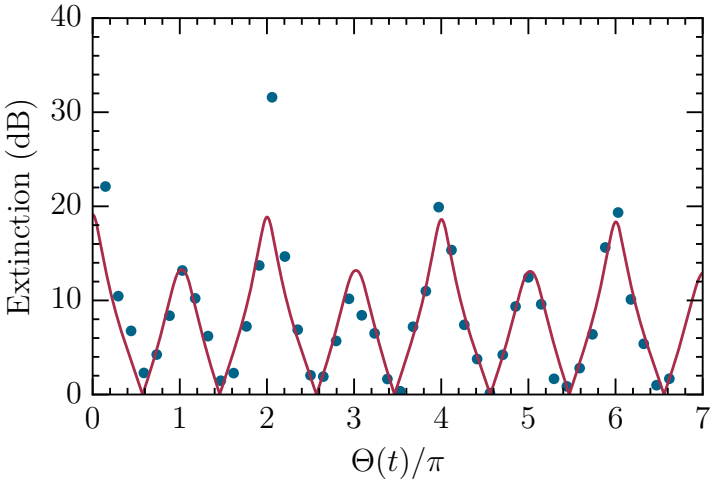

Figure 7.5.: Extinction between early and late photon retrieval from the data shown in figure 7.3 (a) using equation 7.2. The solid line is derived from the fits shown in the same figure. The resolution is limited by the choice of adjusting Θ as a function of t_μ.

at microwave frequencies [244] to couple to low-decoherence optical photons for communication between processing nodes [81, 82].

The quality of a switch is typically given by its switching speed and extinction ratio, such as is discussed for the optical switch used to change the intensity of the coupling laser (see section 4.4.1). The extinction ratio determines how accurately the state of the system can be distinguished from the opposite state. The switching speed determines how rapidly the system can shift from one state to the other.

The extinction ratio can be calculated by observing the ratio between the two traces shown in figure 7.3. This is shown in figure 7.5, expressed in decibels:

$$\text{Extinction} = 10 \times \log_{10}(\, |\overline{n}_{\text{ret}}(E)/\overline{n}_{\text{ret}}(L)| \,), \tag{7.2}$$

where E and L respectively refer to early retrieval (from $|S\rangle$) and late retrieval (from $|P\rangle$).

Due to the low resolution offered by adjusting the length of the microwave pulse, and the strong Θ sensitivity arising from a dependence on $\cos^2(\Theta)/\sin^2(\Theta)$, a maximal

practical extinction is hard to identify. The greatest ratio shown in figure 7.5 of 34 dB greatly exceeds the fit-predicted maximum. For comparison, the AOM used as a switch for the optical trap offers an extinction ratio of 27.61 ± 0.05 dB, and the EOM for the coupling laser of ≈ 20 dB.[1]

7.3. Concept: modulating single photons

Atomic single photon sources have typically made use of either a cavity [245–251] or thermal atoms [252, 253], in order to increase generation rate. Cavity systems have also been used to manipulate the behaviour of single photons such as single photon subtraction [49, 50], implement optical transistors [45, 46, 51] and produce phase shifts [52]. Single atoms in cavities have also been used to control the *shape* of the photons emitted, such as in the work of B. Nisbet-Jones [99, 100, 254].

In addition to its uses for implementing all-optical QIP, photon storage as collective Rydberg polaritons serves as a probabilistic single photon source [44, 53]. This section will demonstrate that, by judicial application of microwave fields, this approach allows the resultant single photons to be intensity modulated at high speed and with low loss.

Section 7.2 demonstrated that the temporal profile of the retrieved light can be adjusted by driving Rabi transitions to a nearby Rydberg state that is non-resonant with the storage retrieval process. Two effects are visible in the data in figure 7.3: the delayed retrieval of population transferred to the dark Rydberg state $|P\rangle$, and more rapid retrieval in the form of a narrow photon pulse on transfer back to $|S\rangle$. The narrowed retrieval window due to $|P\rangle$ arises due to a higher average coupling Rabi frequency Ω_c. Figure 7.3 (d) also shows a weak Rabi oscillation in the envelope of the late retrieval pulse.

Further, while there is a demonstrated loss of efficiency associated with delayed retrieval from $|P\rangle$, this loss arises largely from the time delay, rather than arising from the

[1] The stated extinction of > 47 dB in section 4.4.1 arises from the combination of EOM and PM fibre. Absent the fibre, an extinction ratio of ≈ 20 dB is achieved.

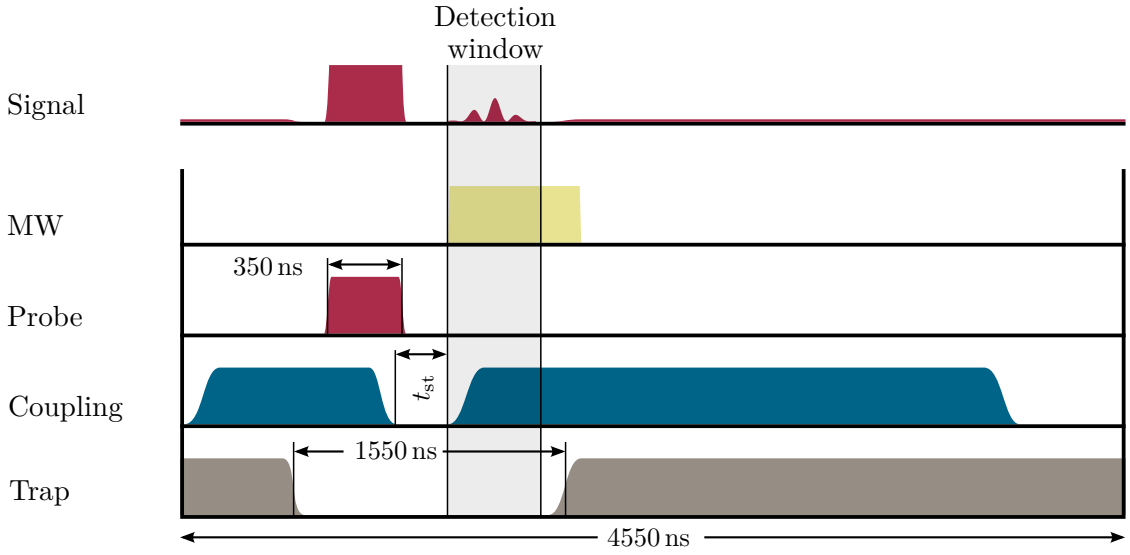

Figure 7.6.: Pulse sequences for fast intensity modulation of photon retrieval. Photons are stored for as short a period as possible (as in chapter 5), and microwaves are applied after the storage window, during retrieval.

use of a state of opposite parity and the concomitant inclusion of resonant dipole-dipole interactions. The second retrieval peak also occurs simultaneously with the driving microwave pulse that restores population from $|P\rangle$ to $|S\rangle$, demonstrating weak Rabi oscillations in the envelope of the retrieved pulse where $\Omega_\mu > \Omega_c$ (figure 7.2 (d)).

Based on these conclusions, microwave driven photon storage could be used as a technique to realise more complicated output shaping of single photons. At the simplest level, the single photons retrieved from the atomic ensemble could be rapidly modulated in intensity by simultaneously driving Rabi oscillations between $|S\rangle$ and $|P\rangle$ during retrieval. More complex schemes may be envisaged where Ω_μ is varied as a function of time. Such variation would be analogous to the approach taken by B. Nisbet-Jones to produce intensity profiles based on the great pyramids of Giza or London's Tower Bridge [99, 254].

A notable feature of the modulation approach suggested here is that it offers the potential for no, or low, loss, of the signal being modulated. Traditional means of achieving intensity modulation are AOMs or EOMs (or for slow modulation at rates $\mathcal{O}(1\,\mathrm{kHz})$ or

lower, physical shutters); such as are used in the laser systems for this experiments (chapter 4). With these technique, unwanted emission is directed into a beam dump to be discarded as heat or diffuse reflections. The microwave-modulation approach avoids unwanted emission by rendering the medium non-emissive instead: when the collective population is in the $|P\rangle$ state, photon retrieval does not occur. The energy is instead stored, or shelved, in a dark state.

All data shown in sections 7.4 to 7.4.3 uses the states $80S_{1/2}$ and $79P_{1/2}$, frequency $\omega_\mu = 7.691 \times 2\pi\,\text{GHz}$, shown in figure 6.2. Data shown in section 7.4.4 uses the states $60S_{1/2}$ and $59P_{1/2}$, frequency $\omega_\mu = 19.005 \times 2\pi\,\text{GHz}$, shown in figure 6.10.

Modelling photon modulation

Modelling the entire collective system is a complicated endeavour due the various additional effects arising from the addition of $|P\rangle$, compared to the description in section 5.4, such as excitation hopping [255]. A simple, analytical approach is taken here. Rather than simulating the entire atomic ensemble, a single ^{87}Rb atom is modelled by the four level optical Bloch equations in the presence of time-dependent EM fields. This is justified by the behaviour of a collective Rydberg excitation as approaching that of a single superatom (sections 3.3 and 6.2.1).

The level system is shown in figure 7.7 (a), and is initialised with the atomic population in $|R_s\rangle$, signifying that a single photon has been stored in a Rydberg state (corresponding to the collective state $|S\rangle$ used throughout chapter 6 and the first half of this chapter).

$$\rho = \begin{pmatrix} \rho_{gg} & \rho_{ge} & \rho_{gR_s} & \rho_{gR_p} \\ \rho_{eg} & \rho_{ee} & \rho_{eR_s} & \rho_{eR_p} \\ \rho_{R_sg} & \rho_{R_se} & \rho_{R_sR_s} & \rho_{R_sR_p} \\ \rho_{R_pg} & \rho_{R_pe} & \rho_{R_pR_s} & \rho_{R_pR_p} \end{pmatrix}, \quad \rho(t=0) = \begin{pmatrix} 0 & 0 & 0 & 0 \\ 0 & 0 & 0 & 0 \\ 0 & 0 & 1 & 0 \\ 0 & 0 & 0 & 0 \end{pmatrix}. \tag{7.3}$$

The system evolves under driving of two time dependent EM fields with Rabi frequen-

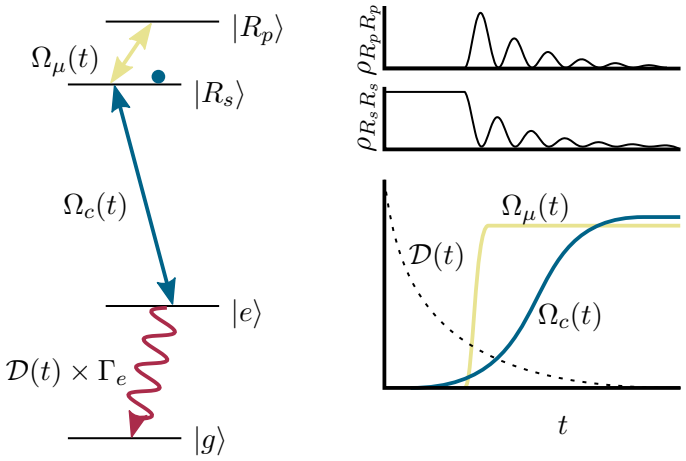

Figure 7.7.: Photon modulation model. The system is modelled as a single four-level atom, initially in state $|R_s\rangle$. Two time dependent resonant EM fields are applied, $\Omega_c(t)$ and $\Omega_\mu(t)$, while the signal is observed as spontaneous emission from $|e\rangle$ to $|g\rangle$.

cies $\Omega_c(t)$ and $\Omega_\mu(t)$ and detunings Δ_c and Δ_μ, yielding a Hamiltonian of

$$\mathcal{H}(t) = \frac{1}{2}\begin{pmatrix} 0 & 0 & 0 & 0 \\ 0 & 0 & \Omega_c(t) & 0 \\ 0 & \Omega_c(t) & -2\Delta_c & \Omega_\mu(t) \\ 0 & 0 & \Omega_\mu(t) & -2\Delta_\mu \end{pmatrix}. \tag{7.4}$$

The system evolves according to equation 3.15, with the phenomenological decay term $\hat{\mathcal{L}}$ given by

$$\hat{\mathcal{L}} = \frac{1}{2}\begin{pmatrix} 2\Gamma_e\rho_{ee} & -\Gamma_e\rho_{ge} & 0 & 0 \\ -\Gamma_e\rho_{eg} & -2\Gamma_e\rho_{ee} & -\Gamma_e\rho_{eR_s} & -\Gamma_e\rho_{eR_p} \\ 0 & -\Gamma_e\rho_{R_se} & 0 & 0 \\ 0 & -\Gamma_e\rho_{R_pe} & 0 & 0 \end{pmatrix}. \tag{7.5}$$

Photon retrieval - i.e. collective emission - is considered to be proportional to the spontaneous emission from the first excited state $|e\rangle$ to the ground state $|g\rangle$, characterised by the lifetime of that state, $1/\Gamma_e$. For ^{87}Rb, the lifetime is 26.2 ns [256]. Due to the lifetime effects of photon storage predicted in section 3.2.3 and exhibited in section 7.2.1, an additional factor is included to simulate time dependent dephasing:

$$\text{Signal} = \Gamma_e\, \rho_{ee}(t)\, \mathcal{D}(t), \tag{7.6}$$

where

$$\mathcal{D}(t) = e^{-t/d_r}. \tag{7.7}$$

Physically, d_r corresponds to the lifetime τ observed in figure 7.4. A diagram of the model is shown in figure 7.7.

The time dependent fields Ω_c and Ω_μ are implemented as sigmoid functions with switch-on time t_0[2] and rise time $t_{10:90}$:

$$\Omega(t, t_0, t_{10:90}) = \frac{\Omega_{\max}}{1 + e^{-4.4(t-t_0)/t_{10:90}}}. \tag{7.8}$$

The loss factor $\mathcal{D}(t)$ and the two field Rabi frequencies are shown in figure 7.7 (b).

The model has only two free parameters: the decay rate d_r, and the delay between the two EM fields switching ($t_{\mu,0} - t_{c,0}$). The maximum Rabi frequencies and rise times are set to the known experimental parameters ($t_{c,10:90} = 185\,\text{ns}$ and $t_{\mu,10:90} = 8\,\text{ns}$, $\Omega_{c,\max} = (6 \pm 2) \times 2\pi\,\text{MHz}$, $\Omega_{\mu,\max}$ as appropriate).

Unmodulated retrieval

The model is first considered in the case where no microwaves are applied, shown in figure 7.8. Data is shown in a solid blue line, and the model in a broken red line. Here, the parameters Ω_c and d_r are varied to match the fit, although in the absence of Rabi oscillations, the two parameters are not independent, and consequently can each take a wide range. If the loss factor d_r is removed (i.e. assumed to represent an insignificant effect across the relatively narrow duration of unmodulated retrieval), then the model yields a value of $\Omega_c = (4.5 \pm 0.2) \times 2\pi\,\text{MHz}$, consistent with the value of $(6 \pm 2) \times 2\pi\,\text{MHz}$ predicted from measuring coupling beam power. The numeric results fit well with observed data.

Modulated photon retrieval

The effect of applying microwave modulation can then be predicted, as shown in figure 7.9. In addition to the parameters identified by the fit in figure 7.8, a microwave field

[2]For the purpose of this model, the switch-on time is defined as $\Omega(t_0) = \Omega_{\max}/2$.

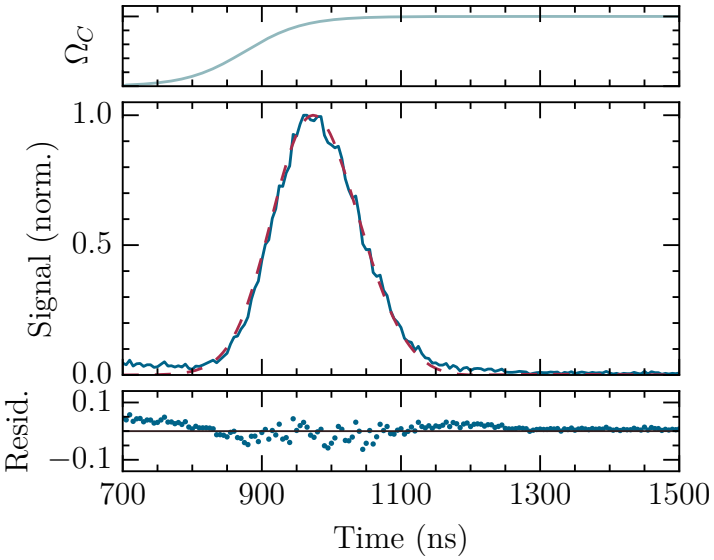

Figure 7.8.: Comparison of single emitter model to unmodulated photon retrieval. Retrieval from $80S_{1/2}$ (solid blue line). Model (broken red line). Coupling laser switch-on time and Rabi frequency as free parameters. With $d_r = 0$, the fit yields $\Omega_c = (4.5 \pm 0.2) \times 2\pi\,\mathrm{MHz}$.

is added with a Rabi frequency of $\Omega_\mu = 8 \times 2\pi\,\mathrm{MHz}$, switching on before the retrieval pulse begins. The results are shown in figure 7.9, with the fitted curve from figure 7.8 overlaid for comparison. The result is to overlay a $\cos^2(\Theta(t))$ intensity modulation on the retrieval envelope. In this figure, the loss parameter $d_r = 0$: the area under both curves is equal, resulting in an additional broadening of the envelope.

7.4. Observing photon modulation

In order to observe modulated photon retrieval, the experimental sequence was modified to that shown in figure 7.6. A microwave pulse was applied from shortly before the beginning of the photon retrieval signal. The timing of the microwave pulse was synchronised as close as possible to the beginning of photon retrieval. As discussed in section 4.5, the rise time of the microwave sensitive diode limited the precision with which this goal could be achieved. The microwave pulse was held at a fixed intensity for

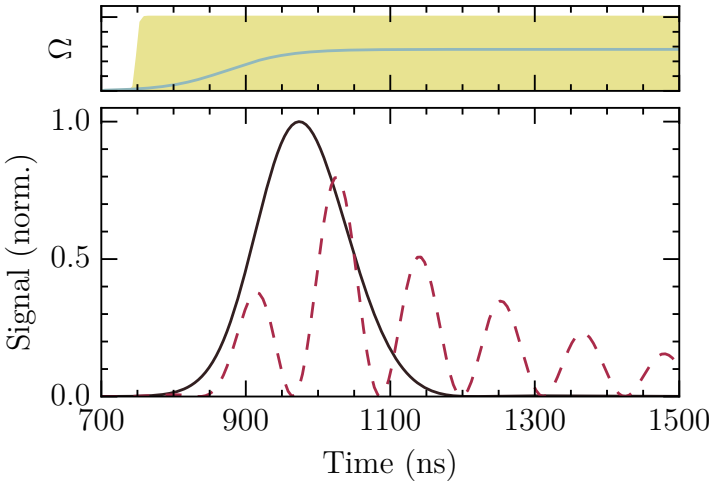

Figure 7.9.: Modelled modulated photon retrieval. A microwave field (yellow) is added to the parameters from figure 7.8 (broken red line). The curve from that figure is overlaid for comparison (black).

a period substantially greater than the length of the retrieval window (typically, ending at the same time as the optical trap power was restored).

Figure 7.10 shows four photon retrieval traces from the state $80S_{1/2}$, three of which are intensity modulated by different microwave powers: yellow ($6\,\mathrm{mV_{rms}}$), red ($19\,\mathrm{mV_{rms}}$) and blue ($38\,\mathrm{mV_{rms}}$).[3] Since the modulation arises from Rabi oscillations between $|S\rangle$ and $|P\rangle$, the modulation occurs at the microwave Rabi frequency ($f_{\mathrm{mod}} = \Omega_\mu/2\pi$). The Rabi frequency can be predicted from the applied field strength and a reference trace such as those shown in chapter 6. Based on the data in figure 6.5, the three microwave powers stated should yield Rabi frequencies of 2.6, 8.0 and 16 $\times\, 2\pi\,\mathrm{MHz}$ respectively. The fourth trace (grey) is a reference trace similar to that shown in figure 7.8. The blue and red traces clearly show intensity modulation to better than 95% depth, with an increase in pulse width as predicted by figure 7.9. The increase in width is a promising hint towards achieving low-loss modulation (discussed in section 7.4.3). None of the data

[3] Nominal values: Signal generator set points were 200, 600 and $1200\,\mathrm{mV_{rms}}$ respectively, followed by $\approx 30\,\mathrm{dB}$ of external attenuation.

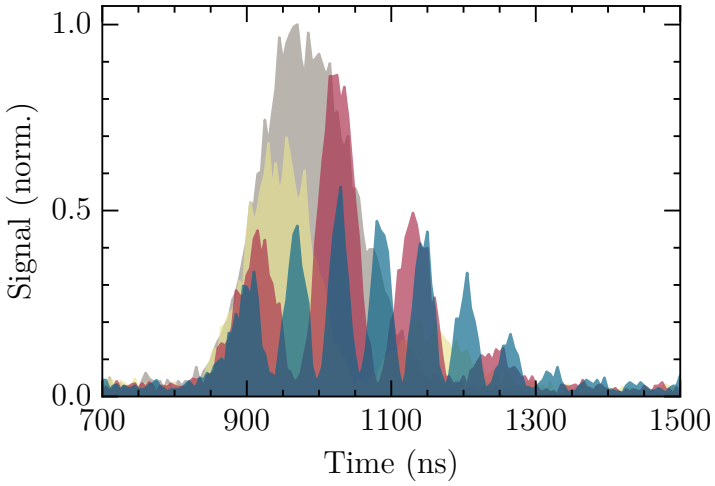

Figure 7.10.: Intensity modulation of photon retrieval. All signals normalised to the peak intensity of retrieval for $\Omega_\mu = 0$.

traces exhibit the extreme tail predicted in figure 7.9, although un-constraining the loss term d_r to factor in motional dephasing may explain the difference.

7.4.1. Applying the single-emitter model to data

Figure 7.11 shows the four retrieval traces from figure 7.10 with best fits to the single emitter model described in section 7.3. Compared to the fit shown in figure 7.9, the loss factor d_r is unconstrained, in order to better describe the effect of motional dephasing upon the long tail predicted in figure 7.9. The model is initialised with the coupling laser parameters developed from figure 7.9 ($t_{c,0}$, $\Omega_{c,\max}$), and the microwave Rabi frequency predicted from the power used in the experiment. The parameters $t_{\mu,0}$, $\Omega_{\mu,\max}$ and d_r are varied to achieve the best fit.[4]

The model demonstrates excellent fit where the microwave modulation is zero or low, with individual large residual values in figures 7.11 (a.2) and (b.2) arising only from noise

[4]Prediction of Ω_μ from microwave power is not exact: attenuation in the microwave signal path may change when elements such as coaxial isolators are removed and replaced due to differences in torque applied to the SMK connectors.

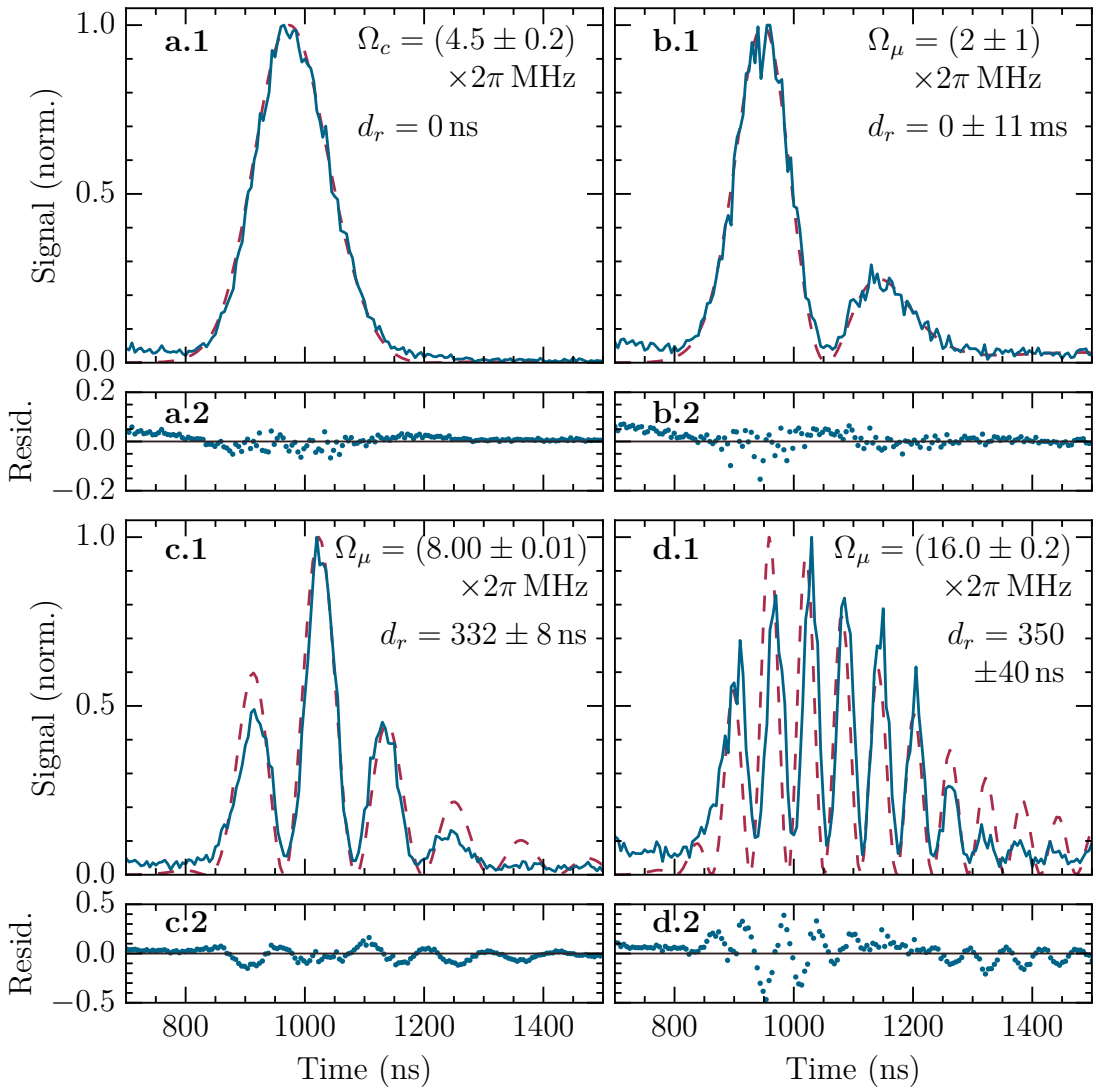

Figure 7.11.: Comparison of single emitter model to intensity modulation. Each data set (solid blue line) is independently normalised to its maximum intensity. Each data set is then fit to the model described in section 7.3. Subplots (b), (c) and (d) use the coupling laser parameters established in subplot (a), which is a duplicate of figure 7.8.

in the data.[5] The model becomes increasingly inaccurate at higher modulation frequencies with clear structure in large residual values, although the values of Ω_μ arising from the fit are all in excellent agreement with predicted values. Principally, the experimental data does not exhibit nearly as long a tail as the model predicts, even after factoring in the loss rate d_r (which was set to zero in figure 7.9). One possible explanation is that induced resonant dipole-dipole interactions play a greater than expected role.

In the experiments presented here, a probe pulse with a photon number of $\overline{n}_{\text{in}} = 5.0 \pm 0.1$, approximately twice the number used in the experiments presented in chapter 5 ($\overline{n}_{\text{in}} = 2.4 \pm 0.2$) where a $g^{(2)}$ value was measured for this Rydberg state, albeit for a shorter storage time ($g_A^{(2)}(80S_{1/2}, t_{\text{st}} = 170\,\text{ns}) = 0.20 \pm 0.04$). The microwave rotation experiments presented in section 6.3 similarly used an input number of $\overline{n}_{\text{in}} = 2.5 \pm 0.2$. Considering the evidence of dipole blockade shown in figure 4.21, the ensemble begins to show signs of saturation by an input photon number of 5, indicating that the signal photon number will not scale in proportion to the input photon number.

Consequently, the underlying assumptions of the single-emitter model may be invalid for the data presented here. If induced resonant dipole-dipole interactions are to blame, it is to be expected that they would manifest as a suppressive effect increasing with the number of Rabi rotations. Resonant dipole-dipole interactions are maximised at non-integer-π rotation angles where the collective excitation state is a superposition of both $|S\rangle$ and $|P\rangle$.

7.4.2. Phenomenological description

This section provides an alternative, phenomenological description of single photon modulation; in contrast to the physical description of the single emitter model detailed in section 7.3. Section 6.3 established that, contrary to previous findings [53], Rabi oscillations between $|S\rangle$ and $|P\rangle$ do take the expected $\cos^2(\Theta)$ form [97]. Analysis of the pulse shape of the retrieved light in section 4.4.3 indicated a Gaussian envelope. A simple

[5] The figure only shows the first 1.75×10^4 shots per MOT load of the total data set: this subject will be discussed in further detail in section 7.4.3.

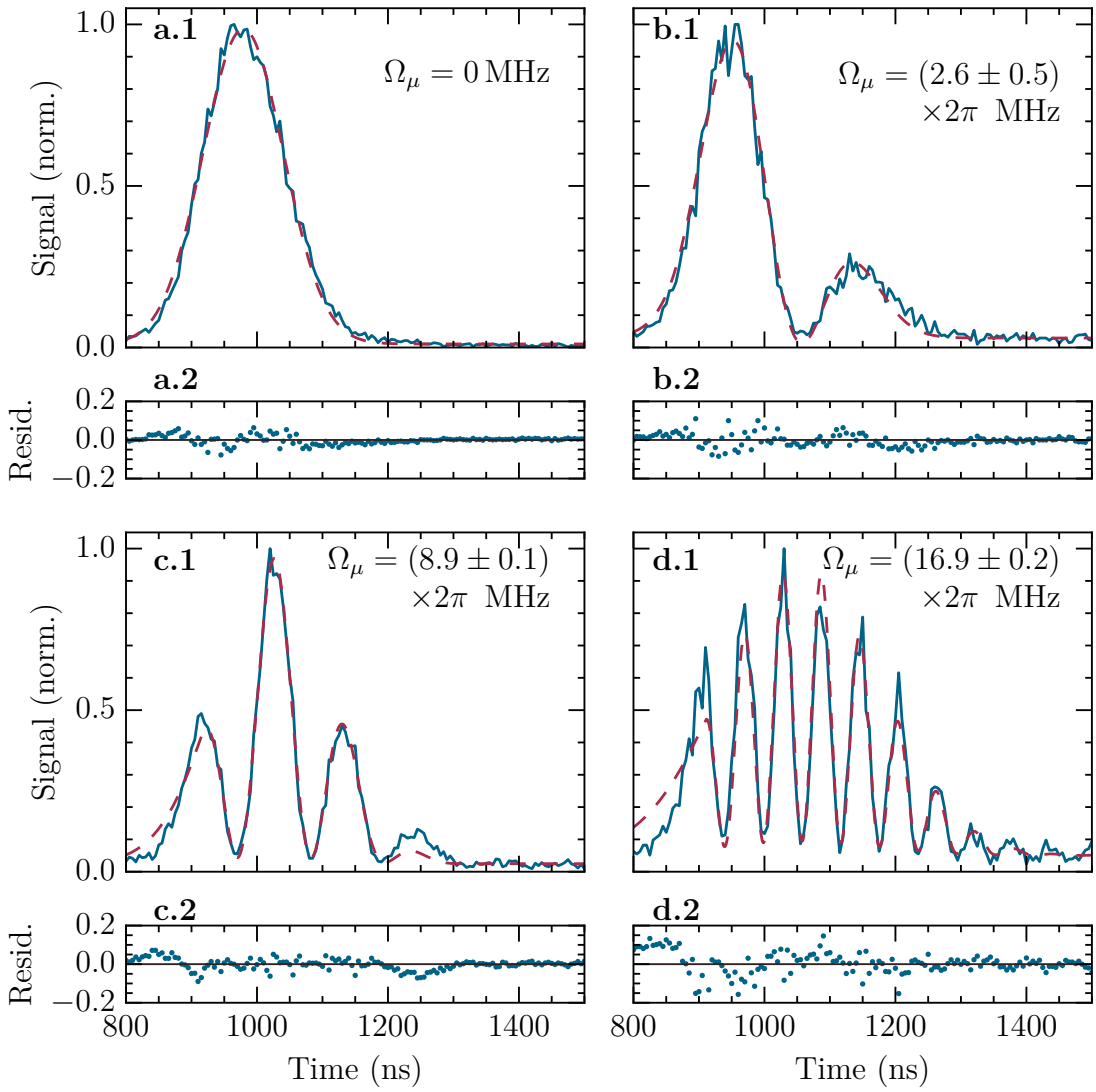

Figure 7.12.: Comparison of phenomenological description to intensity modulation. All data sets independently normalised to their maximum value and fitted to equation 7.9. The Gaussian envelope shows a progressively poorer quality of fit to the rising edge for larger values of Ω_μ (derived from the fit). *a*: $0\,\mathrm{mV_{rms}}$. *b*: $6\,\mathrm{mV_{rms}}$ *c*: $19\,\mathrm{mV_{rms}}$. *d*: $38\,\mathrm{mV_{rms}}$.

mathematical description is therefore proposed, that the modulation can be described by a Gaussian envelope around a $\cos^2$ oscillation, given by the function

$$I(t) = a_0 + e^{\frac{(t-a_1)^2}{a_2^2}} \left[a_3 + a_4 f(t, a_5)\right], \tag{7.9}$$

where

$$\begin{aligned} f(t, a_5) =& 1 && t \leq a_5, \\ =& \cos^2\left(\frac{\Omega_\mu (t - a_5)}{2}\right) && t \geq a_5. \end{aligned}$$

and $a_0 - a_5$ and Ω_μ are fitting parameters. a_1 corresponds to the time of peak retrieval intensity, a_2 to the width of the retrieval pulse, and a_5 to the time at which the microwave pulse is switched on and Rabi oscillations between $|S\rangle$ and $|P\rangle$ begin. a_0 and a_3 fit the background noise and extinction ratio respectively, and a_4 is the amplitude of the oscillations. It is assumed that, due to simultaneous retrieval and microwave driving, the Rydberg-mediated atom loss discussed in section 6.3 contributes only minimally to the system as indicated by figures 6.12 and 6.13. Therefore, the $\mathcal{M}$ term is excluded for simplicity.

Figure 7.12 shows the four data sets previously shown in figures 7.10 and 7.11 fitted to equation 7.9. Figure 7.12 (a.1) provides a reference example of photon retrieval without any microwave driving, and demonstrates an excellent fit to the proposed Gaussian envelope. Figure 7.12 (a.2) a slight, but small, structure in residuals, particularly on the rising edge. Figures 7.12 (b), (c), and (d) predict that the microwave pulse began at $a_5 = 910 \pm 6\,\text{ns}$. The rising edge of the retrieval pulse fits increasingly poorly to the assumed Gaussian envelope as the modulation frequency increases, indicating that while a Gaussian envelope is a reasonable approximation at no, or low, Ω_μ, it becomes an increasingly poor description where the width of the retrieval pulse is significantly expanded. This can most likely be explained by acknowledging that while a Gaussian function is symmetrical around its centre, this is not necessarily a good description of photon retrieval, where the rate of retrieval (the coupling Rabi frequency) increases over time. As the retrieval pulse width expands, photons that remain as collective excitations

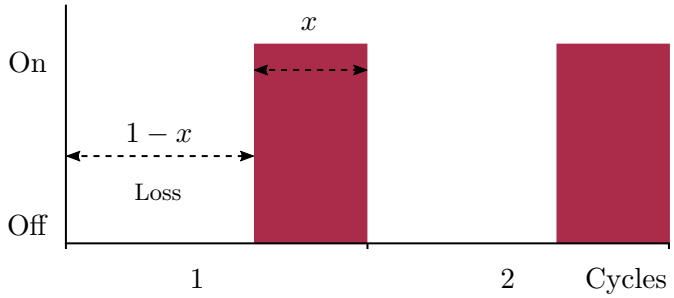

Figure 7.13.: Duty cycles. A modulator with a duty cycle of x exhibits a loss of $1 - x$. A low-loss modulator should have an efficiency $0.5 < e_r < 1.0$

longer are retrieved at a faster rate, resulting in an asymmetry not well described by the proposed Gaussian envelope.

7.4.3. Modulation efficiency

Section 7.3 raised the issue of low-loss modulation. Loss is best considered in the context of the duty cycle of the modulation (figure 7.13). The modulator with a duty cycle of x emits for that fraction of time every cycle. In a lossy modulator such as an AOM, EOM, or shutter, unwanted emission during the $1 - x$ fraction of the cycle is discarded into a beam dump, and consequently, the modulator exhibits a loss of $1 - x$, or an efficiency $e_r = x$.

In this approach, modulation is achieved by not emitting during the period in which emission is unwanted. Energy is instead stored as a collective Rydberg excitation in a dark Rydberg state. In the proof-of-principle form shown in this chapter, modulation is accomplished by Rabi oscillations at a fixed Rabi frequency, corresponding to a duty cycle of 0.5. A lossy modulator with the same duty cycle should show an efficiency of 0.5: time averaged modulated intensity equal to 50% of the unmodulated intensity. A loss-less modulation technique will show an efficiency of 1.0. A low-loss technique should show an efficiency $0.5 < e_r < 1.0$.

Figure 7.14 shows the loss of efficiency per shot as a function of shot number. It demonstrates that the photon retrieval pulse can be intensity modulated with virtually

no loss for a small number of shots, with modulation at $\Omega_\mu = 8.9 \times 2\pi\,\mathrm{MHz}$ showing relative efficiency of $e_r = 0.86$ averaged over the first 2500 shots. However, relative efficiency appears to fall as a function of shot number: behaviour that is reminiscent of the results presented in figure 6.13, indicating that the assumption made that this technique would not show an enhanced atom-loss relative to no modulation was incorrect. The reason for this is unknown.

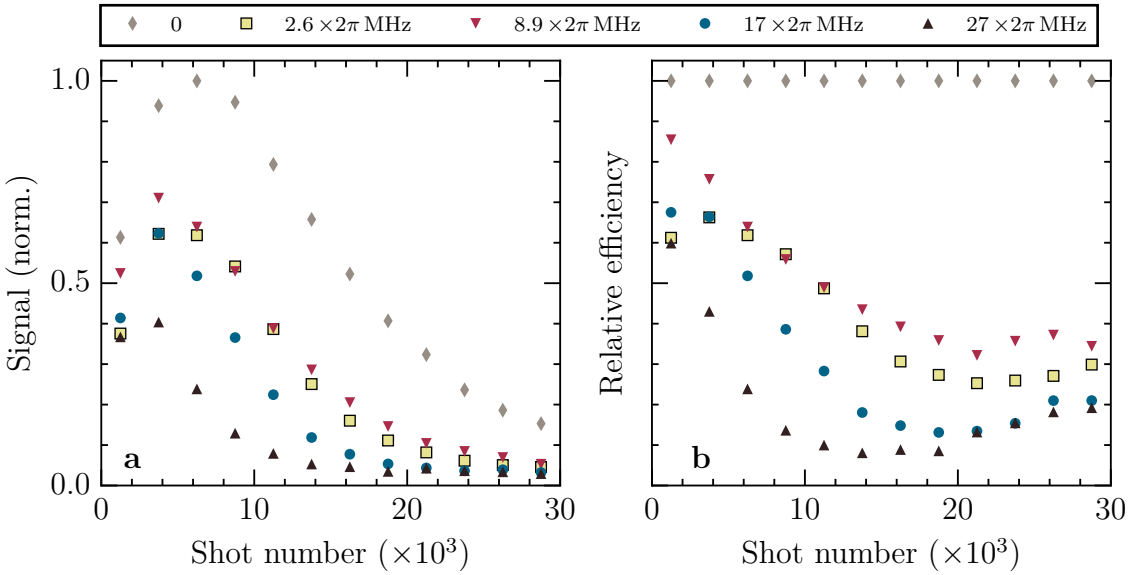

Figure 7.14.: Shot dependency of modulation efficiency. Early in the sub-μs sequence, modulated retrieval is $> 50\%$ as efficient as unmodulated retrieval, and approaches 90% in some cases. It falls off faster than conventional retrieval, with more rapid modulation losing efficiency at a greater rate.

Since the data sets shown in figures 7.12 to 7.14 were taken over a sufficient time period that the performance of the optical trap may have varied, an attempt is made to compensate for this drift in figure 7.15, by considering the degree of photon retrieval as a function of optical trap performance, rather than shot number (which demonstrably is not a linear relationship, figure 4.9).

Figure 7.15 (a) shows the OD of the atomic ensemble as a function of shot number. The optical depth is calculated within a 15 ns window near the end of the probe pulse

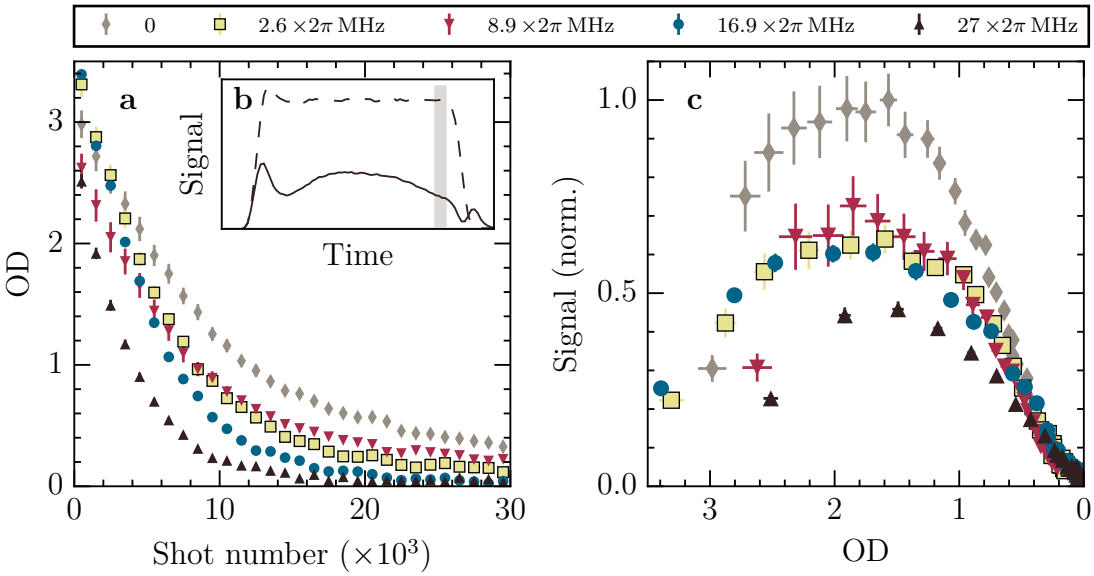

Figure 7.15.: OD dependency of modulation efficiency. *a*: Variation of OD with shot number. *b*: OD calculated by evaluating ensemble transmission during a 15ns window at the end of the probe pulse (grey window). *c*: Retrieval intensity as a function of OD, normalised to the peak retrieval rate of the no-microwave case. Modulated retrieval exhibits very consistent performance when variation in the optical trap is factored out.

(shown in figure 7.15 (b)). A narrow late window is chosen to minimise the influence of the coupling laser on the calculation. The number of photons transmitted through the cloud is compared to the number transmitted in a reference pulse, measured without an atomic ensemble. The reference photon pulse (shown by a broken line in figure 7.15 (b)) was measured, once, approximately halfway through the laboratory time dedicated to this experiment. This technique relies on a general observation that the stability of the excitation laser is substantially greater than that of the optical trapping laser.

This technique is least accurate at high OD values, due to the tiny fraction of probe photons detected with which to compare. The technique shown in figure 4.9, where a Lorentzian curve is fitted across a frequency scan, is more reliable, due to higher transmission off resonance. Since the data shown in figure 7.15 was only measured at resonance, the less accurate method must suffice. However, a substantial systematic

error is present at higher values of OD.

However, even accounting for the systematic limitations, considering the retrieval signal as a function of OD (figure 7.15 (c)) provides a useful means of visualising storage efficiency independently from trap variation over the course of the day. Other contributions to variation, such as power and frequency stability of the coupling laser, cannot be factored out, and may still play a role.

Figure 7.15 (c) shows that all but the fastest modulation frequency exhibit near-identical performance as a function of optical depth. Non-modulated photon storage is similarly efficient at high OD, but becomes much more efficient for a range of OD, before the atomic ensemble depletes sufficiently for storage to fail completely. The fastest modulation is substantially less efficient in all cases.

The observation of non-modulated photon storage/retrieval efficiency falling *below* modulated efficiency for OD ≥ 3 casts a degree of doubt on this method. The variation could arise either from the systemic uncertainties in calculating OD (which are greatest at larger OD), or from variation in either power or frequency stability of the coupling laser.

7.4.4. Fast modulation

Figures 7.12 to 7.15 demonstrate photon modulation at frequencies up to $f_{\text{mod}} = 25\,\text{MHz}$, with lower modulation frequencies exhibiting low loss. This modulation is observed as a variation in the intensity of the photon retrieval signal between individual clock cycles of the FPGA-based detection system described in section 4.2. Since each clock cycle has a finite length (5 ns), it imposes a finite resolution, beyond which intensity modulation cannot be observed. The Nyquist-Shannon sampling theory states that [257]

> If a function $f(t)$ contains no frequencies higher than W cps, it is completely determined by giving its ordinates at a series of points spaced $1/2W$ seconds apart

For the detection system used here (section 4.2), this would yield a maximum detectable modulation frequency of $f_{\text{mod}} = 100\,\text{MHz}$. Higher modulation frequencies can plausibly

be generated due to the high microwave sensitivity of Rydberg excitation, but cannot be observed using the approach taken in sections 7.3 and 7.4. A detection system with an improved resolution would be required.[6]

To observe high modulation frequencies than the noted 100 MHz limit, a different technique must be used. Rather than simultaneously applying a microwave field and observing signal intensity: in which a different microwave rotation angle is observed in each FPGA clock cycle (figure 7.6); the approach used in chapter 6 can be used instead (figure 6.3). In chapter 6, a microwave pulse was applied prior to detection, such that many clock cycles within a single shot all observed the same microwave rotation angle. In effect, each experimental shot is added to a single microwave rotation bin. This allows arbitrarily high Rabi frequencies to be observed, but requires dramatically greater experimental time.

The highest microwave Rabi frequency demonstrated using the apparatus described in this thesis was $\Omega_\mu = 495 \pm 5 \times 2\pi$ MHz, on the transition $60S_{1/2} \leftrightarrow 59P_{1/2}$ (figure 6.10). The data is shown in figure 7.16, with the signal normalised against photon storage conducted without any microwave driving. The rotation angle was varied as a function of microwave power, and the values estimated by fitting to the Rabi frequency. The rotation angles are accurate to $\pm 2\pi$. A rotation angle of 198π and a microwave pulse duration of 400 ns corresponds to a Rabi frequency of $495 \pm 5 \times 2\pi$ MHz. However, this degree of driving results in substantial loss, with a peak retrieval rate (198π) at just 16% of the retrieval level absent microwave driving.

The microwave Rabi frequency is limited here by the microwave signal generator's maximum power output at the resonant frequency (19.005 GHz). Use of the transition $80S_{1/2} \leftrightarrow 79P_{1/2}$ at 7.691 GHz offers both higher maximum microwave power and a greater transition strength. In principle, Ω_μ could exceed $1.5 \times 2\pi$ GHz on this transition, although resultant loss in retrieved signal strength would likely be prohibitive.

[6] The limiting factor in this experiment is the choice of FPGA, which cannot offer much lower than a 5 ns clock cycle. The SPCMs offer a resolution of up to 27 ps.

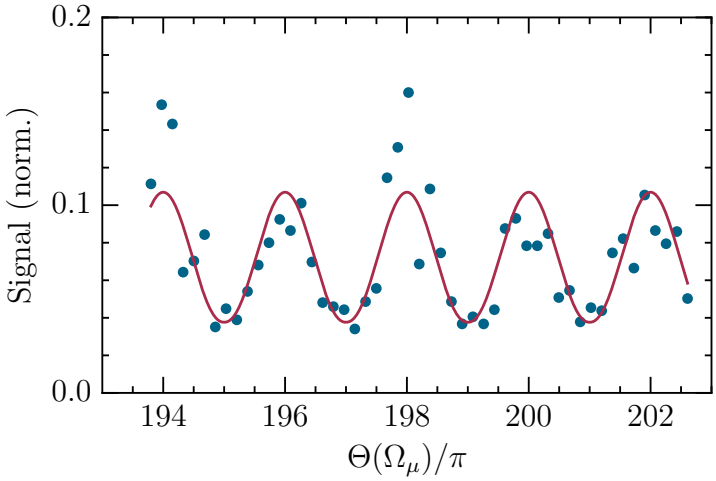

Figure 7.16.: Rapid microwave driving. A high power microwave field resonant with $60S_{1/2} \leftrightarrow 59P_{1/2}$ is applied during the storage window only (as in the sequence shown in figure 6.3). Retrieval is weak, but still present. Signal level normalised to retrieval level in absence of microwaves. Solid line is a fit to equation 6.2.

8. Conclusions and Outlook

In summary, this thesis reports on the construction of a new experimental apparatus to study non-linear quantum optics in cold atoms excited to Rydberg states. It includes description and discussion of experiments demonstrating effective long-range interactions between photons stored as collective excitations in separate, non-overlapping spatial modes. It demonstrates that with the application of controlled microwave fields, the collective Rydberg excitations can be efficiently driven with minimal loss through many-π rotations before retrieval, and that such a technique can be used for efficient optical resolution of separate states.

8.1. Overview of this thesis

The new experimental apparatus is described in chapter 4, as well as in [105, 106]. The apparatus offers a high repetition rate of the order of $\mathcal{O}(100\,\mathrm{kHz})$, owing to the use of a 2D-MOT cold atom source and the ability to effectively recycle the atomic ensemble $\mathcal{O}(10^4)$ times without substantial atom loss. In-vacuum aspheric lenses offer near-diffraction limited performance and are used to optically trap and probe side by side microscopic cold atomic ensembles, spaced at a distance at which dipole-dipole interactions are non-negligible. Eight electrodes and three microwave antennae are located in vacuum to allow the application of electric fields in the frequency range $\mathrm{DC}-40\,\mathrm{GHz}$.

A new integrated experimental control and data acquisition system is implemented. The control system is based on control software and hardware now widely used in Durham, allowing a sharing of expertise and maintenance overhead to maximise the uptime of multiple complex experiments compared to previous generations. The data

acquisition system provides substantially greater insight into the performance of the experiment, recording the arrival time of every single photon detected rather than a drop-in start-stop based coincidence detector. This increased capability comes at the cost of reducing the time resolution from $\mathcal{O}(100\,\text{ps})$ to 5 ns. Due to the limit on total data set size available, even with the high repetition rate, this limitation is not anticipated to prove problematic.

Preliminary data demonstrating non-linearity are shown in the end of chapter 4, including intensity dependent transmission under EIT conditions and the saturation of photon storage at various Rydberg states. Photon storage and retrieval exhibits a substantial reduction in $g^{(2)}$ between the initial laser pulse and the retrieved photon pulse, indicating that highly non-classical states of light are produced by the protocol, given the geometric constraints of the atomic ensemble(s) used, The fast repetition rate of the experiment permit large data sets of photon statistics to be assembled over short time scales even with the low ($\approx 0.1-1\%$) efficiency of photon storage and retrieval achieved.

Non-contact photon-photon interactions

Chapter 5 presents data demonstrating interactions between two photons stored in two independent and non-overlapping atomic ensembles as collective Rydberg excitations [63]. It is shown that photon emission from the two ensembles becomes anti-correlated as a function of increasing vdW interactions. Data showing these anti correlations as a function of interaction strength (principal quantum number) and separation were presented in the work of H. Busche [105], and included here as background to data showing that anti-correlations also increase as a function of interaction time.

The data are compared to a model in which vdW interactions imprint a spatially non-uniform phase shift on nearby collective excitations, resulting in a decreased likelihood of collective emission back into the original mode and a consonant decrease in detection probability. The model is an extension of earlier work by F. Bariani *et al* [65]. The model exhibits a good fit for all three varied parameters (interaction strength, ensemble separation, interaction time).

Microwave electrometry

Chapter 6 presents data demonstrating that cold atoms offer a competitive platform, under certain conditions, for sensitive electrometry of weak microwave fields. Two methods of electrometry are demonstrated, based on microwave-driven photon storage spectroscopy. Photon storage spectroscopy yields a sensitivity that is provisionally competitive with published values in thermal atoms [89], despite the disadvantage of the necessity of cooling atoms beforehand. However, this high sensitivity to microwave fields is shown to arise from a previously unobserved artifact of recycling the atomic ensemble many thousands of times, and as a result, is also highly sensitive to other parameters such as the intensity of the probing field.

Where part of the collective Rydberg population is driven to, and left in, a state that is non-resonant with the photon retrieval process, it is shown that atom loss from the optical trap is dramatically enhanced, leading to the suppression of photon storage/retrieval efficiency at non-integer-π rotation angles seen in previous work [53, 103]. It is this progressive reduction in retrieval efficiency that results in strong microwave sensitivities, but that is itself dependent on parameters such as probe intensity and atomic ensemble recycle number. By including a second microwave driving stage, the fossilised non-resonant population may be re-addressed and disposed of, in order to properly sanitise the atomic ensemble for further recycling.

As a result of the addition of the 'cleaning' microwave pulse, it is demonstrated that collective Rydberg excitations may be efficiently driven through many-π rotations and still be recovered with minimal loss.

Single photon shaping

Chapter 7 takes advantage of the demonstrated ability to perform high fidelity Rabi rotations to implement two schemes of microwave control of single optical photons. The second microwave pulse brings the non-resonant Rydberg state into resonance with the retrieval process, producing a second coherent, collective emission, delayed by $\mathcal{O}(100\,\mathrm{ns})$

relative to the first retrieval pulse. This delay would allows the implementation of TDM[1] via the application of a microwave pulse, such as might be produced by a superconducting circuit [81, 82].

It is also demonstrated that by driving population between the resonant and non-resonant Rydberg states simultaneously with the photon retrieval process, the intensity of the retrieved photon may be rapidly modulated. Since the photon (stored as a collective excitation) is shelved in a non-resonant state, rather than diverted into a signal dump, this intensity modulation technique exhibits substantially lower loss than hardware solutions such as AOMs, EOMs, or shutters. Intensity modulation at up to 25 MHz is demonstrated, and data suggests that rates exceeding 500 MHz are possible; although they cannot be observed by the same technique due to the time resolution of the data acquisition system.

8.2. Outlook

Multiple equipment upgrades are underway to allow a greater range of experiments to be conducted.

Principally, a new optical trapping system will be installed. By introducing an additional trapping beam (specifically, a pair of focused beams crossing at a small angle [167, 168] perpendicularly to the two micro traps discussed in section 4.1.4, the atomic ensembles can in principle be completely confined to a volume smaller than the blockade radius at typical Rydberg states. This additional confinement will both improve the optical depth of the traps and provide much greater certainty in the interaction distance between collective excitations in multiple sites, reducing the 'smearing out' effect seen in chapter 5 as a result of minimal axial confinement.

A second control laser has been installed to permit simultaneous excitation to different Rydberg states (see appendix A), as sequential excitation via two-photon microwave transfer proved impractical (see appendix C). The second laser will allow the two chan-

[1] Time-division multiplexing

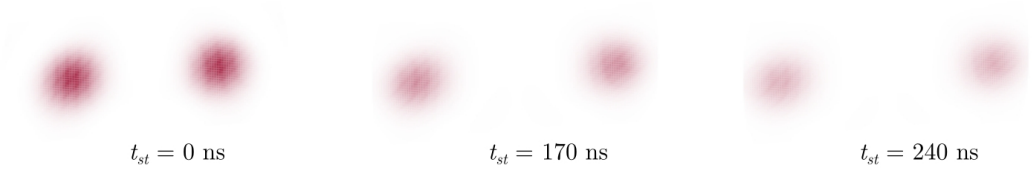

Figure 8.1.: Spatial photon emission. Predicted effect of contactless, Rydberg mediated interactions upon photon retrieval modes. Preliminary modelling based on spherical Gaussian atomic distributions ($\sigma_{\mathrm{rad}} = \sigma_{\mathrm{ax}} = 1.5\,\mu$m, $d = 10\,\mu$m, $80S_{1/2}$) predict a deflection of the emitted modes, rather than an isotropic depletion of intensity, increasing with storage time. Courtesy of H. Busche

nels to be separately addressed by coupling light.

Further experiments are planned to advance the state of the art demonstrated in [63] and chapter 5. The experiments presented in this thesis only considered whether the stored photon was successfully emitted into the original mode whence it originated. The next logical step is to map out the emission pattern outside the original mode that arises from the controlled interaction with a second excitation. It is intended to piezo-actuators to translate the tip of the single-mode fibre that delivered retrieved photons to the SPCM as a dithered multi-pixel imaging array. Figure 8.1 shows a preliminary calculation of the expected mode distribution of emitted photons as a function of storage time. It predicts that rather than an isotropic reduction in forward emitted intensity in favour of a random direction, the collective mode remains relatively directional but that the direction is deflected outwards.

The increased confinement provided by the upgraded optical trapping configuration should also permit an experimental implementation of D. Paredes-Barato's proposed photonic phase-gate [61]. The full two-qubit gate proposal requires that the current two-channel trapping configuration be extended to four-channel, but a proof of principle may be conducted with just two sites. In this proposal, the state of the incident qubits determines the physical position at which the photons are stored as a collective Rydberg excitation. The distance between sites is chosen such that, when photons are stored as collective excitations in the same state, the vdW interactions are negligible; but that if a

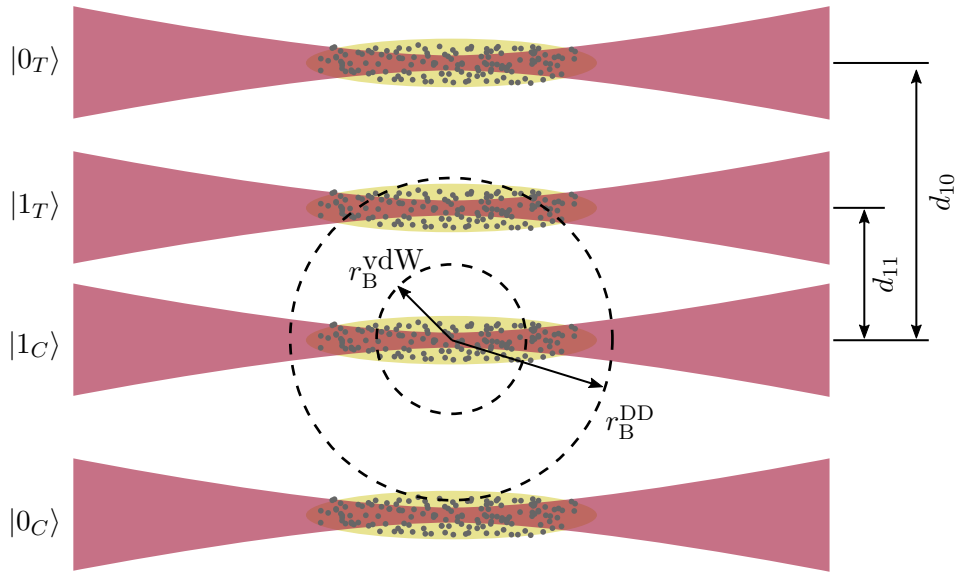

Figure 8.2.: Photonic phase-gate proposal. Adapted from [61]. Two photonic qubits (control C and target T) are stored as collective excitations at different positions depending on their state. Possible positions are separated by $d_{10} \gg r_B^{DD} > d_{11} > r_B^{vdW}$. A microwave field is applied to drive excitations through a 2π rotation from $nS_{1/2}$ to $n'P_j$ and back. If both the control and target qubits are in their $|1\rangle$ locations, resonant dipole-dipole interactions prevent the rotation, and no phase shift results. If one or both qubits are not in their $|1\rangle$ locations, the dipolar interactions are too weak to prevent the rotation and a π phase shift results. Adapted from [61] courtesy of D. Paredes-Barato

microwave field drives a transition to an opposite-polarity state, the resulting resonant dipole-dipole interaction strength is strong enough to result in rapid dephasing. The proposal is illustrated in figure 8.2.

A possible direction to take in the longer term is to consider using different atomic species. Rubidium is a convenient atom to use for several reasons: it is well understood and easy to laser cool, alongside the practical benefit of being currently in use for the experiments presented here: a great deal of appropriate equipment is already available for use. One notable disadvantage, however, is the short dephasing lifetime of collective excitations arising from the mismatch in probe and coupling wavenumbers k_c and k_p. All five alkali species (lithium, sodium, potassium, rubidium, caesium) exhibit a

similar ratio of ≈ 1.7. Considering other this parameter, the most promising candidate species would be ytterbium, which offers an excitation pathway with a probe to coupling wavenumber ratio of 1.005. Several studies [258–260] suggest that the use of an alkaline-earth-like species such as ytterbium would offer the ability to work with denser ensembles before Rydberg-ground-state collisions become a problem as other groups working with rubidium have discovered [261].

A. The Incident

'Is that what we're calling it now?'

- Daredevil

The vacuum chamber was sealed, pumped down, and baked out, in June 2014. The first signal from the MOT was detected in July 2014.

Data presented in the beginning of chapter 5 was taken jointly with Hannes Busche [105] and Paul Huillery [63] in April and May of 2016. Data presented at the end of chapter 5 was taken in December 2016. Data presented in chapters 6 and 7 was taken in June and July of 2016.

At the end of August 2016, the primary 780 nm cooling laser diode (see section 4.1.2) failed, most likely due to age. Replacing this diode and rebuilding the cooling laser system took approximately 3 weeks, with the first absorption signal in the optical trap recovered at the end of September 2016. While the 780 nm laser system was under repair, atoms could not be cooled or loaded into the trap, and so the alignment of the experiment could not be maintained to compensate against the effects of thermal fluctuations and vibration.

At the beginning of October 2016, one month after the first diode failure, the diode in the master laser of the 910 nm optical dipole trap laser system also failed, probably as a result of voltage fluctuations associated with a series of power cuts.

An attempt was made to replace this master laser with a then-unused Toptica DL

Pro, although satisfactory coupling into the homebuilt tapered amplifier could not be achieved, resulting in insufficient power to produce two optical dipole traps. After two weeks, this attempt was abandoned in favour of using the recently installed M^2 SolsTiS2000 titanium sapphire laser. This laser was bought with the intention of providing a second coupling laser at 480 nm to allow for simultaneous storage in two separate $|S\rangle$ states (see appendix C). However, the extreme versatility of this class of laser, along with increasing urgency to restore functionality to the experiment, required its use as an optical trap, also at 910 nm.

Absorption in both optical traps was recovered in late October 2016, although it took until mid November to identify and solve a noise issue that overwhelmed on-resonant effects. This was eventually traced to one of the laser line filters protecting the SPCMs. The first photon storage signal since late July 2016 was recovered in the beginning of the third week of November 2016. The author's laboratory time ended at the end of December 2016.

Unfortunately, due to the prolonged period of downtime in which one or both of the optical trap absorption and photon storage signals were unavailable, the benefit of the previous two years of gradual improvement in experimental efficiency was largely lost, with less than one month in which to collect final data to be included in this thesis. Consequently, storage efficiency and signal-to-noise ratio suffered considerably compared to data taken in June and July 2016. The combination of the lack of time, and sufficient SNR resulted in at least one planned experiment being postponed indefinitely.

It is hoped that, with immediate time pressure reduced, the apparatus can be restored to the peak efficiency achieved and the previously shelved experiments, as well as many new possibilities opened by various on-going upgrades, can be carried out in the very near future.

B. DExTer

DExTer is an extensive application with numerous features not entirely obvious to the inexperienced user. Several features will be enumerated in this appendix

B.1. Time step resolution

DExTer's main logical unit is the time step. Internally, a time step is processed as a series of 64-bit words written to main computer RAM, containing:

- 1 word: header information. Step duration, type (normal or sub-μs), channels changed
- 2 words: digital channel status.
- 2 words: analogue status

Instructions are communicated to the FPGA kernel via a pair of FIFO[1] queues in host computer RAM. One FIFO contains all analogue data ('analogues'); the other contains everything else (header, digital, sub-μs) ('all bar analogues').

Each sub-μs time step is stored as a single 64-bit word, for 32 words in total, stored as the *first* elements in the all bar analogues FIFO. Thereafter, time steps are grouped in order.

When a user begins an experimental sequence via the main terminal UI, the following elements are read into local FPGA memory from the appropriate FIFOs:

1. (All bar analogues) All sub-μs data (32 words),

[1] First-in, first-out

2. (All bar analogues) Header information for the first time step (1 word),

3. (All bar analogues) Digital information for first time step (2 words),

4. (Analogues) Analogue information for first step (2 words).

On subsequent time steps, step 1 is omitted and steps $2-4$ are repeated.

Once data has been read, the kernel repeatedly determines what action to take:

1. If the next time step is flagged as the ending time step, then stop and signal to the main terminal that the sequence is finished,

2. Else if the next time step is a sub-μs sequence, then execute the sub-μs sequence already stored locally,

3. Else if the analogue channels change and the step length is greater than x, then execute both digital and analogue data,

4. Else execute digital data.

Reading words from RAM and executing them requires a finite amount of time. If this time is not compensated for, then each step is extended by the time it takes to read and execute the following step, leading to timing inaccuracy. Compensation is added by measuring the inaccuracy externally (for example, comparing the requested timing to the actual timing on an oscilloscope) and adding a processing step to the timing sequence that shortens each step by the appropriate duration. Currently, this processing is carried out in the FPGA kernel, although it could, in principle, be shifted over to the main terminal processing chain.[2] Typically, the timing delay is $32 \times 25\,\text{ns}$ clock cycles for digital-only changes, and $56 \times 25\,\text{ns}$ clock cycles for analogue changes.

Additionally, a minimum threshold time is applied to the analogue change to ensure that the channel has time to settle at that value. Currently, this is arbitrarily set at

[2]These values are integrated into the kernel software, and adjusting them requires re-compiling to bitcode. Re-compilation can affect the true value they should take, in addition to taking significant time.

2.5 μs (100 $\times$ 25 ns clock cycles). Requested analogue changes in steps shorter than this are ignored. This is a legacy limit that appears to be redundant with the above noted analogue threshold, although due to the relative unimportance of ramping analogue channels in the experiments discussed here, no effort was made to modify it.

B.1.1. Sub-microsecond sequence

The overhead involved in reading each time step is unacceptable in the sub-μs sequence. To avoid the delay, the entire sub-μs sequence (32 words) is read into local FPGA RAM prior to the beginning of synchronous execution. The necessity to fit inside local RAM leads to the various restrictions listed in section 4.3.2. As 32 steps was deemed to be considerably greater than necessary for the experiments discussed in this thesis, no further attempt has been made to adjust resource allocation to lighten any of these restrictions.

B.1.2. Ramping

Analogue channels may be ramped linearly from one value to another within a time step. In the UI this is presented as a boolean flag within the time step. If checked, the channel value will ramp to the given value over the course of the time step.

Internally, ramping is realised by dividing the step into 10^3 individual steps, and rasterising the ramp as a series of small fixed-value steps. For ramps shorter than 2.5 ms, fewer steps are used (with a minimum step length of 2.55 μs). Smoother or faster ramps require the use of an external signal generator.

B.2. Multirun parameter scanning

A sequence can be repeated indefinitely (for example, to provide continuous feedback while tuning an instrument), or a fixed number of times. Over a fixed number of times, one or more parameters can be configured to vary automatically. The length of individual time steps, or the value of analogue or asynchronous channels, or both, may be varied in this manner. Figure B.1 shows a diagram of these repetitions.

For each experimental repetition in which a parameter is changed, DExTer re-processes the entire sequence to be written to main computer RAM. This additional processing time can represent a non-trivial increase to the total time required for an entire experimental execution.

Experimental repetitions are controlled by five parameters set by the user. These are:

- Sub-μs repeats. These are covered in section 4.3.2.
- Multirun steps. These allow one or more numeric parameters to be changed in subsequent experimental repeats.
- Quick repetitions. These immediately repeat the experimental sequence without changing any parameters, avoiding the need to re-process the entire experimental sequence.
- Full scans. These repeat the entire multirun scan, requiring the sequence to be re-processed
- Repetition order.

The total number of repeats of the experimental sequence is given by $N_{\text{multirun}} \times N_{\text{quick}} \times N_{\text{full}}$. Consider an experimental sequence in which a parameter is scanned over 4 values, `a, b, c, d`. 2 quick repetitions and 3 full scans are set. The `default` repetition order varies the multirun parameter from first to last in order, giving:

```
aa bb cc dd aa bb cc dd aa bb cc dd
```

The `reverse` repetition order varies from last to first, producing:

```
dd cc bb aa dd cc bb aa dd cc bb aa
```

The `alternating` repetition order alternates first-to-last, last-to-first:

```
aa bb cc dd dd cc bb aa aa bb cc dd
```

Finally, the `random` repetition ordering will give an entirely random order. Quick repetitions will still be grouped together, but full repetitions may now be interleaved together. For example:

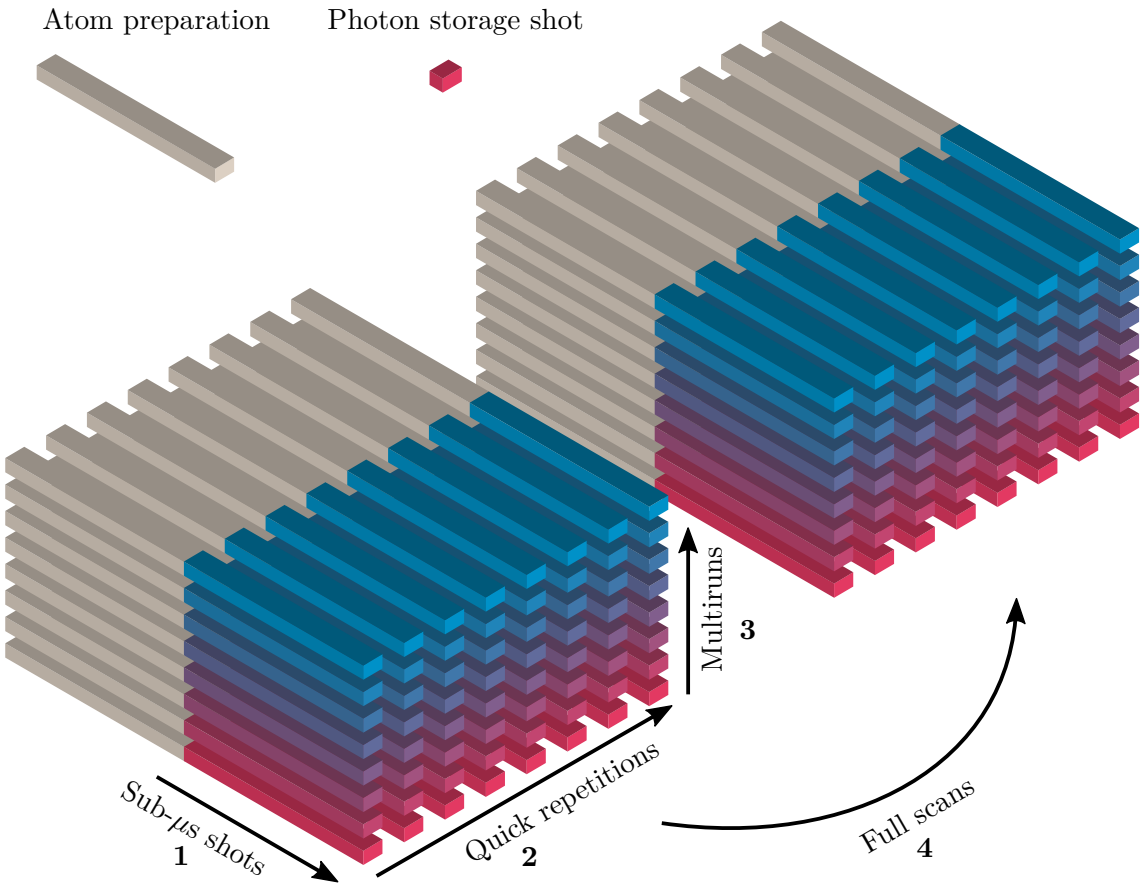

Figure B.1.: DExTer's experimental repetitions. This figure shows the pattern followed if the Repetition Order is the default one. The first `Multirun Step` value is repeated `Quick Repetitions` number of times, followed by the second `Multirun Step` value. After the entire `Multirun Step` range has been carried out, it is repeated in its entirety `Full Scans` number of times.

`cc aa bb bb cc dd aa dd aa bb dd cc`

In all cases, the order is stored in a logfile produced and saved at the end of an experimental execution.

B.3. Photon counting

Each data event (discussed in section 4.3.4) is written to a third FIFO as a 64-bit word. The format of the word is as follows: `TTTT TTTT TTTT`$\cdots$`TTTT 0Aa0 0Bb0 0Cc0 0DdR` where:

- `T` is a bit of time information (48 bits in total),
- `0` is (always) null,
- A is the output status of SPCM A (i.e. photon (1) or no photon (0)),
- a is the gate status of SPCM A (i.e. on (1) or off (0)),
- R is the status of the reference channel.

The component of the main terminal that communicates with the FPGA via main computer RAM also monitors the FIFO into which data is written while the sequence is in progress. 64 bit words are read from the data FIFO and reformatted as strings of 16-digits of hexadecimal (base 16). The reformatted strings are passed to another process, via a queue, which write them to disk. The main terminal does not permit the sequence to be terminated (other than via intrusive interference such as an operating system kill command) until the data FIFO and the queue into which strings are passed have been emptied.

A single digit of hexadecimal encodes 4 bits, rendering the 64-bit word more comprehensible to a human. Consider the example data string `000136C781FE4607`. The first 12 digits are the clock cycle number in which the event occurred. `000136C781FE` $\approx 5.2 \times 10^9$ clock cycles, for a time of $\approx 26.070\,\mathrm{s}$. However, the clock cycle counts are only stored as hexadecimal for convenience, rather than comprehensibility.

The final four digit SPCM status is more easily interpreted: `4607` gives:

- SPCM 1 has a value of 4, corresponding to gate on, nothing detected,
- SPCM 2 has a value of 6, corresponding to gate on, and a photon detected,
- SPCM 3 has a value of 0, corresponding to being gated off,
- SPCM 4 is the only channel that can have an odd value. If the value is odd, then the reference channel has been switched on. Therefore, the value 7 indicates that the reference channel is on, the gate is on, and the SPCM detected a photon.

A value of 2 is in principle possible, corresponding to gate off but photon detected - this indicates that the SPCM is incorrectly connected.

Every time that the sequence repeats - at the beginning of a new quick repetition, full scan, or multirun step - the clock counter is reset to zero.

B.4. Memory performance

A memory leak has been identified, associated with the photon counting module of DExTer. It originates in incorrect garbage collection within LabView associated with the queue opened to pass hexadecimal strings to the the software component for writing data to non-volatile storage. No solution has been found as of time of writing.

As a consequence of the memory leak, re-processing the experimental sequence gradually slows down, leading to an eventual crash when the 32-bit LabView process exceeds its addressable memory. The rate of degradation can be slowed by minimising the use of full scans and multirun scans in favour of quick repetitions, where possible. Full performance can be recovered by restarting the host computer.

C. Two photon microwave transitions

All microwave excitation experiments shown in chapters 6 and 7 concern a transition between states of opposite parity by the absorption of a single microwave photon. Experiments can be considered in which two identical microwave photons are absorbed to transfer between Rydberg states of identical parity, which are not accessible via the absorption of a single photon [130].

Such experiments differ qualitatively from the discussion of EIT in chapter 3. In the former discussion, transitions from the ground to the Rydberg state were achieved by the use of two distinct photons, each resonant with an atomic transition to an intermediate level $|2\rangle$.

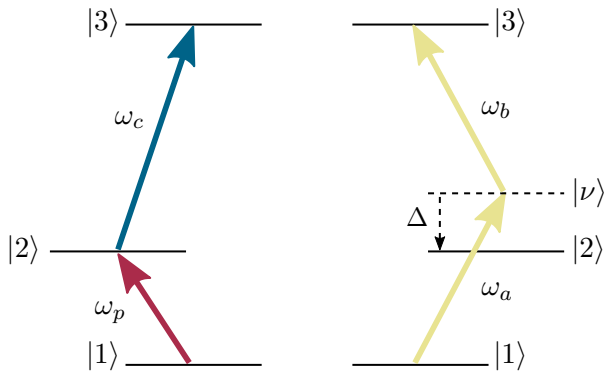

Figure C.1.: Two photon absorption. *Left*: EIT using non-identical photons ω_p and ω_c via a real atomic state. *Right*: Two photon absorption using identical photons $\omega_a = \omega_b$ via a virtual state.

Since only one microwave source was available for use in this experiment,[1] a different approach must be considered, as it is unlikely that an atomic state exists at *exactly* half of the energy difference between the beginning and end states. The process can instead

be described as using a 'virtual' state $|\nu\rangle$, that *is* exactly halfway between the beginning and final states. The first photon causes a transition from $|1\rangle \rightarrow |\nu\rangle$, while the second photon causes the transition $|\nu\rangle \rightarrow |3\rangle$ (see figure C.1).

C.1. Two-photon absorption

Following the approach outlined by W. Ketterle in [262], we present a general theoretical outline to two-photon absorption. The medium is illuminated by an electric field of the form

$$\boldsymbol{\mathcal{E}} = \mathcal{E}_a \boldsymbol{e}_a \cos(\omega_a t) + \mathcal{E}_b \boldsymbol{e}_b \cos(\omega_b t), \tag{C.1}$$

where ω_a and ω_b are not necessarily equal.

The Hamiltonian is of the form $\mathcal{H} = -\boldsymbol{\mathcal{E}} \cdot \boldsymbol{d}$. Combined with equation C.1, this gives

$$\mathcal{H} = -\frac{1}{2}\left(e^{i\omega_a t} + e^{-i\omega_a t}\right)\mathcal{E}_a \boldsymbol{e}_a \cdot \boldsymbol{d} - \frac{1}{2}\left(e^{i\omega_b t} + e^{-i\omega_b t}\right)\mathcal{E}_b \boldsymbol{e}_b \cdot \boldsymbol{d}. \tag{C.2}$$

We define

$$\mathcal{H}_{\nu 1,a} = -\mathcal{E}_a \langle \nu | \, \boldsymbol{e}_a \cdot \boldsymbol{d} \, | 1 \rangle, \qquad \mathcal{H}_{\nu 1,b} = -\mathcal{E}_b \langle \nu | \, \boldsymbol{e}_b \cdot \boldsymbol{d} \, | 1 \rangle, \tag{C.3}$$

The matrix element $\langle \nu | \, \mathcal{H} \, | 1 \rangle$ is:

$$\mathcal{H}_{\nu 1} = \frac{\mathcal{H}_{\nu 1,a}}{2} e^{-i\omega_a t} + \frac{\mathcal{H}_{\nu 1,b}}{2} e^{-i\omega_b t}, \tag{C.4}$$

where the counter-rotating terms have been dropped for simplicity.

The solution for the probability amplitude of existing in $|\nu\rangle$ is given by [262]

$$a_\nu = \frac{1}{2\hbar}\left[\frac{\mathcal{H}_{\nu 1,a}\left(e^{-i(\omega_a - \omega_{\nu 1})} - 1\right)}{\omega_a - \omega_{\nu 1}} + \frac{\mathcal{H}_{\nu 1,b}\left(e^{-i(\omega_b - \omega_{\nu 1})} - 1\right)}{\omega_b - \omega_{\nu 1}}\right]. \tag{C.5}$$

The solution for the probability amplitude of existing in the final state $|3\rangle$ is found from

$$i\hbar \dot{a}_3 = \sum_k \mathcal{H}_{3k} a_k e^{i\omega_{3k} t}. \tag{C.6}$$

[1] A second microwave source (Agilent E8257D PSG, see appendix D) became available near the end of the work presented here, but was not experimentally integrated in time for use.

The contribution to the sum due to state ν is

$$a_3 = \frac{1}{i\hbar}\int_0^t \langle 3|\,\mathcal{H}\,|\nu\rangle\, e^{(i\omega_{3\nu}t')}\mathrm{d}t'. \tag{C.7}$$

Using

$$\mathcal{H}_{3\nu,a} = -\mathcal{E}_a\,\langle 3|\,\boldsymbol{e}_a\cdot\boldsymbol{d}\,|\nu\rangle\,, \qquad \mathcal{H}_{3\nu,b} = -\mathcal{E}_b\,\langle 3|\,\boldsymbol{e}_b\cdot\boldsymbol{d}\,|\nu\rangle\,, \tag{C.8}$$

$$\langle 3|\,\mathcal{H}\,|\nu\rangle = \frac{\mathcal{H}_{3\nu,a}}{2}e^{-i\omega_a t} + \frac{\mathcal{H}_{3\nu,b}}{2}e^{-i\omega_b t}. \tag{C.9}$$

Substituting equation C.9 into equation C.7, we get

$$a_3 = \frac{1}{4\hbar^2}\sum_\nu\Bigg[\frac{\mathcal{H}_{3\nu,a}\mathcal{H}_{\nu1,a}}{\omega_a-\omega_{\nu1}}\frac{e^{i(\omega_{31}-2\omega_a)t}-1}{\omega_{31}-2\omega_a} + \frac{\mathcal{H}_{3\nu,b}\mathcal{H}_{\nu1,b}}{\omega_b-\omega_{\nu1}}\frac{e^{i(\omega_{31}-2\omega_b)t}-1}{\omega_{31}-2\omega_b} + \frac{\mathcal{H}_{3\nu,b}\mathcal{H}_{\nu1,a}}{\omega_a-\omega_{\nu1}}\frac{e^{i(\omega_{31}-\omega_a-\omega_b)t}-1}{\omega_{31}-\omega_a-\omega_b} + \frac{\mathcal{H}_{3\nu,a}\mathcal{H}_{\nu1,b}}{\omega_b-\omega_{\nu1}}\frac{e^{i(\omega_{31}-\omega_a-\omega_b)t}-1}{\omega_{31}-\omega_a-\omega_b}\Bigg]. \tag{C.10}$$

The first two terms involve absorbing two photons from the same source, while the final two terms involved absorbing one photon from each source. When the two sources a and b are of different frequencies ($\omega_a \neq \omega_b$), the first two terms are far from resonance and may often be neglected (such as in the case of the ladder EIT scheme used to store photons in this thesis). In the proposed two-photon microwave transition, the two sources are identical (originating from the same microwave signal generator), and all four terms contribute.

C.2. Energy levels in the Rydberg manifold

Figure C.2 illustrates part of the local Rydberg manifold around the principal Rydberg state used for photon storage in this thesis ($80S_{1/2}$). Only lower energy levels are shown, but higher energy levels are qualitatively symmetric.

Two two-photon transition pathways are depicted, to $n-1$ and $n-2$ S states respectively. In the case of an $n-1$ transition to $79S_{1/2}$, the intermediate virtual level is extremely close to both $79P_J$ states (detuned by 82.7 MHz and 278 MHz respectively). In the case of an $n-2$ transition to $78S_{1/2}$, the intermediate virtual level is far detuned by (7.5 ± 0.2) GHz from all four intermediate P states ($79P_{1/2}$, $79P_{3/2}$, $78P_{1/2}$ and $78P_{3/2}$).

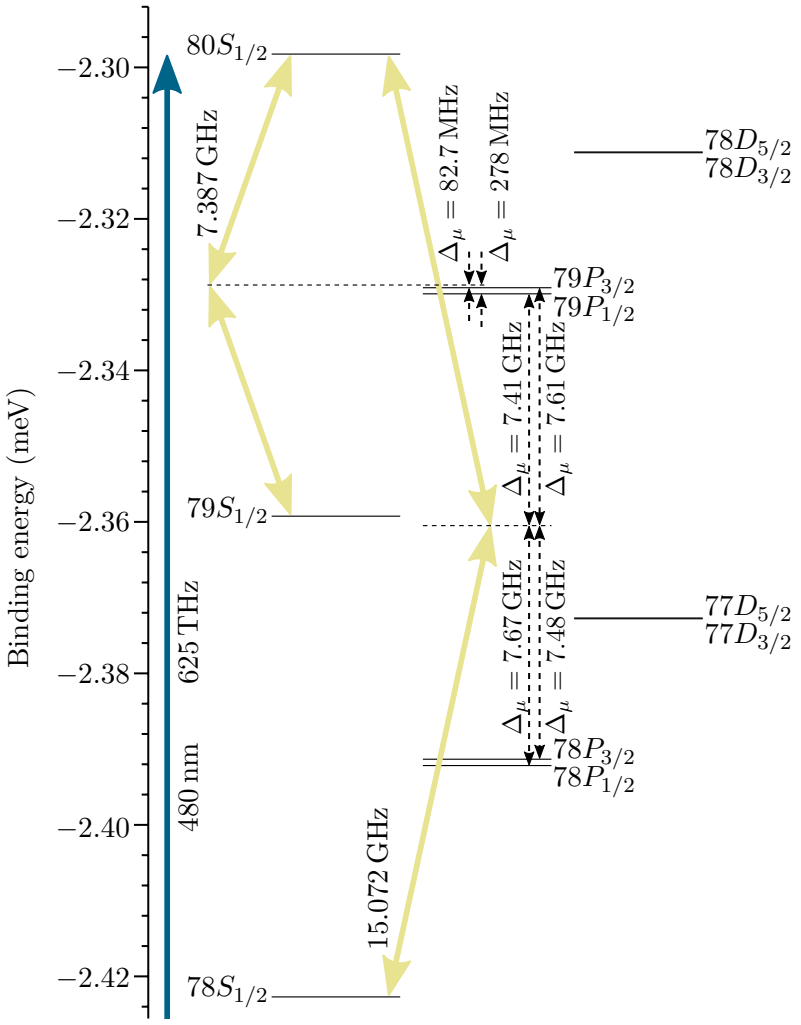

Figure C.2.: Symmetrical two photon microwave transitions from $80S_{1/2}$. Transitions are shown only to lower n states, but the approach is broadly symmetrical.

C.3. Two-photon spectroscopy

The pathway to $(n-1)S$ is not far detuned from the intermediate state $79P_{3/2}$, and is consequently not a promising candidate. An initial search was made for the $(n-2)S$ transition, with a predicted frequency of $\omega_{\text{pred}} = 15.072 \times 2\pi\,\text{GHz}$. The results are shown in figure C.3. A 450 ns microwave pulse was used, yielding a narrower but deeper feature. In order to provide maximum possible microwave intensity, all attenuators and the coaxial isolator were removed from the microwave pathway, and the microwave generator was set to a high power output in order to generate a visible signal. Whereas the data shown in figure 7.12 (d) used a microwave power of $38\,\text{mV}_{\text{rms}}$;[2] here a power of $1600\,\text{mV}_{\text{rms}}$ was set.[3]

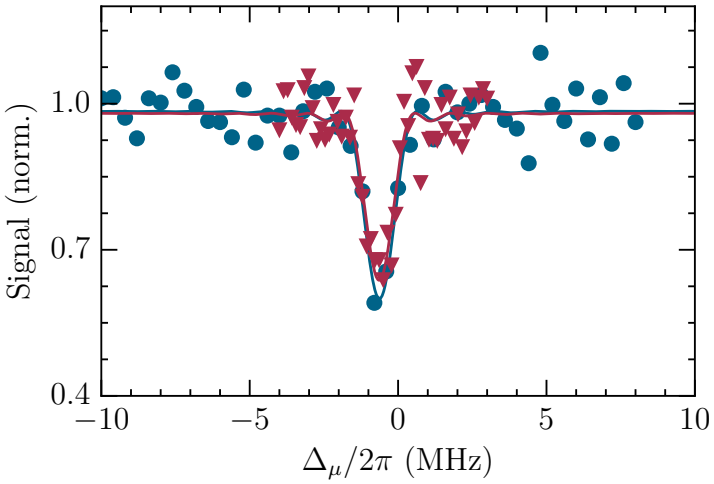

Figure C.3.: Two-photon spectroscopy of the transition $80S_{1/2} \rightarrow 78S_{1/2}$. Coarse and fine resolution microwave frequency scans are shown in blue circles and red triangles respectively. The two photon absorption feature is found at $\Delta_\mu = \omega_\mu - \omega_{\text{pred}} < 1 \times 2\pi\,\text{MHz}$. Solid lines are a fit to equation 6.1 with a microwave pulse duration of $a_1 = t_\mu = 450\,\text{ns}$.

[2] Up to $1200\,\text{mV}_{\text{rms}}$ signal generator set point plus $\approx 30\,\text{dB}$ of additional attenuation.

[3] The exact maximum power at 15 GHz is unknown and may be lower than $1600\,\text{mV}_{\text{rms}}$. The known maximum powers were later found to be $1650\,\text{mV}_{\text{rms}}$ at 7.7 GHz and $1180\,\text{mV}_{\text{rms}}$ at 19.0 GHz.

The feature was identified substantially closer to the predicted value ($\Delta < 1 \times 2\pi$ MHz) than was the case for the $nS_{1/2} \rightarrow nP_{1/2}$ transitions considered in chapters 6 and 7 (see for example figure 6.4). The inaccuacy found previously was theorised to arise from stray electric fields that were not sufficiently compensated. Since the transition here is between two similar states (with the same angular momentum quantum number), it is likely that they experience extremely similar energy shifts as a result of any stray electric field, leading to an extremely small *differential* shift.

However, due to the large detuning from the intermediate states ($79P_{1/2}$, $79P_{3/2}$, $78P_{1/2}$ and $78P_{3/2}$), the Rabi frequency that can be achieved is sharply limited. Achieving higher Rabi frequencies would either require a microwave amplifier; or a second microwave signal generator. The use of a second generator at a second frequency would permit the detuning to be tailored to achieve the desired two-photon Rabi frequency.

Even so, the time requirements make it probable that TDM creation of collective Rydberg excitations in different $nS_{1/2}$ states is prohibitive. A preferable technique would be the use of a second coupling laser resonant with a second Rydberg state. A titanium-sapphire laser was recently installed for this purpose, but due to the failure of the optical trap laser diode (see appendix A), was not available for this purpose.

D. Working with microwaves: a guide for quantum opticians

The optical techniques described throughout this thesis are all relatively well understood in the quantum optics community. Although the experiment itself is unique, and some methods - such as optical read-out of Rydberg states - are unusual, every individual element of the experiment is comprehensible to a student of similar experience - for instance, working on another cold atomic experiment.

The exception to this principle, in the author's opinion, is the use of, and techniques required, for employing microwaves. This tends to require knowledge of electronic engineering, and frequency effects in areas not usually relevant to optical experiments. Consequently, this appendix has been written to cover some of the more 'exotic' - or obscure - facts and techniques involved.

D.1. Skin depth

Current density flowing through a uniform conductor can naively assumed to be spread uniformly throughout. In the case of a direct current - i.e., time invariant - in a cylindrical conductor, this is correct. However, this pattern is complicated either in more complex geometries, and crucially, in the case of alternating - i.e., time variant - currents. Here, we consider the simple geometry of a cylindrical conductor - a wire, or cable - carrying a high or very high frequency current.

A current flowing through a conductor under the influence of a driving electric field induces a magnetic field around the conductor. An alternating current results in an

alternating induced magnetic field. This induced magnetic field in turns induces secondary alternating currents. From Lenz's law, we know that these induced currents in turn induce a secondary magnetic flux, opposite in polarity to the original magnetic field producing the secondary currents. consequently, the total magnetic flux is reduced. The magnitude of this reduction depends on the nature of the conductor - its conductivity (affecting the induced currents) and its permeability (affecting the secondary indcued magnetic flux).

Consider the interface between a conductor and a non-conductor. The conductor has a conductivity of σ and a permeability of μ, and carries a sinusoidal current with angular frequency ω. Further assume that the current density vector is parallel to the surface and travelling in the z direction, such that $\boldsymbol{J} = J_z \boldsymbol{u}_z$ depending only on y, the distance from the interface. Following the proof in chapter 20 of [263], we can derive the form of the skin effect.

Starting from the differential form of Maxwell's equations, and assuming that the medium is a good conductor, we neglect the displacement of current density:

$$\nabla \times \boldsymbol{E} = -j\omega \boldsymbol{B}, \tag{D.1}$$

$$\nabla \times \boldsymbol{H} = \boldsymbol{J}. \tag{D.2}$$

Since $\boldsymbol{E} = \boldsymbol{J}/\sigma$ and $\boldsymbol{H} = \boldsymbol{B}/\mu$, these become:

$$\nabla \times \boldsymbol{J} = -j\omega\sigma \boldsymbol{B}, \tag{D.3}$$

$$\nabla \times \boldsymbol{B} = \mu \boldsymbol{J}. \tag{D.4}$$

We started with the assumption that the current density vector only had a z component, dependent on y. From symmetry and the Biot-Savart law, the $\boldsymbol{B}$ vector therefore only has an x component. We can therefore move from the curl operator to (ordinary) derivatives in y, as follows:

$$\frac{dJ_z}{dy} = -j\omega\sigma B_x, \tag{D.5}$$

$$-\frac{dB_x}{dy} = \mu J_z. \tag{D.6}$$

We can eliminate B_z from these equations to obtain

$$\frac{d^2 J_z}{dy^2} = j\omega\sigma\mu J_z, \tag{D.7}$$

which can be solved by the solution $J_z(y) = J_1 e^{Ky} + J_2 e^{-Kr}$, where K is given by

$$K = \sqrt{j\omega\sigma\mu} = (1+j)\sqrt{\frac{\omega\sigma\mu}{2}} = (1+j)k \tag{D.8}$$

Finally, we apply boundary conditions to find these constants. Assume that at $y = 0$ (at the interface between conductive and non conductive medium), the current density is $J_z(0)$. As $y \to \infty$, the current density will increase indefinitely unless $J_1 = 0$. Therefore, we get

$$J_z(y) = J_z(0) e^{-ky} e^{-jky}. \tag{D.9}$$

The current density vector decreases exponentially with increasing distance from the interface (i.e. depth into the conductor). We can define the distance at which the amplitude of the vector has decreased to $1/e$ of the surface value as

$$\delta = 1/k = \sqrt{\frac{2}{\omega\sigma\mu}}, \tag{D.10}$$

which is known as the *skin depth*.

To illustrate the effects of frequency, table D.1 presents the skin depths of several materials at frequencies between 1 Hz and 65 GHz (the highest frequency of the microwave synthesiser used in this thesis). Gold ($\sigma = 44 \times 10^6\,\mathrm{S\,m^{-1}}$, $\mu = \mu_0$), copper ($\sigma = 59 \times 10^6\,\mathrm{S\,m^{-1}}$, $\mu = \mu_0$), iron ($\sigma = 10^7\,\mathrm{S\,m^{-1}}$, $\mu = 1000\mu_0$), seawater ($\sigma = 4\,\mathrm{S\,m^{-1}}$, $\mu = \mu_0$), and wet soil ($\sigma = 0.01\,\mathrm{S\,m^{-1}}$, $\mu = \mu_0$).

At microwave frequencies (officially $\mathrm{f} = 0.3 - 300\,\mathrm{GHz}$ [150], but for the purposes of this thesis, approximately $\mathrm{f} = 5 - 40\,\mathrm{GHz}$), excellent conductors such as copper, gold, silver and aluminium have skin depths of around $1 - 0.1\,\mu\mathrm{m}$. This results in a very small effective conductor cross section, and consequently high resistive losses. The principle effect is that microwave-capable components require specialised and highly precise manufacturing techniques, with consequent high costs. In the laboratory, the most important consequence to be aware of is the specialised and delicate coaxial connectors used to connect microwave components with a minimum of loss.

Material	f= 1 Hz	f= 50 Hz	f= 1 kHz	f= 1 MHz	f= 1 GHz	f= 65 GHz
Gold	75.7 mm	10.71 mm	2.40 mm	75.7 μm	2.40 μm	0.30 μm
Copper	65.8 mm	9.31 mm	2.08 mm	65.8 μm	2.08 μm	0.26 μm
Iron	1.59 mm	0.23 mm	50.3 μm	1.59 μm	50.3 nm	6.24 nm
Seawater	252 m	35.6 m	7.96 m	252 mm	7.96 mm	0.99 mm
Wet soil	5 km	712 m	159 m	5.04 m	159 mm	19.7 mm

Table D.1.: Skin depths δ for a range of materials and frequencies. 63% of the current is conducted within δ of the conductor surface, and 95% within 3δ. Materials such as wet soil, that have an exceptionally low conductivity have a drastically reduced skin depth effect, while materials with high permeability, such as iron, experience a much stronger effect.

D.2. Microwave connectors

At lower frequencies, a variety of coaxial connectors are used in typical laboratory and industrial settings. The BNC[1] socket is common on all equipment for frequencies below 1 GHz, with the 3.5 mm SMA[2] is common for analogue radio frequencies (50 MHz – 4 GHz). N-type is used for radio frequencies at higher power than SMA.

A number of similar connectors have been developed based on the 3.5 mm SMA standard, for different frequency ranges. We use several of these SMA-style connectors in the laboratory, and care must be taken to identify which one is which. Attempting to connect two superficially similar but different connectors will damage them, leading to dramatically higher losses in that connection.

- Precision 3.5 mm SMA (DC−26.5 GHz): this is nominally the same as a typical 3.5 mm SMA connector. However, it is manufactured to significantly higher tolerances. These are mostly indistinguishable from typical 3.5 mm SMA connectors.
- 2.92 mm SMK (DC−40 GHz): the male pin is shorter and narrower than 3.5 mm

[1] Bayonet Neill-Concelmann
[2] SubMiniture version A

SMA connectors. A 2.92 mm male connector **should not** be used with female 3.5 mm connectors. 2.92 mm female connectors **MUST not** be used with any other type of SMA-style connector. This is the commonest RF connector used in the experiment described in this thesis.

- 1.85 mm SMV (DC−67.5 GHz): the male pin is again shorter and narrower. Again, the male connector **should not** be used with any other type of connector. The female **MUST not** be used with any other type.

D.3. Microwave equipment

In this thesis, two microwave synthesisers were used:

- Anristu MG6936A source capable of producing signals between 2 GHz and 65 GHz, nominally at powers between 10 μW (−20 dBm) and 100 mW (+20 dBm). 1.85 mm SMV
- Agilent E8257D PSG capable of 250 kHz − 20 GHz nominally between 0.1 fW (−130 dBm) and 25 mW (+14 dBm). Precision 3.5 mm SMA

Nominal power ranges are given. Practical maximum power falls off dramatically towards both ends of the frequency scale. Exact maximum power for a given frequency can either be measured using an RF power meter, or determined experimentally using the techniques shown in chapter 6.

Virtually all microwave equipment and electronics used in this experiment has a direct or close equivalent used in the optical laser systems. Considerations taken into account in the design and implementation of these systems translates over very well to the implementation of microwave excitation.

Key components that might not otherwise be considered in the context of electronics are listed below:

- Isolator/circulator: this is identical in purpose and working to the optical isolator: it acts to prevent signals from being reflected back into the source by means of Faraday rotation of polarisation.

- Directional coupler: this is analogous to an optical beam sampler. A directional coupler is a 4-port device which is intended to split off a fraction of the signal traversing the device in one direction only (hence the name). In addition to an input and output port for the primary signal, there is a coupled port (into which a fraction of the signal travelling from the input to the output is coupled); and an isolated port. This is typically terminated with an absorptive load. Signal travelling *from* the *output* to the *input* is coupled into this fourth, isolated port, and only extremely weakly into the third. These devices are typically connected to a signal or network analyser for measurement and monitoring.

Care must be taken to identify the frequency compatibility of different components. Just as in optics, some components may be broadband, while others may be much narrower. In this experiment, broad-band components (typically DC-40 GHz) were preferred where possible, to encompass the entire frequency range in user. However, performance, cost, and availability constraints resulted in a range of narrow-band components in places.

Even within a specified frequency range, performance should be verified whenever possible. Microwave attenuators, just as with optical 'neutral' density filters, must be assumed to have at least a weak frequency dependence.

D.4. Microwave bands

Outside of academic physics, the radio and microwave frequency spectrum tend to be referred to by arbitrary names of bandwidths, rather than by frequency or by wavelength. This means that identifying appropriate equipment can be complicated where it is labelled only by band, and not more specifically. The following tables will give the conversions between frequency and several common groups of band names.

Further complications arise as different organisations use the same designators, but to refer to different frequency ranges. Where an instrument or piece of equipment is defined by a band designation, it is important to identify to what standard or institutional definition the designation refers.

Band	Frequency (GHz)
VHF	0.03 - 0.3
UHF	0.3 - 1
L	1 - 2
S	2 - 4
C	4 - 8
X	8 - 12
Ku	12 - 18
K	18 - 27
Ka	27 - 40
V	40 - 75
W	75 - 110
mm	110 - 300

Table D.2.: IEEE radar frequency bands as amended [264]. In some cases, the mm band (millimetric, meaning millimetre wavelengths) is used to refer to the entire range from $30 - 300\,\mathrm{GHz}$. Note that the K and V bands respectively give rise to the naming of the SMK and SMV[3] connectors that are used for those wavelength ranges.

D.5. Sources of microwave noise

Optical experiments are typically able to operate in very low nose environments. External sources of light - such as the sun, laboratory lighting and status LEDs on instruments - may be blocked easily by simple barriers (such as blinds and insulating tape), or filtered (spatially by apertures and fibres, or spectrally by interference or bandpass filters). Thermal noise may be minimised by cooling, and electrical noise by means of more elaborate galvanic isolation schemes.

Microwave and radio frequency noise is harder to block, since optical barriers - such as doors, walls and floors - are generally transparent to these frequencies. There are also many more sources of such noise - such as laboratory and consumer electronics; wireless networking; mobile phone signals; amateur radio; thermal background; etc. In the

Band	Frequency (GHz)	EIA Designation (US)	RCSC Designation (UK)
R	1.7 - 2.6	WR430 /RG104	WG8
D	2.2-3.3	WR340	WG9A
S	2.6 - 3.95	WR284 /RG48	WG10
E	3.3 - 4.9	WR229	WG11A
G	3.95 - 5.85	WR187 /RG49	WG12
F	4.9 - 7.05	WR159	WG13
C	5.85 - 8.2	WR137 /RG50	WG14
H	7.05 - 10.1	WR112 /RG51	WG15
X	8.2 - 12.4	WR90 /RG52	WG16
Ku	12.4 - 18.0	WR62 /RG91	WG18
K	15.0 - 26.5	WR42 /RG53	WG20
Ka	26.5 - 40.0	WR28 /RG96	WG22
Q	33.0 - 50.0	WR22 /RG97	WG23
U	40.0 - 60.0	WR19	WG24
V	50.0 - 75.0	WR15 /RG98	WG25
W	75.0 - 110.0	WR15 /RG99	WG26

Table D.3.: Waveguide frequency bands as defined by the Electronic Industries Alliance (EIA), and equivalent Radio Components Standardisation Committee (RCSC) in the US and UK respectively

United Kingdom, the Office of Communications (Ofcom) is the governmental regulator responsible for licensing use of the radio spectrum, in co-operation with the Ministry of Defence (which licenses bands for military use) and international co-ordination organisations.

Ofcom maintain an information sheet detailing the current state of spectrum licensing in the United Kingdom at [205]. This covers the entire radio frequency spectrum from 9 kHz to 105 GHz.

Of primary interest to us is the range approximately 3 GHz - 40 GHz. This is limited at

Latest system		Alternative system	
Band	Frequency (GHz)	Band	Frequency (GHz)
D	1.0 - 2.0	L	0.39 - 1.55
E	2.0 - 3.0	S	1.55 - 3.9
F	3.0 - 4.0	C	3.9 - 6.2
G	4.0 - 6.0	X	6.2 - 10.9
H	6.0 - 8.0	K	10.9 - 36.0
I	8.0 - 10.0	Ku	10.9 - 20.0
J	10.0 - 20.0	Ka	20.0 - 36.0
K	20.0 - 40.0	Q	36.0 - 46.0
L	40.0 - 60.0	V	46.0 - 56.0
M	60.0 - 100.0	W	56.0 - 100.0

Table D.4.: NATO radio frequency band designations (subset) [265]. Deprecated for civilian use since 1992, but included for completeness and potential identification of legacy high frequency equipment

the high frequency end (n=46 for $nS_{1/2} \leftrightarrow nP_{3/2}$) by the frequency range of our chamber antennae feedthroughs; and at the low end by Rydberg states to which we can stably lock a coupling laser (n$\approx$ 100). Within that range, the greatest source of noise is IEEE 802.11n/ac [266] ('WiFi'). In Europe, the 5 GHz WiFi band is specified by European Standard EN 300 328 V1.8.1 (from January 2015) [267].

5 GHz WiFi

The 5 GHz WiFi band specifies a number of channels (of widths of 20, 80, or 160 MHz) between (in Europe) $5.15 - 5.725$ GHz. Devices compatible with the IEEE 802.11n/ac standards may attempt to broadcast beyond this range, due to slightly different bands in use in Japan and the United States. The specification is given in [266].

Initial measurements of the 5 GHz spectrum within the laboratory were made with a Oneplus A001 ('Oneplus One') smartphone, indicating noise levels of -70 - -50 dBm

centred at 5.15, 5.575 and 5.725 GHz. More detailed measurements will be made with a signal analyser if any attempt is made to perform microwave transitions below 6 GHz. For $nS_{1/2} \leftrightarrow nP_{3/2}$, this covers n=85 to n=90 inclusive. However, barring attempts to implement TCP/IP via cold atoms, this part of the spectrum would seem to be irredeemably tainted by widespread public use.

E. About this thesis

This thesis was typeset in LaTeX using the **MikTeX 2.9**[1] distribution and edited with the **TeXnicCentre** editor.[2] The thesis is laid out using the **scrbook** class of **komascript**.[3]

Figures were generated using **Inkscape 0.9.2.0**[4] and **Python 2.7**[5] relying principally on `NumPy v1.10.4-1`[6] and `SciPy v0.17.1-1`[7] for analysis and `matplotlib v1.5.1-5`[8] for graph plotting.

Property	Value
Compile date	2017/11/20
Compile time	19:09
LaTeX ver.	`3.1415926-2.3-1.40.12 (MiKTeX 2.9)`
BibTeX ver.	`BibTeX 0.99d (MiKTeX 2.9)`
Word count	$\approx 53,000$

Table E.1.: Compilation properties

[1] https://miktex.org/
[2] http://www.texniccenter.org/
[3] https://www.ctan.org/pkg/koma-script
[4] https://inkscape.org/en/
[5] https://www.python.org/download/releases/2.7/
[6] http://www.numpy.org/
[7] http://www.scipy.org/
[8] http://www.matplotlib.org/

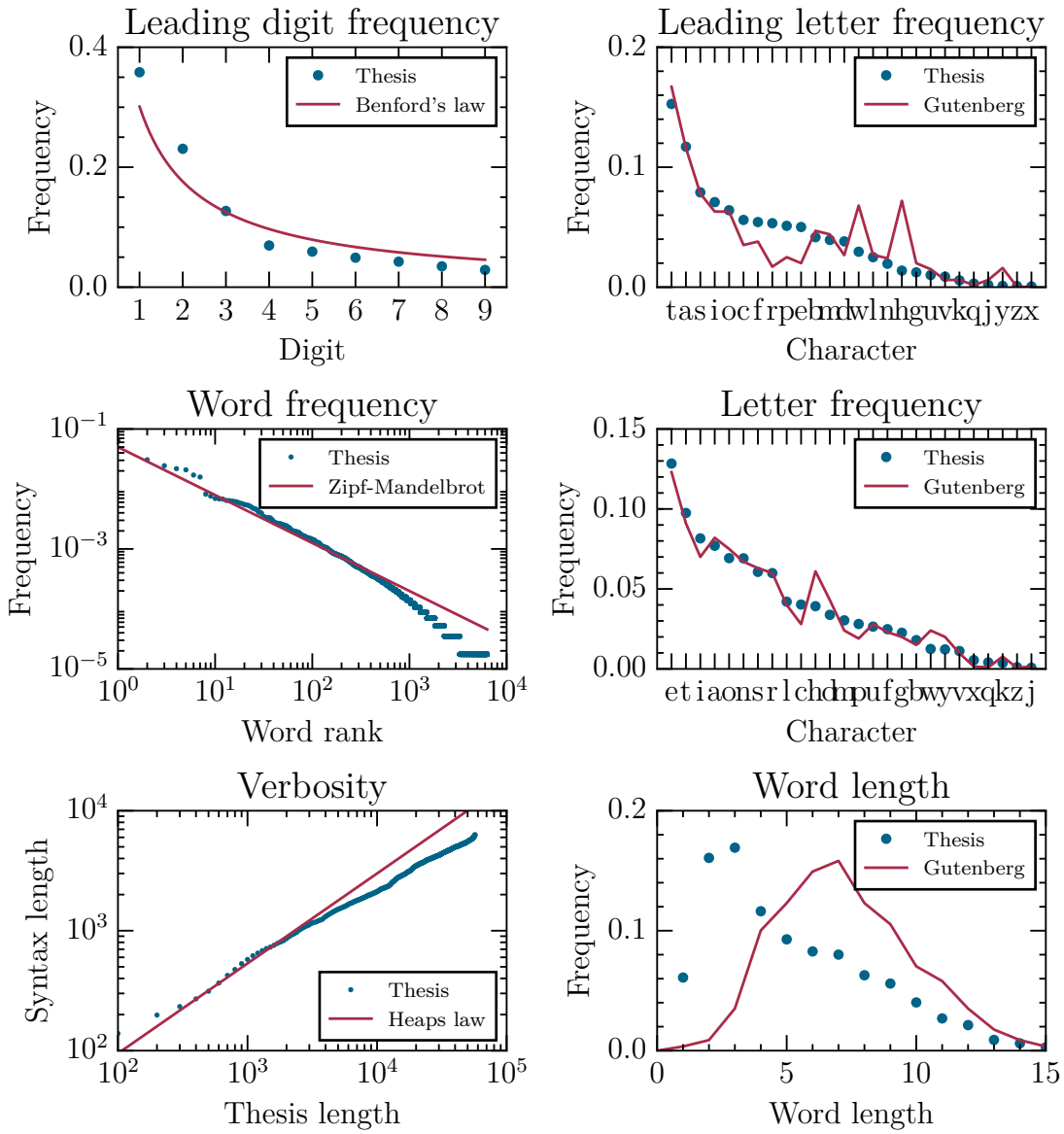

Figure E.1.: Linguistic statistics of this thesis. Benford's law and Gutenberg distributions from [268]. Zipf-Mandelbrot and Heaps distributions from [269].

Bibliography

[1] A. L. Schawlow and C. H. Townes. "Infrared and Optical Masers", *Phys. Rev.* **112** (Dec. 1958), pp. 1940–1949. DOI: 10.1103/PhysRev.112.1940.

[2] D. Deutsch. "Quantum Theory, the Church-Turing Principle and the Universal Quantum Computer", *Proc. Math. Phys. Eng. Sci.* **400**.1818 (July 1985), pp. 97–117. DOI: 10.1098/rspa.1985.0070.

[3] M. A. Nielsen and I. L. Chuang. *Quantum Computation and Quantum Information*. Cambridge University Pr., Dec. 11, 2010. ISBN: 1107002176.

[4] W. C. Campbell et al. "Ultrafast Gates for Single Atomic Qubits", *Phys. Rev. Lett.* **105** (Aug. 2010), p. 090502. DOI: 10.1103/PhysRevLett.105.090502.

[5] M. Saffman, T. G. Walker, and K. Mølmer. "Quantum information with Rydberg atoms", *Rev. Mod. Phys.* **82** (Aug. 2010), pp. 2313–2363. DOI: 10.1103/RevModPhys.82.2313.

[6] J. Ahn. "Information Storage and Retrieval Through Quantum Phase", *Science* **287**.5452 (Jan. 2000), pp. 463–465. DOI: 10.1126/science.287.5452.463.

[7] J. M. Chow et al. "Optimized driving of superconducting artificial atoms for improved single-qubit gates", *Phys. Rev. A* **82**.4 (Oct. 2010). DOI: 10.1103/physreva.82.040305.

[8] H. Paik et al. "Observation of High Coherence in Josephson Junction Qubits Measured in a Three-Dimensional Circuit QED Architecture", *Phys. Rev. Lett.* **107**.24 (Dec. 2011). DOI: 10.1103/physrevlett.107.240501.

[9] J. J. L. Morton et al. "Solid-state quantum memory using the 31P nuclear spin", *Nature* **455**.7216 (Oct. 2008), pp. 1085–1088. DOI: 10.1038/nature07295.

[10] J. O'Brien. "Optical Quantum Computing", *Science* **318** (2007), p. 1567. DOI: 10.1126/science.1142892.

[11] K. Kao and G. Hockham. "Dielectric-fibre surface waveguides for optical frequencies", *Proc. Inst. Electr. Eng.* **113**.7 (July 1966), pp. 1151–1158. DOI: 10.1049/piee.1966.0189.

[12] D. E. Chang, V. Vuletić, and M. D. Lukin. "Quantum nonlinear optics — photon by photon", *Nat. Photonics* **8**.9 (Aug. 2014), pp. 685–694. DOI: 10.1038/nphoton.2014.192.

[13] P. A. Franken and J. F. Ward. "Optical Harmonics and Nonlinear Phenomena", *Rev. Mod. Phys.* **35**.1 (Jan. 1963), pp. 23–39. DOI: 10.1103/revmodphys.35.23.

[14] J.-M. R. Serge Haroche. *Exploring the Quantum*. Oxford University Press, Apr. 11, 2013. 616 pp. ISBN: 0199680310.

[15] M. H. Devoret and R. J. Schoelkopf. "Superconducting Circuits for Quantum Information: An Outlook", *Science* **339**.6124 (Mar. 2013), pp. 1169–1174. DOI: 10.1126/science.1231930.

[16] J. M. Raimond, M. Brune, and S. Haroche. "Manipulating quantum entanglement with atoms and photons in a cavity", *Rev. Mod. Phys.* **73**.3 (Aug. 2001), pp. 565–582. DOI: 10.1103/revmodphys.73.565.

[17] S. Haroche. "Nobel Lecture: Controlling photons in a box and exploring the quantum to classical boundary", *Rev. Mod. Phys.* **85**.3 (July 2013), pp. 1083–1102. DOI: 10.1103/revmodphys.85.1083.

[18] H. J. Kimble. "Strong Interactions of Single Atoms and Photons in Cavity QED", *Phys. Scr.* **T76**.1 (1998), p. 127. DOI: 10.1238/physica.topical.076a00127.

[19] A. Reiserer and G. Rempe. "Cavity-based quantum networks with single atoms and optical photons", *Rev. Mod. Phys.* **87**.4 (Dec. 2015), pp. 1379–1418. DOI: 10.1103/revmodphys.87.1379.

[20] W. Chen et al. "All-Optical Switch and Transistor Gated by One Stored Photon", *Science* **341**.6147 (July 2013), pp. 768–770. DOI: 10.1126/science.1238169.

[21] K. M. Beck et al. "Large conditional single-photon cross-phase modulation", *Proc. Natl. Acad. Sci.* **113**.35 (Aug. 2016), pp. 9740–9744. DOI: 10.1073/pnas.1524117113.

[22] B. Hacker et al. "A photon–photon quantum gate based on a single atom in an optical resonator", *Nature* **536**.7615 (July 2016), pp. 193–196. DOI: 10.1038/nature18592.

[23] P. Michler. "A Quantum Dot Single-Photon Turnstile Device", *Science* **290**.5500 (Dec. 2000), pp. 2282–2285. DOI: 10.1126/science.290.5500.2282.

[24] M. Pelton et al. "Efficient Source of Single Photons: A Single Quantum Dot in a Micropost Microcavity", *Phys. Rev. Lett.* **89**.23 (Nov. 2002). DOI: 10.1103/physrevlett.89.233602.

[25] T. Gallagher. *Rydberg Atoms*. Cambridge University Press, 1994.

[26] L. Béguin et al. "Direct Measurement of the van der Waals Interaction between Two Rydberg Atoms", *Phys Rev Lett* **110**.26 (June 2013). DOI: 10.1103/physrevlett.110.263201.

[27] J. D. Pritchard et al. "Cooperative Atom-Light Interaction in a Blockaded Rydberg Ensemble", *Phys. Rev. Lett.* **105** (Nov. 2010), p. 193603. DOI: 10.1103/PhysRevLett.105.193603.

[28] O Firstenberg, C. S. Adams, and S Hofferberth. "Nonlinear quantum optics mediated by Rydberg interactions", *J. Phys. B: At., Mol. Opt. Phys.* **49**.15 (June 2016), p. 152003. DOI: 10.1088/0953-4075/49/15/152003.

[29] C. Murray and T. Pohl. "Quantum and Nonlinear Optics in Strongly Interacting Atomic Ensembles", *Advances In Atomic, Molecular, and Optical Physics*. Elsevier BV, 2016, pp. 321–372. DOI: 10.1016/bs.aamop.2016.04.005.

[30] S. E. Harris, J. E. Field, and A. Imamoğlu. "Nonlinear optical processes using electromagnetically induced transparency", *Phys. Rev. Lett.* **64**.10 (Mar. 1990), pp. 1107–1110. DOI: 10.1103/physrevlett.64.1107.

[31] K.-J. Boller, A. Imamoğlu, and S. E. Harris. "Observation of electromagnetically induced transparency", *Phys. Rev. Lett.* **66** (May 1991), pp. 2593–2596. DOI: 10.1103/PhysRevLett.66.2593.

[32] M. Fleischhauer, A. Imamoğlu, and J. P. Marangos. "Electromagnetically induced transparency: Optics in coherent media", *Rev. Mod. Phys.* **77** (July 2005), pp. 633–673. DOI: 10.1103/RevModPhys.77.633.

[33] A. K. Mohapatra, T. R. Jackson, and C. S. Adams. "Coherent Optical Detection of Highly Excited Rydberg States Using Electromagnetically Induced Transparency", *Phys. Rev. Lett.* **98**.11 (Mar. 2007). DOI: 10.1103/physrevlett.98.113003.

[34] M. D. Lukin et al. "Dipole Blockade and Quantum Information Processing in Mesoscopic Atomic Ensembles", *Phys. Rev. Lett.* **87**.3 (June 2001). DOI: 10.1103/physrevlett.87.037901.

[35] K. Singer et al. "Suppression of Excitation and Spectral Broadening Induced by Interactions in a Cold Gas of Rydberg Atoms", *Phys. Rev. Lett.* **93**.16 (Oct. 2004). DOI: 10.1103/physrevlett.93.163001.

[36] D. Tong et al. "Local Blockade of Rydberg Excitation in an Ultracold Gas", *Phys. Rev. Lett.* **93**.6 (Aug. 2004). DOI: 10.1103/physrevlett.93.063001.

[37] A. Gaëtan et al. "Observation of collective excitation of two individual atoms in the Rydberg blockade regime", *Nat. Phys.* **5**.2 (Jan. 2009), pp. 115–118. DOI: 10.1038/nphys1183.

[38] E. Urban et al. "Observation of Rydberg blockade between two atoms", *Nat. Phys.* **5**.2 (Jan. 2009), pp. 110–114. DOI: 10.1038/nphys1178.

[39] D. Comparat and P. Pillet. "Dipole blockade in a cold Rydberg atomic sample [Invited]", *Journal of the Optical Society of America B* **27**.6 (June 2010), A208. DOI: 10.1364/josab.27.00a208.

[40] M. Fleischhauer and M. D. Lukin. "Dark-State Polaritons in Electromagnetically Induced Transparency", *Phys. Rev. Lett.* **84**.22 (May 2000), pp. 5094–5097. DOI: 10.1103/physrevlett.84.5094.

[41] C. Liu et al. "Observation of coherent optical information storage in an atomic medium using halted light pulses", *Nature* **409**.6819 (Jan. 2001), pp. 490–493. DOI: 10.1038/35054017.

[42] T. Peyronel et al. "Quantum nonlinear optics with single photons enabled by strongly interacting atoms", *Nature* **488**.7409 (July 2012), pp. 57–60. DOI: 10.1038/nature11361.

[43] C. S. Hofmann et al. "Sub-Poissonian Statistics of Rydberg-Interacting Dark-State Polaritons", *Phys. Rev. Lett.* **110**.20 (May 2013). DOI: 10.1103/physrevlett.110.203601.

[44] Y. Dudin and A. Kuzmich. "Strongly Interacting Rydberg Excitations of a Cold Atomic Gas", *Science* **336** (May 2012), p. 887. DOI: 10.1126/science.1217901.

[45] H. Gorniaczyk et al. "Single-Photon Transistor Mediated by Interstate Rydberg Interactions", *Phys. Rev. Lett.* **113** (July 2014), p. 053601. DOI: 10.1103/PhysRevLett.113.053601.

[46] D. Tiarks et al. "Single-Photon Transistor Using a Förster Resonance", *Phys. Rev. Lett.* **113** (July 2014), p. 053602. DOI: 10.1103/PhysRevLett.113.053602.

[47] H. Gorniaczyk et al. "Enhancement of Rydberg-mediated single-photon nonlinearities by electrically tuned Förster resonances", *Nat. Commun.* **7** (Aug. 2016), p. 12480. DOI: 10.1038/ncomms12480.

[48] L. Li, Y. O. Dudin, and A. Kuzmich. "Entanglement between light and an optical atomic excitation", *Nature* **498**.7455 (June 2013), pp. 466–469. DOI: 10.1038/nature12227.

[49] J. Honer et al. "Artificial Atoms Can Do More Than Atoms: Deterministic Single Photon Subtraction from Arbitrary Light Fields", *Phys. Rev. Lett.* **107**.9 (Aug. 2011). DOI: 10.1103/physrevlett.107.093601.

[50] C. Tresp et al. "Single-Photon Absorber Based on Strongly Interacting Rydberg Atoms", *Phys. Rev. Lett.* **117**.22 (Nov. 2016). DOI: 10.1103/physrevlett.117.223001.

[51] T. Tiecke et al. "Nanophotonic quantum phase switch with a single atom", *Nature* **508** (Apr. 2014), pp. 241–244. DOI: 10.1038/nature13188.

[52] D. Tiarks et al. "Optical π phase shift created with a single-photon pulse", *Sci. Adv.* **2**.4 (Apr. 2016), e1600036. DOI: 10.1126/sciadv.1600036.

[53] D. Maxwell et al. "Storage and Control of Optical Photons Using Rydberg Polaritons", *Phys. Rev. Lett.* **110** (Mar. 2013), p. 103001. DOI: 10.1103/PhysRevLett.110.103001.

[54] D. Maxwell et al. "Microwave control of the interaction between two optical photons", *Phys. Rev. A* **89** (Apr. 2014), p. 043827. DOI: 10.1103/PhysRevA.89.043827.

[55] L. V. Hau et al. "Light speed reduction to 17 metres per second in an ultracold atomic gas", *Nature* **397** (Feb. 1999), pp. 594–598. DOI: 10.1038/17561.

[56] J. H. Shapiro. "Single-photon Kerr nonlinearities do not help quantum computation", *Phys. Rev. A* **73**.6 (June 2006). DOI: 10.1103/physreva.73.062305.

[57] J. Gea-Banacloche. "Impossibility of large phase shifts via the giant Kerr effect with single-photon wave packets", *Phys. Rev. A* **81**.4 (Apr. 2010). DOI: 10.1103/physreva.81.043823.

[58] A. V. Gorshkov et al. "Photon-Photon Interactions via Rydberg Blockade", *Phys. Rev. Lett.* **107** (Sept. 2011), p. 133602. DOI: 10.1103/PhysRevLett.107.133602.

[59] P. Bienias et al. "Scattering resonances and bound states for strongly interacting Rydberg polaritons", *Phys. Rev. A* **90**.5 (Nov. 2014). DOI: 10.1103/physreva.90.053804.

[60] L. Isenhower et al. "Demonstration of a Neutral Atom Controlled-NOT Quantum Gate", *Phys. Rev. Lett.* **104**.1 (Jan. 2010). DOI: 10.1103/physrevlett.104.010503.

[61] D. Paredes-Barato and C. S. Adams. "All-Optical Quantum Information Processing Using Rydberg Gates", *Phys. Rev. Lett.* **112** (Jan. 2014), p. 040501. DOI: 10.1103/PhysRevLett.112.040501.

[62] M. Khazali, K. Heshami, and C. Simon. "Photon-photon gate via the interaction between two collective Rydberg excitations", *Phys. Rev. A* **91**.3 (Mar. 2015). DOI: 10.1103/physreva.91.030301.

[63] H. Busche et al. "Contactless nonlinear optics mediated by long-range Rydberg interactions", *Nat. Phys.* **13**.7 (Mar. 2017), pp. 655–658. DOI: 10.1038/nphys4058.

[64] M. Ebert et al. "Coherence and Rydberg Blockade of Atomic Ensemble Qubits", *Phys. Rev. Lett.* **115**.9 (Aug. 2015). DOI: 10.1103/physrevlett.115.093601.

[65] F. Bariani et al. "Dephasing of Multiparticle Rydberg Excitations for Fast Entanglement Generation", *Phys. Rev. Lett.* **108**.3 (Jan. 2012). DOI: 10.1103/physrevlett.108.030501.

[66] E. Distante et al. "Storage Enhanced Nonlinearities in a Cold Atomic Rydberg Ensemble", *Phys. Rev. Lett.* **117**.11 (Sept. 2016). DOI: 10.1103/physrevlett.117.113001.

[67] J. D. Thompson et al. "Symmetry-protected collisions between strongly interacting photons", *Nature* **542**.7640 (Jan. 2017), pp. 206–209. DOI: 10.1038/nature20823.

[68] J. I. Cirac et al. "Quantum State Transfer and Entanglement Distribution among Distant Nodes in a Quantum Network", *Phys. Rev. Lett.* **78**.16 (Apr. 1997), pp. 3221–3224. DOI: 10.1103/physrevlett.78.3221.

[69] Z.-L. Xiang et al. "Hybrid quantum circuits: Superconducting circuits interacting with other quantum systems", *Rev. Mod. Phys.* **85**.2 (Apr. 2013), pp. 623–653. DOI: 10.1103/revmodphys.85.623.

[70] G. Kurizki et al. "Quantum technologies with hybrid systems", *Proc. Natl. Acad. Sci.* **112**.13 (Mar. 2015), pp. 3866–3873. DOI: 10.1073/pnas.1419326112.

[71] H. J. Kimble. "The quantum internet", *Nature* **453**.7198 (June 2008), pp. 1023–1030. DOI: 10.1038/nature07127.

[72] K. Hammerer, A. S. Sørensen, and E. S. Polzik. "Quantum interface between light and atomic ensembles", *Rev. Mod. Phys.* **82** (Apr. 2010), pp. 1041–1093. DOI: 10.1103/RevModPhys.82.1041.

[73] R. J. Schoelkopf and S. M. Girvin. "Wiring up quantum systems", *Nature* **451**.7179 (Feb. 2008), pp. 664–669. DOI: 10.1038/451664a.

[74] J. Clarke and F. K. Wilhelm. "Superconducting quantum bits", *Nature* **453**.7198 (June 2008), pp. 1031–1042. DOI: 10.1038/nature07128.

[75] J. Q. You and F. Nori. "Atomic physics and quantum optics using superconducting circuits", *Nature* **474**.7353 (June 2011), pp. 589–597. DOI: 10.1038/nature10122.

[76] R. Barends et al. "Superconducting quantum circuits at the surface code threshold for fault tolerance", *Nature* **508**.7497 (Apr. 2014), pp. 500–503. DOI: 10.1038/nature13171.

[77] R. Vijay, D. H. Slichter, and I. Siddiqi. "Observation of Quantum Jumps in a Superconducting Artificial Atom", *Phys. Rev. Lett.* **106**.11 (Mar. 2011). DOI: 10.1103/physrevlett.106.110502.

[78] L. Sun et al. "Tracking photon jumps with repeated quantum non-demolition parity measurements", *Nature* **511**.7510 (July 2014), pp. 444–448. DOI: 10.1038/nature13436.

[79] C. Eichler et al. "Observation of Entanglement between Itinerant Microwave Photons and a Superconducting Qubit", *Phys. Rev. Lett.* **109** (Dec. 2012), p. 240501. DOI: 10.1103/PhysRevLett.109.240501.

[80] N. Roch et al. "Observation of Measurement-Induced Entanglement and Quantum Trajectories of Remote Superconducting Qubits", *Phys. Rev. Lett.* **112** (Apr. 2014), p. 170501. DOI: 10.1103/PhysRevLett.112.170501.

[81] Z.-L. Xiang et al. "Intracity Quantum Communication via Thermal Microwave Networks", *Phys. Rev. X* **7**.1 (Mar. 2017). DOI: 10.1103/physrevx.7.011035.

[82] B. Vermersch et al. "Quantum State Transfer via Noisy Photonic and Phononic Waveguides", *Phys. Rev. Lett.* **118**.13 (Mar. 2017). DOI: 10.1103/physrevlett.118.133601.

[83] M. Anderlini et al. "Controlled exchange interaction between pairs of neutral atoms in an optical lattice", *Nature* **448**.7152 (July 2007), pp. 452–456. DOI: 10.1038/nature06011.

[84] O. Mandel et al. "Controlled collisions for multi-particle entanglement of optically trapped atoms", *Nature* **425**.6961 (Oct. 2003), pp. 937–940. DOI: 10.1038/nature02008.

[85] D. Leibfried et al. "Quantum dynamics of single trapped ions", *Rev. Mod. Phys.* **75**.1 (Mar. 2003), pp. 281–324. DOI: 10.1103/revmodphys.75.281.

[86] R. Blatt and D. Wineland. "Entangled states of trapped atomic ions", *Nature* **453**.7198 (June 2008), pp. 1008–1015. DOI: 10.1038/nature07125.

[87] M. D. Barrett et al. "Deterministic quantum teleportation of atomic qubits", *Nature* **429**.6993 (June 2004), pp. 737–739. DOI: 10.1038/nature02608.

[88] P. Goy et al. "Rydberg-atom masers. II. Triggering by external radiation and application to millimeter-wave detectors", *Phys. Rev. A* **27**.4 (Apr. 1983), pp. 2065–2081. DOI: 10.1103/physreva.27.2065.

[89] J. A. Sedlacek et al. "Microwave electrometry with Rydberg atoms in a vapour cell using bright atomic resonances", *Nat. Phys.* **8**.11 (Sept. 2012), pp. 819–824. DOI: 10.1038/nphys2423.

[90] H. Fan et al. "Atom based RF electric field sensing", *J. Phys. B: At., Mol. Opt. Phys.* **48**.20 (Sept. 2015), p. 202001. DOI: 10.1088/0953-4075/48/20/202001.

[91] J. Verdú et al. "Strong Magnetic Coupling of an Ultracold Gas to a Superconducting Waveguide Cavity", *Phys. Rev. Lett.* **103**.4 (July 2009). DOI: 10.1103/physrevlett.103.043603.

[92] R. W. Andrews et al. "Bidirectional and efficient conversion between microwave and optical light", *Nat. Phys.* **10**.4 (Mar. 2014), pp. 321–326. DOI: 10.1038/nphys2911.

[93] R. W. Andrews et al. "Connecting microwave and optical frequencies with a vibrational degree of freedom", *Proc. SPIE* **9343** (2015), pp. 934309–934309–8. DOI: 10.1117/12.2082941.

[94] A. Rueda et al. "Efficient microwave to optical photon conversion: an electro-optical realization", *Optica* **3**.6 (June 2016), p. 597. DOI: 10.1364/optica.3.000597.

[95] C. G. Wade et al. "Real-time near-field terahertz imaging with atomic optical fluorescence", *Nat. Photonics* **11**.1 (Nov. 2016), pp. 40–43. DOI: 10.1038/nphoton.2016.214.

[96] J. Han et al. "Free-space microwave-to-optical conversion via six-wave mixing in Rydberg atoms", *ArXiv* (2017). arXiv: 1701.07969v1 [physics.atom-ph].

[97] S. Bettelli et al. "Exciton dynamics in emergent Rydberg lattices", *Phys. Rev. A* **88** (Oct. 2013), p. 043436. DOI: 10.1103/PhysRevA.88.043436.

[98] P. Kolchin et al. "Electro-Optic Modulation of Single Photons", *Phys. Rev. Lett.* **101**.10 (Sept. 2008). DOI: 10.1103/physrevlett.101.103601.

[99] P. B. R. Nisbet-Jones et al. "Highly efficient source for indistinguishable single photons of controlled shape", *New J. Phys.* **13**.10 (Oct. 2011), p. 103036. DOI: 10.1088/1367-2630/13/10/103036.

[100] M. Himsworth et al. "EIT-based quantum memory for single photons from cavity-QED", *Appl. Phys. B* **103**.3 (May 2011), pp. 579–589. DOI: 10.1007/s00340-011-4523-2.

[101] J. D. Pritchard et al. "Optical non-linearity in a dynamical Rydberg gas", *J. Phys. B: At., Mol. Opt. Phys.* **44**.18 (Sept. 2011), p. 184019. DOI: 10.1088/0953-4075/44/18/184019.

[102] J. Pritchard. "Cooperative Optical Non-linearity in a blockaded Rydberg ensemble". PhD thesis. Durham University, 2011.

[103] D. Maxwell. "Light storage and control of photon-photon interactions in a cold Rydberg gas". PhD thesis. Durham University, 2013.

[104] D. Paredes-Barato. "Towards optical quantum information processing using Rydberg dark-state polaritons". PhD thesis. Durham University, 2014.

[105] H. Busche. "Contactless non-linear optics mediated by long-range Rydberg interactions". PhD thesis. Durham University, 2017.

[106] H. Busche, S. W. Ball, and P. Huillery. "A high repetition rate experimental setup for quantum non-linear optics with cold Rydberg atoms", *The European Physical Journal Special Topics* **225**.15 (2016), pp. 2839–2861. ISSN: 1951-6401. DOI: 10.1140/epjst/e2015-50338-3.

[107] W. Li et al. "Millimeter-wave spectroscopy of cold Rb Rydberg atoms in a magneto-optical trap: Quantum defects of thens,np, andndseries", *Phys. Rev. A* **67**.5 (May 2003). DOI: 10.1103/physreva.67.052502.

[108] J. Han et al. "Rb nF quantum defects from millimeter-wave spectroscopy of cold ^{85}Rb Rydberg atoms", *Phys. Rev. A* **74**.5 (Nov. 2006). DOI: 10.1103/physreva.74.054502.

[109] K. Afrousheh et al. "Determination of the ^{85}Rb nG-series quantum defect by electric-field-induced resonant energy transfer between cold Rydberg atoms", *Phys. Rev. A* **74**.6 (Dec. 2006). DOI: 10.1103/physreva.74.062712.

[110] C. A. Brau. *Modern Problems in Classical Electrodynamics (Physics)*. Oxford University Press, 2003. ISBN: 0195146654.

[111] T. G. Walker and M. Saffman. "Consequences of Zeeman degeneracy for the van der Waals blockade between Rydberg atoms", *Phys. Rev. A* **77**.3 (Mar. 2008). DOI: 10.1103/physreva.77.032723.

[112] K. A. Safinya et al. "Resonant Rydberg-Atom-Rydberg-Atom Collisions", *Phys. Rev. Lett.* **47**.6 (Aug. 1981), pp. 405–408. DOI: 10.1103/physrevlett.47.405.

[113] I. Mourachko et al. "Many-Body Effects in a Frozen Rydberg Gas", *Phys. Rev. Lett.* **80**.2 (Jan. 1998), pp. 253–256. DOI: 10.1103/physrevlett.80.253.

[114] T. Vogt et al. "Dipole Blockade at Förster Resonances in High Resolution Laser Excitation of Rydberg States of Cesium Atoms", *Phys. Rev. Lett.* **97** (Aug. 2006), p. 083003. DOI: 10.1103/PhysRevLett.97.083003.

[115] J. A. Petrus, P Bohlouli-Zanjani, and J. D. D. Martin. "ac electric-field-induced resonant energy transfer between cold Rydberg atoms", *J. Phys. B: At., Mol. Opt. Phys.* **41**.24 (Dec. 2008), p. 245001. DOI: 10.1088/0953-4075/41/24/245001.

[116] T. F. Gallagher et al. "Resonant Rydberg-atom — Rydbert-atom collisions", *Phys. Rev. A* **25** (Apr. 1982), pp. 1905–1917. DOI: 10.1103/PhysRevA.25.1905.

[117] S. H. Autler and C. H. Townes. "Stark Effect in Rapidly Varying Fields", *Phys. Rev.* **100** (Oct. 1955), pp. 703–722. DOI: 10.1103/PhysRev.100.703.

[118] M Tanasittikosol et al. "Microwave dressing of Rydberg dark states", *J. Phys. B: At., Mol. Opt. Phys.* **44**.18 (Sept. 2011), p. 184020. DOI: 10.1088/0953-4075/44/18/184020.

[119] E. Brekke, J. O. Day, and T. G. Walker. "Excitation suppression due to interactions between microwave-dressed Rydberg atoms", *Phys. Rev. A* **86**.3 (Sept. 2012). DOI: 10.1103/physreva.86.033406.

[120] M. Weidemüller. "Rydberg atoms: There can be only one", *Nat. Phys.* **5**.2 (Feb. 2009), pp. 91–92. DOI: 10.1038/nphys1193.

[121] R. Heidemann et al. "Evidence for Coherent Collective Rydberg Excitation in the Strong Blockade Regime", *Phys. Rev. Lett.* **99**.16 (Oct. 2007). DOI: 10.1103/physrevlett.99.163601.

[122] M. Saffman and T. G. Walker. "Creating single-atom and single-photon sources from entangled atomic ensembles", *Phys. Rev. A* **66** (Dec. 2002), p. 065403. DOI: 10.1103/PhysRevA.66.065403.

[123] L. H. Pedersen and K. Mølmer. "Few qubit atom-light interfaces with collective encoding", *Phys. Rev. A* **79**.1 (Jan. 2009). DOI: 10.1103/physreva.79.012320.

[124] T. C. Liebisch et al. "Atom Counting Statistics in Ensembles of Interacting Rydberg Atoms", *Phys. Rev. Lett.* **95**.25 (Dec. 2005). DOI: 10.1103/physrevlett.95.253002.

[125] M. Viteau et al. "Cooperative Excitation and Many-Body Interactions in a Cold Rydberg Gas", *Phys. Rev. Lett.* **109**.5 (July 2012). DOI: 10.1103/physrevlett.109.053002.

[126] H. Schempp et al. "Full Counting Statistics of Laser Excited Rydberg Aggregates in a One-Dimensional Geometry", *Phys. Rev. Lett.* **112**.1 (Jan. 2014). DOI: 10.1103/physrevlett.112.013002.

[127] T. Pohl, E. Demler, and M. D. Lukin. "Dynamical Crystallization in the Dipole Blockade of Ultracold Atoms", *Phys. Rev. Lett.* **104**.4 (Jan. 2010). DOI: 10.1103/physrevlett.104.043002.

[128] R. M. W. van Bijnen et al. "Adiabatic formation of Rydberg crystals with chirped laser pulses", *J. Phys. B: At., Mol. Opt. Phys.* **44**.18 (Sept. 2011), p. 184008. DOI: 10.1088/0953-4075/44/18/184008.

[129] J. Gea-Banacloche et al. "Electromagnetically induced transparency in ladder-type inhomogeneously broadened media: Theory and experiment", *Phys. Rev. A* **51** (Jan. 1995), pp. 576–584. DOI: 10.1103/PhysRevA.51.576.

[130] C. Cohen-Tannoudji, J. Dupont-Roc, and G. Grynberg. *Atom-Photon Interactions: Basic Processes and Applications*. Wiley-VCH, 1998. ISBN: 978-0-471-29336-1.

[131] D. Suter. *The Physics of Laser-Atom Interactions*. Cambridge University Press, Oct. 11, 1997. 472 pp. ISBN: 0521462398.

[132] C. J. Foot. *Atomic Physics*. Oxford University Press, Nov. 25, 2004. 344 pp. ISBN: 0198506961.

[133] G. Lindblad. "On the generators of quantum dynamical semigroups", *Commun Math Phys* **48**.2 (1976), pp. 119–130. ISSN: 1432-0916. DOI: 10.1007/BF01608499.

[134] R. Loudon. *The Quantum Theory of Light*. Oxford University Press, 2000.

[135] P. Lambropoulos and D. Petrosyan. *Fundamentals of quantum optics and quantum information*. Springer, 2007.

[136] M. D. Lukin et al. "Spectroscopy in Dense Coherent Media: Line Narrowing and Interference Effects", *Phys. Rev. Lett.* **79** (Oct. 1997), pp. 2959–2962. DOI: 10.1103/PhysRevLett.79.2959.

[137] S. E. Harris, J. E. Field, and A. Kasapi. "Dispersive properties of electromagnetically induced transparency", *Phys. Rev. A* **46** (July 1992), R29–R32. DOI: 10.1103/PhysRevA.46.R29.

[138] M. M. Kash et al. "Ultraslow Group Velocity and Enhanced Nonlinear Optical Effects in a Coherently Driven Hot Atomic Gas", *Phys. Rev. Lett.* **82** (June 1999), pp. 5229–5232. DOI: 10.1103/PhysRevLett.82.5229.

[139] D. Budker et al. "Nonlinear Magneto-optics and Reduced Group Velocity of Light in Atomic Vapor with Slow Ground State Relaxation", *Phys. Rev. Lett.* **83** (Aug. 1999), pp. 1767–1770. DOI: 10.1103/PhysRevLett.83.1767.

[140] S. E. Harris and L. V. Hau. "Nonlinear Optics at Low Light Levels", *Phys. Rev. Lett.* **82** (June 1999), pp. 4611–4614. DOI: 10.1103/PhysRevLett.82.4611.

[141] A. V. Gorshkov et al. "Photon storage in Λ-type optically dense atomic media. II. Free-space model", *Phys. Rev. A* **76** (Sept. 2007), p. 033805. DOI: 10.1103/PhysRevA.76.033805.

[142] D. F. Phillips et al. "Storage of Light in Atomic Vapor", *Phys. Rev. Lett.* **86** (Jan. 2001), pp. 783–786. DOI: 10.1103/PhysRevLett.86.783.

[143] M. Fleischhauer and M. D. Lukin. "Quantum memory for photons: Dark-state polaritons", *Phys. Rev. A* **65** (Jan. 2002), p. 022314. DOI: 10.1103/PhysRevA.65.022314.

[144] Y.-F. Hsiao et al. "EIT-based photonic memory with near-unity storage efficiency", *ArXiv* (May 2016). arXiv: 1605.08519v1 [quant-ph].

[145] Y. O. Dudin, L. Li, and A. Kuzmich. "Light storage on the time scale of a minute", *Phys. Rev. A* **87** (Mar. 2013), p. 031801. DOI: 10.1103/PhysRevA.87.031801.

[146] F. Ripka et al. "Rydberg polaritons in a thermal vapor", *Phys. Rev. A* **93** (May 2016), p. 053429. DOI: 10.1103/PhysRevA.93.053429.

[147] A. V. Gorshkov et al. "Universal Approach to Optimal Photon Storage in Atomic Media", *Phys. Rev. Lett.* **98** (Mar. 2007), p. 123601. DOI: 10.1103/PhysRevLett.98.123601.

[148] N. B. Phillips, A. V. Gorshkov, and I. Novikova. "Optimal light storage in atomic vapor", *Phys. Rev. A* **78** (Aug. 2008), p. 023801. DOI: 10.1103/PhysRevA.78.023801.

[149] F. Bariani, P. M. Goldbart, and T. A. B. Kennedy. "Dephasing dynamics of Rydberg atom spin waves", *Phys. Rev. A* **86** (Oct. 2012), p. 041802. DOI: 10.1103/PhysRevA.86.041802.

[150] R. Sorrentino and G. Bianchi. *Microwave and RF Engineering*. John Wiley & Sons, Apr. 18, 2010. 912 pp.

[151] J. Zeiher et al. "Microscopic Characterization of Scalable Coherent Rydberg Superatoms", *Phys. Rev. X* **5** (Aug. 2015), p. 031015. DOI: 10.1103/PhysRevX.5.031015.

[152] K. Dieckmann et al. "Two-dimensional magneto-optical trap as a source of slow atoms", *Phys. Rev. A* **58** (Nov. 1998), pp. 3891–3895. DOI: 10.1103/PhysRevA.58.3891.

[153] C. Hofmann et al. "An experimental approach for investigating many-body phenomena in Rydberg-interacting quantum systems", *Frontiers of Physics* **9**.5 (2014), p. 571.

[154] S. Götz et al. "Versatile cold atom target apparatus", *Rev. Sci. Instrum.* **83**.073112, 073112 (2012). DOI: 10.1063/1.4738643.

[155] S. Chaudhuri, S. Roy, and C. S. Unnikrishnan. "Realization of an intense cold Rb atomic beam based on a two-dimensional magneto-optical trap: Experiments and comparison with simulations", *Phys. Rev. A* **74** (Aug. 2006), p. 023406. DOI: 10.1103/PhysRevA.74.023406.

[156] T. G. Tiecke et al. "High-flux two-dimensional magneto-optical-trap source for cold lithium atoms", *Phys. Rev. A* **80** (July 2009), p. 013409. DOI: 10.1103/PhysRevA.80.013409.

[157] H Kurisu et al. "Application of titanium materials to vacuum chambers and components", *J. Phys. Conf. Ser.* **100**.9 (Mar. 2008), p. 092002. DOI: 10.1088/1742-6596/100/9/092002.

[158] J. D. Carter, O. Cherry, and J. D. D. Martin. "Electric-field sensing near the surface microstructure of an atom chip using cold Rydberg atoms", *Phys. Rev. A* **86**.5 (Nov. 2012). DOI: 10.1103/physreva.86.053401.

[159] J. Sedlacek et al. "Electric Field Cancellation on Quartz by Rb Adsorbate-Induced Negative Electron Affinity", *Phys. Rev. Lett.* **116**.13 (Mar. 2016). DOI: 10.1103/physrevlett.116.133201.

[160] W. Petrich et al. "Behavior of atoms in a compressed magneto-optical trap", *J. Opt. Soc. Am. B* **11**.8 (Aug. 1994), pp. 1332–1335. DOI: 10.1364/JOSAB.11.001332.

[161] D. A. Steck. "Rubidium 87 D Line Data". v2.1.5. Jan. 2015.

[162] D. J. McCarron, S. A. King, and S. L. Cornish. "Modulation transfer spectroscopy in atomic Rb", *Meas. Sci. Technol.* **19**.10 (Oct. 2008), p. 105601. DOI: 10.1088/0957-0233/19/10/105601.

[163] R. W. P. Drever et al. "Laser phase and frequency stabilization using an optical resonator", *Appl. Phys. B* **31**.2 (1983), pp. 97–105. ISSN: 1432-0649. DOI: 10.1007/BF00702605.

[164] W. Ketterle et al. "High densities of cold atoms in a dark spontaneous-force optical trap", *Phys. Rev. Lett.* **70** (Apr. 1993), pp. 2253–2256. DOI: 10.1103/PhysRevLett.70.2253.

[165] P. D. Lett et al. "Observation of Atoms Laser Cooled below the Doppler Limit", *Phys. Rev. Lett.* **61** (July 1988), pp. 169–172. DOI: 10.1103/PhysRevLett.61.169.

[166] C. Adams and E. Riis. "Laser cooling and trapping of neutral atoms", *Progress in Quantum Optics* **21**.1 (1997), pp. 1–79.

[167] C. S. Adams et al. "Evaporative Cooling in a Crossed Dipole Trap", *Phys. Rev. Lett.* **74** (May 1995), pp. 3577–3580. DOI: 10.1103/PhysRevLett.74.3577.

[168] R. Grimm, M. Weidemüller, and Y. B. Ovchinnikov. *Optical Dipole Traps for Neutral Atoms*. Ed. by B. Bederson and H. Walther. Vol. 42. Advances In Atomic, Molecular, and Optical Physics. Academic Press, 2000, pp. 95 –170. DOI: 10.1016/S1049-250X(08)60186-X.

[169] W. T. Silfvast. *Laser Fundamentals*. Cambridge University Press, July 11, 2008. ISBN: 0521541050.

[170] R. Löw et al. "An experimental and theoretical guide to strongly interacting Rydberg gases", *J. Phys. B: At., Mol. Opt. Phys.* **45**.11 (May 2012), p. 113001. DOI: 10.1088/0953-4075/45/11/113001.

[171] G. Günter et al. "Interaction Enhanced Imaging of Individual Rydberg Atoms in Dense Gases", *Phys. Rev. Lett.* **108**.1 (Jan. 2012). DOI: 10.1103/physrevlett.108.013002.

[172] G. Gunter et al. "Observing the Dynamics of Dipole-Mediated Energy Transport by Interaction-Enhanced Imaging", *Science* **342**.6161 (Nov. 2013), pp. 954–956. DOI: 10.1126/science.1244843.

[173] R. Hanbury Brown and R. Q. Twiss. "A Test of a New Type of Stellar Interferometer on Sirius", *Nature* **178** (Nov. 1956), p. 1046. DOI: 10.1038/1781046a0.

[174] P. Griffin. "Laser Cooling and Loading of Rb into A Large Period, Quasi-Electrostatic, Optical Lattice". PhD thesis. Durham University, 2005.

[175] K. Weatherill. "A CO_2 laser lattice experiment for cold atoms". PhD thesis. Durham University, 2007.

[176] T. Wiles. "Dynamics of Bright Solitary Matter-Waves". PhD thesis. Durham University, 2013.

[177] A. L. Marchant et al. "Quantum reflection of bright solitary matter waves from a narrow attractive potential", *Phys. Rev. A* **93**.2 (Feb. 2016). DOI: 10.1103/physreva.93.021604.

[178] P. D. Gregory et al. "Controlling the rotational and hyperfine state of ultracold $^{87}Rb^{133}Cs$ molecules", *Phys. Rev. A* **94**.4 (Oct. 2016). DOI: 10.1103/physreva.94.041403.

[179] S. A. Hopkins et al. "A versatile dual-species Zeeman slower for caesium and ytterbium", *Rev. Sci. Instrum.* **87**.4 (Apr. 2016), p. 043109. DOI: 10.1063/1.4945795.

[180] R. K. Hanley et al. "Probing interactions of thermal Sr Rydberg atoms using simultaneous optical and ion detection", *J. Phys. B: At., Mol. Opt. Phys.* **50**.11 (May 2017), p. 115002. DOI: 10.1088/1361-6455/aa6e79.

[181] N. Šibalić et al. "ARC: An open-source library for calculating properties of alkali Rydberg atoms", *Comput. Phys. Commun.* **220** (Nov. 2017), pp. 319–331. DOI: 10.1016/j.cpc.2017.06.015.

[182] R. P. Abel et al. "Laser frequency stabilization to excited state transitions using electromagnetically induced transparency in a cascade system", *Appl. Phys. Lett.* **94**.7, 071107 (2009). DOI: 10.1063/1.3086305.

[183] G. Marconi. *Transmitting electrical signals*. US Patent 586,193. July 1897.

[184] M. M. Weiner. *Monopole Antennas*. CRC Press, 2003. ISBN: 0824704967.

[185] O. Firstenberg et al. "Attractive photons in a quantum nonlinear medium", *Nature* **502**.7469 (Sept. 2013), pp. 71–75. DOI: 10.1038/nature12512.

[186] E. Distante et al. "Storing single photons emitted by a quantum memory on a highly excited Rydberg state", *Nat. Commun.* **8** (Jan. 2017), p. 14072. DOI: 10.1038/ncomms14072.

[187] F. Nogrette et al. "Single-Atom Trapping in Holographic 2D Arrays of Microtraps with Arbitrary Geometries", *Phys. Rev. X* **4**.2 (May 2014). DOI: 10.1103/physrevx.4.021034.

[188] H. Labuhn et al. "Tunable two-dimensional arrays of single Rydberg atoms for realizing quantum Ising models", *Nature* **534**.7609 (June 2016), pp. 667–670. DOI: 10.1038/nature18274.

[189] H. Labuhn. "Creating arbitrary 2D arrays of single atoms for the simulation of spin systems with Rydberg states", *The European Physical Journal Special Topics* **225**.15-16 (Dec. 2016), pp. 2817–2838. DOI: 10.1140/epjst/e2015-50336-5.

[190] D. Barredo et al. "An atom-by-atom assembler of defect-free arbitrary two-dimensional atomic arrays", *Science* **354**.6315 (Nov. 2016), pp. 1021–1023. DOI: 10.1126/science.aah3778.

[191] R. H. Dicke. "Coherence in Spontaneous Radiation Processes", *Phys. Rev.* **93**.1 (Jan. 1954), pp. 99–110. DOI: 10.1103/physrev.93.99.

[192] M. O. Scully et al. "Directed Spontaneous Emission from an Extended Ensemble of N Atoms: Timing Is Everything", *Phys. Rev. Lett.* **96**.1 (Jan. 2006). DOI: 10.1103/physrevlett.96.010501.

[193] R. W. Boyd. *Nonlinear Optics*. Elsevier, May 11, 2008. 640 pp. ISBN: 0123694701.

[194] J. Nipper et al. "Highly Resolved Measurements of Stark-Tuned Förster Resonances between Rydberg Atoms", *Phys. Rev. Lett.* **108**.11 (Mar. 2012). DOI: 10.1103/physrevlett.108.113001.

[195] M. R. Sprague et al. "Broadband single-photon-level memory in a hollow-core photonic crystal fibre", *Nat. Photonics* **8**.4 (Mar. 2014), pp. 287–291. DOI: 10.1038/nphoton.2014.45.

[196] C. Sayrin et al. "Storage of fiber-guided light in a nanofiber-trapped ensemble of cold atoms", *Optica* **2**.4 (Apr. 2015), p. 353. DOI: 10.1364/optica.2.000353.

[197] B. Gouraud et al. "Demonstration of a Memory for Tightly Guided Light in an Optical Nanofiber", *Phys. Rev. Lett.* **114**.18 (May 2015). DOI: 10.1103/physrevlett.114.180503.

[198] A. Politi et al. "Silica-on-Silicon Waveguide Quantum Circuits", *Science* **320**.5876 (May 2008), pp. 646–649. DOI: 10.1126/science.1155441.

[199] M. Kohnen et al. "An array of integrated atom–photon junctions", *Nat. Photonics* **5**.1 (Nov. 2010), pp. 35–38. DOI: 10.1038/nphoton.2010.255.

[200] I. G. Hughes and T. P. A. Hase. *Measurements and their Uncertainties A practical guide to modern error analysis*. Oxford University Press, July 11, 2010. 160 pp. ISBN: 019956633X.

[201] W. Riley and D. Howe. "Handbook of Frequency Stability Analysis", *Spec. Publ. (NISP SP)* **1065** (2008).

[202] A. Rose. "The Sensitivity Performance of the Human Eye on an Absolute Scale", *J. Opt. Soc. Am.* **38**.2 (Feb. 1948), p. 196. DOI: 10.1364/josa.38.000196.

[203] J. A. Gordon et al. "2010 Int'l Symp. on electromagnetic compatibility", 2010.

[204] S. W. Ellingson. "Sensitivity of Antenna Arrays for Long-Wavelength Radio Astronomy", *IEEE Trans. Antennas Propag.* **59**.6 (June 2011), pp. 1855–1863. DOI: 10.1109/tap.2011.2122230.

[205] Ofcom. *United Kingdom Table of Radio Frequency Allocations 9 kHz - 105 GHz*. Accessed December 2015. 2015.

[206] E. F. Knott, M. T. Tuley, and J. F. Shaeffer. *Radar Cross Section*. Scitech Pub., Nov. 11, 2003. 611 pp. ISBN: 1891121251.

[207] K. Zikidis, A. Skondras, and C. Tokas. "Low observable principles, stealth aircraft and anti-stealth technologies", *2nd int'l conf. on applications of mathematics and informatics in military sciences*. 2013.

[208] V. A. Tishchenko. "The beginning of the metrology of radio frequency electromagnetic fields and the first standards of electric field strength", *Meas. Tech.* **46**.1 (2003), pp. 76–84. DOI: 10.1023/a:1023425908932.

[209] M. Kanda and R. D. Orr. "Generation of standard electromegnetic fields in a TEM cell", *NBS technical note* **1319** (1988).

[210] M. Kanda. "Standard Probes for Electromagnetic Field Measurements", *IEEE Trans. Antennas Propag.* **41**.10 (Oct. 1993).

[211] J. Hall. "Defining and measuring optical frequencies", *Nobel Lecture* (2006).

[212] I. M. Savukov et al. "Tunable Atomic Magnetometer for Detection of Radio-Frequency Magnetic Fields", *Phys. Rev. Lett.* **95**.6 (Aug. 2005). DOI: 10.1103/physrevlett.95.063004.

[213] M. V. Balabas et al. "Polarized Alkali-Metal Vapor with Minute-Long Transverse Spin-Relaxation Time", *Phys. Rev. Lett.* **105**.7 (Aug. 2010). DOI: 10.1103/physrevlett.105.070801.

[214] W. Wasilewski et al. "Quantum Noise Limited and Entanglement-Assisted Magnetometry", *Phys. Rev. Lett.* **104**.13 (Mar. 2010). DOI: 10.1103/physrevlett.104.133601.

[215] M. Brune et al. "Quantum Rabi Oscillation: A Direct Test of Field Quantization in a Cavity", *Phys. Rev. Lett.* **76**.11 (Mar. 1996), pp. 1800–1803. DOI: 10.1103/physrevlett.76.1800.

[216] B. R. Johnson et al. "Quantum non-demolition detection of single microwave photons in a circuit", *Nat. Phys.* **6**.9 (June 2010), pp. 663–667. DOI: 10.1038/nphys1710.

[217] D Bozyigit et al. "Correlation measurements of individual microwave photons emitted from a symmetric cavity", *J. Phys. Conf. Ser.* **264** (Jan. 2011), p. 012024. DOI: 10.1088/1742-6596/264/1/012024.

[218] K. Inomata et al. "Single microwave-photon detector using an artificial Λ-type three-level system", *Nat. Commun.* **7** (July 2016), p. 12303. DOI: 10.1038/ncomms12303.

[219] J. A. Sedlacek et al. "Atom-Based Vector Microwave Electrometry Using Rubidium Rydberg Atoms in a Vapor Cell", *Phys. Rev. Lett.* **111**.6 (Aug. 2013). DOI: 10.1103/physrevlett.111.063001.

[220] D. Allan. "Statistics of atomic frequency standards", *Proc. IEEE* **54**.2 (1966), pp. 221–230. DOI: 10.1109/proc.1966.4634.

[221] J. J. Stambaugh, R. K. Lee, and W. H. Cantrell. "The 4 GHz bandwidth millimetre-wave radar", *Lincoln Laboratory Journal* **19**.2 (2012).

[222] S. E. Anderson. "Trapping Rydberg atoms in ponderomotive optical lattices". PhD thesis. University of Michigan, 2014.

[223] U Volz and H Schmoranzer. "Precision lifetime measurements on alkali atoms and on helium by beam–gas–laser spectroscopy", *Phys. Scr.* **T65** (Jan. 1996), pp. 48–56. DOI: 10.1088/0031-8949/1996/t65/007.

[224] S. K. Dutta et al. "Ponderomotive Optical Lattice for Rydberg Atoms", *Phys. Rev. Lett.* **85** (Dec. 2000), pp. 5551–5554. DOI: 10.1103/PhysRevLett.85.5551.

[225] K. C. Younge et al. "State-Dependent Energy Shifts of Rydberg Atoms in a Ponderomotive Optical Lattice", *Phys. Rev. Lett.* **104**.17 (Apr. 2010). DOI: 10.1103/physrevlett.104.173001.

[226] R Mukherjee et al. "Many-body physics with alkaline-earth Rydberg lattices", *J. Phys. B: At., Mol. Opt. Phys.* **44**.18 (Sept. 2011), p. 184010. DOI: 10.1088/0953-4075/44/18/184010.

[227] K. C. Younge, S. E. Anderson, and G. Raithel. "Adiabatic potentials for Rydberg atoms in a ponderomotive optical lattice", *New J. Phys.* **12**.2 (Feb. 2010), p. 023031. DOI: 10.1088/1367-2630/12/2/023031.

[228] M. Saffman and T. G. Walker. "Analysis of a quantum logic device based on dipole-dipole interactions of optically trapped Rydberg atoms", *Phys. Rev. A* **72** (Aug. 2005), p. 022347. DOI: 10.1103/PhysRevA.72.022347.

[229] S. Zhang, F. Robicheaux, and M. Saffman. "Magic-wavelength optical traps for Rydberg atoms", *Phys. Rev. A* **84** (Oct. 2011), p. 043408. DOI: 10.1103/PhysRevA.84.043408.

[230] E. A. Goldschmidt et al. "Magic wavelengths for the 5s–18s transition in rubidium", *Phys. Rev. A* **91** (Mar. 2015), p. 032518. DOI: 10.1103/PhysRevA.91.032518.

[231] R. M. Potvliege and C. S. Adams. "Photo-ionization in far-off-resonance optical lattices", *New J. Phys.* **8**.8 (2006), p. 163.

[232] J. Tallant, D. Booth, and J. P. Shaffer. "Photoionization rates of Cs Rydberg atoms in a 1064-nm far-off-resonance trap", *Phys. Rev. A* **82** (Dec. 2010), p. 063406. DOI: 10.1103/PhysRevA.82.063406.

[233] T. D. Ladd et al. "Quantum computers", *Nature* **464**.7285 (Mar. 2010), pp. 45–53. DOI: 10.1038/nature08812.

[234] M. Hafezi et al. "Atomic interface between microwave and optical photons", *Phys. Rev. A* **85**.2 (Feb. 2012). DOI: 10.1103/physreva.85.020302.

[235] J. L. O'Brien, A. Furusawa, and J. Vučković. "Photonic quantum technologies", *Nat. Photonics* **3**.12 (Dec. 2009), pp. 687–695. DOI: 10.1038/nphoton.2009.229.

[236] A. Imamoğlu. "Cavity QED Based on Collective Magnetic Dipole Coupling: Spin Ensembles as Hybrid Two-Level Systems", *Phys. Rev. Lett.* **102**.8 (Feb. 2009). DOI: 10.1103/physrevlett.102.083602.

[237] D. Marcos et al. "Coupling Nitrogen-Vacancy Centers in Diamond to Superconducting Flux Qubits", *Phys. Rev. Lett.* **105**.21 (Nov. 2010). DOI: 10.1103/physrevlett.105.210501.

[238] H. Wu et al. "Storage of Multiple Coherent Microwave Excitations in an Electron Spin Ensemble", *Phys. Rev. Lett.* **105**.14 (Sept. 2010). DOI: 10.1103/physrevlett.105.140503.

[239] Y. Kubo et al. "Strong Coupling of a Spin Ensemble to a Superconducting Resonator", *Phys. Rev. Lett.* **105**.14 (Sept. 2010). DOI: 10.1103/physrevlett.105.140502.

[240] R. Amsüss et al. "Cavity QED with Magnetically Coupled Collective Spin States", *Phys. Rev. Lett.* **107**.6 (Aug. 2011). DOI: 10.1103/physrevlett.107.060502.

[241] M. Tsang. "Cavity quantum electro-optics", *Phys. Rev. A* **81**.6 (June 2010). DOI: 10.1103/physreva.81.063837.

[242] C. A. Regal and K. W. Lehnert. "From cavity electromechanics to cavity optomechanics", *J. Phys. Conf. Ser.* **264** (Jan. 2011), p. 012025. DOI: 10.1088/1742-6596/264/1/012025.

[243] J. M. Taylor et al. "Laser Cooling and Optical Detection of Excitations in a LC Electrical Circuit", *Phys. Rev. Lett.* **107**.27 (Dec. 2011). DOI: 10.1103/physrevlett.107.273601.

[244] D. Kim et al. "Microwave-driven coherent operation of a semiconductor quantum dot charge qubit", *Nat. Nanotechnol.* **10**.3 (Feb. 2015), pp. 243–247. DOI: 10.1038/nnano.2014.336.

[245] A. Kuhn, M. Hennrich, and G. Rempe. "Deterministic Single-Photon Source for Distributed Quantum Networking", *Phys. Rev. Lett.* **89** (July 2002), p. 067901. DOI: 10.1103/PhysRevLett.89.067901.

[246] L.-M. Duan, A. Kuzmich, and H. J. Kimble. "Cavity QED and quantum-information processing with 'hot' trapped atoms", *Phys. Rev. A* **67** (Mar. 2003), p. 032305. DOI: 10.1103/PhysRevA.67.032305.

[247] J. McKeever et al. "Deterministic generation of single photons from one atom trapped in a cavity", *Science* **3o3**.5666 (2004), pp. 1992–1994.

[248] A. Kuhn and D. Ljunggren. "Cavity-based single-photon sources", *Contemp. Phys.* **51**.4 (2010), pp. 289–313. DOI: 10.1080/00107511003602990.

[249] G. S. Vasilev, D. Ljunggren, and A. Kuhn. "Single photons made-to-measure", *New J. Phys.* **12**.6 (June 2010), p. 063024. DOI: 10.1088/1367-2630/12/6/063024.

[250] M. Mücke et al. "Generation of single photons from an atom-cavity system", *Phys. Rev. A* **87**.6 (June 2013). DOI: 10.1103/physreva.87.063805.

[251] E. Bimbard et al. "Homodyne Tomography of a Single Photon Retrieved on Demand from a Cavity-Enhanced Cold Atom Memory", *Phys. Rev. Lett.* **112**.3 (Jan. 2014). DOI: 10.1103/physrevlett.112.033601.

[252] M. M. Müller et al. "Room-temperature Rydberg single-photon source", *Phys. Rev. A* **87**.5 (May 2013). DOI: 10.1103/physreva.87.053412.

[253] D. Whiting et al. "Single-Photon Interference due to Motion in an Atomic Collective Excitation", *Phys. Rev. Lett.* **118**.25 (June 2017). DOI: 10.1103/physrevlett.118.253601.

[254] P. Nisbet-Jones. "Shaping single photons". PhD thesis. Oxford University, 2012.

[255] D. Barredo et al. "Coherent Excitation Transfer in a Spin Chain of Three Rydberg Atoms", *Phys. Rev. Lett.* **114**.11 (Mar. 2015). DOI: 10.1103/physrevlett.114.113002.

[256] S. A. Lee et al. "Doppler-free two-photon transitions to Rydberg levels: convenient, useful, and precise reference wavelengths for dye lasers", *Opt. Lett.* **3**.4 (Oct. 1978), p. 141. DOI: 10.1364/ol.3.000141.

[257] C. E. Shannon. "Communication in the Presence of Noise", *Proc. IRE* **37**.1 (Jan. 1949), pp. 10–21. ISSN: 0096-8390. DOI: 10.1109/JRPROC.1949.232969.

[258] A. Gaj et al. "From molecular spectra to a density shift in dense Rydberg gases", *Nat. Commun.* **5** (Aug. 2014). DOI: 10.1038/ncomms5546.

[259] M. Schlagmüller et al. "Probing an Electron Scattering Resonance using Rydberg Molecules within a Dense and Ultracold Gas", *Phys. Rev. Lett.* **116**.5 (Feb. 2016). DOI: 10.1103/physrevlett.116.053001.

[260] F. Camargo et al. "Lifetimes of ultra-long-range strontium Rydberg molecules", *Phys. Rev. A* **93**.2 (Feb. 2016). DOI: 10.1103/physreva.93.022702.

[261] J. B. Balewski et al. "Coupling a single electron to a Bose–Einstein condensate", *Nature* **502**.7473 (Oct. 2013), pp. 664–667. DOI: 10.1038/nature12592.

[262] W. Ketterle. "Spring 2006 Lecture notes (Ch. 9)". MIT. 2006.

[263] Z. Popović and B. Popović. *Introductory Electromagnetics*. Prentice Hall, 1999.

[264] *521-2002 - IEEE Standard Letter Designations for Radar-Frequency Bands*. 1976.

[265] *Request for Approval of the NATO Joint Civil Military Frequency Agreement (NFJA) 2002*. North Atlantic Council, 2002.

[266] I. S. Association. *IEEE Standards for Information Technology - Telecommunications and information exhcange between systems. Local and metropolitan area networks - specific requirements. Part 11: Wireless LAN medium access Control (MAC) and Physical Layer (PHY) Specifications. Amendment 4: Enhancements for Very High Throughput for Operation in Bands below 6GHz*. 2013.

[267] IETF. *Electromagnetic compatibility and Radio spectrum Matters (ERM); Wideband transmission systems; Data transmission equipment operating in the 2.4 GHz ISM band and using wide band modulation techniques; Harmonised EN covering the essential requirements of the article 3.2 of the R&TTE Directive*. Accessed December 2015. 2015.

[268] D. J. C. MacKay. *Information Theory, Inference and Learning Algorithms*. Cambridge University Pr., Sept. 11, 2003. ISBN: 0521642981.

[269] E. G. Altmann and M. Gerlach. "Statistical Laws in Linguistics", *Lecture Notes in Morphogenesis*. Springer International Publishing, 2016, pp. 7–26. DOI: 10.1007/978-3-319-24403-7_2.